Characterization and Modeling of Nanoporous Carbon Structures

Dissertation
zur Erlangung des Grades
des Doktors der Naturwissenschaften
der Naturwissenschaftlich-Technischen Fakultät III
Chemie, Pharmazie, Bio- und Werkstoffwissenschaften
der Universität des Saarlandes

Erarbeitet unter gemeinsamer Betreuung mit der École
nationale supérieure des mines de Paris

von Torben Prill

Saarbrücken

9.1.2015

Tag des Kolloquiums: 17.12.2014

Dekan: Univ.-Prof. Dr.-Ing. Dirk Bähre

Berichterstatter: PD Dr. habil. Martin Spies
                       Prof. Dominique Jeulin
                       Prof. Dr.-Ing. Frank Mücklich
Vorsitz: Prof. Dr. Christian Motz
Akad. Mitarbeiter: Dr.-Ing. Frank Aubertin

"I am eye. I am a mechanical eye. I, a machine, am showing you a world, the likes of which only I can see."

Dziga Vertov

Abstract

Characterization and Modeling of Nanoporous Carbon Structures

by Torben Prill

The aim of the work presented here is to optimize nanoporous carbon materials by means of 'virtual material design'. On this length scale ($\approx$ 10nm) Focused Ion Beam - Scanning Electron Microscopy Nanotomography (FIB-SEM) is the only imaging technique providing three-dimensional geometric information. Yet, for the optimization, the pore space of the materials must be reconstructed from the resulting image data, which was a generally unsolved problem so far.

To overcome this problem, a simulation method for FIB-SEM images was developed. The resulting synthetic FIB-SEM images could then be used to test and validate segmentation algorithms. Using simulated image data, a new algorithm for the morphological segmentation of the highly porous structures from FIB-SEM data was developed, enabling the reconstruction of the three-dimensional pore space from FIB-SEM images.

Two case studies with nanoporous carbons used for energy storage are presented, using the new techniques for the characterization and optimization of electrodes of Li-ion batteries and electric double layer capacitors (EDLC's), respectively. The reconstructed pore space is modeled geometrically by means of stochastic geometry. Finally, the electrical properties of the materials were simulated using both imaged real and modeled structures.

In the first part of the thesis, a novel simulation program for FIB-SEM nanotomography is described. The program can, for the first time, generate completely artificial FIB-SEM tomographic images of highly porous materials, described by Boolean models of spheres or cylinders. The computation of which, using standard methods, would have taken weeks, even on high-performance machines. To this end, new acceleration techniques were developed and combined with existing techniques, reducing the simulation time by several orders of magnitude, without loss of physical accuracy. Results of simulated FIB-SEM nanotomograms of highly complex structures are presented, consisting of more than one hundred 2D images.

In the second part, a new segmentation algorithm for FIB-SEM data is presented, enabling the reconstruction of the three-dimensional structure of highly porous materials, imaged by FIB-SEM nanotomography. The new method uses mathematical morphology, and is shown to be the best performing documented in literature so far. For the first time, simulated FIB-SEM data has been used to verify the correctness of the new

method. In two case studies, the geometric structure of a nanoporous additive for Li-ion battery electrodes and nanoporous carbon electrodes for electric double layer capacitors (EDLC's) are reconstructed.

The optimization of porous materials requires virtual representations of their pore space. This is achieved by using models from stochastic geometry, as described in the third part of the thesis. Virtual models are described, representing the nanoporous additive as well as the EDLC electrodes. The additive is modeled by level sets of a Gaussian random field, while for the EDLC electrodes a modified version of the Boolean model of spheres has been used. The modified Boolean model has been fitted to the observed structure by means of simulating realizations of the model and minimizing a similarity measure using stochastic optimization. The models, fitted to the reconstructed pore spaces of both materials, show good agreement.

In the final part of the thesis, electrical properties of the electrodes made from the nanoporous carbons are predicted using physical simulations.

For Lithium-Ion batteries, the influence of the nanoporous carbon on the charging behavior is investigated using simulations. A multi-scale model is employed using the segmented FIB-SEM and synchrotron radiation computed tomography data. This establishes for the first time a multi-scale process for simulations, combining both experimental techniques. The additive is homogenized on the nanoscale and inserted as an effective medium into the microscale electrode. It is found, that the additive has a non negligible influence on the charging behavior.

Multi-scale simulations are also used to investigate the electrical behavior of nanoporous carbon electrodes for EDLC's. To this end, the effective resistivities and capacitances of the electrodes are computed using the segmented FIB-SEM data sets. Then, a macro-homogeneous model is fitted to a measured electric impedance spectrum of one of the samples, using the computed effective properties. Finally, the microscale simulations are performed on model realizations with a given parameter range. This enables us to optimize the resistance and the capacitance of the electrode.

Résumé

Caractérisation et Modélisation de Structures Carbonées Nanoporeuses

par Torben Prill

L'objectif de la thèse présentée ici est l'optimisation de matériaux carbonés nanoporeux au moyen de la "conception de matériaux virtuels". En ce qui concerne cette échelle de travail ($\approx$ 10nm) la Nanotomographie FIB-SEM est la seule technique d'imagerie donnant accès à une information sur la géométrie tridimensionnelle. Cependant, pour l'optimisation du comportement, l'espace des pores doit être reconstruit à partir des données tirées des images obtenues. Jusqu'à présent ce problème n'était pas résolu.

Pour pouvoir le maîtriser, on a developpé une simulation d'images FIB-SEM. Les images FIB-SEM simulées peuvent être utilisées pour la vérification et la validation des algorithmes de segmentation. En utilisant les données d'image simulées, un nouvel algorithme pour la reconstruction de l'espace des pores à partir des données FIB-SEM a été developpé.

Deux études de cas avec des carbones nanoporeux utilisés pour le stockage d'énergie sont présentées, en utilisant les nouvelles techniques pour la caractérisation et l'optimisation des électrodes Li-ion de type EDLC'S (" electric double-layer capacitors ", soit super-condensateurs). L'espace des pores reconstruit est modélisé géométriquement à l'aide de la géométrie stochastique. Enfin, on a simulé les propriétés électriques des matériaux en utilisant des structures modélisées et simulées.

Dans la première partie de cette thèse un nouveau logiciel de simulation pour la nanotomographie FIB-SEM est décrit. Ce logiciel donne pour la première fois la possibilité de générer des images tomographiques FIB-SEM complètement artificielles de matériaux fortement poreux décrits par des modèles booléens de sphères ou de cylindres. En utilisant des méthodes standard, la simulation correspondante aurait pris des semaines, même sur des machines très performantes. A cette fin, de nouveaux outils d'accélération ont été developpés et combinés à des algorithmes existant, réduisant le temps de simulation par différentes méthodes de réduction de dimension - sans perte d'exactitude physique. Des résultats de nanotomogrammes FIB-SEM simulés de structures hautement complexes, qui se composent de plus de cent images, sont présentés.

Dans la deuxième partie, un nouvel algorithme de segmentation des données FIB-SEM est présenté, rendant possible la reconstruction de la structure tridimensionnelle de matériaux fortement poreux imagés par nanotomographie FIB-SEM. La nouvelle méthode utilise la morphologie mathématique, et de toute évidence est la méthode la

plus performante de la littérature jusqu'à présent. Pour la première fois des données FIB-SEM simulées ont été utilisées pour démontrer l'exactitude de cette nouvelle méthode. Dans deux études de cas, la structure géométrique d'un liant nanoporeux pour des électrodes de batteries lithium-ion et des électrodes de carbone nanoporeux pour des EDLC'S sont reconstruits.

L'optimisation de matériaux poreux demande des représentations virtuelles de leur espace poreux. On les obtient par l'usage de modèles de géomètrie stochastique, comme décrit dans la troisième partie de cette thèse. Des modèles virtuels sont décrits, représentant le liant nanoporeux ainsi que les électrodes EDLC. Le liant est modélisé par seuillage d'un champ aléatoire gaussien tandis qu'une version modifiée du modèle booléen de sphères a été utilisée pour les électrodes EDLC. Le modèle booléen modifié a été calé sur la structure observée en simulant des réalisations du modèle et en minimisant les écarts entre simulation et observations par optimisation stochastique. Les modèles ajustés de l'espace poreux des deux matériaux montrent une bonne équivalence.

Dans la dernière partie de la thèse, des propriétés électriques des électrodes en carbone nanoporeux sont prédites par des simulations physiques.

Pour les batteries lithium-ion, l'influence du carbone nanoporeux sur le comportement en cours de chargement est examinée par des simulations. Un modèle multi-échelles est employé en utilisant les données FIB-SEM segmentées et les données tomographiques obtenues par rayonnement synchrotron. Pour cela, un processus de simulations multi-échelles, combinant les deux techniques expérimentales, est mis en oeuvre. Le liant est homogénéisé à l'échelle nanométrique et intégré comme milieu effectif dans la microstructure de l'électrode. On a constaté que le liant exerce une influence non négligeable sur le comportement en cours de chargement.

On utilise des simulations multi-échelles également pour l'étude du comportement en chargement électrique des électrodes de carbone nanoporeux pour des EDLC's. A cette fin, les résistivités effectives et les capacités électriques des électrodes sont calculées en utilisant des jeux de données FIB-SEM segmentés. Ensuite, un modèle macro-homogène est adapté au spectre d'impédance électrique mesuré sur un des échantillons en utilisant les propriétés effectives calculées. Finalement, des simulations sont effectuées à l'échelle micro sur des réalisations de modèles pour un domaine de variation des paramètres. Ceci nous permet d'optimiser la résistance et de la capacité électrique de l'électrode.

Zusammenfassung

Charakterisierung und Modellierung nanoporöser Kohlenstoffstrukturen

von Torben Prill

Das Ziel dieser Arbeit ist die Optimierung von nanoporösen Kohlenstoffmaterialien durch virtuelles Materialdesign. Auf dieser Längenskala (≈ 10 nm) kann nur die Focused Ion Beam - Scanning Electron Microscopy Nanotomography (FIB-SEM) die Geometrie einer Probe dreidimensional abbilden. Jedoch muss für eine Optimierung des Materials der Porenraum aus den Bilddaten rekonstruiert werden. Dies war ein bisher im Allgemeinen ungelöstes Problem.

Um das Rekonstruktionsproblem zu lösen, wurde eine Simulationsmethode für FIB-SEM-Bilder entwickelt. Die sich daraus ergebenden synthetischen Bilder konnten dann benutzt werden, um Segmentierungsalgorithmen zu testen und zu validieren. Mit den simulierten Daten wurde ein neuer, auf mathematischer Morphologie basierender Segmentierungsalgorithmus entwickelt, welcher es erlaubt den dreidimensionalen Porenraum hochporöser Materialien zu rekonstruieren.

In dieser Arbeit werden zwei Fallstudien mit nanoporösen Kohlenstoffen für Energiespeicherung vorgestellt, in denen die neuen Techniken zur Charakterisierung und Optimierung von Elektrodenmaterialien für Li-Ionen-Akkus sowie Doppelschichtkondensatoren (EDLCs) eingesetzt werden. Dann wurde der rekonstruierte Porenraum mit Hilfe der stochastischen Geometrie geometrisch modelliert. Letztendlich wurden die elektrischen Eigenschaften der Materialien simuliert, sowohl auf echten abgebildeten Strukturen, als auch auf modellierten Strukturen.

Im ersten Teil der Arbeit wird ein neues Simulationsprogramm für FIB-SEM-Nanotomographie vorgestellt. Das Programm erlaubt es erstmals vollständige künstliche FIB-SEM-Tomographiebilder hochporöser Materialien zu erstellen, welche durch Boolesche Modelle aus Kugeln oder Zylindern beschrieben werden. Eine Rechnung dieser Art würde, durchgeführt mit Standardmethoden, selbst auf Hochleistungsrechnern Wochen in Anspruch nehmen. Daher wurden neue Beschleunigungsverfahren entwickelt und mit existierenden Verfahren kombiniert, was die Rechenzeit um mehrere Größenordnungen reduziert, ohne die physikalische Korrektheit zu beeinträchtigen. Am Ende des ersten Teils werden simulierte FIB-SEM-Daten hochkomplexer Strukturen vorgestellt, welche jeweils aus über 100 Einzelbildern bestehen.

Im anschließenden zweiten Teil der Arbeit wird ein neuer Segmentierungsalgorithmus für FIB-SEM-Daten vorgestellt, welcher es ermglicht, die dreidimensionale Struktur

hochporöser Materialien zu rekonstruieren, welche mit FIB-SEM abgebildet wurden. Die neue Methode basiert auf mathematischer Morphologie und es konnte gezeigt werden, dass sie bessere Ergebnisse liefert als die in der Literatur dokumentierten Segmentierungsmethoden. Zum ersten Mal wurden auch synthetische FIB-SEM-Daten benutzt, um die Korrektheit der neuen Segmentierungsmethode zu verifizieren. Für die zwei Fallstudien wurden die nanoporöse Geometrie des Additivs und des EDLC-Elektrodenmaterials rekonstruiert.

Die Optimierung poröser Materialien benötigt virtuelle Darstellungen ihrer Porenräume. Dies wird erreicht durch Modellierung mittels stochastischer Geometrie, wie sie im dritten Teil der Arbeit beschrieben wird. Stochastische Modelle werden beschrieben, welche die Struktur des nanoporösen Additivs sowie der EDLC-Elektroden reproduzieren. Das Additiv wird durch Level-Sets eines Gaussian-Random-Fields modelliert, während ein modifiziertes Boolesches Modell für die Modellierung der EDLC-Elektroden benutzt wurde. Das modifizierte Boolesche Modell wurde mittels der Minimierung eines Ähnlichkeitsmaßes, welche aus Realisierungen des Modells berechnet wurde, an die beobachtete Struktur angepasst. Für die Minimierung wurde ein stochastischer Optimierungsalgorithmus verwendet. Die beobachteten Strukturen zeigen jeweils gute Übereinstimmung mit den Modellen.

Im letzten Teil der Arbeit werden die elektrischen Eigenschaften der Elektroden berechnet, welche aus nanoporösen Kohlenstoffen hergestellt wurden.

In der ersten Simulationsstudie wird der Einfluss des nanoporösen Additivs auf das Ladeverhalten der Li-Ionen-Batterie untersucht. Dazu wird eine Multiskalensimulation auf den segmentierten Datensätzen des Additivs und eine Synchrotron-Tomographieaufnahme verwendet. Dies erlaubt zum ersten Mal in einem Multiskalenprozess, Daten aus beiden experimentellen Techniken in einer Simulation zu kombinieren. Dazu wird die Ionenleitfähigkeit des Additivs auf der Nanoskala homogenisiert und als effektive Leitfähigkeit auf der Mikroskala in die Elektrode eingebracht. Die Simulationsstudie hat ergab, dass das Additiv einen nicht vernachlässigbaren Einfluss auf das Ladeverhalten der Batterie hat.

Ebenfalls mit einem Multiskalenmodell wurde das elektrische Verhalten der nanoporösen EDLC Elektrode simuliert. Dazu wurden die effektiven Leitfähigkeiten für elektrischen Strom in der festen Phase und fü Ionen im Porenraum berechnet. Dann wurde ein makrohomogenes Modell an experimentelle Impedanzspektroskopiedaten angepasst, unter Verwendung der berechneten Eigenschaften. Schlussendlich werden Simulationen auf der Mikroskala verwendet, um die elektrische Leitfähigkeit und die Kapazität von Modellrealisierungen zu berechnen. Diese Daten können dann dazu verwendet werden, Leitfähigkeit und Kapazität der Elektroden zu optimieren.

Danksagung

Contents

List of Figures

List of Tables

1

Introduction

Energy storage plays an important role in modern industrialized societies. It is widely assumed, that due to climate change and a foreseeable scarcity of fossil resources, the production and storage of energy will be of increasing importance. To tackle these challenges, new technologies are needed, which leads to a pressure for innovation and development of energy storage technology. Thus, the materials science of energy materials is of vital importance.

Materials with pore spaces on the microscopic scale play a special role in energy materials, since they provide a high surface area and permit transport of mass and charge through the pore space. Simultaneously, the ever increasing power of modern computers has created a trend to design materials virtually, using modeling and physical simulations, a process called virtual material design. An exemplary workflow for the virtual design of a porous material is depicted in Figure 1.1. First, a structural analysis of the material is made, reconstructing the pore space of the material. In order to optimize the pore structure, a model is developed and fitted to the reconstruction. This allows systematic modifications made to the virtual pore structure. Then, using physical simulations, the properties of the modeled structure are predicted. In an iterative loop, the model is modified and simulations are made for the modified model in order to find the optimal structure to a given requirement. Finally, the information gained on the optimal structure is used as a goal for the production of the optimal material.

The motivation of the work for this thesis, was to improve materials for energy storage by virtual material design. To this end, new techniques for the analysis, characterization and modeling of a class of energy materials were developed. Also, two applications are discussed, where the new techniques have been used to either optimize an existing class of materials or to achieve a better understanding of a material.
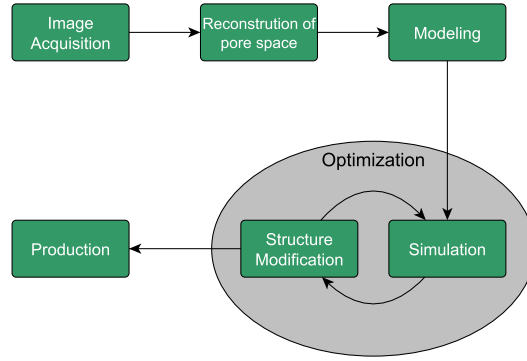
FIGURE 1.1: Virtual Material Design Workflow

1.1   Thesis Outline

The starting point of this work was the problem posed by the segmentation of Focused Ion Beam Scanning Electron Microscopy nanotomography (FIB-SEM) data of a nanoporous additive in a Li-ion battery, which is the application case given in Section 1.2.1. At the time, the segmentation problem could not be solved, in particular due to the 'shine-through'-artifacts introduced by the FIB-SEM imaging process (see Figure 3.4 on Page 60). For FIB-SEM datasets there is no ground truth available, yet it was needed for the development and testing of the segmentation algorithms for FIB-SEM data. Hence, a decision was made to develop a simulation program for FIB-SEM nanotomography. This program could then be used to test segmentation algorithms on synthetic data, which have a known result. With the simulation at hand, a new segmentation algorithm was then developed using mathematical morphology. After work on the segmentation algorithm was finished, application cases were found in the battery additive mentioned before as well as in a class of nanoporous battery electrodes for electric double layer capacitors. For both case studies, FIB-SEM data were segmented, reconstructing the pore space. Then, for both materials, stochastic models were fitted to the reconstructed structures. Finally, simulation studies were made for both applications.

Reflecting the course of the work, the thesis has four main parts, each laid out as one chapter:

- Simulation of FIB-SEM Data Sets,

- Morphological Segmentation of FIB-SEM Data,

- Stochastic Modeling of Porous Microstructures,

- Simulation of Physical Properties,

where each chapter builds upon the results of the preceding one.

The FIB-SEM simulation program is described in Chapter 2 and has also been published in Prill and Schladitz [2013], Prill et al. [2012]. The segmentation algorithm is described in Chapter 3 and has been published in Prill et al. [2013b]. Testing on synthetic data revealed that it outperformed any segmentation documented in literature at the time. Also, from Chapter 3 on, results for both case studies are presented in the results section of each chapter.

In order to optimize the microstructure of both materials, the need for modeling of the segmented structures arose. Models from stochastic geometry fitted to both electrode materials are shown in Chapter 4. A version of a Gaussian Random Field Cut model was fitted to the nanoporous additive for Li-ion batteries. In order to model the EDLC electrodes a non-standard version of a Boolean model was used, which emulates the smooth morphology of the electrode material by a Gaussian filter and subsequent thresholding.

In Chapter 5 simulations of the physical behavior of both systems are discussed. For the lithium-ion battery electrode, a study was made to compute the influence of the nanoporous additive on the charging of the battery. The resulting charging curves are shown in Section 5.3. For the EDLC electrode, important electrical properties have been computed, to investigate the influence of the mesopores on the electrical properties of the electrodes. Also, properties of modeled structures were computed, which can be used to optimize the pore space properties to given requirements.

But first of all, in this chapter, a more detailed description of the materials discussed in this thesis is given. Then, important concepts of stochastic geometry and mathematical morphology are discussed, which are necessary for understanding the image processing and modeling in this thesis.

1.2 Materials

Two porous materials are discussed in this thesis, which have been studied experimentally and theoretically. The analysis and modeling techniques developed for this thesis have been applied to both systems, to achieve a better understanding of the materials and to make suggestions for possible improvements.

1.2.1   Li-Ion Batteries

In the first case study, the segmentation, modeling and simulations were used to assess the influence of a nanoporous additive on the charging and discharging behavior. The electrode material consists of a 70 μm thick layer of Timcal SLP30 graphite particles applied to a copper foil. The particles have a diameter of about $d = 30$ μm and are responsible for the ion storage in the electrode, hence they are called 'active particles'. An SEM image of the active particles is shown in Figure 1.2. When the electrode charges, lithium ions intercalate into the active particles, storing charge in the electrode. To improve the conductivity between the particles and the mechanical stability, an additive consisting of Timcal Super P Li particles and a binder is added to the material, which can be seen as a third phase in the SEM image. The additive has a particle size of about $d = 40$ nm, which cannot be resolved by μCT.
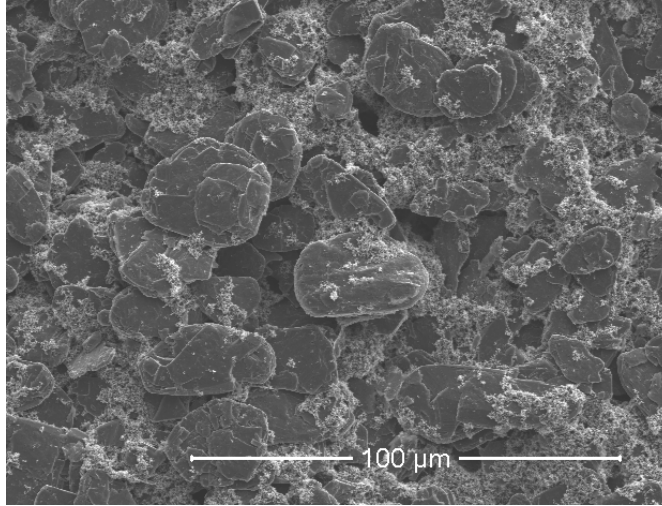
FIGURE 1.2: SEM image of active particles in the lithium ion battery electrode.

This additive is porous at the nanoscale. The porosity can be seen in Figure 1.3, where a magnified view is shown of the additive taken with an SEM. The porosity allows the lithium ions to penetrate through the additive, improving the lithium flow into the electrode. Yet, the additive still represents a diffusion resistance for the lithium ions. To investigate the influence of the active particles on the ion transport during the discharge of the battery has been one application for the analysis and modeling methods developed in this thesis.

For the study, the additive has been imaged using FIB-SEM nanotomography. Then with the segmentation algorithm, the nanoporous structure has been reconstructed. The segmentation of the nanoporous additive is shown in Section 3.5.1. The pore space between the active particles has been imaged using micro computed tomography at a beam line at ESRF (see Figure 1.4).
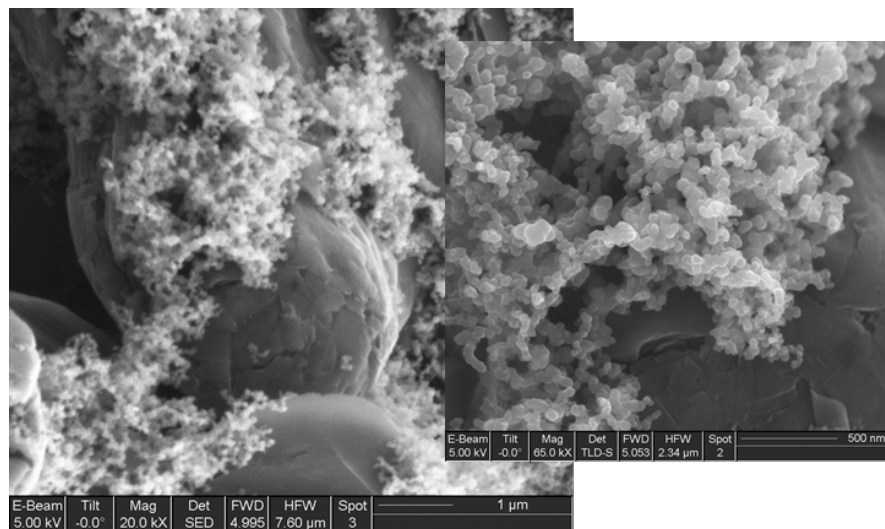
FIGURE 1.3: Zoom into the additive improving the conductivity between the active particles.
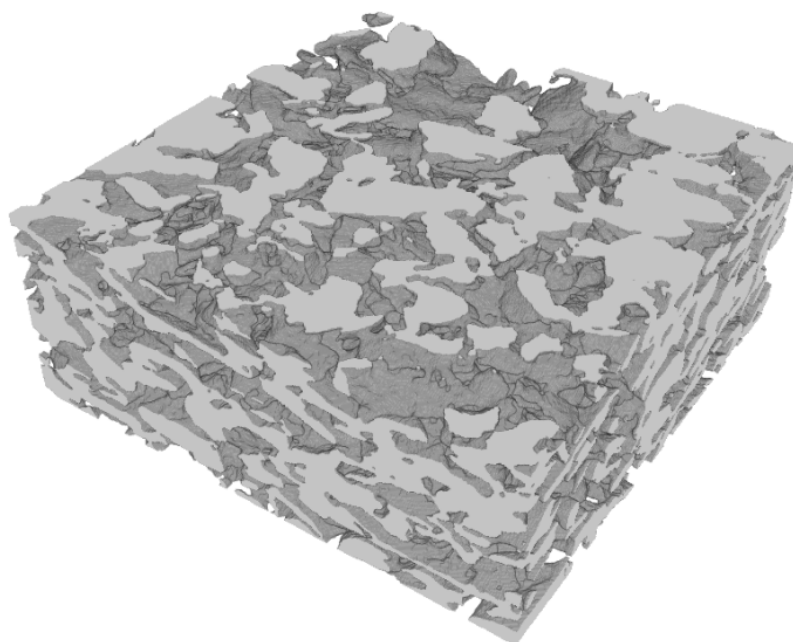
FIGURE 1.4: Volume rendering of the segmented porous electrode without additive.

Then the diffusion resistance of the additive has been calculated by simulating the diffusion on the segmented solid phase of the additive, as shown in Section 5.3. This results in an effective diffusivity for the additive, which can be used in macroscopic simulations. Finally, the discharging of the electrode has been simulated using the CT dataset. Several simulations have been made at different loads, with and without considering the additive in the simulation. The resulting discharge curves are shown in Section 5.3.2, and an interpretation on the additives influence on the curves is given.

1.2.2   Electric Double Layer Capacitor

The second material investigated in this thesis is a nanoporous electrode for electrical double layer capacitors (EDLC's). The electrode material is a nanoporous carbon with a two scale pore space. Measurements on the material have shown that the smaller pores have a diameter below two nanometers, and thus cannot be resolved with the SEM. These pores are referred to as micropores in the following. The bigger pores are called mesopores and have diameters of tens of nanometers. These pores can be resolved with SEM and were imaged three dimensionally with FIB-SEM nanotomography.

The bulk material consists of activated carbon nanoparticles, which form the micropores during activation. Also, the nanoparticles are sintered during the activation process. To prevent the particles form completely 'baking together', a pore stabilizer is added, to produce larger pores, called the mesopores. The size of the mesopores can be influenced by the amount of pore stabilizer added (Bruno et al. [2010]). There have been two samples of the material, produced in the same process, yet with different a amount of stabilizer, yielding two different microstructures (see Figure 1.5). The two data sets are referred to as S12 (Figure 1.5, left) and S14 (Figure 1.5, right).
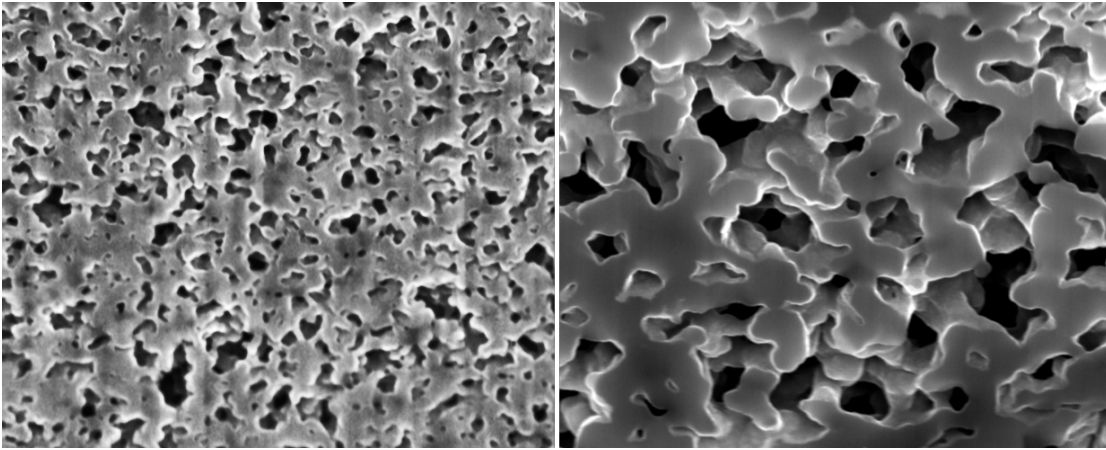
FIGURE 1.5: SEM images of the two mirostructures of EDLC electrodes, S12 (left) and S14 (right).

The goal of the analysis of this material is to optimize the mesopore structure. Therefore, the datasets have been segmented in Chapter 3. A stochastic model has been developed to model the mesopore space, while mimicking the sintering of the particles. The model has been fitted to the samples S12 and S14 in Chapter 4, yielding different parameters each. Then, the dependence of the resistance and the capacitance of the mesopore structure has been investigated using multi-scale simulations (see Chapter 5). Finally, both properties are computed on realizations of the stochastic model. This information can be used to optimize the pore structure to given requirements.

1.3 Mathematical Preliminaries

In this Section some mathematical concepts important throughout the thesis will be introduced. Other mathematical models and theories, specific to the chapters, will be introduced as they are needed.

1.3.1 Random Closed Sets

Later in the thesis microstructures will be modeled by random structures, which will be represented by random sets. Since specific random models are used throughout the thesis, the necessary theory will be introduced in this section. As we talk about random sets, the theory of sets is revised based on the review given in Stoyan et al. [1995]. Extensive treatments of random sets can be found in Matheron [1975], Schneider and Weil [2008], Serra [1988], Stoyan et al. [1995].

1.3.1.1 Basic Elements of Set Theory

A set is a collection of mathematical objects and is usually written with braces. For examples the set S defined as

$$S = \{1, 2, 3, 4\}, \tag{1.1}$$

is the set containing the numbers 1 through 4. All objects x in the set are called elements of the set, in mathematical notation $x \in S$.

Important mathematical operations on sets are the union, the intersection and the difference defined by

$$A \cup B = \quad \{x \in S : x \in A \text{ or } x \in B\}, \tag{1.2}$$

$$A \cap B = \quad \{x \in S : x \in A \text{ and } x \in B\}, \tag{1.3}$$

$$A \setminus B = \quad \{x \in S : x \in A \text{ but not } x \in B\}. \tag{1.4}$$

The latter definition is used to define the complementary set given by

$$A^c = \{x \in S : x \notin A\}. \tag{1.5}$$

Even though it is not explicitly given this definition depends on some superset S, where $A \subset S$. In this thesis the superset will be either an image, where the complement comprises the pixels/voxels of the image not in the set A, or Euclidean space, where the complement will be all points in space not in the set A.

Also, implicit definitions of sets can be given, like the interval

$$(a, b) = \{x \in \mathbb{R} : a < x < b\} \tag{1.6}$$

which contains all real numbers greater than a and less than b. Thus (a,b) is a subset of $\mathbb{R}$, $(a, b) \subset \mathbb{R}$.

For the models in this thesis, it is sufficient to consider subsets S of the n-dimensional Euclidean space $S \subset \mathbb{R}^n$. As all structures will be either linear $S \subset \mathbb{R}$, planar $S \subset \mathbb{R}^2$ or three dimensional $S \subset \mathbb{R}^3$. Since all elements of the sets are elements of a vector space, they allow the operations of addition and multiplication. To define these operations for the sets, the operations are computed on the elements of the set. Hence, the set multiplication is defined by

$$cA = \{cx : x \in A\} \tag{1.7}$$

for real $c \in \mathbb{R}$ and $A \subset \mathbb{R}^n$. If $c = -1$ the multiplied set is called the reflected set $\check{A}$

$$\check{A} = -A = \{-x : x \in A\}. \tag{1.8}$$

With the elementwise addition, sets can be translated. Thus the translated set by a vector x is given by

$$A_x = A + x = \{y + x : y \in A\}, \tag{1.9}$$

for $A \subset \mathbb{R}^n$. Both the reflected set and the translated set will be used to define morphological operations.

Other operations on sets needed later are the Minkowski addition and subtraction of two sets A and B with $A, B \subset \mathbb{R}^n$. The Minkowski addition is defined by

$$A \oplus B = \{x + y : x \in A, y \in B\}. \tag{1.10}$$

The Minkowski subtraction is analogously defined by

$$A \ominus B = \{x - y : x \in A, y \in B\}. \tag{1.11}$$

The effect of these operations on subsets of Euclidean spaces can be seen when using them in morphological operations as in Section 1.3.3.

1.3.1.2 Random Closed Sets

Many microstructures and all microstructures in this thesis are modeled as random closed sets (RACS). RACS comprise a huge class of models and are thus a quite general concept. Later, some prominent examples will be introduced, but before that, some theory with some important definitions will be reiterated. The Theory of RACS has been intensively studied by G. Matheron (Matheron [1975]).

A RACS is an extension of a random number to closed subsets of a general space. In this thesis, we will restrict ourselves to closed subsets of $\mathbb{R}^d$. Just like a random number is a measurable mapping from some probability space Ω into the real numbers $\mathbb{R}$ with a suitable σ-algebra, a random set is a mapping from a probability space Ω into the subsets of $\mathbb{R}^d$, again with a suitable σ-algebra. The technicalities are quite tricky and are discussed in Stoyan et al. [1995] and Schneider and Weil [2008]. Intuitively, as each realization of a real number is a number drawn from a distribution (e.g. normal, Poisson), each realization of a RACS is a subset of $\mathbb{R}^d$. The equivalent of the distribution is determined by the model, i.e. the definition of the RACS. Thus the definition of the RACS is a broad concept which leaves a lot of space for model building. Still, some general results and properties are defined in the next section.

1.3.1.3 The Choquet Theorem

An important result from the theory of RACS is the Choquet Theorem. It states that any RACS Ξ can be characterized by its Choquet Capacity

$$T_\Xi(K) = P(\Xi \cap K \neq \emptyset). \tag{1.12}$$

The argument of the Choquet capacity are all compact subsets of $\mathbb{R}^d$, denoted K. For each K, the Choquet capacity take values between 0 and 1. It can be shown, that the Choquet capacity completely characterizes the random set. In practice the complete capacity cannot be computed, so one resorts to a number of compact sets to characterize the RACS. For example, the set consisting of the two points $\{x, x + h\}$ separated by a vector h will be used to measure the covariance of the set. Also, a ball of radius r will be used to determine the spherical contact distribution function. In general, the characterization becomes more descriptive the more sets are used. The exact choice of sets yet remains intuitive and dependent on the model.

1.3.1.4 Stationarity and Isotropy

Stationarity of a RACS is the equivalent to homogeneity in physical theories. A RACS is stationary if the distribution is invariant under translation, i.e. the set Ξ and the translated set Ξ_x by a vector x have the same Choquet capacity. Thus $\forall x \in \mathbb{R}, K \in \mathbb{K}$,

$$T_\Xi(K) = T_{\Xi_x}(K). \tag{1.13}$$

Similarly, the set is said to be isotropic iff. its distribution is invariant under rotation, i.e.

$$T_\Xi(K) = T_{R\Xi}(K), \tag{1.14}$$

where $R\Xi$ is the rotated set and R is some rotation matrix.

1.3.1.5 Ergodicity

Another important property of RACS, in the context of measurements, is ergodicity. A random set Ξ is ergodic if:

$$\lim_{n \to \infty} \frac{1}{\text{Vol}(W_n)} \int [1 - T_\Xi(K \cup K'_x)]dV = (1 - T_\Xi(K))(1 - T_\Xi(K'_x)), \tag{1.15}$$

where W_n is a convex observation window of size n, e.g. a ball of radius n, and K and K' are convex sets.

This is important, since properties of RACS are often given by spatial averages of the form

$$\frac{1}{\text{Vol}(W_n)} \int_{W_n} f(\Xi)dV. \tag{1.16}$$

For ergodic sets it can be proven, that estimations on one realization of these spatial averages converge to the ensemble average over all realizations in the limit of an infinitely

large observation window, i.e.

$$\lim_{n\to\infty} \frac{1}{\mathrm{Vol}(W_n)} \int_{W_n} f(\Xi)dV = E(f(\Xi)),\tag{1.17}$$

where the expectation is taken over all realizations.

In particular, the ergodicity implies that estimations of properties of RACS like covariance and granulometry (see Section 4.2 for definitions), taken on one realization, will converge to a deterministic value for large observations windows. This enables to estimate these properties on single images of a structure. All RACS in this thesis, i.e. Poisson point procsses, Boolean Models and Random Fields are ergodic random sets.

1.3.2 The Poisson Point process

For the acceleration of the SEM simulation, the SE generation will be modeled as a Poisson point process. Also, the Poisson point process is the basis for the stochastic modeling of microstructures in Chapter 4. Hence, the Poisson point process will be described in this section in quite general form, starting with general point processes.

A general point process is a locally finite set of points

$$\Phi = \{x_0, \dots, x_n\}\tag{1.18}$$

randomly distributed in space $\mathbb{R}^n$ (see Figure 1.6). Typical n used in this thesis, will be $n = 1$ where the Poisson point process is a collection of point on the real line, $n = 2$ which corresponds to a collection of point on a two-dimensional space, e.g. an image, and $n = 3$ which corresponds to a distribution of points in space, what will be used to model three-dimensional microstructures. Figure 1.6 shows a realization of a point process in two dimensions. It can be shown that Φ is a random closed set as defines in Section 1.3.1.

A simple example for a point process, is the stationary Poisson point process. The Poisson point process can be defined in different ways, but the two following properties suffice:

1. The number of points of Φ in a bounded set is Poisson distributed with some density parameter $\lambda > 0$ of the process, thus

$$P(\Phi(B) = m) = (\lambda V(B))^m \frac{exp(-\lambda V(B))}{m!}.\tag{1.19}$$
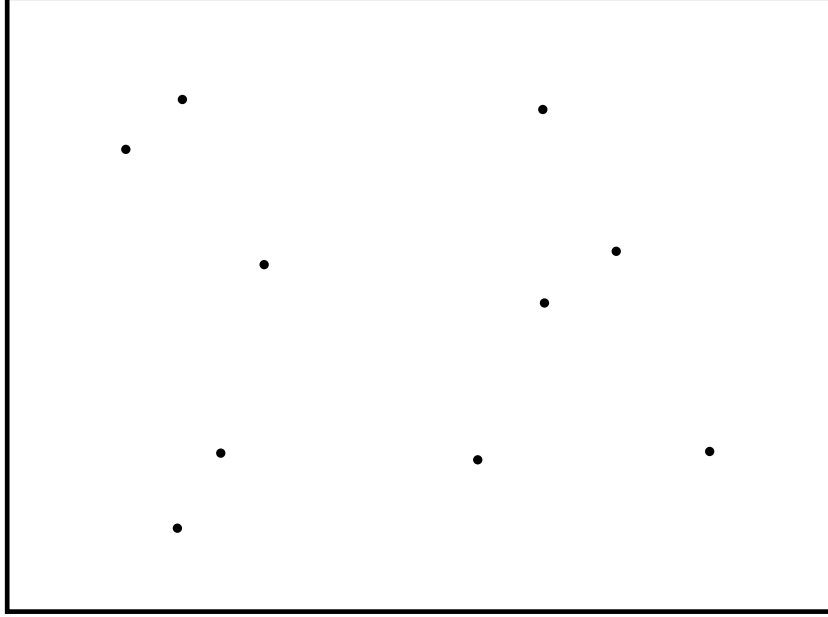
FIGURE 1.6: Realization of a point process: Points are randomly placed in a two dimensional space.

Where $P(\Phi(B) = m)$ is the probability of having m points in the set B and $V(B)$ is the volume of B.

2. The number of points in disjoint subsets of $\mathbb{R}^n$ are independent random variables.

Like any other RACS, the Poisson point process is completely characterized by its Choquet capacity (see the Choquet theorem in 1.3.1.3). Even though the Choquet capacity is defined for all compact sets, individual void probabilities of different measurable sets B are important properties of the process. A common characteristic is the void probability, which is given by

$$\nu_B = P(\Phi \cap B = \emptyset), \tag{1.20}$$

where B is a compact subset of $\mathbb{R}^n$. For a stationary Poisson process, the void probability is given by

$$\nu_B = e^{-\lambda \text{Vol}(B)}. \tag{1.21}$$

Another common characteristic is the contact distribution function, which is closely related to the void probability. The contact distribution function for the set B is given by:

$$H_B(r) = 1 - \nu_{rB} = 1 - P(rB \cap \Phi = \emptyset). \tag{1.22}$$

Important special cases of B are the unit ball which yields the spherical contact distribution H_S with

$$H_S(r) = 1 - exp(-\lambda V_B^d(r)), \tag{1.23}$$

where $V_B(r)$ is the volume of a ball of radius r in d dimensions. Thus

$$V_B^1(r) = \quad 2r \text{ in 1D,} \tag{1.24}$$

$$V_B^2(r) = \quad 4\pi r^2 \text{ in 2D,} \tag{1.25}$$

$$V_B^3(r) = \quad \tfrac{4}{3}\pi r^3 \text{ in 3D.} \tag{1.26}$$

The spherical contact distribution function is the probability of hitting at least one point of the process with a randomly placed sphere in space. Also for stationary processes it is the distribution function of the distance from the origin to the closest point of the process.

The stationary Poisson point process can be generalized to the definition of the general Poisson point process, which also includes a variable intensity $\lambda(x)$. Then property one in the above definition has to be extended to

$$P(\Phi(B) = m) = \quad \Lambda(B)^m \frac{exp(-\Lambda(B))}{m!} \tag{1.27}$$

$$\Lambda(B) = \quad \int_B \lambda(x)dx, \tag{1.28}$$

while property (2) remains unchanged.

Intuitively the variable intensity can be interpreted as $\lambda(x)$ being the probability of having a point at position x. The general process is not stationary, unless the intensity $\lambda(x)$ is invariant under translation. When using a variable intensity, the void probabilities and contact distribution functions have to be modified accordingly.

1.3.3 Mathematical Morphology

Mathematical Morphology is a method used in image processing which contrary to most other methods works with sets instead of functions. For an overview see Serra [1988]. Although the mathematical framework is defined for sets, these sets can be represented by binary images. Also, mathematical morphology can be defined for gray level images. The basis of morphology is made of two fundamental operations, erosion and dilation. Even though more complex operations are possible (and widely used) all of them are based on the two fundamental ones. Both dilation and erosion can be defined using the Minkowski addition and subtraction respectively.
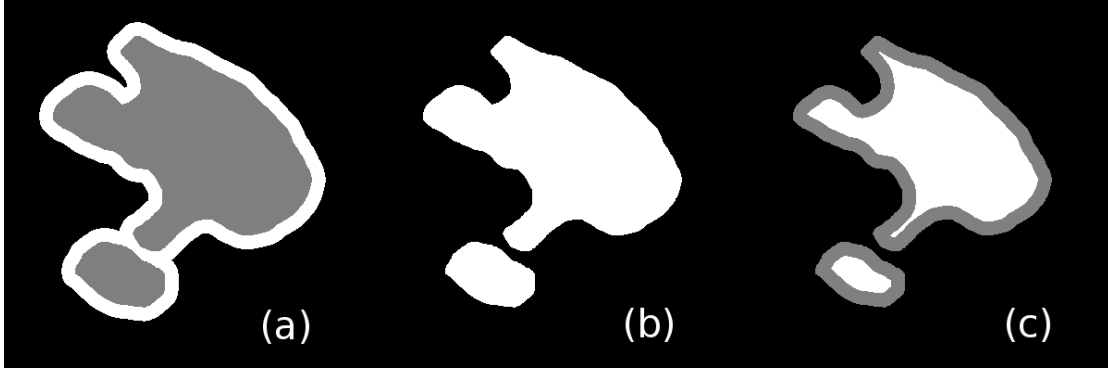
FIGURE 1.7: Effects of the morphological dilation and erosion on a dummy set (b):
the dilation enlarges the set and closes small gaps as in (a), the erosion makes the set
smaller and erases small details as in (c). (The original set is indicated in gray)

1.3.3.1   Dilation and Erosion

The dilation of A with B is defined as

$$A \rightarrow A \oplus \check{B}, \tag{1.29}$$

where $\check{B}$ is the reflected set of B and $\oplus$ is the Minkowski addition as in (1.10)

$$\check{B} = \{-x : x \in B\}. \tag{1.30}$$

Analogously to the dilation we can define the erosion by

$$A \rightarrow A \ominus \check{B}. \tag{1.31}$$

with the Minkowski subtraction as in (1.11).

The effect of these operations is demonstrated in Figure 1.7. In a dilation, the reflected
set $\check{B}$ is translated over all space. Every point covered by the set B, if it still intersects A
is included in the dilated set. In an erosion all points which are covered by $\check{B}$ during the
translation while still hitting the complement are removed from the set. Thus the shape
of B determines the outcome of the dilation. In the terminology of morphology, the set
B is called the structuring element. Usual structuring elements are line segments, balls,
and squares of various sizes.

In the course of this thesis we adopt the notation in Soille [1999]. So the dilated set is
written as

$$\delta_B(A) = \bigcup_{b \in B} A_{-b} \tag{1.32}$$

and the eroded set is written as

$$\epsilon_B(A) = \bigcap_{b \in B} A_{-b}. \tag{1.33}$$

1.3.3.2 Opening and Closing

In the course of the thesis more complex operations are used, either for image processing in Chapter 3 or for image analysis in Chapter 4. These operations can be constructed from combinations of erosions and dilations. The simplest ones are the morphological closing and opening. The closing $\gamma_B(A)$ is defined by a dilation with the SE and a consecutive erosion with the reflected structuring element

$$\phi_B(A) = \epsilon_{\check{B}}[\delta_B]. \tag{1.34}$$

Analogously the opening is defined by

$$\gamma_B(A) = \delta_{\check{B}}[\epsilon_B]. \tag{1.35}$$

1.3.3.3 Grayscale Morphology

Although originally defined for sets, morphological operations can be extended to grayscale images. Since all morphological operations are defined with the fundamental dilation and erosion, a definition of these operations for grayscale images is sufficient. Therefore, the union and the intersection are replaced by the infimum and the supremum operation, respectively. This leads to the definition of the dilation on an image f with structuring element B as

$$\delta_B(f) = \bigvee_{b \in B} f_{-b} \tag{1.36}$$

with the supremum operation $\bigvee$. The erosion on grayscale images is defined analogously with the infimum operation $\bigwedge$ as

$$\epsilon_B(f) = \bigwedge_{b \in B} f_{-b}. \tag{1.37}$$

The opening and closing operations are defined as before, but with the new grayscale dilation and erosion operation.

1.3.3.4 Morphological Gradient

Another common operation on gray scale images as well as on sets is the morphological gradient ρ_B with the structuring element B (see Beucher [1990]). The morphological gradient is defined as the difference of between the dilation and erosion

$$\rho_B(f) = \delta_B(f) - \epsilon_B(f).$$ (1.38)

For grayscale images, the morphological gradient has similar properties than the usual gradient magnitude operator in standard image processing. If the structuring element is a ball of radius λ, it can be shown that in the limit

$$\rho_B = \lim_{\lambda \to 0} \frac{\delta_{\lambda B} - \epsilon_{\lambda B}}{2\lambda}$$ (1.39)

on a differentiable function the morphological gradient is equivalent to the norm of the gradient $\rho(f) = \|\nabla f\|$. These and more complex operations will be used to solve the segmentation problem in Chapter 3 and to characterize random sets in Chapter 4.

2
Simulation of FIB-SEM Data Sets

The work in this chapter has been published in:

T. Prill and K. Schladitz. Simulation of FIB-SEM images for analysis of porous microstructures. *Scanning*, 35(3):189–195, 2013

and

T. Prill, K. Schladitz, and C. Wieser. Simulation of FIB-SEM images for segmentation of porous microstructures. *Proceedings of the 1st International Conference on 3D Materials Science*, pages 159–164, 2012

2.1 Scanning Electron Microscopy and FIB-SEM Nanotomography

Scanning Electron Microscopy (SEM) (Reimer [1998]) is a high resolution imaging technique, designed to analyze materials down to the nanoscale. It is a 2D imaging technique which can, depending on the signal used, resolve topological or chemical information (For a picture of an SEM equipment see Figure 2.1). Its fields of application range from the analysis of biological specimens to crystallography and material science. It is typically used for the analysis on length scales from several micrometers to several nanometers. Thus, its resolution lies between the microanalysis with micro-Computed Tomography (micro CT) and sub-nanometer analysis with instruments such as the atomic force microscope and transmission electron microscope. In the course of this dissertation, it is used to analyze the topology of nanoporous carbon structures.
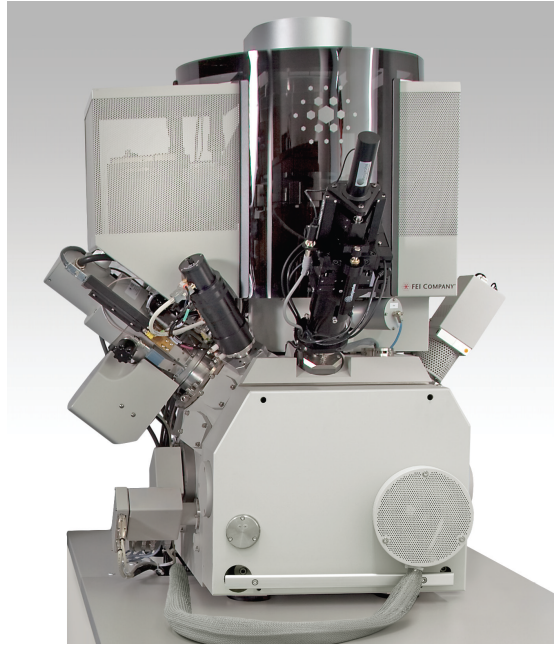
FIGURE 2.1: Photo of a FEI Helios Nanolab 600i Dual Beam FIB-SEM station (source:
FEI Helios NanoLab 600i Datasheet from www.fei.com)

For the imaging, an electron beam is generated by a cathode and focused by an array
of coils onto the specimen (Fig 2.2). When the beam hits the specimen, it interacts
with the specimen and generates signals, which can be detected by different detectors.
To form an image, the electron beam scans the specimen line by line and the signal
intensity is displayed as gray values on a screen. The result is a two-dimensional image
of the corresponding signal. The signals most commonly used consist of electrons that
are radiated from the focus point, such as the backscattered electron signal (BSE) and
the secondary electron signal (SE), but also X-rays which can be detected. Each signal
contains different information on the material and through the scanning, the signals
can be resolved spatially. The BSE and the X-ray signal can be used to resolve the
chemical composition of the specimen while the SE signal is mostly used to analyze the
topography of the specimen, i.e. the microstructure. Since the electron beam can be
focused to a very small area, SEM provides a very high resolution down to the nanometer
scale.

For the interpretation of the images, it is necessary to understand the generation of the
different signals. In general, at the interaction point the electrons enter the specimen
and diffuse through the material, forming a diffusion cloud also called the interaction
volume (see Figure 2.3). As can be seen in Figure 2.3, there is usually a non-zero electron
density at the surface, thus electrons from the beam can escape from the surface. When
detected, they form the backscattered electron signal (BSE). Throughout the diffusion
process the electrons lose energy through inelastic scattering with the atoms or molecules
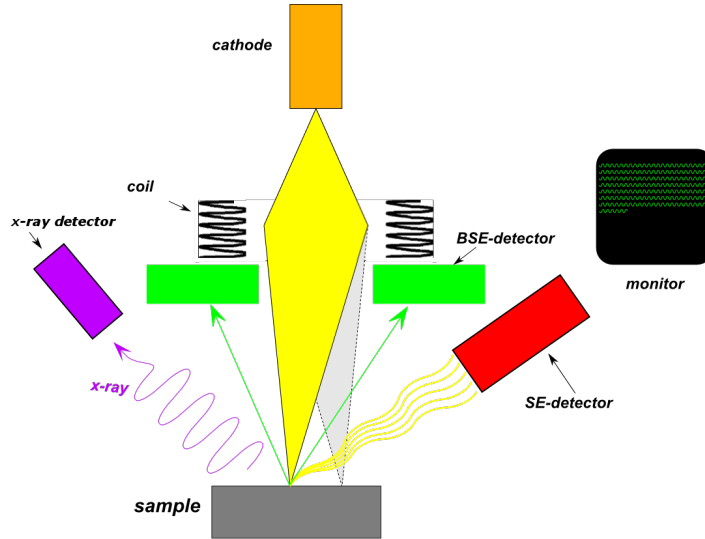
FIGURE 2.2: Schematic view of the Scanning Electron Microscope.

of the material. Since the intensity of the BSE signal is roughly proportional to the area of intersection of the diffusion cloud with the surface, the intensity of the BSE signal rises with the angle of incidence of the beam. This results in a shading effect from the specimen surface.

As the electrons from the beam diffuse through the material, they scatter inelastically at the atoms and molecules. In this process, they lose energy which is usually converted into heat, but sometimes the energy liberates a bound electron from an atom or molecule in the crystal structure which then in turn diffuses through the specimen. These electrons are called secondary electrons (SE). The SE have a lower energy and a lower range than the primary electrons ($\approx$ 1 nm). This can be used to extract information with an even higher resolution, since most SE are generated in a very small volume around the focus point. The lower kinetic energy of the SE makes them distinguishable from the BSE. It is conventional to define electrons with a kinetic energy of less than 50 eV as SE. As can be seen in Figure 2.2, the SE and BSE are counted by different detectors.

Aside from the electron signals, the beam-specimen interaction also produces radiation, mainly in the X-ray spectrum. This can be used mainly for chemical analysis, but this topic is not persued in this thesis.

2.1.1 FIB-SEM Nanotomography

As indicated in the last section, the SEM is a two-dimensional imaging device by design. Yet, it is often desirable to analyze the three-dimensional microstructure or the three-dimensional distribution of different elements in a specimen. For that purpose, the Focused Ion Beam nanotomography (FIB-SEM) has been developed. It uses a focused
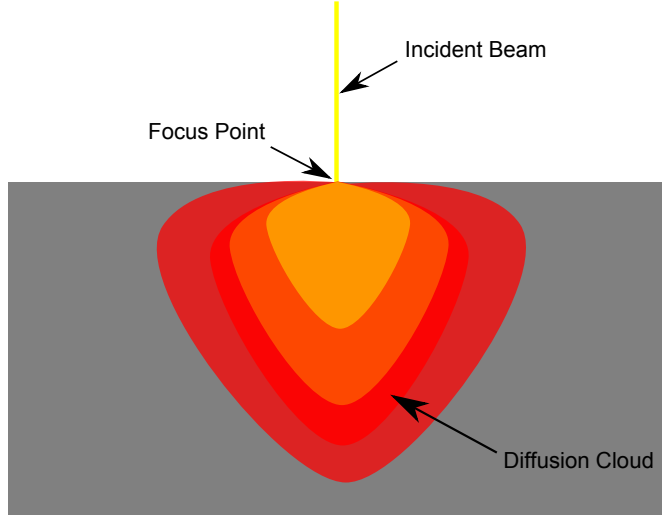
FIGURE 2.3: Schematic view of beam-specimen interaction: The electrons enter the specimen (incident beam in yellow) and diffuse through the specimen. The electrons get the more dispersed the further they get from the focus point. (The electron density is color-coded from yellow to pale-red)

ion beam to mill material off the surface of the specimen. This allows, in combination with the SEM, to obtain a depth resolution of the specimen. Over the years, a standard setup for FIB-SEM has been developed which is depicted in Figure 2.4. Here, a trench-like structure is milled out of the surface laying bare a block of material to be analyzed. Then, an SEM-image is taken, showing the front of the block (indicated by the electron beam in Figure 2.4). To produce 3D-data, the FI-beam mills slices of the block of material and after each slicing one SEM-image is taken. The result is a stack of SEM-images, which contains 3D-information. Figure 2.5 shows a first slice of such a FIB-SEM image stack. Due to the difference between the resolution of the SEM and the precision of the FIB-milling, the voxel size in the 3D-data is mostly anisotropic, with the lowest resolution usually in the slicing direction. Also, to perform the milling and the imaging in one step, it is necessary to tilt the specimen with respect to the electron beam. The most widely used tilt angles are $\alpha = 52°$ and $\alpha = 54°$. This again results in an anisotropy in resolution, with the edge length of voxels in y-direction being given by $\sin(\frac{1}{\alpha})$.

However, the spatial structure of the specimen cannot be reconstructed on a voxel by voxel basis. This is due to the finite interaction volume of the electron beam. Also, for porous microstructures, the pore space is transparent for the SEM. This leads to 'shine-through' artifacts, where structures from lower-lying slices are visible in higher slices (for details see Chapter 3).

The motivation for this thesis was to develop methods to analyze FIB-SEM data. The work presented in this section, is the development of a program to simulate FIB-SEM nanotomography. The simulation is needed to generate synthetic FIB-SEM dataset, on
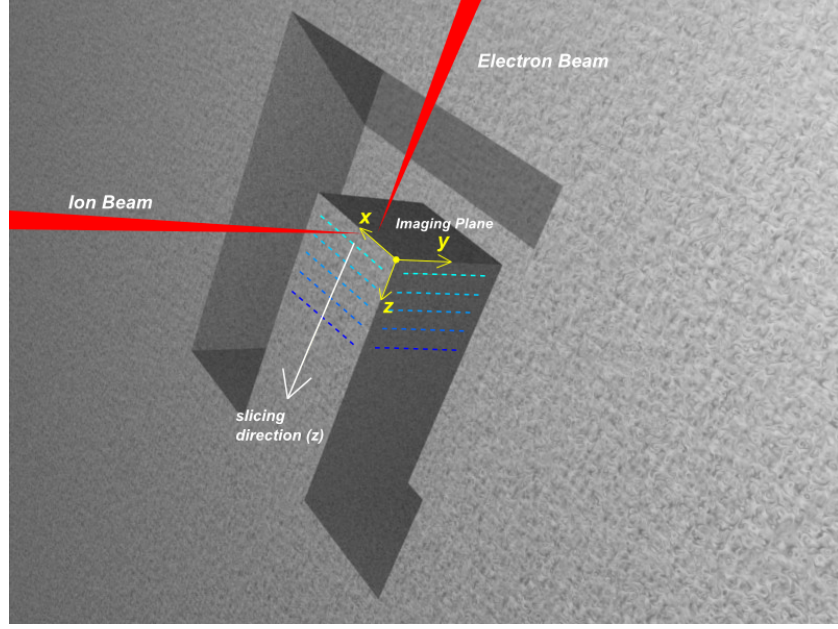
FIGURE 2.4: Schematic view of the FIB-SEM setup.
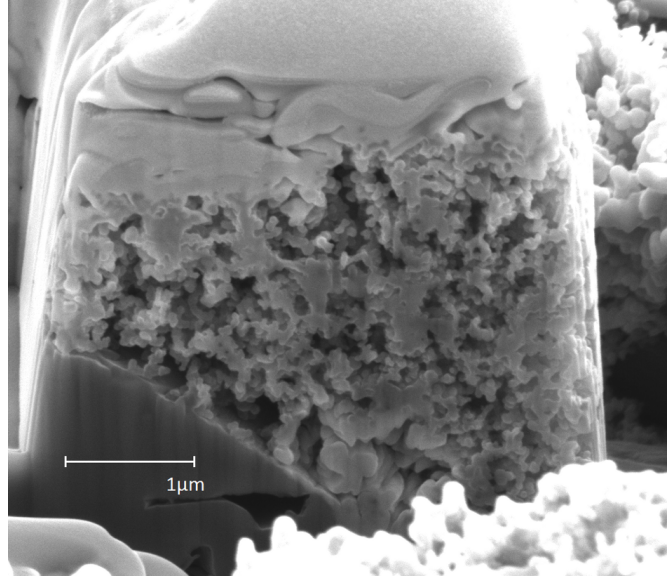
FIGURE 2.5: SEM image if the FIB-SEM setup: The porous material in the middle was coated with a layer of platinum, to improve the accuracy of the milling.

which algorithms for analysis and segmentation of experimental FIB-SEM datasets can be developed.

2.2 Simulation of SEM Images

To generate accurate SEM images, a model for the simulation has to be developed, containing the setup within the SEM, in which the images were generated. In the
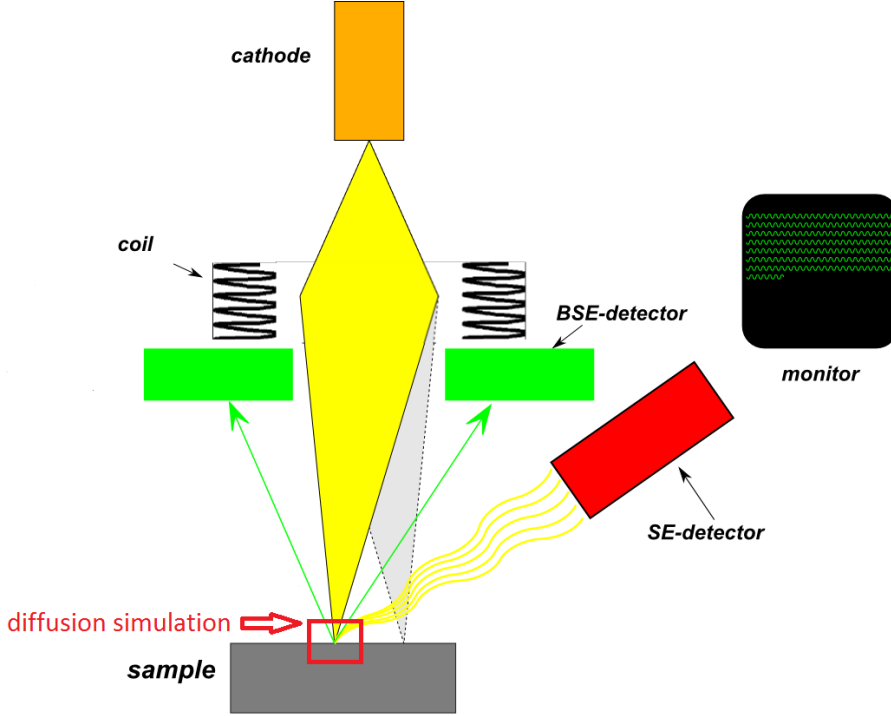
FIGURE 2.6: Schematic view of the simulation setup: The diffusion is simulated at a small scale (red square), with the boundary conditions determined by the surrounding detector and beam setup.

simulation, the SEM is effectively modeled at two different scales. At the small scale, the diffusion, i.e. the beam-specimen interaction is simulated. At the larger scale, a model for the chamber and the positions of the detectors has to be found, where the large-scale model effectively determines the boundary conditions of the small-scale model (see Figure 2.6).

In the model, it is assumed that the specimen is much smaller than the chamber. The beam always enters the diffusion simulation perpendicular to the x-y-plane, since it is assumed that the electron gun is infinitely far from the specimen. This determines the initial conditions for the diffusion simulation. In the coordinate system of the small-scale simulation, the beam electrons will enter the geometry along the z-axis, coming from $z = -\infty$ (see Figure 2.7). The electron beam scans the geometry along the x-y-Plane, with $z = 0$. Since the point of view of any SEM image is the beam source, this will produce images looking at the geometry from the top. To account for the finite beam width, the electron beam's position in the x-y-plane is distributed following a normal distribution centered around the focus point and with the spot size as its variance. To generate an image, the signals have to be estimated for every pixel depending on the underlying geometry. Therefore, the initial conditions are varied such that the beam scans the three-dimensional geometry along the x-y-plane. Then the diffusion simulation
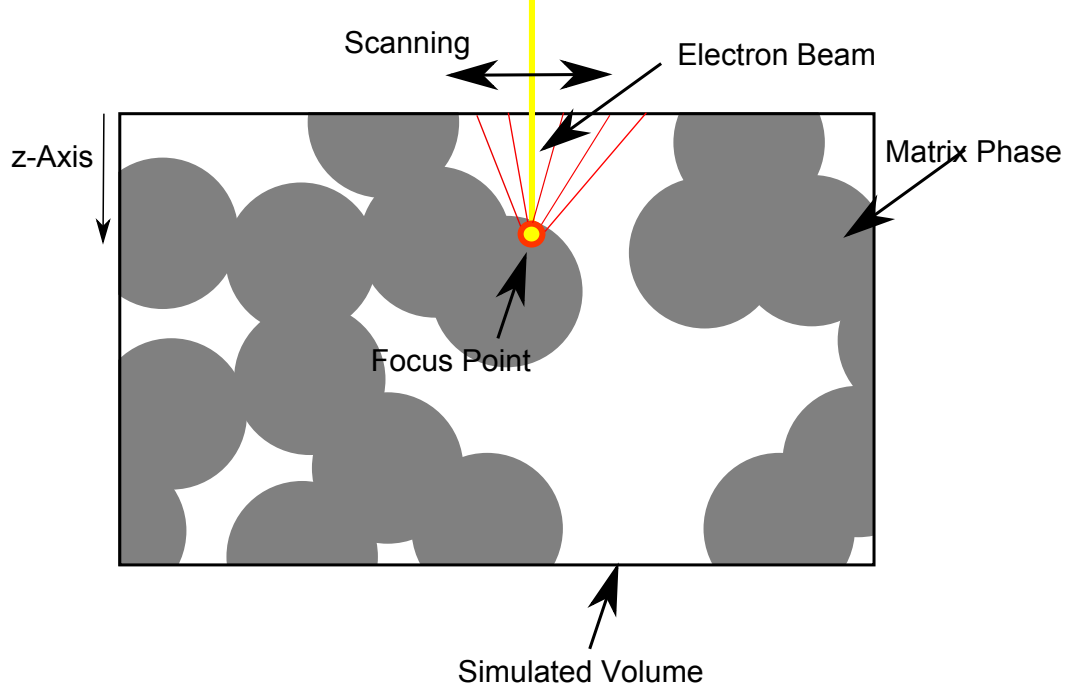
FIGURE 2.7: Schematic view of the simulation setup: the electron beam scans the geometry. For each pixel, the diffusion from the focus point is simulated and the escaping electrons are tracked until they leave the simulated volume.

is run and the estimated intensities are converted to the graylevel in the image (see Figure 2.7 for a sketch).

At the small scale, due to constraints from the binning, the simulated volume is finite and any electrons leaving this volume will not be simulated (see simulated volume in Figure 2.7). After the diffusion of the electrons has been simulated, any electron leaving the simulated volume will be counted as either detected or absorbed in the chamber. Due to the small size of the simulated volume in comparison to the SEM chamber, which houses the detectors, we assume that the detection rate of electrons depends only on the electrons' energy and direction, but not on the position. To determine the detection rate, the electrons' path from the specimen through the chamber to the detector would have to be simulated. Therefore, the individual chamber design of the microscope would have to be known and digitized, including the electric fields often used to draw SE to the SE detector. Although this was done before, e.g. in Konvalina and Müllerová [2006], it is very time consuming and would undermine the goal of creating a general purpose simulation. Therefore, a threshold on the angle between the electron's momentum and the z-axis is used to discriminate electrons that are not detected. The threshold angles are parameters of the simulation and can be chosen for the BSE and the SE independently. This corresponds to a situation where the specimen is much smaller than the detectors and the specimen is facing the detector towards the z-direction. Also, it is assumed that no electric fields exist in the chamber. Although this is an
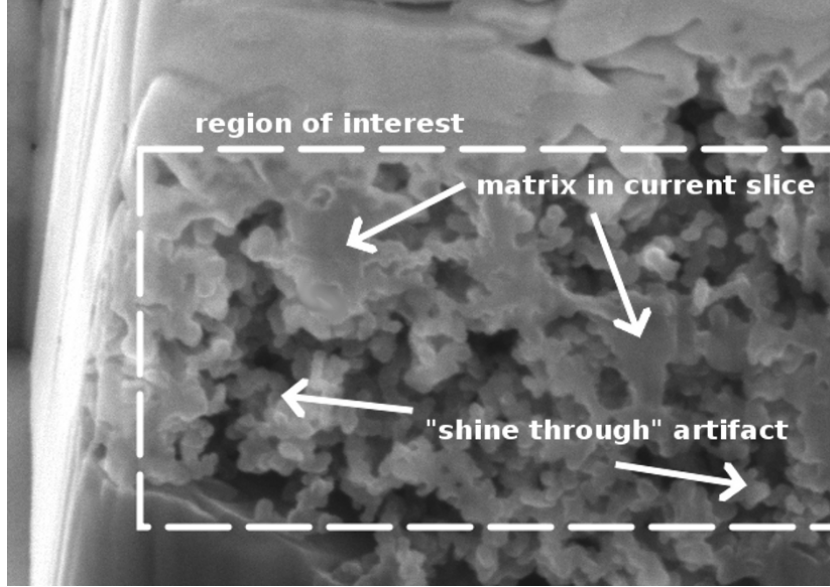
FIGURE 2.8: Experimental image showing the region of interest to be simulated, arrows indicate shine through artifacts and the matrix of the porous material to be characterized.

approximation, most features of the SEM images can be simulated accurately, since they depend on the geometry and the diffusion simulation.

2.2.1   Simulation of Electron Diffusion

For the small-scale simulation, it is most important to reproduce the beam-specimen interaction, i.e. the diffusion cloud. In a diffusion process, particles propagate through a medium in a non-deterministic way, along random paths. In general, depending on the application, different avenues of modeling the diffusion process have been followed. One is the Monte-Carlo method, described in the next section. Other methods rely on analytical methods. For instance, for energies above 5 keV the backscattering coefficient of a planar surface can be approximated by

$$\eta(Z,\phi) = (1 + cos\phi)^{\frac{-9}{\sqrt{Z}}}, \tag{2.1}$$

where ϕ is the angle of incidence of the beam- or primary electrons (PE) and Z is the atomic number of the specimen element (Reimer [1998], p.142). This gives a reasonable fit for the described scenario and can be used in a first attempt to model BSE-images. But in a complex geometry, the model constraints are violated, for instance on edges. There the diffusion cloud touches more surface area than in the bulk region and the edge appears brighter. That effect cannot be modeled by this simple empirical formula.

A more sophisticated technique to model the diffusion cloud effects is an analytical method based on the modeling of the diffusion by a partial differential equation. The equation describes the evolution of the electron density in time as the electrons propagate. In this field, a number of methods have been proposed (see Reimer [1998] p.106). Even though the models differ in the approximations made, all rely on solving a radiative transport equation (RTE) of the form

$$\frac{\partial f}{\partial s} + v\nabla f = N \int [f(\vec{x}, \vec{v'}, s) - f(\vec{x}, \vec{v}, s)]\sigma(\|\vec{v} - \vec{v'}\|)d\vec{v'}, \qquad (2.2)$$

where f is the electron density, $\vec{v}$ the direction of propagation and s an ordering parameter, e.g. time, σ being the scattering cross section of the electrons with the medium (see Section 2.2.2 for a definition). In its most general form the RTE is defined in an 8-dimensional configuration space (3 space dimensions + 3 directions + electron energy + time) and is only hardly solvable numerically. Therefore, to solve the equation a number of approximations have been proposed, e.g. the restriction to single scattering or small angle scattering as in Lewis [1950] or Fernández-Varea et al. [1993]). Other models are based on a point source beneath the surface plus single scattering as in (Archard [1961]). Another problem is the simulation of the propagation of secondary electrons, which have a much smaller range than the primary electrons. Thus, the discretization has to be very fine, using exorbitantly much memory. So to avoid these problems and to achieve the necessary physical accuracy while using a small amount of memory, the Monte Carlo technique was chosen for the simulation.

2.2.1.1 The Monte Carlo Method

To simulate the electron diffusion process, the Monte Carlo method is the most widely used. It was pioneered in SEM simulation among others by Myklebust et al. [1976] and Joy [1995]. There are numerous implementations of the technique documented in the literature. Examples are the MONSEL series developed by the NIST (Karabekov et al. [2003], Lowney [1995a], Lowney and Marx [1994], Lowney [1995b, 1996]), which we will use for the path generation. Other examples are MCSEM by Gnieser et al. [2008], PENELOPE by Salvat et al. [2011] or the CASINO series (Demers et al. [2011], Drouin et al. [2007]).

However, MONSEL is designed to simulate specific line width applications and cannot deal with complex structures. Also, it is too slow to simulate complete FIB-SEM stacks with hundreds of images. This holds for the other programs, too. In the course of this work, it was decided to use MONSEL 2 for the physical simulation, which means
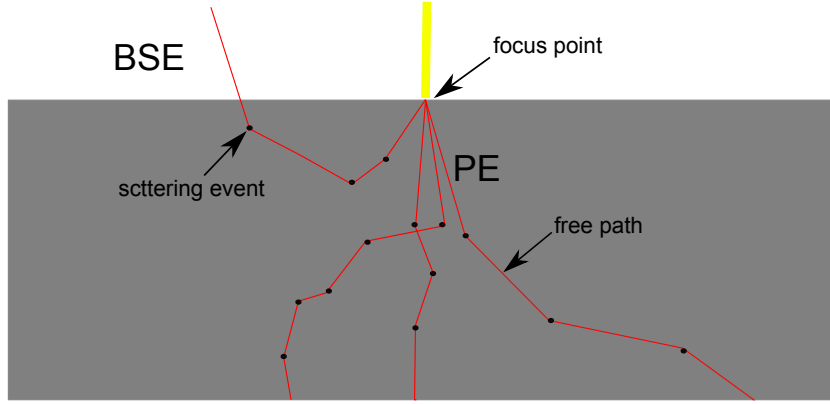
FIGURE 2.9: Illustration of the diffusion model: the primary electrons enter along the yellow line, then a few random electron tracks are shown. The red lines represent a free path, while the black dots represent scattering events.

the generation of the electron paths. The generated paths are used by the simulation program for the simulation of FIB-SEM nanotomography of complex microstructures, as described later in this section.

In the Monte Carlo method, the electrons are tracked individually through the material, which means that the electrons propagate through the matrix along random paths which consist of random steps. Each step consists of a free path where the electron propagates along a straight line and a scattering event, where the electron changes its energy and/or direction (see Figure 2.9 for a sketch and Figure 2.11 for a simulation).

The validity of the method rests on the important assumption, that the electrons do not interact. This enables to simulate each electron individually. If this were not the case, different paths of the process would influence each other, making the simulation much more complicated. Also it is assumed, that the scattering centers are distributed randomly inside the matrix at a constant density, which means, that the length of free paths is homogeneous and isotropic within the matrix, i.e. it does not depend on the position or direction of flight of the electron. Also, the scattering probabilities are the same for every point in the specimen. Even though it would be possible to simulate varying material properties, it is not incorporated into the simulation. An exception is the case, where the electron propagates through the vacuum and no scattering occurs at all.

Each path the electrons take through the specimen is characterized by a sequence of random state vectors. The state at the end of each step is characterized by the state vector x_n which consists of the position, the direction of the momentum and kinetic energy of the electron $x_n = (\vec{r}_n, \vec{d}_n, e_n) \in \mathbb{R}^3 \times S^2 \times \mathbb{R}^+$ (see Figure 2.9). All paths can

be modeled by a sequence of random state vectors

$$(X) = (X_0, X_1, \ldots, X_n). \tag{2.3}$$

The vectors X_i are random vectors containing the random position vector $\vec{R}$, the random direction vector $\vec{D}$ and the random energy E. Each realization (x) of the random sequence X represents a path taken by an electron,

$$(x) = (x_0, x_1, \ldots, x_n), \tag{2.4}$$

where sequence (x) is the path and the $x_i = (\vec{r}_i, \vec{d}_i, e_i)$ are the state vectors in it. To model the process, the transition probabilities have to be known. The transition probability to the new state depends on the current state only. That means, that the electron path sequence is a realization of a Markov process. The transition probability has the form

$$P(X_{n+1} = x_{n+1}|X_n = x_n \ldots X_0 = x_0) = P(X_{n+1} = x_{n+1}|X_n = x_n). \tag{2.5}$$

This has important implications for the simulation, since it means that each path taken from the current state vector x_n is valid in the sense that it is a realization of X. This will be used later to accelerate the simulation. Also, the transition probability contains all the physical information needed for the accurate modeling of the diffusion process. It contains the change of the position, the direction, and energy after every step:

$$P(X_{n+1} = x_{n+1}|X_n = x_n) =$$
$$P(R_{n+1} = r_{n+1}, D_{n+1} = d_{n+1}, E_{n+1} = e_{n+1}|R_n = r_n, D_n = d_n, E_n = e_n). \tag{2.6}$$

In order to form a sensible path, the position vector has to perform incremental steps. In the model, it is assumed that between each scattering event the electron travels along a straight line of a random length, called the free path length S (see red lines in Figure 2.9). The free path length S is a random number that has a distribution which depends on the kinetic energy of the electron. The position of the new state depends on the kinetic energy and the direction of momentum in the current state through the relation

$$\vec{R}_{n+1} = \vec{R}_n + \vec{D}_nS. \tag{2.7}$$

The expectation of S is called the mean free path length $\Lambda = E[S]$. After the electron has passed through the free path along a straight line, it scatters and its momentum changes. The new momentum vector $\vec{\delta v}$ is a random vector which depends on the azimuthal angle ϕ and polar angle θ relative to the current momentum of the electron (see Figure 2.10).
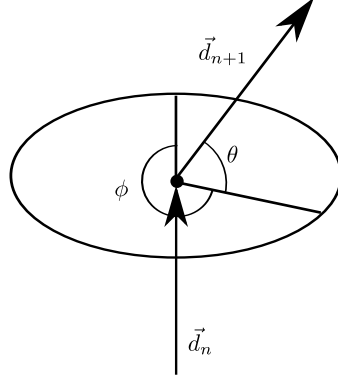
FIGURE 2.10: Parametrisation of the scattering angles: polar angle θ and the azimuthal angle ϕ between the direction vector before $\vec{d_n}$ and after scattering $\vec{d_{n+1}}$

$$\vec{D}_{n+1} = \vec{D_{n+1}}(\theta(D_n), \phi(D_n)) \tag{2.8}$$

A similar relation holds for the kinetic energy of the electron. The energy of the new state is given by the current energy minus some energy loss δE:

$$E_{n+1} = E_n - \delta E(E_n). \tag{2.9}$$

where δE is again a random number depending on the current state's energy. The exact form of the transition probability depends on the physical model used and is described in more detail in Section 2.2.2. As an example, Figure 2.11 shows 100 simulated paths.

The initial condition x_0 of every path corresponds to the electron from the beam entering the specimen. In the simulation, all incident electrons have the beam energy E_0 and the direction $\vec{d} = (0, 0, -1)$. The initial position is the focus point where the beam hits the specimen. The path ends either when the energy of the electron is so low that it is absorbed in the material or when the electron exits the simulated volume. Then the signal intensities are estimated from the statistics of the paths.

The simulated signal intensities are detection probabilities and are given by the back scattering coefficient η and the secondary electron yield δ. They can be estimated by expectations over all simulated paths. If the electron exits the specimen in a way that it can be detected, the electron is counted as a BSE or a SE, respectively, depending on its energy. In the simulation, the detected final states are given by all states where the electron exits the simulated volume and has a minimal angle towards the surface. Details are given in Section 2.2.3. In practice this can be changed easily. The signal intensities of the BSE and SE signals can then be estimated by counting the electrons which have a detected final state. The BSE signal is given by the back scattering coefficient η, which is the probability of a primary electron to resurface from the specimen and being
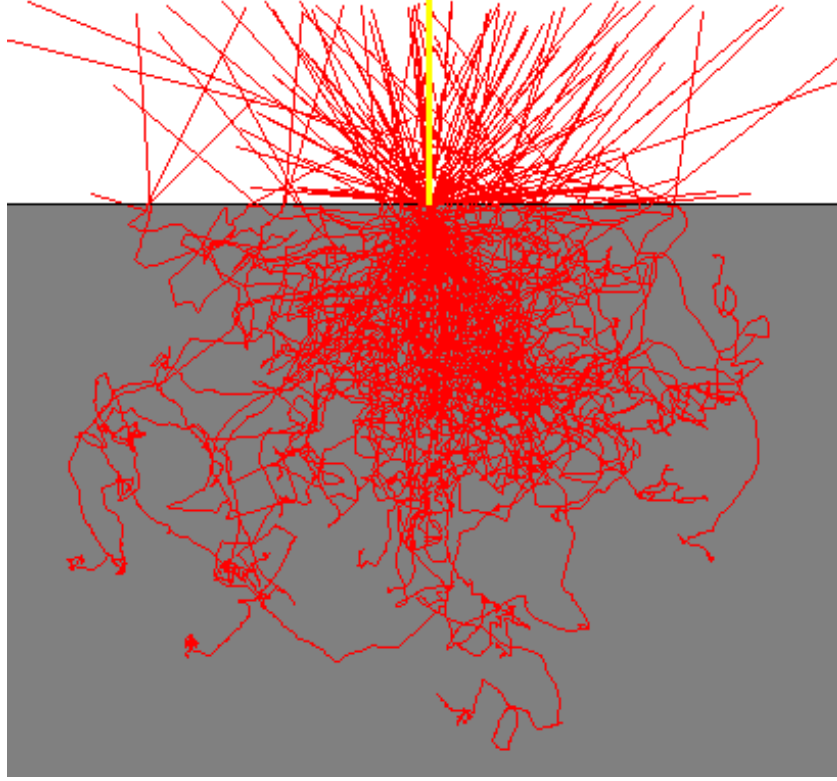
FIGURE 2.11: The illustration shows 100 simulated paths. The paths start at the focus point and end after they either either left the material or were absorbed by it.

detected. By using the Monte Carlo method, η can be estimated by simulating a large number of electron paths

$$\overline{X} = \{(x^0), (x^1), \ldots, (x^n)\} \tag{2.10}$$

and then counting the paths which have a state in the set of detected final state X_f, e.g. all states with a position in the upper half space $X_f = \{x_i | r_z \geq 0\}$. The estimator for the back scattering coefficient $\overline{\eta}$ is then given by the fraction of detected electrons

$$\overline{\eta} = \frac{1}{|\overline{X}|} \sum_{(x^k) \in \overline{X}} \mathbb{1}(X_f \cap (x^k) \neq \emptyset), \tag{2.11}$$

where $\overline{X}$ is a set of simulated paths and the x^k are the realizations in it. Since a path can either be detected or not, which is a binary event, the number of detected electrons is binomially distributed. Thus, the number of paths which end in a detected state follows a binomial distribution with the backscattering coefficient η and the number of simulated paths $N = |\overline{X}|$ as parameters,

$$n_{BSE} = \overline{\eta} N \propto B(N, \eta). \tag{2.12}$$

For large N, the distribution can be approximated by the Poisson distribution with the parameter $\lambda = N\eta$. The mean and the variance of n_{BSE} are

$$E(n_{BSE}) = N\eta, \tag{2.13}$$

$$\text{var}(n_{BSE}) = N\eta(1-\eta) \tag{2.14}$$

and the mean and variance of the estimator $\bar{\eta} = \frac{n_{BSE}}{N}$ are

$$E(\bar{\eta}) = \eta, \tag{2.15}$$

$$\text{var}(\bar{\eta}) = \frac{\eta(1-\eta)}{N}. \tag{2.16}$$

A good measure for the image quality is the standard deviation of the estimator which is given by

$$\text{SdtDev}(\bar{\eta}) = \sqrt{\frac{\eta(1-\eta)}{N}}. \tag{2.17}$$

One has to keep in mind, though, that the parameter η is different for each pixel, so the standard deviation also changes. But still the dependence on N is the same throughout the image, which means that to half the standard deviation four times as many electrons have to be simulated.

A similar relation holds for the secondary electron yield δ. But it has to be taken into account, that one primary electron can produce more than one secondary electron. Which means that if the normalization is done with respect to the primary electrons, the SE yield can become greater than one. This leads to a deviation from the binomial statistics and usually a greater variance, which means a poorer image quality for the same number of PE paths (a detailed treatment can be found in Reimer [1998], p. 166).

2.2.2 Physical Model

In order to simulate the right paths for the diffusion simulation of electrons, the paths have to have the proper physical properties. The physical modeling enters in the transition probability, i.e. the step length (free path length) and the change of momentum and energy through the scattering events. To have a simple and yet accurate model, MONSEL 2 presented in Lowney [1995a] is used. It incorporates the simulation of primary and secondary electrons through a wide range of energies. Especially the fact that MONSEL 2 uses the Monte Carlo technique for the processes at low energies, which in other programs are mostly simulated with a so called parametric model, and not with the Monte Carlo technique, is important. This allows the use of the Monte Carlo technique for all electrons.

2.2.2.1 The Scattering Model

The physical modeling of the electron paths is done by the differential scattering cross section (DCS). All scattering events are described by their DCS $\frac{d\sigma}{d\Omega dW}$. The DCS is the probability of a particle being scattered by a target into the solid angle element $d\Omega$ and in the process loosing the energy dW. Thus, the DCS is the combined probability distribution of D_{n+1} in Equation 2.8 and δE in (2.9). The solid angle element is taken in the electrons system of reference (see Figure 2.10) and only depends on the polar angle θ. This means, that the azimuthal angle is distributed uniformly in $[0, 2\pi)$. Thus, it is sufficient to know the distribution of θ and s to characterize the paths. Later, this will be used for the acceleration of the SE simulation.

Even though they will be treated equally, one simulated scattering event subsumes several distinct physical events. For details refer to Chapter 3 in Reimer [1998]. In general, scattering events are classified as either inelastic scattering events, where the electron loses energy to the material, or elastic scattering events, where it does not. The combined DCS of different types of scattering is given by the sum of the individual events. MONSEL 2 uses the quantum mechanical Mott-DCS for the elastic scattering cross section, which is important for the wide angle scattering behavior (see Figure 2.12 for an examples for two elements). For the inelastic processes, the model uses the Møller-DCS (Møller [1932]) to simulate the ionization of valence electrons, combined with a model for the density of the valence electrons in the medium. Of special importance is the ability of MONSEL 2 to simulate the SE with the Monte Carlo method. Therefore, the model of Kotera et al. [1990] has been implemented, which simulates the generation of SE through the generation of plasmons by the PE and their subsequent decay into SE, which is the dominant process of SE generation at low energies.

2.2.2.2 Energy Loss

Since in the diffusion process the electron loses energy through inelastic scattering, the energy loss has to be modeled. Therefore, MONSEL 2 uses the continuously slowing down approximation (CSDA) or Bethe-approximation (for details again see Reimer [1998]). In the approximation, it is assumed that the electrons continuously transfer energy to the material as they propagate. The energy loss is modeled by the stopping power T. This is the energy loss per unit path length and can be approximated by

$$T(E) = \left| \frac{dE}{\rho ds} \right| = 7.8 * 10^{10} \frac{Z}{A} \frac{1}{E} \ln \left(1.166 \frac{J}{1 + k\frac{J}{E}} \right), \tag{2.18}$$
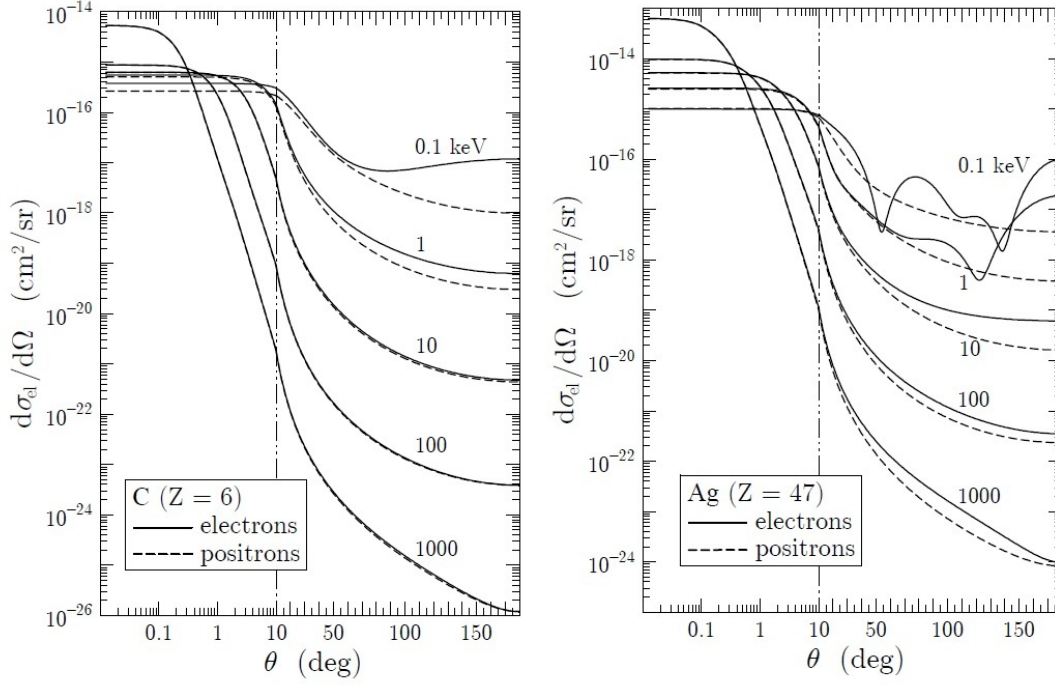
FIGURE 2.12: The elastic scattering cross section of electrons and positrons on carbon (left) and gold (right) atoms. The plots show the dependence on the scattering angle θ in Figure 2.10 for different energies. (Images taken from Salvat et al. [2011]).

where ρ is the material density, Z is the atomic number, A is the atomic weight, E is the electron's energy and J and k are material parameters included in the MONSEL 2 simulation (see Joy and Luo [1989]). Since this models a continuous energy loss over the path, the kinetic energy of the electron is a continuous function of the path length followed by the electron. Also, the energy loss is much stronger at lower kinetic energies. These two facts will be used later on, for the acceleration of the simulation.

2.2.2.3   The Free Path Length

The distribution of the free electron path length S can be calculated with the scattering cross section σ. This is the probability of any interaction happening with a target and can be calculated by integrating the DCS over the solid angle and all energies

$$\sigma = \int_0^\infty \int_{\mathbb{S}^2} \frac{d\sigma}{d\Omega dW} d\Omega dW. \tag{2.19}$$

Since all scattering events are independent of each other, the number of scattering events follows a binomial distribution, with the number of scattering centers (e.g. atoms or molecules) passed by the electron N and the scattering probability σ as parameters.

Thus, the number of interactions n_s is given by

$$P(n_s = k) = B(N, \sigma) = \binom{N}{k} \sigma^k (1 - \sigma)^{(N-k)}. \tag{2.20}$$

In the model, it is assumed that the scattering centers are distributed continuously along the path of the electron, thus the binomial distribution goes to its continuous limit, the Poisson distribution. In the limit, the number of scattering centers has to be replaced by their density n. The number of scatterings along some path length s is thus given by

$$P(n_s = k) = \text{Pois}(\lambda s) = \frac{(\lambda s)^k}{k!} e^{-\lambda s} \tag{2.21}$$

with the intensity parameter $\lambda = n\sigma L$. When thinking of the scattering events as points distributed on the path length, i.e. on the real line, the scattering events with the property in Equation 2.21 constitute a Poisson point process with the intensity λ (see Section 1.3.2 or the References Stoyan et al. [1995] and Schneider and Weil [2008]). This can be used to derive the distribution of the free path length. The probability of at least one scattering event in a free path length s is the probability of not having a scattering in [0,s], and thus not having a point of the process in [0,s]. This probability is given by the contact distribution function of an interval [0,s]

$$P(s \leq S) = P([0, s] \cap \Phi \neq \emptyset) = 1 - exp(-\lambda s), \tag{2.22}$$

which is the cumulative distribution function of the free path length S. Thus the density function is given by the derivative of the cumulative distribution function

$$P(S = s) = \frac{d}{dS} P(s \leq S) = \lambda exp(-\lambda S). \tag{2.23}$$

Also the mean free path length can be calculated. The mean free path length Λ is defined as

$$\Lambda = \langle S \rangle = E[S] = \frac{1}{n\sigma}, \tag{2.24}$$

which depends on the total scattering cross section σ and the density of scattering centers n.

2.2.3 Geometric Model

For the diffusion simulation in the simulated volume (see Figure 2.7), a description has to be found, which points belong to the matrix phase and which - the complement - are considered to be vacuum. The simulation is designed for porous materials with a

random microstructure (see region of interest in Figure 2.8), thus the geometry must be able to model very complex microstructures.

Some of the most prominent options for a description are either a voxel grid or an analytic description by either a polygon mesh or a union or intersection of primitives. The first option (voxel grid) is not suitable, since the small range of the SE compared to the range of the SE would demand a very fine resolution and thus would be very demanding memory-wise. Among the analytical descriptions, the most prominent examples are either made for a specific application, such as line width metrology (Karabekov et al. [2003], Lowney [1995a], Lowney and Marx [1994], Lowney [1995b, 1996]) or surface analytics (Demers et al. [2011], Drouin et al. [2007]). More general descriptions use for example constructive quadric solid geometry or constructive solid geometry as in Gnieser et al. [2008], or Ritchie [2005],Yan et al. [1998] and Ding and Li [2005]. A polygon mesh is used in Zhang et al. [2011], but has the disadvantage that testing if a point is included in the matrix is complicated and lengthy, which slows down the simulation. Also, meshes of very complex structures become very memory-consuming. Thus, for the sake of speed and our specific application, we have chosen a simple analytic description. Since the simulation will be used to simulate geometries generated by random models, such as realizations of a Boolean model (Stoyan et al. [1995]), and the simulation of FIB-SEM needs to be highly optimized, we have chosen an analytic description as a union of primitives. The primitives can be either spheres or cylinders, which are quick to test for intersection. Examples are shown in Figure 2.13. Each point inside one of the primitives is considered to be inside the matrix phase. Therefore, the microstructure is modeled by the union of the primitives. This analytic description requires only a very simple description of the geometry in the memory, namely a list of position vectors and radii for the spheres and a list of vectors for position and orientation for the cylinders together with their heights and radii. This lean description can easily cope with complex geometries of thousands of primitives. The geometry is read into the simulation as a text file containing the vectors and numbers describing the primitives.

Even though the primitives in the realization of a Boolean model are randomly placed in space, the model also allows for the generation of more ordered geometries, such as fiber systems (see Figure 2.14). To model the fiber systems, the fiber is approximated by a chain of spheres as in Altendorf and Jeulin [2011]. Then cylinders are added, connecting adjacent spheres (see Figure 2.14). This gives the appearance of a smooth fiber with a fixed diameter.

Despite being fast, the description has one important drawback, namely that modeling more than two phases (matrix and vacuum), is complicated. Since this thesis is mostly
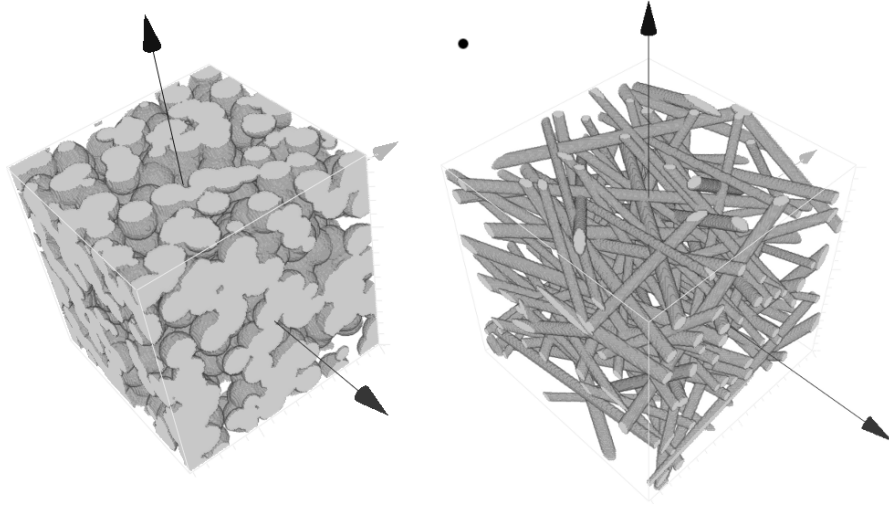
FIGURE 2.13: Examples of geometries from Boolean models with spheres and cylinders.
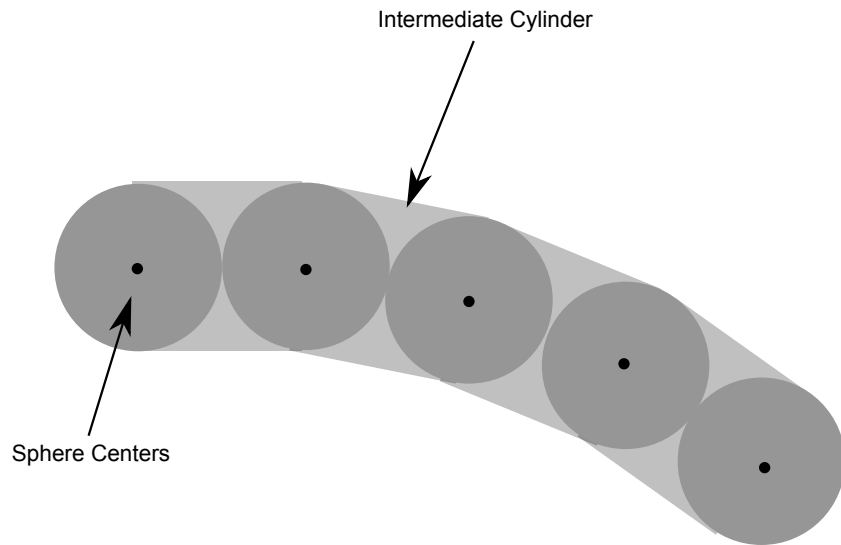
FIGURE 2.14: Fibers are modeled using spheres centered in the fiber. Cylinders are placed between the spheres to smoothen the model.

concerned with a microstructure and not with the chemical composition, multiphase materials will be neglected, but could be added in a later stage.

2.2.4 Acceleration Techniques

To simulate the images with reasonable computational effort, several acceleration techniques had to be developed. A naive simulation with packages such as MONSEL 2 would be too slow, to accomplish this task. In an infinite medium, the MONSEL 2 simulator can simulate approximately 500 electrons/sec on a notebook machine. For a typical FIB-SEM dataset of a 3D volume with a 400 voxels edge length and 10^4 simulated electrons per voxel, which are needed for a sufficient image quality, $400^3 * 10^4 = 6.4 * 10^{11}$

electrons have to be simulated. With the standard MONSEL2 simulator (even disregarding the complex geometry), this would take 41.6 years on a single core notebook computer. Even with massive parallelization this is too much time for a common usage. To tackle this problem, several acceleration techniques have been implemented, among them some were already documented in literature and some were newly developed. The techniques are based on precomputation, binning, and parallelization.

2.2.4.1   Precomputation

The precomputation principle was applied for the first time to this specific problem by Seeger (Seeger et al. [2003]). The technique is based on the precomputation of a library containing a large number ($O(10^4)$) of electron paths in an infinite matrix (see Figure 2.15 a). Later, a sample with a smaller number of paths ($O(10^3)$) is drawn from the precomputed paths for each individual pixel. These are used to estimate the intensity of the BSE and SE signal. This leads to a speed-up, since the slow physical simulation with MONSEL 2 does not have to be repeated for every pixel but only for the precomputed paths. The electron paths are saved as a list of the difference vectors between the individual steps. The current energy of the electron is saved as meta information for each step. Since fast secondary electrons (FSE) are generated during the precomputation, branching points would have to be included. Although this can be added, as for the SE (see below), it was omitted for simplicity reasons. Also, the contribution of FSE to the BSE signal is very small ($\approx 1\%$), thus the image quality is not affected.

For the image generation, the precomputed paths are tracked through the geometry by simply adding the difference vectors. After each step, a test is performed whether the electron is still inside the matrix. If so, the next step is added, else the intersection point between the path and the surface of the matrix is computed. Then it is assumed that in vacuum, since no scattering occurs, the electrons propagate along straight lines, retaining their state of energy and momentum (see Figure 2.15). Electric fields within the specimen are hereby implicitly neglected. Then, an intersection test is done. In the intersection test, every other primitive is tested to find the nearest intersection point of the matrix with the trajectory. If no intersection is found, the electron is assumed to have left the simulation volume, either to be counted by the detectors or not. If an intersection is found, the position of the electron is updated to the intersection point and the remaining free path from the last step is added. By the Markovian nature of the paths, the simulation can be continued with the next scattering event in the precomputed track. Since the state of the electron, other than its position, did not change, all future
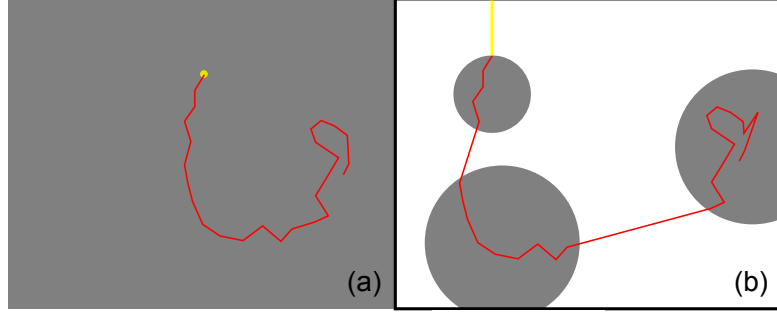
FIGURE 2.15: Schematic view of the precomputation algorithm: precomputed electron path (a) and the adapted version with straight lines inserted (b)
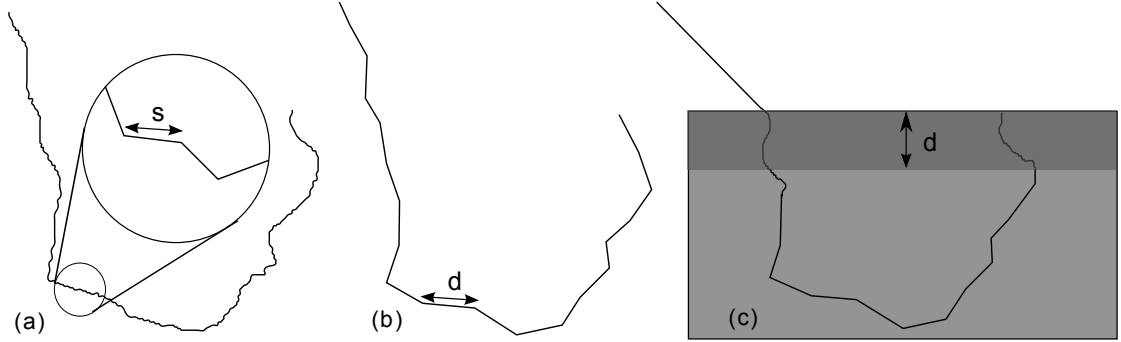
FIGURE 2.16: Schematic view of the track compression algorithm: (a) simulated PE in an infinite medium, (b) compressed PE path with step length s, (c) simulated path in real geometry with SE depth d.

scattering events are sampled from the right distribution, depending on the energy and direction. Thus, the path is a valid electron path.

To preserve randomness, the number of precomputed paths should exceed the number of paths used for each pixel by a given factor (≈ 10). Thus, each two pixels share only a small number of precomputed paths ($\approx 1\%$).

2.2.4.2   Path Compression

To further improve the method beyond what was documented in literature, a compression algorithm for the precomputed paths was developed. As indicated earlier, BSE paths are stored in a list of difference vectors, each representing one step after a scattering process. Together with the meta information (energy, step length), each vector represents one differential step of the track, where the original path can be restored by successively adding up the segments. Since the complete path is known beforehand, the position of the electron is known after any path length. This can be used to calculate a coarser path with fewer segments, needing fewer tests to track through the geometry, thus speeding up the simulation.

The algorithm to calculate the coarse path uses the parameter d, which is an upper limit for the step length of the coarser path. The length d should be chosen above the range of the SE, but ideally much longer than the step length s of the original path, such that

$$d > \text{ SE range} \wedge d \gg s. \tag{2.25}$$

Starting at the beginning of the path, the step vectors of the original path are added up until a further step would violate the limit. The sum vector represents one step in the coarse path and is added to a list, representing the coarse path (see Figure 2.16(b)). Then, the next vectors are added to compute the next coarse step. This coarser path has fewer steps than the physically correct path, thus during the tracking fewer tests are necessary to determine whether the electron has left the matrix. This leads to a speed-up in the tracking through the geometry. The information on the direction of the individual steps, which is important when the electron exits the geometry, is lost in the process. Thus, if the electron is close to the surface, the tracking algorithm needs to resort to the finer physical path. Here, the depth information of the individual primitives can be used. Since d is an upper bound for the step length, the electron cannot escape in one step. In the implementation of the algorithm, each step of the coarser path carries the step number of the finer path as meta information. Such that, if the electron depth is below the threshold, starting from the point where the coarser path ends, the corresponding step of the finer path is added, and then the simulation resumes with a finer scale (see Figure 2.16(c)).

Quantifying the speedup exactly is difficult, since it strongly depends on the geometry and ratio between the SE and the BSE range. In the best case, the electron enters the specimen vertically, the finer path is used until the depth threshold is reached, and only the coarser path is simulated until the electron is absorbed by the material. Then a physical path with $O(10^3)$ is compressed to less than 100 steps. In this case, the speed-up can be up to a factor of ≈ 100, since only a very small portion of the finer track is used at the beginning. In the worst case, the SE range is of the order of the BSE range, where only the finer track is used and no speed-up occurs at all.

2.2.4.3   Decoupling of Secondary Electrons

Yet further acceleration becomes possible, when simulating the SE. This is due to the much smaller range of the SE compared to the BSE, which represents a separation of scales in the problem. Since the SE can reach the detector only from a small layer below the surface of the geometry, the simulation of all SEs is not required. Therefore, we restrict the SE simulation only to SE generated close to the surface of the geometry. To
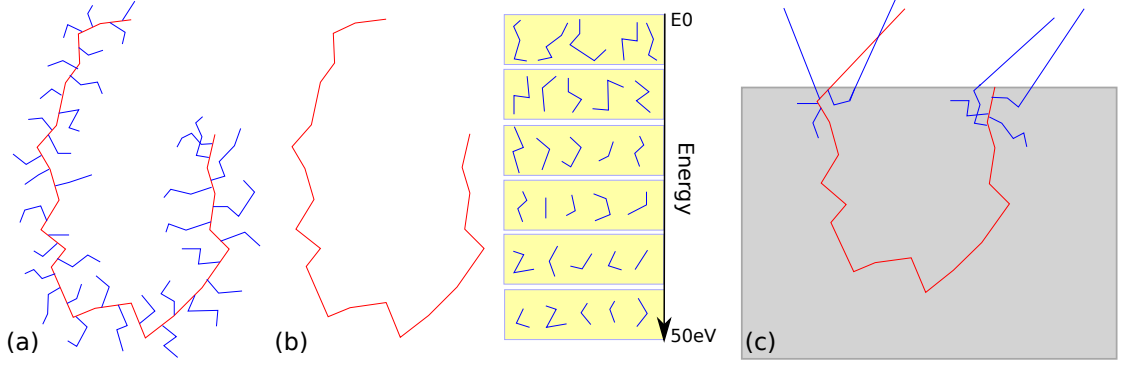
FIGURE 2.17: Schematic view of the SE precomputation algorithm: (a) simulated PE and SE cascade (b) PE and SE decouple, with SE tracks stored in bins (c) simulated track in real geometry with SE depth d

achieve this, the SE simulation is decoupled from the PE simulation. When an electron is generated in the precomputation with an energy of less than 50 eV, it is classified as an SE. Then the track is stored separately from the PE track (see Figure 2.17(a)). Unlike for the PE, only the path lengths and the scattering angles between the segments are stored. The azimuthal angle (ϕ in Figure. 2.10) of the SE generation and scattering can be disregarded and will later be drawn from a uniform distribution in $(0; 2\pi]$. Also, unlike for the PE, cascading effects are not neglected. To achieve this, branching points are stored as meta information with the SE tracks. The tracking than happens recursively. Since, other than for the PE, the SE cascades only comprise several steps $(O(10))$ a track compression is neither necessary nor advantageous. The probability of SE generation only depends on the energy of the PE and the angle between the generated SE and the PE momentum. So for each SE cascade, the angle between the first segment of the cascade and the PE's momentum is stored as meta information.

For the tracking of the SE through the geometry, a new algorithm has been developed modeling the SE generation and diffusion from the information gained in the precomputation. The algorithm assumes that the generation of the SE can be modeled by a Poisson process in the energy domain, where the intensity of the process depends only on the energy of the PE

$$\lambda = \lambda(E). \tag{2.26}$$

Due to the CSDA approximation implemented on MONSEL 2, i.e. the PE continuously loses energy as it moves, the path length covered by an electron from the start is a continuous function of its kinetic energy. Thus, the energy can be used to measure the step length of the electron and the number of scattering centers passed by the electron. This leads to the intensity of the process in the energy domain, given by

$$\lambda(E) = \frac{dn_{SE}}{dE} = \frac{dn_{SE}}{ds}\frac{ds}{dE} = \rho\sigma_{SE}\frac{1}{S}, \tag{2.27}$$

where $\frac{dn_{SE}}{dE}$ is the number of SE generated per unit energy loss. The intensity $\lambda(E)$ can be estimated from the precomputation. To achieve that, the SE cascades are sorted after precomputation according to the PE energy and stored in bins (see Figure 2.17 b). Each of the bins covers an energy interval which is stored as meta information with the bin. Through the binning, the energy dependent cross section is being estimated from the energy interval, covered by each bin. Thus, a histogram of the SE generation probability is generated, approximating the intensity by a piecewise constant function. This leads to the approximated intensity

$$\lambda_i = \frac{n_{SE,i}}{\Delta E_i}, \tag{2.28}$$

where ΔE_i is the energy interval covered by the i-th bin and $n_{SE,i}$ is the number of secondary electrons in the respective bin. For a better approximation of the peak in the intensity at low energies, a non-uniform bin size has been chosen, where each bin contains a given number of electrons. In practice, the number of SE cascades per bin should not be chosen below 1000, since the SE drawn from the first bin contribute considerably to the SE signal. As long as the energy of the PE remains within ΔE_i, the intensity of the Poisson process is λ_i. The generation rate of SE in each step of the PE path follows a Poisson distribution

$$n_{SE} \propto \text{Pois}(\lambda_i \delta E_i). \tag{2.29}$$

So the probability of k SE being generated during the step is

$$P(n_{SE} = k) = \frac{(\lambda_i \delta E)^k}{k!} e^{-(\lambda_i \delta E)}. \tag{2.30}$$

During the PE tracking the number of SE generated is drawn from (2.30), where δE is the energy lost during the last step of the PE. In the event of a SE generation, using the Markov property of the track, a random SE cascade can be drawn from the corresponding energy bin. The SE cascade is then attached to the PE track, where the azimuthal angles are random numbers, drawn from $(0; 2\pi]$ (see Figure 2.17 (c)). The SE is then tracked until it is either absorbed, or it exits the geometry.

In some materials, the SE cross section is very low and only a small number of SE are generated in the small volume below the surface. This leads to a poor image quality. Therefore, a multiplicative constant m was introduced in the intensity, which is a parameter of the simulation. Through the parameter m, the SE cross section can be raised

by a factor

$$\lambda_i \to \lambda_i * m. \tag{2.31}$$

A higher m can improve the SE statistic by raising the number of SE generated and thus improving the SE image quality.

2.2.4.4 Binning

To further speed up the tracking, a binning technique, originally developed for ray-tracing programs for computer graphics, was implemented (see Glassner [1984], Fujimoto et al. [1986] and Cleary and Wyvill [1988]). It is also based on a precomputation principle, but here instead of precomputing the physics, the tracking of the precomputed paths through the geometry is accelerated. As was mentioned before, the highest computational cost is due to two testing routines, one testing whether a point is inside the matrix phase and the other is to find the nearest point of intersection between a ray and the matrix phase. For both times the test is required on all primitives, so in a geometry with 10.000 primitives, the test has to be repeated 10.000 times. The binning technique uses precomputed knowledge to reduce the number of tests. To this end, the volume is subdivided into an orthogonal grid and each cell in the grid is intersected with each primitive in the geometry. Then, for each cell the primitives intersecting the cell are stored (see Figure 2.18).

If, in the first test, the cell in which a point lies is known (which can be easily computed) only the primitives intersecting the corresponding cell have to be tested whether the point is included (see test point in Figure 2.18).

To test the intersection of a ray with the geometry is more elaborate. The problem to solve is to find the minimal s where the ray $\vec{r} = \vec{d} * s + \vec{p}$ intersects with a primitive. This requires a grid traversing algorithm which selects the bins intersected by the ray in the right order, so the nearest intersection can be found. To solve the problem several algorithms were proposed. For this simulation the algorithm proposed in Amanatides and Woo [1987] is implemented. It is very efficient and finds the primitive intersecting the ray for minimal s without any additional computations.

2.2.4.5 Parallelization

Even though the computation runs very fast on a desktop computer, the simulation of a whole FIB-SEM dataset with hundreds of images and a good image quality can
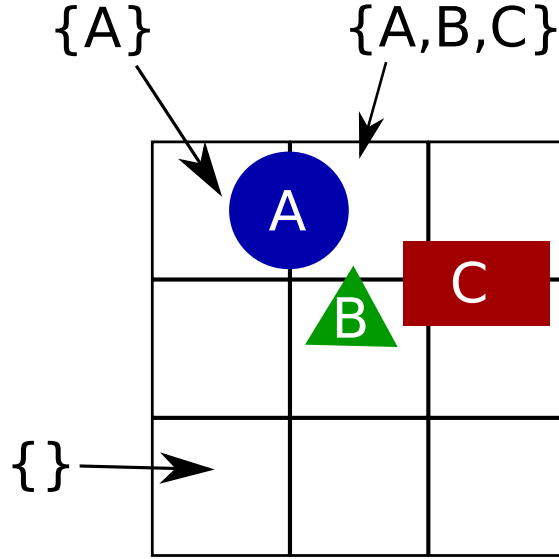
FIGURE 2.18: Schematic view of the track binning algorithm, the arrows indicate which primitive is included in which cell, i.e. for the test point only primitive A has to be checked

be very time consuming. Therefore, as a last step of acceleration, the simulation can be run in parallel on multi core machines as well as on a cluster. Since all electron tracks are independent, each image of the FIB-SEM data and each pixel of each image can be computed independently. For single image generation on a desktop or a laptop machine, the easiest way is to parallelize the calculation of all pixels. But to create a thread for each pixel would produce much overhead and might eventually slow down the calculation. Therefore, the calculation is parallelized along the columns of the image. Meaning, the computation of the columns of the image is distributed on the available threads. In the implementation, this is done by using OpenMP's parallel directive in the loop counting the columns of the image. By choosing the maximal number of threads (ideally the number of CPU cores) OpenMP distributes the simulation of the columns on the threads and thus the cores (For example, on a 4 core machine, each core computes 25 columns of a 100x100 pixel image).

2.3 Simulation of FIB-SEM Nanotomography

The simulation of FIB-SEM tomography differs from the usual SEM simulation mostly in computational effort, since several hundreds of images have to be simulated. Also the FIB-SEM setup must be simulated, which includes the milling of the FI-beam. Therefore, in the geometric model, the x-y-plane is used as the milling plane. As the FI-beam mills deeper slices, the geometry is shifted in the negative z-direction (see Figure 2.19). Again, we restrict ourselves to the simulation of the porous material, shown in
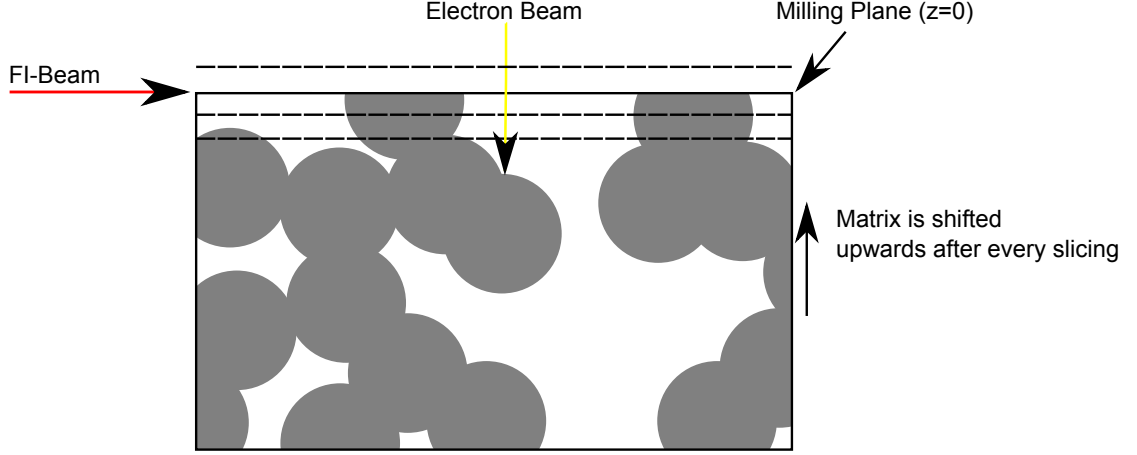
FIGURE 2.19: Simulation of the FIB-SEM process: the matrix is shifted upwards after every step, effectively cutting it at the x-y-plane.

Figure 2.8 as the region of interest. We omit the detailed setup, i.e. the trench and eventual coatings, since it will probably differ from dataset to dataset. Also, the fact that milled material might break away is omitted.

For the simulation of whole FIB-SEM datasets, a parallelization on a cluster is usually necessary. Here, the easiest way of parallelization is by image, i.e. assigning one image to each job. By that parallelization no shared memory and no communication between the jobs is necessary. The implementation was done via a script, assigning one image to each job and passing the initial conditions and the feed for the random number generator. With the parallelization, the simulation of one FIB-SEM dataset can be achieved on a cluster within an hour up to one day.

2.3.1 Implementation

In the course of this work, a new software package was developed which can simulate a complete FIB-SEM nanotomography process. The software was implemented in C++, with a Qt graphical interface (see Figure 2.20). The GUI shows a 2D projection of the geometry with spheres represented by circles and cylinders represented by lines. The user can choose the imaging parameters such as pixel size and physical scale of the simulation, while the beam parameters such as energy and material are fixed by the precomputation. For the precomputation, the MONSEL 2 model was modified to write the computed paths into files which can be read by the simulation tool. Also, the electron paths can be displayed for testing.
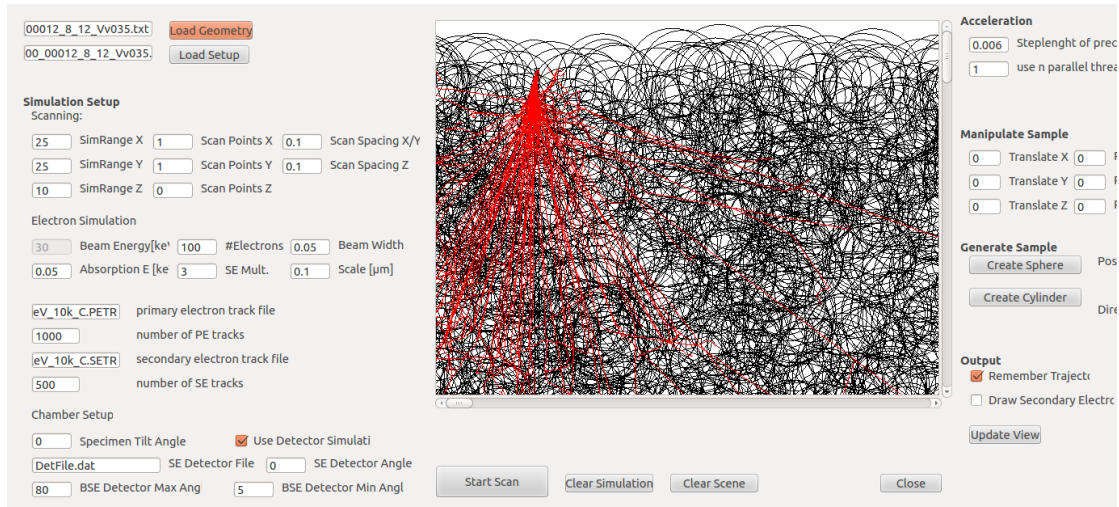
FIGURE 2.20: Graphical User Interface of the SEM Simulation tool.
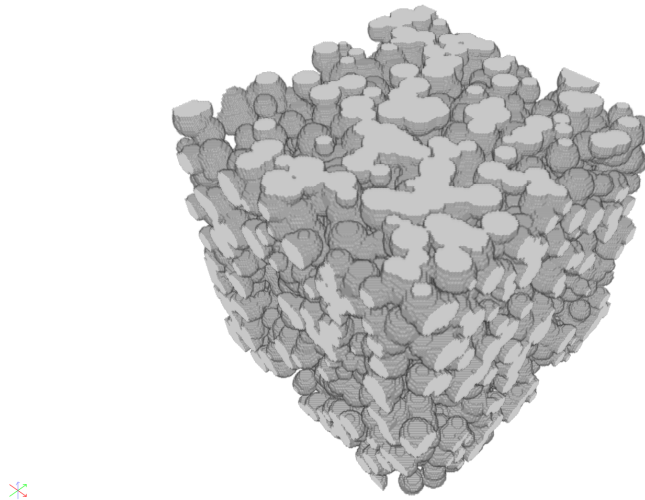
FIGURE 2.21: Realization of a Boolean model designed to resemble the nanoporous
additive shown in Figure 2.8.

2.4   Results

In this section, results of the simulations are presented. The resulting images depend
very much on the parameters and the underlying geometry. Therefore, a collection of
images is shown that were used in different case studies.

2.4.1   Simulations of Carbon Nanostructures

First, a simulated FIB-SEM dataset is presented that was used to validate the segmen-
tation algorithm presented in Chapter 3. The simulated structure is a realization of a
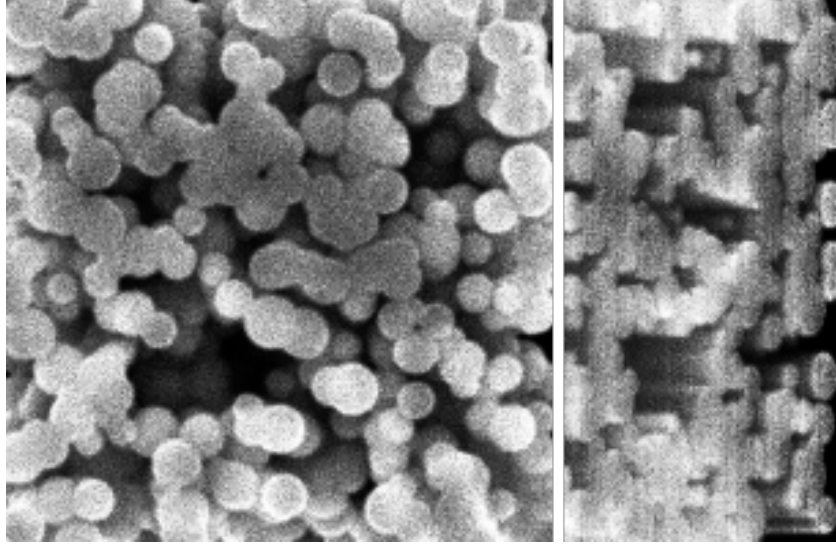
FIGURE 2.22: Volume rendering of the underlying geometry of the simulations in Figure 2.23.

model designed to resemble the pore structure of a nanoporous carbon used as an additive to improve conduction and binding of electrodes in lithium-ion batteries, shown in Figure 2.8. The matrix was modeled by a Boolean model of spheres filled with carbon (a volume rendering is shown in Figure 2.21). The radii of the spheres, which are the typical structure size of the model, are distributed around 50 nm. To make the simulation suitable for validation, the imaging parameters of the simulation have been chosen according to the experimental image.

Figure 2.22 shows the FIB-SEM dataset generated from the simulated SE images. For the dataset 100 images were simulated each with 200x200 pixels. For each pixel 10.000 electrons have been simulated with an initial energy of 5 keV. The pixel and the spot size were chosen to be 5 nm and the SE multiplier was $m = 1$. The simulation of one image took about 2 hours on a cluster node.

The smooth appearance of the image stems from the small structure size, compared for example to the images in Section 2.4.3. Also, a finite volume effect can be observed, where the pixels at the boundaries appear brighter than in the bulk region. The effect comes from the fact that close to the boundary of the structure, the electrons can escape to the side of the simulated volume and thus more electrons are being counted, giving a stronger signal. The same effect can be observed at the boundaries on Figure 2.5.

A comparison of the simulated images with the experimental ones is shown in Figure 2.23. The image shows a slice view of the ground truth and two simulations, with a gold and a carbon matrix (Figures 2.23 (b) and (c)), to compare the effect of these materials on the imaging. Figure 2.23 (d) shows a slice of an experimental dataset. As can be seen, the image of the carbon matrix matches the experimental one much better. The
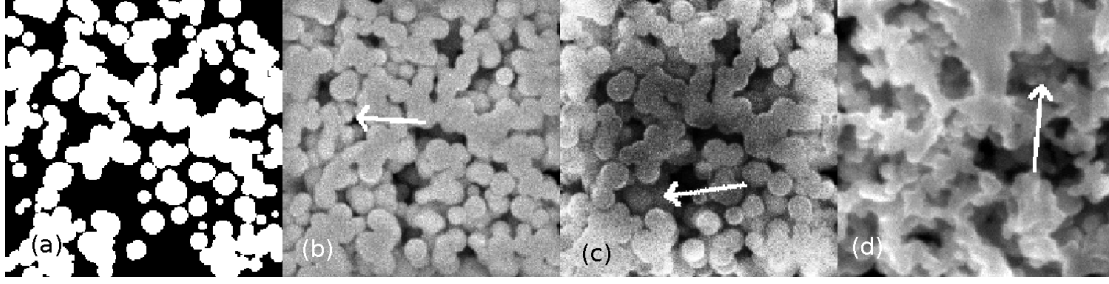
FIGURE 2.23: A comparison of two simulated SEM images with an experimental one: (a) slice view of the underlying geometry; (b) simulated SEM image with a gold matrix; (c) simulated image with carbon matrix; (d)experimental image with carbon matrix.
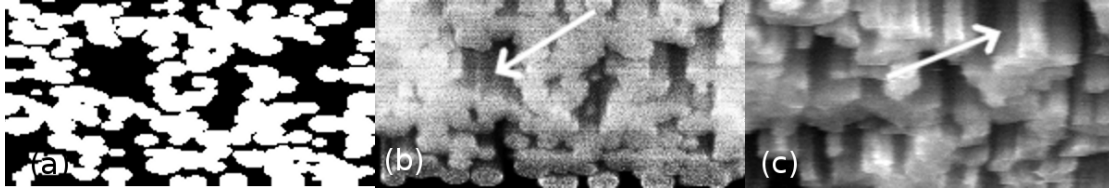
FIGURE 2.24: Cross section views of the FIB-SEM dataset in Figure 2.22: (a) slice view of geometry; (b) simulated carbon dataset; (c) experimental data.

contrast of the simulated gold structure is much higher than in Figures 2.23 (c) and (d). Also the image appears much sharper. Both effects can be explained by the higher scattering cross section σ of gold, which makes the diffusion cloud much smaller and the interaction more local, resulting in a sharper image and stronger contrast. A difference between the simulated and the experimental image is the noise level of the images, which seems to be lower in the experimental image. This is due to the low contrast of carbon, and can be remedied by simulating more electrons per pixel, which would reduce the variance in Equation (2.15).

For the validation of segmentation algorithms, special attention has been given to the reproduction of the 'shine through' artifacts indicated by the arrows. These artifacts stem from the fact that in FIB-SEM datasets, lower lying structures are visible through the pore space. They present a major obstacle to segmentation (more in Chapter 3).

Figure 2.24 shows the comparison of the cross section view of the simulated dataset above, with the carbon matrix (Figure 2.24 (b)) and the experimental image (Figure 2.24 (c)). In addition, the ground truth image is shown in Figure 2.24 (a). Again the 'shine through' artifacts are indicated with arrows and match between the simulation and experimental data. As in both images the matrix is visible through the pores in the higher slices, creating the impression of columns in the cross section view. The milling was simulated with a 10 nm slice thickness.
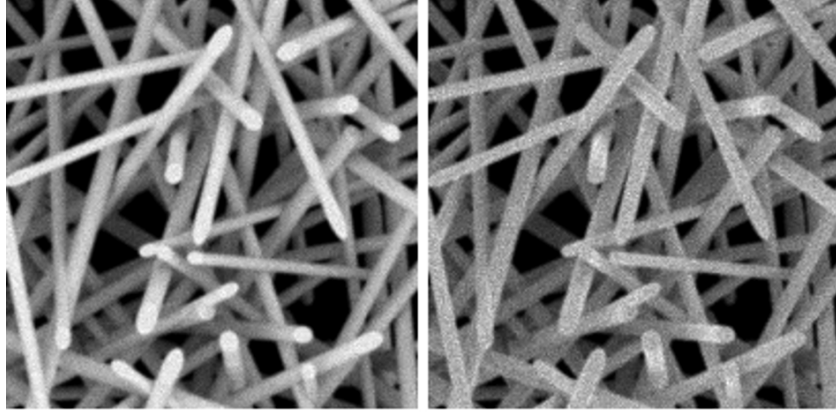
FIGURE 2.25: A simulated FIB-SEM dataset showing the BSE signal (left) and SE signal (right) of a Boolean model of randomly oriented cylinders with carbon as matrix.

2.4.2 Simulation of Fiber Systems

To demonstrate the ability to simulate SEM images of cylinder systems, Figure 2.25 shows the realization of a Boolean model of cylinders. The imaging parameters are the same as in Figure 2.23 and in Figure 2.24. The BSE signal is shown on the left and the SE signal on the right. The simulation of both images took about 1 hour on a lenovo T60 notebook.

Also, fiber systems have been simulated, one of which is shown in Figure 2.26. For the modeling of the fibers, the method described in Section 2.2.3 has been used. As can be seen, even with a simple approximation with spheres and cylinders, the fibers appear smooth. This is due to the fact, that the distance between the spheres is very small. For each pixel 20.000 electrons have been simulated, yet the computation was made in a matter of hours, emphasizing the fact that even very complex geometries with tens of thousands of spheres and cylinders can be simulated on a regular basis.

2.4.3 Simulation of Carbon Microstructures

The following images show microstructures also made of carbon, but on a larger length scale of micrometers rather than nanometers. Thus, in the following images, it can be observed that the appearance of the images depends on the physical size of the structure. To illustrate this, realizations of Boolean models of spheres and cylinders were generated. A volume rendering of the geometry is shown in Figure 2.27. Each simulation shows a view on the top of the volume on the left and a cross section view of the image stack on the right. Figure 2.28 shows a simulated FIB-SEM dataset with a carbon matrix, 5 keV beam energy and a pixel size of 5 nm. For each pixel 10.000 primary electrons have been simulated. In both the slice and the cross section view the BSE signal was used. As
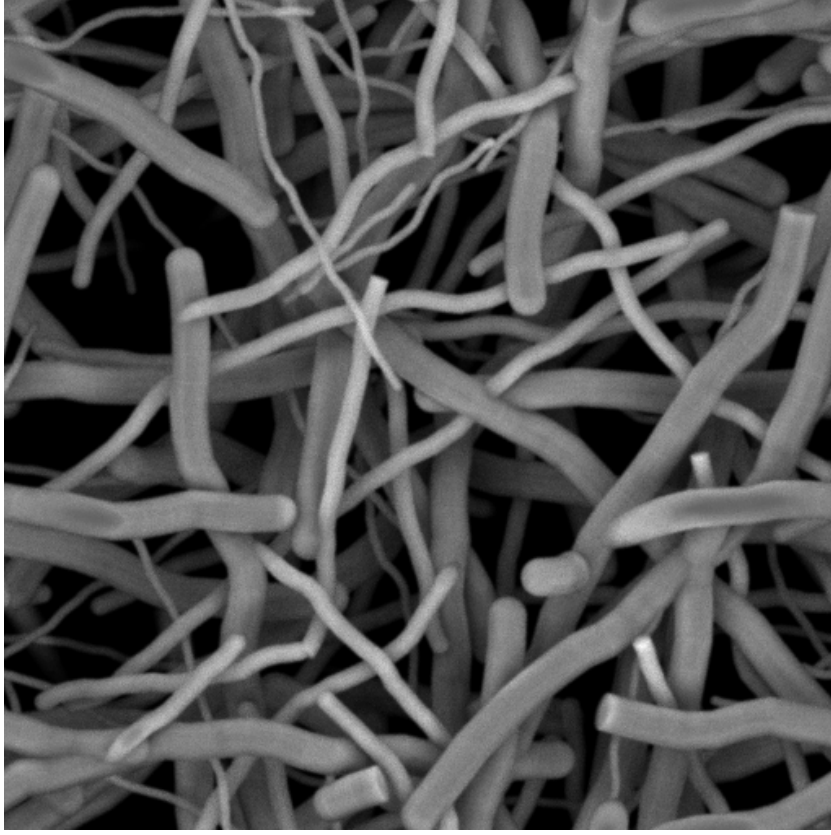
FIGURE 2.26: BSE image of a system of curved fibers.

can be seen, the edge effects are finer and the milling plane has an almost uniform gray value. This indicates that the interaction volume with the matrix is small compared to the pixel and structure size.

Figure 2.29 show the corresponding SE image to Figure 2.28. In the SE images the edge effects are more pronounced, due to the fact that the SE emission has a different angular distribution than the BSE emission. This leads to an overall impression of a higher contrast in the SE images. Also, the SE image seems to have a lower signal to noise ratio, which is due to the different statistics of the SE signal, differing from the usual binomial statistics. To improve the SE image quality in Figure 2.29, the SE multiplier m was set to $m = 3$. This increases the number of SE generated and counted which results in less noisy images. Also, in both cases the 'shine through'-artifacts are clearly visible in the cross section view. Further results are shown in Figures 2.31 and 2.32 where both show a geometry of cylinders, also generated from a realization of a Boolean model. The 'shine through'-artifacts are much stronger in the cylinder geometry due to the lower volume fraction, which leads to a 'deeper' view into the structure. Also, the same differences between the BSE and SE images can be observed.
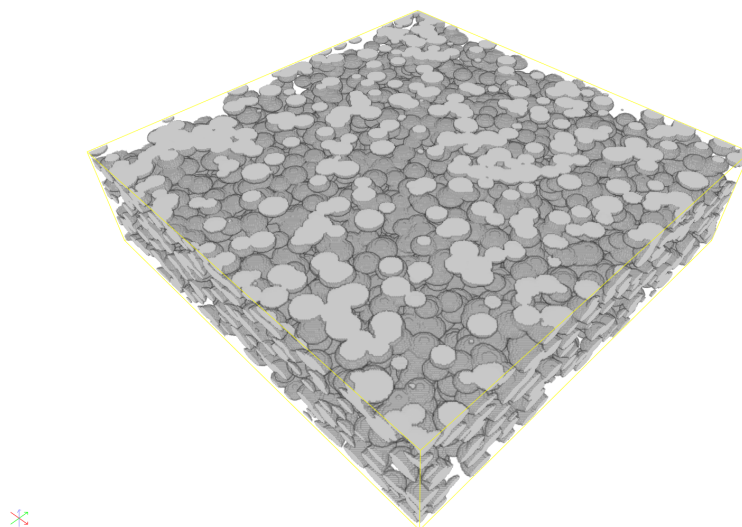
FIGURE 2.27: Underlying geometry of Figures 2.28 and 2.29: a realization of a Boolean model with spheres as grains.
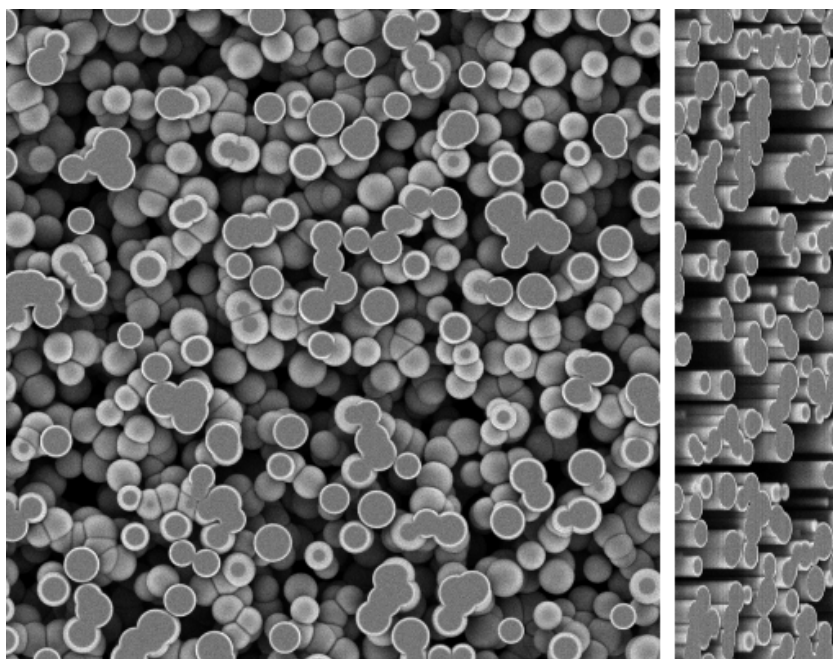
FIGURE 2.28: Slice view and cross section on a simulated FIB-SEM BSE signal dataset (parameters: carbon matrix, 5 keV beam energy, 5 x 5 x 10 nm voxel size, 10.000 electrons/voxel).
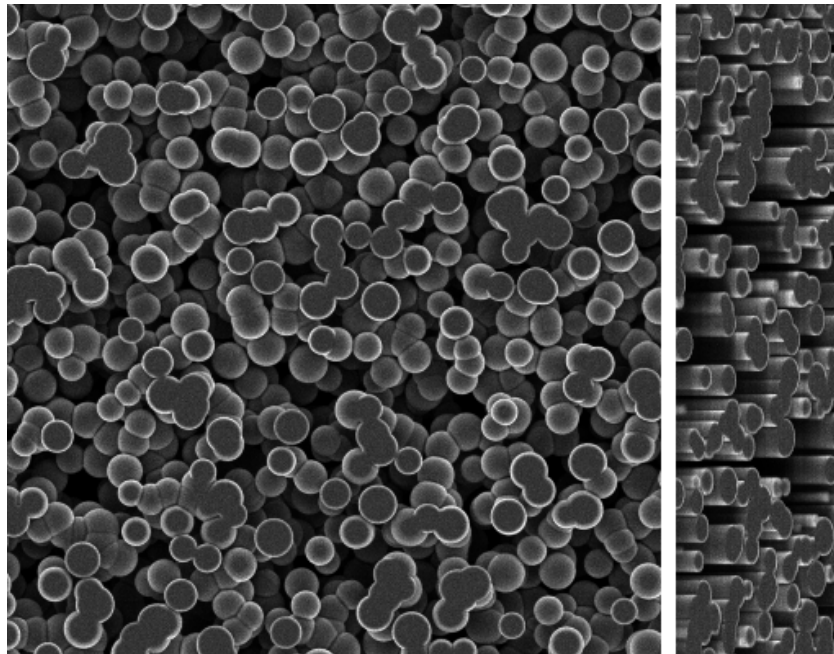
FIGURE 2.29: Slice view and cross section on a simulated FIB-SEM SE signal dataset (parameters: carbon matrix, 5 keV beam energy, 5 x 5 x 10 nm voxel size, 10.000 electrons/voxel).
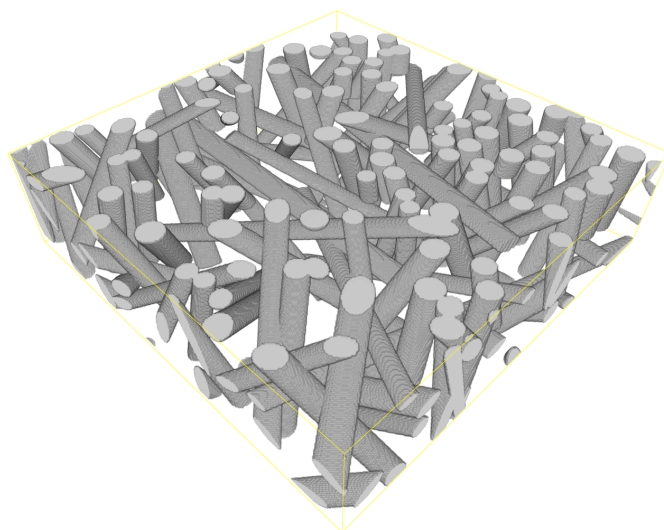
FIGURE 2.30: Underlying geometry of Figures 2.31 and 2.32: a realization of a Boolean model with cylinders as grains.
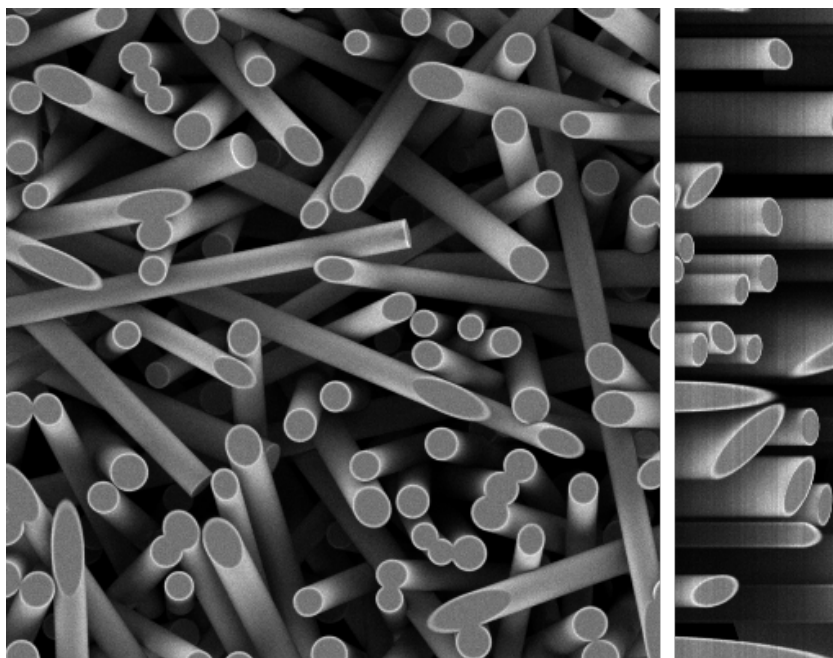
FIGURE 2.31: Slice view and cross section on a simulated FIB-SEM BSE signal dataset (parameters: carbon matrix, 5 keV beam energy, 5 x 5 x 10 nm voxel size, 10.000 electrons/voxel).
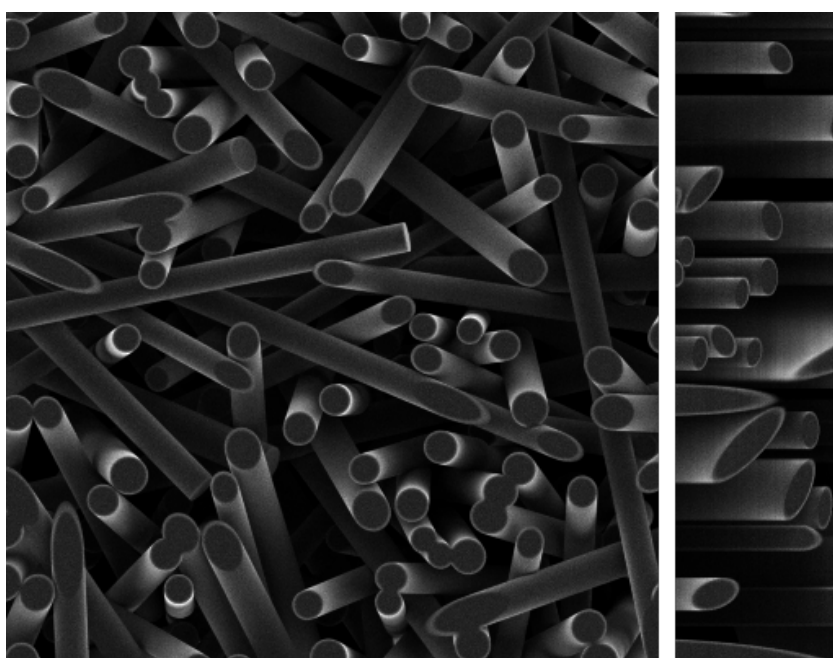
FIGURE 2.32: Slice view and cross section on a simulated FIB-SEM SE signal dataset (parameters: carbon matrix, 5 keV beam energy, 5 x 5 x 10 nm voxel size, 10.000 electrons/voxel).

2.5   Discussion and Outlook

2.5.1   Discussion

In the preceding sections it was shown that the simulation of FIB-SEM datasets is possible, and moreover feasible on a regular basis. Given the state of the field before, this was by not necessarily clear. After a short introduction on the general principles of SEM and the aims of the project, the Monte Carlo technique was motivated and explained in the context of SEM simulation. Then a physical model was introduced, which after evaluation with the Monte Carlo technique gives accurate simulations of the beam-specimen interaction on a small scale. Starting from the work in Seeger et al. [2003], the model was used to simulate SEM images of simple structures. Then, the work was extended to include more complex geometries, tailored to the application of imaging random microstructures. The model is capable of simulating packings of spheres, cylinders as well as curved fibers. To further accelerate the SEM simulation, new acceleration algorithms were developed exploiting computational aspects (path compression) and physical properties (SE decoupling) of the problem. Other existing techniques were implemented (precomputation, binning). Also, a geometric model was developed to model the SEM in general and the FIB-SEM setup especially.

In the last section, results were presented and the simulated images were compared to experimental ones and similarities and differences were discussed. By and large, the simulation can accurately reproduce properties of the images dependent on scale, material properties, SEM imaging parameters, and geometry of the specimen.

In its current state, the simulation cannot reproduce surface roughness, as it is not included in the geometric model. Also, the chamber setup cannot be reproduced, which also has to be modeled. As of today, geometries of specimen composed of different chemical phases cannot be simulated, although this point could be added.

2.5.2   Outlook

Starting form the state of the simulation as it is, two obvious avenues of research are possible. One is to model more complex specimen, i.e. with more than one phase and with a more complex geometry. More complex geometries can be modeled very easily, by applying more complex geometric descriptions, such as constructive solid geometry. In general, any description can be added very easily, provided the two tests of intersection with a point and a ray can be provided with a sufficient speed. The addition of more than one phase is more complicated, since the precomputation technique relies on the fact

that complete paths, except the straight segments in vacuum, are known beforehand. If the scattering cross section changes within the specimen, this can no longer be assumed. But if the path library is enhanced with paths in different materials, the path tracking algorithm can be extended to track electrons through multiple phases.

Also, the simulation can be amended by adding simulations of the detectors and the electron trajectories in the chamber as in Konvalina and Müllerová [2006]. With their high energy, the BSE propagate along straight lines in the chamber, which is accurately represented in the simulation. For SE usually an electric field is used to attract the SE towards the detector. To amend the simulation, the electric field in the chamber could be calculated and then the electrons could be tracked through the field and if they hit the detector, they would be counted for the signal.

Also, to check the accuracy of the simulation, a geometry of a real microstructure could be reconstructed and then simulated. Then the simulated images could be compared to the experimental ones. In a first step, a reconstruction algorithm was developed for FIB-SEM data, which is described in the next chapter.

3

Morphological Segmentation of FIB-SEM Data

The work in this chapter has been published in:

and further results will be published in

3.1   The Segmentation Problem

In image processing, segmentation is the problem to partition an image into regions in a meaningful way. A classical example is to segment a car in an image. In this PhD work, the task to be solved is to segment the matrix phase of a highly porous material in a FIB-SEM dataset, i.e. dividing the image into an area which corresponds to the pore space and an area corresponding to the matrix. If completed successfully, the segmentation allows to analyze the micro- or nanostructure of the porous medium. An illustration of the problem is given in Figure 3.1, where the overlay indicates the segmented matrix phase. The dataset shown in the image was simulated as described in Chapter 2, which means that the ground truth, i.e. the correct result of the segmentation was known
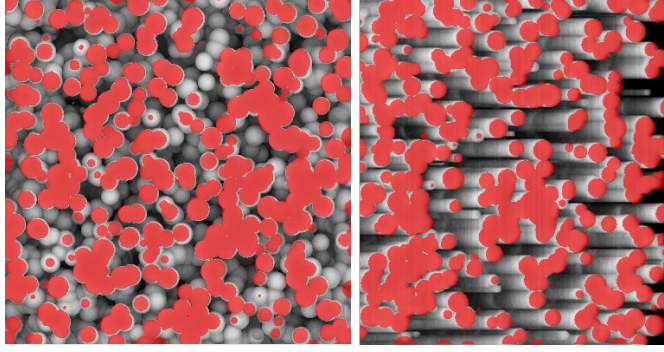
FIGURE 3.1: Illustration of the segmentation problem on simulated data (where the
ground truth is known and indicated by the red overlay).

beforehand, thus the segmentation was trivial. The challenge posed for this PhD thesis
is to develop a segmentation algorithm which finds the segmentation of the matrix in
an experimental FIB-SEM dataset.

3.1.1   The Sample Material

To test and validate the segmentation during development, a dataset of a nanoporous
material is needed. To this end, an experimental dataset of a nanoporous carbon struc-
ture was generated. The sample material used is a structured carbon coating, which has
been applied to a copper foil. In practice, the material is used as a negative Li-ion battery
electrode. The coating consists of three phases plus the pore space. A microstructure,
which is the main part of the coating is used as active material, responsible for the ion
storage. The microparticles have an average diameter of 32 μm and make up 90 % of
the weight. To enhance the conductivity, which is important for the electrochemical
behaviour, the active phase is complemented with a nanoporous phase, which will be
referred to as the additive. The nanoporous additive accounts for 6 % of the weight and
has a typical structure size of $d \approx 40$ nm. The overall thickness of the coating is 70 μm.
The remaining 4 % of the mass is made up by a polymeric binder which stengthens the
structure. Since the microstructure is too big to be analyzed with FIB-SEM nanoto-
mography, we will be concerned with the nanoporous additive on which we will test and
verify our segmentation.

3.1.2   The FIB-SEM Dataset

As described in the previous chapter, FIB-SEM datasets are stacks of SEM images. The
data used in this chapter was generated using an FEI Helios Nano Lab 600 device. The
original data consisted of 370 SEM images with the dimension 1024 x 884 pixels. The
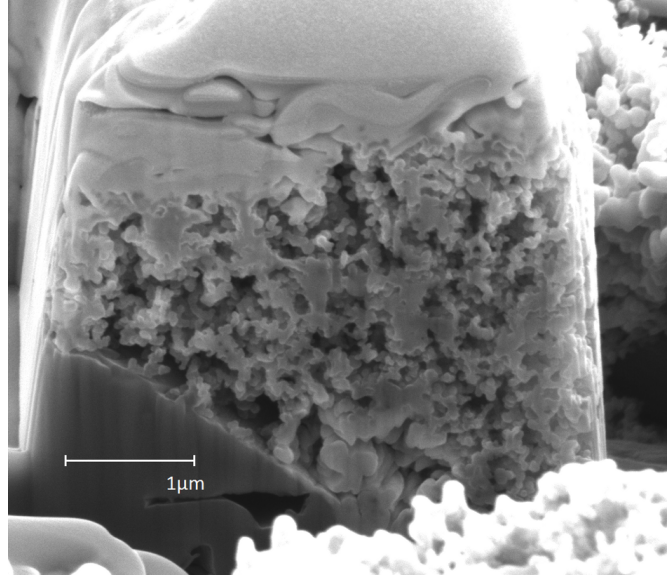
FIGURE 3.2: The first slice of the FIB-SEM dataset used for the segmentation.

SEM was operated at 5 keV beam energy and the SE signal was used for the imaging. The first slice of the dataset is shown in Figure 3.2.

The figure shows the typical FIB-SEM setup (see Section 2.1.1) with the block of porous material to be segmented at the center. Surrounding the block is the trench-like structure depicted in Figure 2.4. The background showing the trench and the surrounding area of the structure will later be used for the alignment, since it represents a static frame of reference. One of the microparticles hosting the nanoporous additive can be seen. Also, a layer with a very high contrast on top of the block is visible. This layer consists of platinum that was sputtered onto the specimen to enhance the accuracy of the FIB sectioning.

In the FIB-SEM imaging process slices of 10 nm thickness were milled off the block of porous material, to be seen in the middle of the image. This leads to a voxel size of 10 nm in the z-direction. Due to the tilting of the specimen for the FIB milling, the voxel size is also not isotropic in the x-y-plane. The original voxel size in the image plane is 5 nm in the x- and y-direction, but the tilting of the specimen with an angle of 52° leads to a voxel size in the y-direction of 6.27 nm. Thus, one voxel represents a volume of 5 nm x 6.27 nm x 10 nm. The SE signal is encoded in the gray values of the image which is coded in 8 bit gray scales.

3.1.3 The Artifacts

By the FIB-SEM image acquisition process, several artifacts are created, some of them due to SEM imaging, some due to the FIB milling process. Additional to the typical
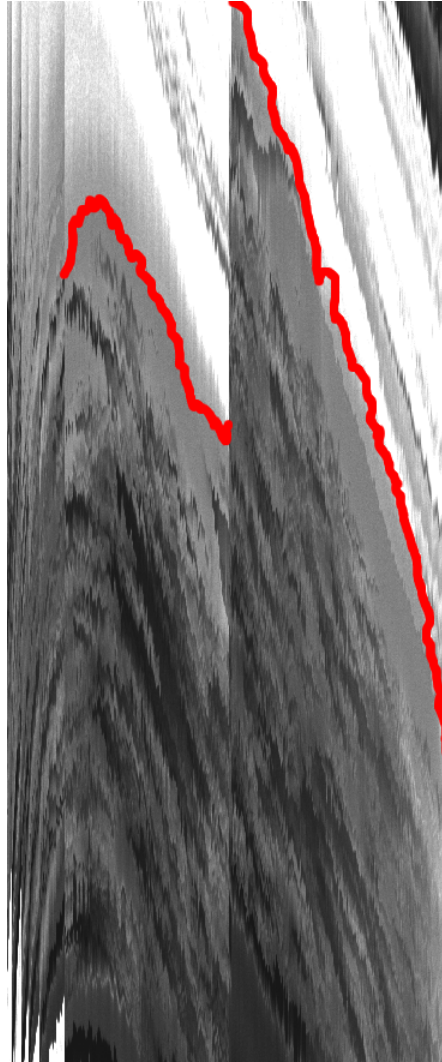
FIGURE 3.3: A cross section view of the raw FIB-SEM dataset. The red markers indicate the misalignment from specimen drift and beam drift.

SEM related artifacts such as edge effects and transparency of thin structures, which make a segmentation by thresholding difficult, the FIB-SEM process adds other specific ones.

3.1.3.1   Beam Drift or Specimen Drift

For the FIB-SEM dataset to make sense as a three-dimensional representation on a three-dimensional grid, a pixel in the first images has to refer to the same x- and y-coordinate in space in every other image. This requires a perfect alignment of the images. Yet, in practice, the specimen stage moves during the tilting process and also the specimen itself deforms due to the mechanical forces applied. This phenomenon is usually referred to as specimen drift. Also, the beam of the SEM can sometimes not be kept stable for such a long time, which means that towards the end of the process the beam scans a

slightly different area of the specimen than at the beginning. This is called beam drift and like the specimen drift causes a misalignment of the images in the dataset. Figure 3.3 shows a cross section view of the FIB-SEM dataset before preprocessing. As can be seen, the structure of the specimen drifts to the lower part of the image. After about half of the images, the SEM was realigned and then the drift continues towards the end. These artifacts are common and need to be corrected through computational alignment during the preprocessing (see Section 3.3.1).

3.1.3.2   Brightness and Contrast Differences

Since each image of the stack is acquired independently of the others, the brightness and contrast differ between each of the images. This leads to changes of gray values between different pixels in different images, without a physical reason. Also, due to the setup of the detector and the chamber, changes in brightness can occur on large scales in the images. Typically, the lower part of the images is slightly darker. This is due to the fact that electrons from the deeper part of the structure have a higher probability to be absorbed by the surroundings. Thus, they are not detected and the images darken. These effects also have to be corrected in a preprocessing step (see Section 3.3.1).

3.1.3.3   'Shine-Through' Artifacts

The most complicated artifacts in the data are the so called 'shine-through' artifacts. To correct for these artifacts is the main challenge in the segmentation of FIB-SEM data and the development of a segmentation method is the main topic of this chapter. The artifacts stem from the fact that lower lying structures are visible through the pore space. Since the pore space is transparent in the SEM images, structures in the pore space are visible through the pores (indicated by arrows in Figure 2.8). In the dataset, the artifacts are three-dimensional. This becomes obvious in the cross section view, as indicated in the slice view in Figure 2.8. These structures can have gray values similar to those of structures outside the pore space, thus rendering segmentation by thresholding not feasible. In the cross section view the artifacts appear as ramps in the gray value, sometimes giving the impression of columns in the cross section slices. Figure 3.4 shows a blow-up of Figure 3.6 with and without an overlay indicating the structure to be segmented and the 'shine-through' artifacts. It can be seen that the gray value rises from the left to the right. This is due to the fact that as more and more slices are milled off the structure, more electrons can escape to the detector, yielding a stronger signal. When the milling plane reaches the structure, the gray value either reaches a peak from
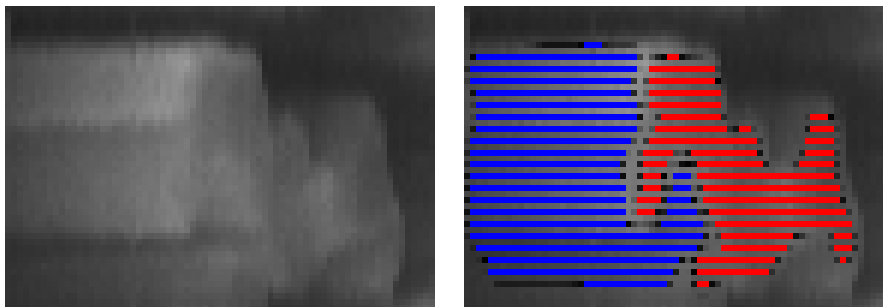
FIGURE 3.4: A blow-up of the cross section view of the aligned FIB-SEM dataset (right), with overlays of the 'shine-through'-artifacts (blue) and the structure (red) on the left.

edge effects or a plateau corresponding to the constant gray value of a planar surface. These features will be used later to identify the 'shine-through' artifacts in the data.

3.1.4   Previous Work

Several attempts to segment FIB-SEM data have been made. Nonetheless, the segmentation of FIB-SEM data is still a problem awaiting a general solution. Simple methods, such as gray level thresholding are applicable for low levels of porosity. This approach uses the fact that when the electron beam scans through the pores, fewer electrons can escape to the detector and the signal appears darker. Unfortunately, for high levels of porosity larger regions of the image lie in the pore space. This makes it easier for electrons to escape, raising the intensity in the pore space.

Improvements have been made through adaptive thresholding methods, as in Blayvas et al. [2006], and also through taking derivatives and edges into account, e.g. in the level-set based method in Jørgensen et al. [2010]. Further improvement could be made by using a two-stage approach combining Jørgensen et al. [2010]'s method with a threshold back propagation approach (see Salzer et al. [2012]). Even though these methods give reasonable results judged by visual inspection (the authors of Jørgensen et al. [2010] give a misclassification rate of 15% by comparison with manual segmentation), no quantitative error estimates based on ground truth data have been made. In this thesis, we will present a new segmentation method and, using the simulation described in the previous chapter, we will give a quantitative error measure.

For the segmentation we will use morphological image processing. The morphological methods provide a fast way to process large three-dimensional datasets. Also, morphology can extract global features such as minima with a certain dynamic, which is not possible with the usual linear-filter-based approach. Furthermore, with the geodesic reconstruction and watershed transformation, morphology provides natural segmentation

methods. A short recapitulation of the more advanced morphological methods used for the segmentation will be given in the next section.

3.2 Elements from Advanced Mathematical Morphology

To segment the type of data under concern, some more advanced morphological operations are needed, which will now be introduced. All of them can be constructed with the basic operations defined in Section 1.3.3. Again we are following the notation in Soille [1999]. Unfortunately, the structuring element and the secondary electron share the same abbreviation (SE) in the literature of their respective fields. Also, both abbreviations are vital, widely used and appear frequently in this chapter. Hence, in this chapter and in this chapter only, the structuring element is abbreviated by SE, while in the other chapters SE stands for secondary electron.

3.2.1 Morphological Half-Gradient

Similar to the morphological gradient, the morphological half-gradient can be constructed by replacing one of the operations in the morphological gradient by the identity. According to the remaining transformation, the morphological half-gradient by erosion is defined by

$$\rho_B^-(f) = f - \epsilon_B(f) \tag{3.1}$$

and the morphological gradient by dilation is defined by

$$\rho_B^+(f) = \delta_B(f) - f. \tag{3.2}$$

The morphological half-gradient behaves similar to the morphological gradient. But in the context of the segmentation, it will be used to extract directional information. Therefore, an anisotropic structuring element (SE) is used.

3.2.2 Hit-or-Miss Transformation

The hit-or-miss transformation is an advanced morphological transformation, which uses a combined SE instead of a normal one. The combined SE consists of one SE acting on the foreground of the image and one SE acting on the background, thus the combined SE B is given by

$$B = \{B_{FG}, B_{BG}\}. \tag{3.3}$$

The hit-or-miss transformation can then be written as a union of erosions

$$\text{HMT}_B(f) = \epsilon_{B_{FG}}(f) \cap \epsilon_{B_{BG}}(f^C). \tag{3.4}$$

From the definition it is clear that the hit-or-miss transformation is true, if the foreground SE is included in the foreground and the background SE is included in the background. Since an SE cannot be included in the foreground and the background at the same time, it is clear that B_{FG} and B_{BG} cannot intersect. Provided that the SE is much smaller than the set itself, the hit-or-miss transformation can be used to detect boundaries of the set.

3.2.3   Geodesic Reconstruction

A morphological reconstruction is the repeated application of a transformation until idempotence, i.e. until the resulting image does not change any further under the transformation. In the case of geodesic reconstruction, so-called geodesic transformations are applied, i.e. geodesic erosion and geodesic dilation. Both transformations accept two images and a SE as input, instead of just one image and one SE like the standard erosion and dilation.

The geodesic erosion of size one is defined as

$$\epsilon_B^{(1)}(f, g) = \epsilon_B(f) \vee g \tag{3.5}$$

with the so-called marker image f and the mask image g as arguments, where the marker image must be greater than the mask image, $f \geq g$. As can be seen, the geodesic erosion is the supremum of the eroded marker image and the mask image. Geodesic erosions of larger size are then defined recursively as successive geodesic erosions of size one according to

$$\epsilon_B^{(n)}(f, g) = \epsilon_B^{(1)}[\epsilon_B^{(n-1)}(f, g), g], \tag{3.6}$$

where the geodesic erosion of size zero is simply the input image

$$\epsilon_B^{(0)}(f, g) = f. \tag{3.7}$$

The geodesic dilation of size one is defined analogously as the infimum of the dilated marker image and the mask image, i.e.

$$\delta_B^{(1)} = \delta_B(f) \wedge g. \tag{3.8}$$

Here the marker image must be less than the mask image, $f \leq g$. Also, the geodesic dilations of size 0 and size n are defined accordingly

$$\delta_B^{(0)}(f,g) = \qquad f, \tag{3.9}$$

$$\delta_B^{(n)}(f,g) = \quad \delta_B^{(1)}[\delta_B^{(n-1)}(f,g), g]. \tag{3.10}$$

As stated, a reconstruction means that a transformation is applied until idempotence. For the geodesic erosion, that is

$$\epsilon_B^{(i)}(f,g) = \epsilon_B^{(i+1)}(f,g). \tag{3.11}$$

In mathematical notation, the geodesic reconstruction by erosion is written as

$$R_B^\epsilon(f,g) = \epsilon_B^{(i)}(f,g), \tag{3.12}$$

where i is the first step for which Equation 3.11 holds.

Analogously, the geodesic reconstruction by dilation is defined as

$$R_B^\epsilon(f,g) = \delta_B^{(i)}(f,g), \tag{3.13}$$

where $\delta_B^{(i)}(f,g) = \delta_B^{(i+1)}(f,g)$.

The geodesic reconstruction can detect local gray value minima with a minimum depth and it will be used in that role later on.

3.2.4 Watershed Transformation

The natural way of segmentation in morphological image processing is the watershed transformation. The watershed is easily explained, yet a formal definition is more complex. Intuitively, for the watershed transformation a gray value image is thought of as a relief where the local height corresponds to the gray value of the voxels in the image. Then a rainfall on the relief is considered, with the water flowing through the relief. Intuitively the water will accumulate at the minima, with each basin growing as more and more water flows into the basin. In the segmentation, each basin is considered to be a segment of the image. If two segments meet, a watershed is installed dividing them.

Of course the analogy only goes so far, since the flow of water is not actually simulated. In the algorithm, the regional minima of the image are determined, yielding a seed for a region growing algorithm. Then each region is grown, depending on the gray value in the image. For a formal definition see Beucher and Lantuéjoul [1979].
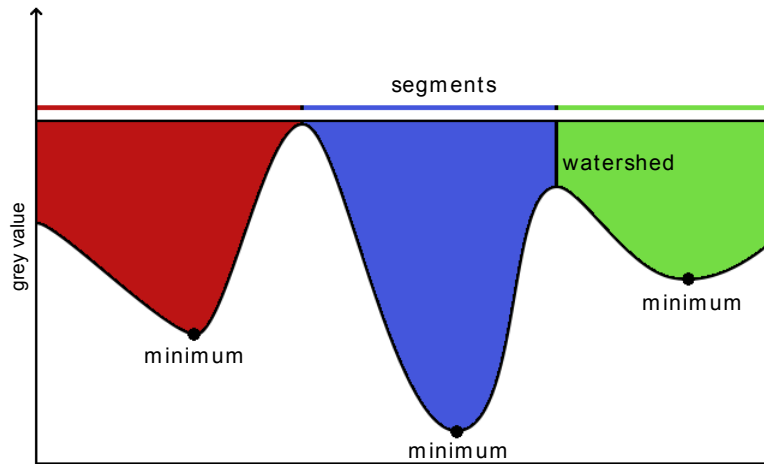
FIGURE 3.5: A one-dimensional example of a watershed segmentation.

A one-dimensional example of a watershed segmentation is shown in Figure 3.5. In this thesis the three-dimensional version of the watershed is used.

A special case of the watershed transformation is the constrained watershed transformation (Beucher and Lantuéjoul [1979], Beucher [1990]). Instead of using the minima as initial basins, the initial basins are fed into the transformation as an argument. Therefore, a labeled image is passed to the algorithm and each label is grown according to the watershed algorithm.

3.3   Morphological Segmentation Method

With the advanced morphological transformations at hand, the new segmentation algorithm developed in this thesis can be described.

An outline of the general workflow is depicted in Figure 3.11, at the end of this section. First, a preprocessing of the dataset is made, enhancing the quality of the data. Then feature images are generated to identify characteristic points or regions. The feature images are subsequently used to generate a preliminary segmentation, which is in turn used to generate markers for a constrained watershed transformation. This refines the preliminary segmentation, yielding the final result.

In this section, a detailed description of the segmentation algorithm will be given incorporating the preprocessing, a discussion of the features used to segment that data and the segmentation step itself. At the end, a summary of the algorithm will be given.

3.3.1 Preprocessing

Before the actual segmentation, the dataset undergoes some preprocessing steps, to improve the quality of the data. This is mainly an alignment of the images and a contrast and brightness correction of the images.

3.3.1.1 Alignment

The individual SEM images can be shifted against one another. As indicated in Section 3.1.3, this might be due to specimen- or beam-drift or perturbations in the mechanics of the tilting stage. In order to get a representative voxel volume, this needs to be corrected as the segmentation relies on the change in intensity of one pixel through the images of the stack. As shown in Figure 3.3, this is not possible in the original dataset. For the alignment of the data, several techniques can be used. For the data investigated here, the 'Linear Stack Alignment with SIFT' plug-in of the Fiji software (Schindelin et al. [2012]) was used. Even though the dataset will eventually be cropped to the region of interest as shown in Figure 2.8, the alignment was made without cropping. That way, the surrounding of the ROI, which is not affected by the FIB slicing, can be used as landmarks for the alignment, improving its quality. A cross section view of the resulting aligned dataset can be seen in Figure 3.6.

3.3.1.2 Cropping and Brightness Correction

After the alignment, the dataset can be interpreted as a 3D-voxel grid, where one voxel represents a cuboidal volume in space. Then, the dataset is cropped, such that it covers the region of interest in Figure 2.8, which represents the porous structure to be segmented. After the cropping, differences in the brightness in different regions and between the images have to be corrected to improve the segmentation result.

To correct for large-scale differences in the brightness within the images, a mean-filter with a filter mask with of a 100 voxels radius was applied to the images. Then, the mean-filtered image was subtracted from the original image. This removes large-scale variations in the gray value and leaves smaller-scale variations like the structure. Thus, for every dataset the filter mask has to be much larger than the typical structure size. The images have to be converted to a 32-bit floating point voxel type, since negative numbers can occur in the subtraction, which cannot be encoded in 8-bit-unsigned gray values. After the preprocessing, the data is converted back to 8-bit gray scale to save memory.
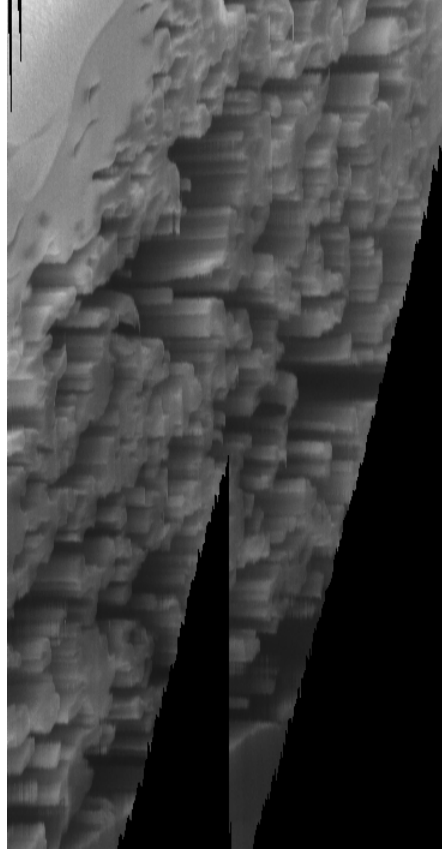
FIGURE 3.6: A cross section view of the aligned FIB-SEM dataset.

In a second preprocessing step, a histogram normalization and equalization, again with Fiji, is done. The resulting dataset is depicted in Figure 3.7.

3.3.2   Feature Images

After the preprocessing step described in Section 3.3.1, a number of feature images are generated extracting information from the data. These will then be used to mark or delineate the regions to be segmented, may it be pore space or matrix. Ideally, the features are exact and universal, meaning they perfectly identify the regions and work on all datasets. Yet, the fact that features are never perfect and universal is self-evident, so, to motivate some universality, a physical reasoning derived from the imaging process of the structure will be given for each feature. The examples for the feature images are taken from the segmentation in the validation in Section 3.4, where a simulated FIB-SEM dataset was segmented.
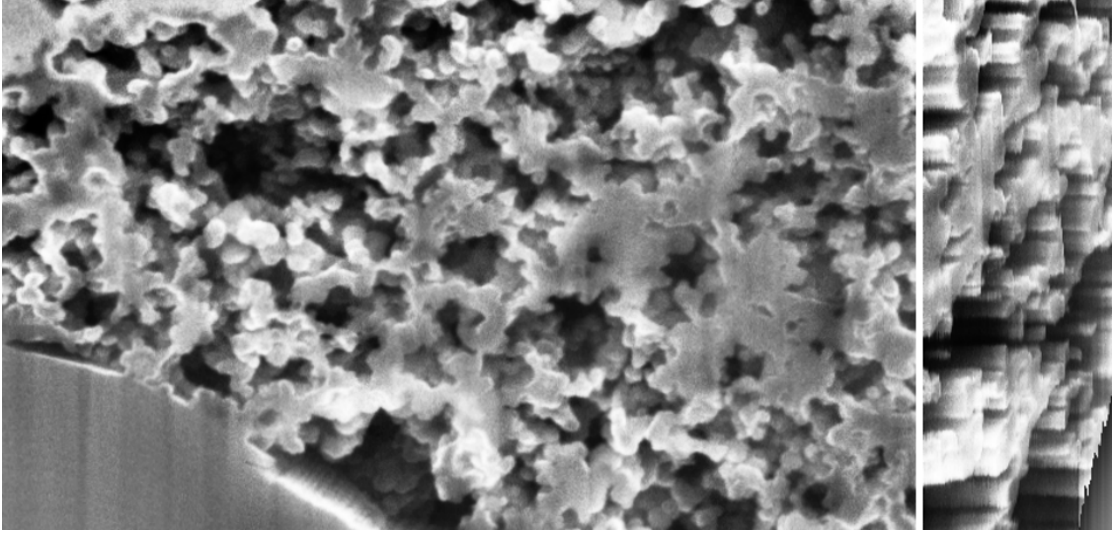
FIGURE 3.7: A slice view and a cross section view of the FIB-SEM dataset after preprocessing.

3.3.2.1 Threshold Image

The simplest feature to use is a threshold on the gray values of the image. The threshold is used to mark voxels belonging to the void phase of the image. When the electron beam enters deep into the pores, the BSE and SE have a low probability of exiting from inside the pores, since they are absorbed by the surrounding structure. Thus, a low intensity indicates pore space in the image. In principle, the intensity feature can be exploited with any thresholding algorithm, from the simple global thresholding to local approaches. But in practical tests, a simple global threshold was sufficient. Unfortunately, due to the 'shine-through'-artifacts, which have a high intensity, the thresholding approach has a high misclassification rate (see Table 3.1 on page 79), yet it contributes a first estimate to the segmentation. And if the threshold is chosen correctly, an exclusion of a set of voxels definitely belonging to the pore space can be made.

The corresponding feature image is given by

$$F_{GV} = \text{Th}_{0,g_{min}}(F_{in}).\tag{3.14}$$

Here, F_{GV} is the feature image and $\text{Th}_{min,max}$ is the thresholding operation selecting all voxels that have intensity in $[min, max]$. An example of the feature image can be seen in Figure 3.10 (a). As can be seen, the feature detects dark areas within the pore space.
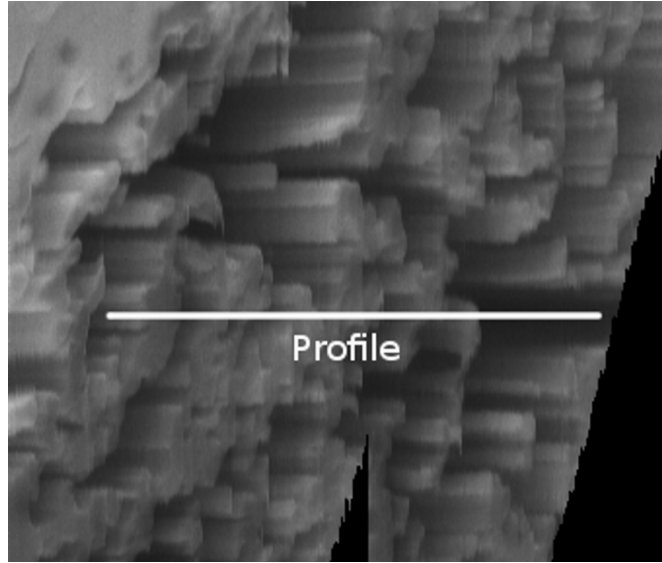
FIGURE 3.8: A profile of a pixel as overlay on the cross section view of the dataset.
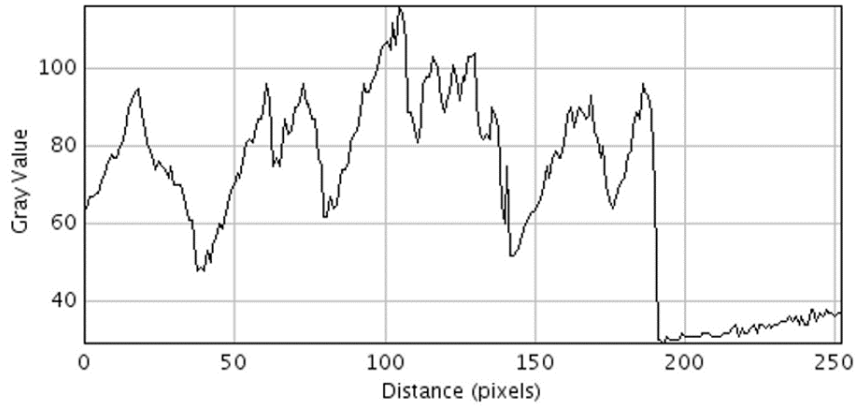
FIGURE 3.9: The corresponding gray value profile of the pixel marked in Figure 3.8.

3.3.2.2   Feature Images from Z-Profiles

For the more advanced features, the z-profiles of the image will be used. To this end, the three-dimensional image $F_{in}(x, y, z)$ is interpreted as a set of one-dimensional lines $F_{in}^{(x,y)}(z)$, each representing the change in gray value of one pixel in the slices of the dataset. An illustration is given in Figures 3.8 and 3.9. The graph in Figure 3.9 depicts the gray value of the pixel marked by the white line in Figure 3.8, which will be called the z-profile of the pixel from here on. For the preliminary segmentation, morphological operations will be applied to the z-profiles instead of the complete three-dimensional image. Therefore, the SE of the morphology will be restricted to one dimension along the z-axis. The exact form of the SE will be given for each transformation.

The first feature to be detected concerns the 'shine-through'-artifacts. In the profile, these artifacts show a characteristic rise in gray value towards the positive z-axis. Since
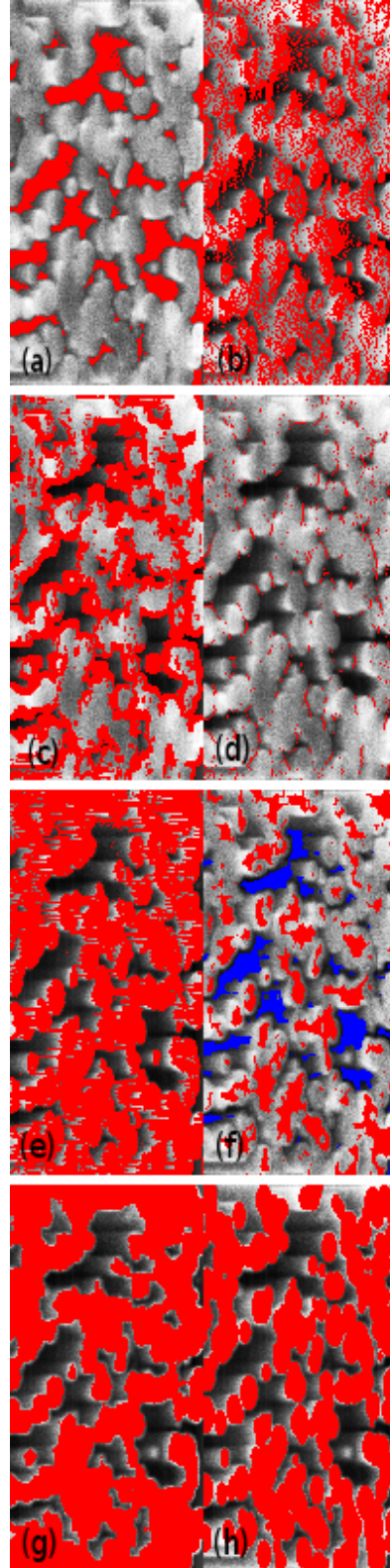
FIGURE 3.10: Feature images used for the segmentation: (a) gray value feature F_{GV}; (b) artifact image F_{Art}; (c) boundary detection F_{Bound}; (d) relevant minima $F_{min}^{(2)}$; (e) preliminary segmentation; (f) label image F_{Label}; (g) final segmentation result F_{Res}; (h) and for comparison the ground truth.

only a few electrons can escape from inside the pores, the structure visible inside the pores appears darker. Then, as further slices are milled away, more and more electrons can reach the detector leading to a characteristic rise in gray value in the profile. When the milling plane has reached the deeper lying structure, the gray level reaches a plateau or a maximum and then falls off again. The maximum is mostly due to edge effects, which appear when the structure is cut. A subsequent plateau indicates that the milling plane has reached a massive structure with the electron beam incident at a right angle, yielding a constant intensity.

To detect the 'shine-through'-artifacts, the morphological half-gradient by dilation is used with a suitable SE. The SE is made of a line segment which extends l voxels from the origin in the positive z-direction, denoted z_{l+}, where l is a parameter of the algorithm. This half-gradient can be used to detect positive gradients in z-direction. If the intensity in the profile rises, the half-gradient is positive, otherwise it is zero. To generate a marker image, the half-gradient image is thresholded. The resulting image marks regions where the intensity rose by a threshold value d within the SE. Since the marker indicates artifacts, the complement has to be used to detect matrix. The corresponding feature image has the form:

$$F_{Art} = [\mathrm{Th}_{0,d}[\delta_{z_{l+}}(F_{in}) - F_{in}]]^C. \qquad (3.15)$$

Figure 3.10(b) shows the corresponding image in the segmentation, where the marker indicates mostly the beginning of the structure to be segmented.

The second feature to be extracted from the profile is a sharp drop in intensity with a subsequent minimum. This feature appears when a structure in the foreground is milled off and the underlying pore space is revealed. Then the intensity either drops to almost zero, when dark pore space is revealed, or, when a (still darker) 'shine-through'-artifact is revealed a sharp drop in the profile happens. In any case, the gray value either remains almost zero and then rises with subsequent slices, or if an artifact is revealed, the gray value starts rising again immediately. Either way, a minimum will occur.

The geodesic reconstruction by dilation is used to detect these minima. There, the original data serves as the marker image and the mask image is given by the original data subtracted by a constant d_{min}. The constant d_{min} will be the minimum dynamic, i.e. the minimum depth of the minima to be detected. This is necessary to discriminate minima arising from noise or edge effects, which are not descriptive and will from here on be called the irrelevant minima opposed to the relevant ones needed for the segmentation. A line segment z_3 serves as the SE, only this time the segment is centered at the origin, extending one voxel in the positive and the negative z-direction, yielding the connectivity on the z-profile. In the reconstructed image, minima with a dynamic lower than d_{min}

will be 'filled up'. Then the remaining minima in the profile are computed. Since the minima can be intervals on the profile, a hit-or-miss transformation is used to select the first voxel in the interval. This yields the voxel closest to the matrix. This results in the following expression for the feature image:

$$F_{min} = \text{HMT}_{(0,-1)}[\text{Min}_{z_3}[R^{\delta}_{z_3}(F_{in}, F_{in} - d_{min})]]. \tag{3.16}$$

To further suppress the irrelevant minima, the feature image is modified to include only the minima lying close to edges. This should suppress minima inside the matrix, due to edge effects. These minima arise when due to SEM imaging, the edges appear brighter than the bulk of the matrix, thus forming a minimum in the bulk. Therefore, an edge detection has to be made, for which a morphological gradient image is used. The same gradient image will be used later for the constrained watershed transformation. For the data in this thesis, the morphological gradient with a 26 neighborhood in three dimensions (N26) as the SE was chosen, which gives the feature image

$$F_{Grad} = \rho_{N26}(F_{in}). \tag{3.17}$$

For the minima suppression, the gradient image is thresholded, yielding a feature image which indicates the boundary of the structure (see Figure 3.10(c) for an example)

$$F_{\text{Bound}} = \text{Th}_{g,\infty}(F_{Grad}). \tag{3.18}$$

The intersection of the gradient image and the minima image give only the minima near the edges $F^{(2)}_{min}$:

$$F^{(2)}_{min} = F_{min} \cap F_{\text{Bound}}, \tag{3.19}$$

where g is a parameter used for the edge detection. As can be seen in Figure 3.10 (d), the minima occur at the end of the structure in the profile, with some irrelevant minima remaining inside the structure.

3.3.3 Preliminary Segmentation and Constrained Watershed

With the information from the feature images, a preliminary segmentation can be generated. For the preliminary segmentation, the information on the artifacts from the half-gradient is combined with the minima indicating the end of the structure. To achieve this, the complement of the artifact marker is extended to the minima. This will generate a marker which starts at the end of the 'shine-through'-artifact and extends

to the minima, i.e. to the end of the structure in the profile. The necessary transformation can be implemented as a reconstruction by dilation with a suitable SE, having the advantage that only well known morphological transformations are used and with a good implementation, a fast computation is possible. In the transformation, the artifact image serves as the marker image and a mask image is used where the marker extension will stop. The mask image is the union of the minima image and the gray value feature image

$$F_{\text{Mask}} = [F_{min}^{(2)} \cup F_{GV}]^C. \tag{3.20}$$

Then the reconstruction by dilation is used for the marker extension. The SE consists of the voxel at the origin and the neighboring voxel in positive z-direction. Thereby, at each iteration of the geodesic dilation, the markers are extended by one voxel in positive z-direction until either a relevant minimum occurs or the gray value drops below the threshold, indicating the pore space. The preliminary segmentation image thus becomes:

$$F_{\text{Seg}} = R_{0,+1}^{\delta}(F_{Art}, F_{\text{Mask}}). \tag{3.21}$$

3.3.3.1   Refinement with Constrained Watershed

If the features were perfectly consistent and accurate, the segmentation would be finished by now. Yet, unfortunately due to noise and other artifacts, the segmentation still has a large rate of misclassified voxels (as shown in Figure 3.10 (e)). To improve the segmentation, a constrained watershed transformation is used, which exploits the edge information in the gradient image to fit the segmentation to the boundaries of the matrix phase. The preliminary segmentation F_{Seg} is used as an initial guess. For the constrained watershed transformation, the labels of the preliminary segmentation are used as initial basins for the region growing process. However, the image is already segmented. Hence, each voxel is assigned to either void or matrix phase already. Thus, some of the labels have to be removed to make room for the fitting.

In practice, both segments are to be separated along the boundaries. Therefore, the labels in the preliminary segmentation are split to separate images, yielding one image for the void phase markers and the matrix phase markers, each. Then both images are eroded to separate the markers. The structuring element of the erosion can be chosen by hand, depending on the quality of the preliminary segmentation. In practice, an erosion of the matrix markers with an ellipsoidal structuring element E(2,2,1) with radius $r = 2$ in the xy-plane and radius $r = 1$ in z-direction, has given good results, i.e.

$$F_{\text{Matrix}} = \epsilon_{\text{E}(2,2,1)}(F_{Seg}). \tag{3.22}$$

For the void markers, it has proven beneficial to differentiate between the preliminary segmentation and the gray value feature image. By construction, the gray value feature is included in the void marker. Yet, when the threshold of the gray value is chosen such that no false-positives occur, i.e. no matrix voxels are marked as void, then a smaller SE in the gray value image can be used. From testing it is known, that this gives a more accurate result. The void markers are then given by the union of both erosions, i.e.

$$F_{\text{Void}} = \epsilon_{\text{E}(2,2,1)}(F_{Seg}^C) \cup \epsilon_{N26}(F_{GV}) \tag{3.23}$$

To generate a label image as input for the constrained watershed segmentation, the void marker image is multiplied by two and added to a zero valued image $I(0)$. Then the matrix markers are added to the same image. That yields a label image F_{Label} (Figure 3.10 (f)) where the matrix markers are given by label 1, the void markers by label 2, and the unmarked phase by label 0.

$$F_{\text{Label}} = I(0) + F_{\text{Matrix}} + 2F_{\text{Void}}. \tag{3.24}$$

The final result is then obtained by running the constrained watershed transform on the gradient image F_{Grad} from Equation 3.17, according to

$$F_{Res} = \text{CWS}(F_{\text{Label}}, F_{\text{Grad}}). \tag{3.25}$$

As can be seen in Figure 3.10 (g) this considerably improves the segmentation. The segmentation does, however, not exactly match the ground truth in Figure 3.10 (h), thus a quantification of the errors in the segmentation is desirable. This will be discussed in depth in the next section.

3.3.4   Summary of the Algorithm

A summary of the segmentation algorithm is depicted in Figure 3.11. First a preprocessing step is performed, where the slices in the data are aligned to get meaningful z-profiles and illumination differences are corrected to get meaningful thresholds and gradients (Section 3.3.1).

Then, feature images are computed on the preprocessed data (Section 3.4.2.2, second column in Figure 3.11). A morphological gradient is computed for the edge recognition and as an input parameter for the constrained watershed transformation. On the morphological gradient, a thresholding is made (Figure 3.10 (c)), to detect edges which are
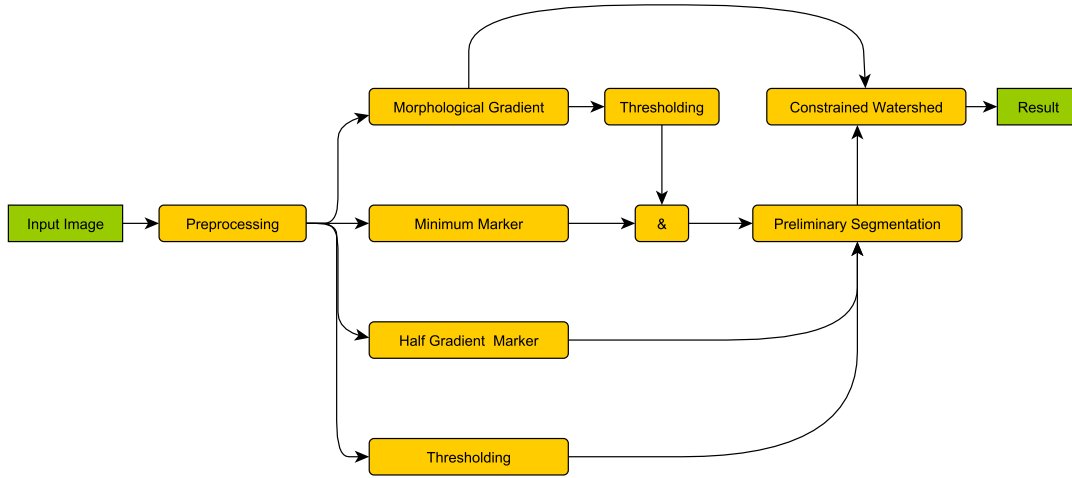
FIGURE 3.11: A flowchart of the segmentation algorithm: the input image goes through a preprocessing stage, then feature images are created, which are combined to give a preliminary segmentation. Subsequentially, the preliminary segmentation is used as input for a constrained watershed transformation.

used to discriminate the relevant minima. Also, a half-gradient image is computed and thresholded to compute the artifact marker image (Figure 3.10 (b)). A morphological reconstruction is used to compute the minima in the profile which have a minimal dynamic. Then the edge recognition is used to get the relevant minima (Figure 3.10 (d)). The remaining feature image is a threshold on the gray value in the data to attribute dark areas in the image to the pore space (Figure 3.10 (a)).

To generate a segmentation from the features (third column in Figure 3.11), a preliminary segmentation is generated by morphological reconstruction. The morphological reconstruction selects the solid phase by extending the half-gradient marker to the relevant minima or the thresholded pore space (Figure 3.10 (e). To remove the artifacts from the preliminary segmentation, the image is split into a marker image for the solid and the pore phase. In the next step, both images are eroded to separate the phase markers from each other. Then, the images are added to give a label image as input for the constrained watershed transformation (3.10 (f)). The constrained watershed transformation extends the marker to the edges in the image, yielding the final segmentation result (Figure 3.10 (g)).

3.4   Verification and Error Analysis on Simulated Data

After the segmentation algorithm has been developed, it is important to study the accuracy of the segmentation. This gives confidence in the method and allows comparisons
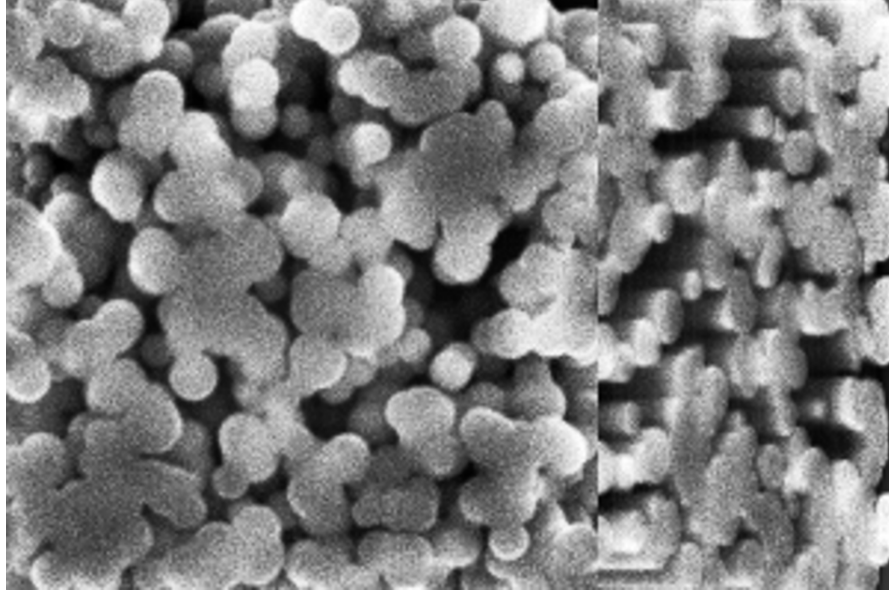
FIGURE 3.12: The simulated FIB-SEM dataset used for the verification of the segmentation algorithm.

with other methods. To this end, the algorithm was tested on synthetic data, which also enables studies on the stability of the result with respect to parameter changes.

3.4.1 The Simulated Data

Since the ground truth cannot be obtained for real FIB-SEM data, a synthetic dataset with known ground truth is needed for the verification of the segmentation. For this purpose, we use simulated data as described in Section 2.4.1. Even though the exact structure of the experimental data is unknown, the simulated geometry should resemble the structure of the porous material in Figure 3.7. As stated in Section 2.4.1, the simulated geometry is a realization of a Boolean model with spheres as primitives. The dataset consists of 100 simulated slices with each slice having the dimension 200 x 200 pixels. The porosity of the model is 44 %, resembling the porous carbon structure in Figure 2.8.

3.4.2 Segmentation and Choice of Parameters

3.4.2.1 Preprocessing

As described in the previous section, the segmentation begins with a preprocessing of the data. Since neither specimen drift nor beam drift occur in the simulation, the slices are already perfectly aligned. Hence, the alignment step is superfluous. The illumination
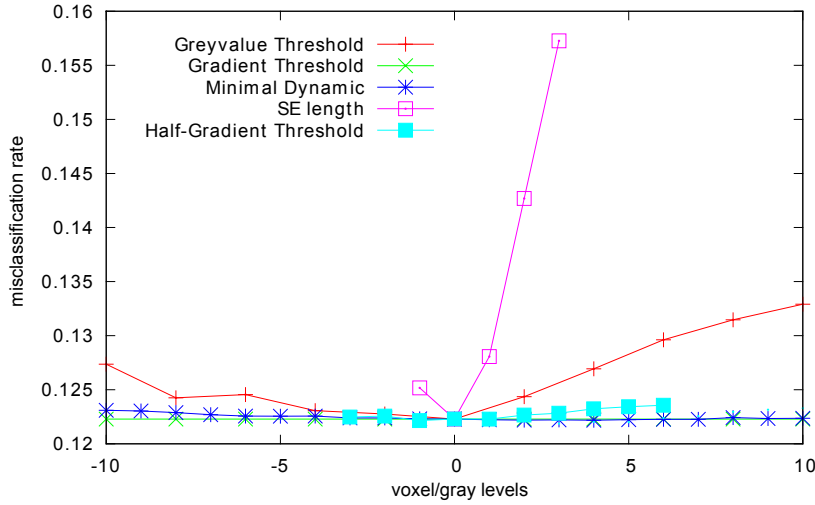
FIGURE 3.13: Misclassification rate with respect to variation of the segmentation parameters from the chosen values.

was corrected by an average filter as described. Due to the small image size, a radius of the filter mask of 50 voxels was sufficient. A front and cross section view of the dataset after preprocessing is depicted in Figure 3.12.

After the preprocessing step, the foreground structure was morphologically segmented. In the following section, the segmentation for the verification will be discussed and the choice of parameters will be motivated.

3.4.2.2　Feature Images

In a first step, the gray value feature image is generated. To this end, a global thresholding is used, selecting all voxels with a gray value lower than 60 as void space. The corresponding feature image is shown in Figure 3.10 (a). The threshold value can be motivated physically by the histogram. In the data, the solid structure has an approximately constant gray value throughout the image, which generates a characteristic peak in the gray value histogram. Depending on the dataset, this peak is more or less pronounced, but can almost always be identified. The other two regions either have a peak at a gray value that is much darker (void phase) or have no peak at all (artifacts). Since the artifacts show a ramp like structure in the z-direction, the neighboring voxels should have an either lower or higher gray value for each voxel, leading to a plateau-like structure in the histogram. Having that information, the gray value threshold can be estimated as lying just below the highest peak in the histogram (in this case at around 60). As can be seen in Figure 3.13, a small variation of the threshold value does not have a big effect on the segmentation. The largest effect can be seen when increasing the threshold, and thus cutting into the peak.

In a second step, the half-gradient feature image shown in Figure 3.10 (b) was computed. The half-gradient feature in Equation 3.15 has two free parameters, the threshold d and the length of the SE z_{l+}, l. The choice of both parameters depends strongly on the data and happens basically by trial and error. For the data at hand, the threshold value was $d = 4$ and the length was $l = 2$. As shown in Figure 3.13, the threshold d has almost no effect on the segmentation result, while the segmentation is most sensitive to the SE length l.

Next, the minima are detected by a morphological reconstruction. The parameter of the reconstruction d_{min} gives the minimal dynamic of the minima detected. In general, the parameters should be chosen as the minimal value, which successfully suppresses minima arising from noise and other artifacts. Yet, as can be seen from the dark-blue curve in Figure 3.13, the parameter is almost universal in the neighborhood of 20, i.e. a change in the parameters does not alter the misclassification rate. From experience, this is true even for other vastly different datasets. The feature image of the data is shown in Figure 3.10(d). For further suppression, the gradient image is thresholded at a gray value of 75. Again, the parameters should be chosen as the minimal value which can successfully detect the edges in the data. Of special importance here are the edges in the z-direction in the image, which the preliminary segmentation relies on. As can be seen in Figure 3.13, also the gradient threshold is almost universal. The resulting edges are shown in Figure 3.10(c).

After the feature detection, the preliminary segmentation was generated, with the transformation in Equation 3.21. The resulting image is shown in Figure 3.10 (e). Then the label image for the constrained watershed transformation was generated according to Equation 3.24 and the segmentation was refined. The corresponding images are shown together with the ground truth in Figure 3.10 (h). The segmentation will be compared quantitatively with the ground truth in the next section.

3.4.3   Error Analysis

After a reference segmentation is achieved, the quality of the segmentation is measured using a variety of methods. For comparison, a ground truth image was generated using the geometry file. Knowing the positions and radii of the spheres, the volume was rastered, meaning for the center of each voxel, a test was performed if the point is inside one of the spheres. This method is more accurate than simply drawing spheres of voxels, since it is less prone to errors from rounding the positions of the spheres and their radii. The rastered volume image is then used as ground truth to assess the segmentation of
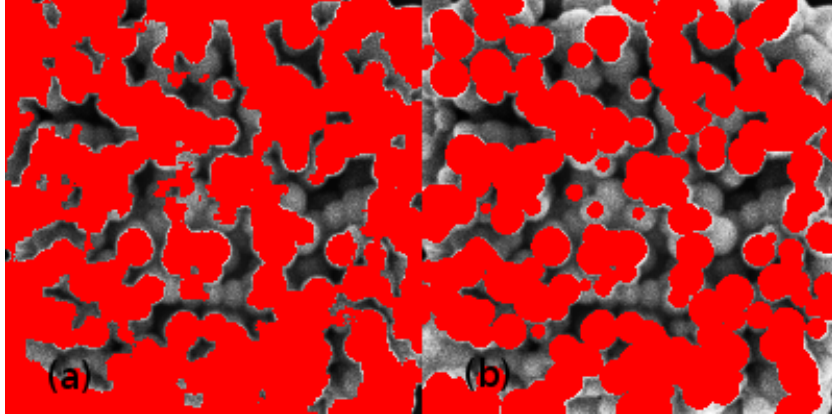
FIGURE 3.14: The segmentation result (a) and the ground truth (b) as overlays on the simulated FIB-SEM dataset.

the image. Figure 3.14 shows the segmentation and the ground truth as overlays on the simulated data.

One main source of errors can be identified visually. Through the watershed transform small features in the ground truth are eliminated. This is partly due to the erosion of the markers, during which small isolated regions in the ground truth are removed. Then the watershed transform is unable to reach these areas through region growing, thus classifying the corresponding voxels as void. On the other hand, small structures, especially at the boundaries, have a high gray value and a high gradient value. This makes it harder for the watershed transform to identify the boundary of the matrix phase, which in turn leads to a blurring of the boundary. The resulting effect is that small void structures along the boundaries are classified as matrix. Empirically, the latter effect seems to have a bigger impact, leading to a slight systematic overestimation of the volume fraction of the matrix phase (see Table 3.1).

With the ground truth available, the quality of the segmentation can be measured. Figure 3.14 (a) shows the misclassified voxels as a red overlay. Apparently, a large proportion of the error appears at the boundaries of the image. This mainly stems from less information being available at the boundaries of the image. Since the segmentation relies heavily on minima in the image to detect the ending of the matrix phase, the algorithm is unable to classify voxels lying between the first and last minimum and the image boundary. Furthermore, the constrained watershed transformation produces errors, since there are no markers of the opposing phase beyond the boundary. This leads the watershed transform to grow the phase having markers closest to the boundary until they are stopped by it. In the case of the present data, this leads to a large misclassification as false positives, which are shown in Figure 3.15 as the red overlay.

Also shown in Figure 3.15 are the false negatives in blue. They mainly appear at the boundary and are due to simple inaccuracy in detecting the boundary. In general, due to the specific effects described above, the false positives slightly outweigh the false negatives, leading to an overestimation of the volume fraction. Yet, that effect can be mitigated by restricting to a smaller subwindow, masking out voxels with a given distance to the boundary. Therefore, a subwindow has been selected, leaving out all voxels having a distance of up to 20 voxels to the boundaries in x- and y-direction and 10 voxels in the z-direction.

The results are summarized in Table 3.1. For the full dataset, the misclassification rate is 17.7 %. Among these are 13.6 % false-positives and 4.1 % false-negatives. The volume fraction is estimated at 66 %, confirming the trend discussed above. Inside the subwindow, the error rate drops considerably to 12.3 %, among these 7.1 % false-positives and 5.2 % false-negatives. The estimated volume fraction is 63.4 %, which is only 1.9 % off the true value, again confirming the trend, that most errors occur at the boundaries.

error	morphol. seg.	in window	Sauvola (window)	Otsu (window)
total	17.7 %	**12.3 %**	17.5 %	29.2 %
false pos.	13.6 %	**7.1 %**	14.4 %	6.0 %
false neg.	4.1 %	**5.2 %**	3.0 %	23.2 %
vol. frac.	66.0 %	**63.4 %**	72.9 %	44.3 %

TABLE 3.1: Error analysis of the simulated dataset, the volume fraction of the ground truth image is 57% (in the window 61.5%).

Together with the newly developed method, segmentations with standard methods were performed for comparison. As can be seen in Table 3.1, the morphological segmentation performs best on most measurements. In comparison with Otsu's global thresholding method (Otsu [1979]), the morphological segmentation has about the third of the error rate. Also, most of the misclassifications in the Otsu thresholding come from the false negatives which leads to a vast underestimation of the volume fraction. The other standard technique used is the local thresholding method in Sauvola and Pietikäinen [2000]. Although the overall misclassification rate is better than with Otsu's method, almost all errors are false positives, which leads to a vast overestimation of the volume fraction. And again, the morphological segmentation outperforms the standard method.

To verify the accuracy of the error estimate, a study has been made on whether the volume is representative, i.e. whether enough data is available to estimate the misclassification rate. Hence, the subwindow has been divided into four subwindows, each with the dimension 80 x 80 x 80 voxels. Then the misclassification rates were measured on each subwindow. The resulting error rates are 12.7 %, 11.6 %, 12.1 %, and 12.8 %, thus the standard deviation being 0.6 %. Thus, it can be concluded that the estimate of
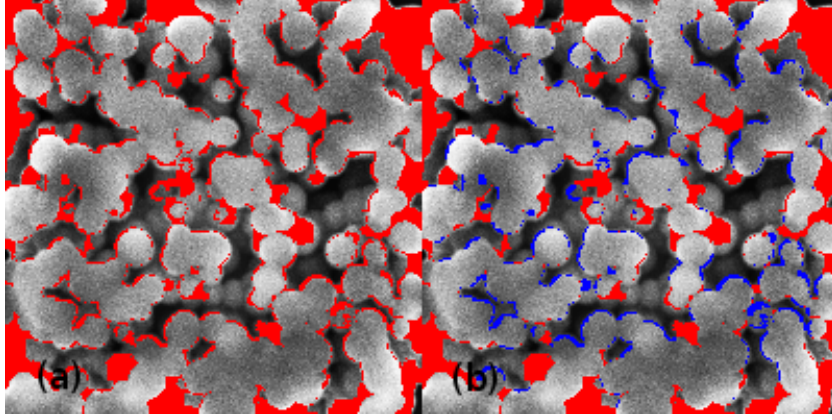
FIGURE 3.15: (a): Total misclassified voxels as overlay on the dataset; (b) errors as false positives (red) and false negatives (blue).

the misclassification rate for the window in Table 3.1 is representative with a standard deviation of less than 0.6 %.

Apart from the misclassification rates, two morphological measures are frequently used to characterize materials. These are the covariance and the granulometry as defined in Section 4.2. The covariance is used to characterize the spatial composition and characteristic length scales of a structure. The granulometry on the other hand, can be used to measure particle sizes or the size of connected components in general. To test the segmentation, both measurements were made on the ground truth data and the segmented structure.

The resulting curves for the covariance are shown in Figure 3.16. In the plot, the curves were normalized, such that the covariance $Cov(d = 0) = 1$. In the x- and y-directions, the curves for the ground truth and the segmentation are in good agreement. Still, the covariance is slightly underestimated. In z-direction, the covariance is underestimated by a large margin, meaning that the characteristic length scale is much smaller. The discrepancy in this direction can be explained by the anisotropic voxel size of 5 nm x 5 nm x 10 nm and the specific errors coming from the fact that the segmentation works on profiles in z-direction. Both effects lead to specific errors. Nonetheless, in all cases the range of the covariance, i.e. the characteristic length scale in the data is reconstructed very accurately.

As a second morphological characteristic, a granulometry by opening was estimated on the segmentation and on the ground truth. The openings were made with a rhombocubocahedron as the SE, which gives a good approximation for a ball. The resulting curve is shown in Figure 3.17. The curve of the ground truth shows a distribution peaking at about 5 voxels, while the distribution of the segmentation peaks at about 7 voxels. Thus, the grain sizes are overestimated by about 2 voxels. This is mainly
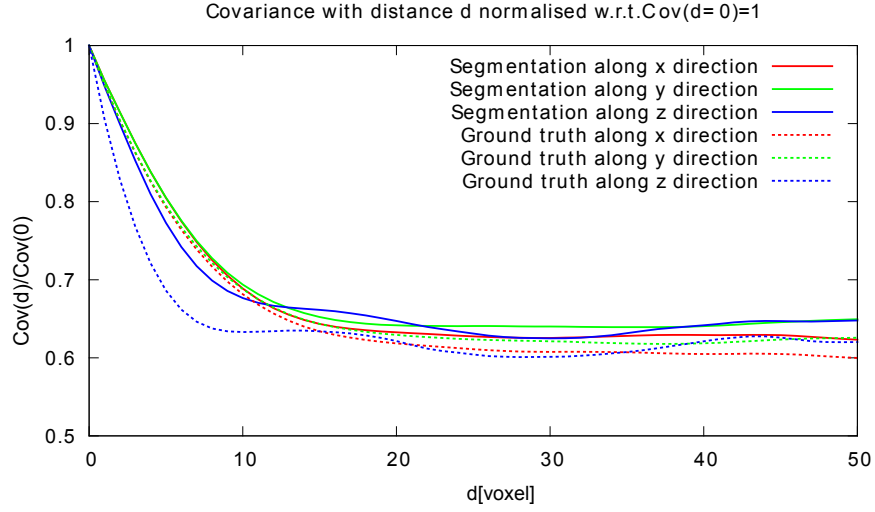
FIGURE 3.16: Covariance measurements on the segmentation and the ground truth data, with d given in voxels.
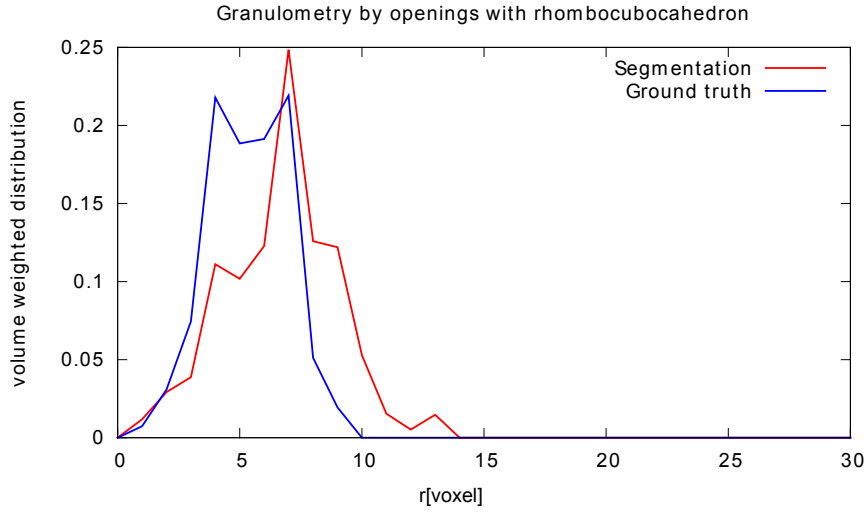
FIGURE 3.17: Comparison of the granulometry of the segmentation and the ground truth.

due to the watershed transform as discussed above. Still the connected components are reconstructed very accurately, meaning there are no outliers in both phases hampering the size measurement. Also, the width of both distributions is identical, allowing an estimation of the range of particle sizes based on the segmentation.

3.5   Results

Aside from synthetic data, the segmentation has been used on real FIB-SEM images for testing and also for characterizing porous materials.
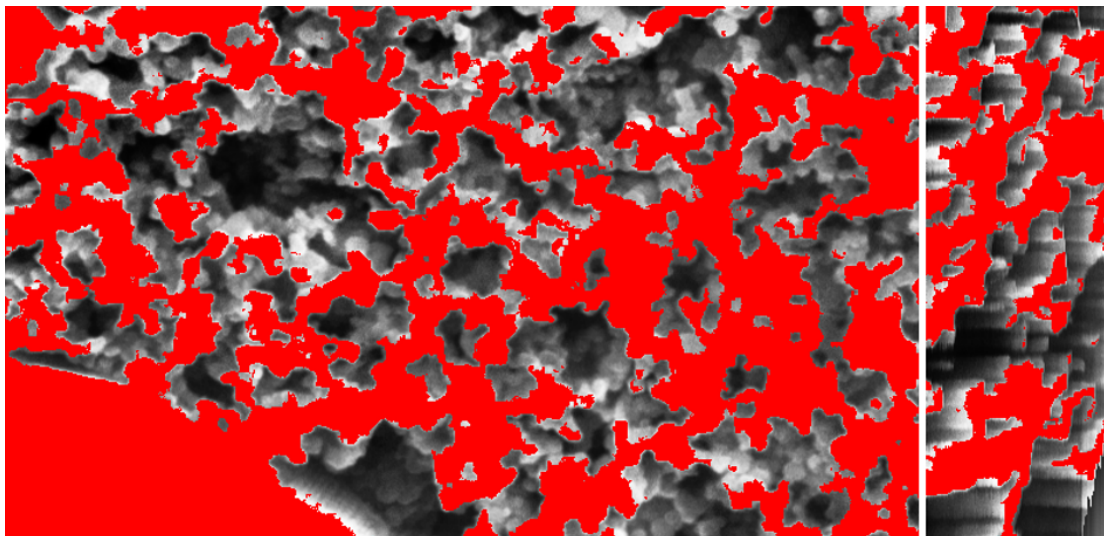
FIGURE 3.18: The segmentation of the dataset in Figure 3.7 as a red overlay on the original image.

3.5.1   Nanoporous Additive

The main application for the segmentation is the dataset depicted in Figure 3.2. For the segmentation a subwindow of the dataset was selected using the first 137 slices. Then a region of interest was cropped with the dimensions 662 x 387 x 137 voxels. The dataset after preprocessing is shown in Figure 3.7. Then the image was segmented with the parameters chosen according to the guidelines given in Section 3.4.2. The global gray value threshold was 80. The threshold on the morphological gradient image was 60 and the half-gradient markers were calculated with an SE length of 5 and a threshold value of 1. The minimal dynamic of the minima was 20. Then the preliminary segmentation was generated and refined with the watershed transformation. The result is depicted in Figure 3.18 as a red overlay on Figure 3.7. By visual inspection, it can be concluded that the main sources of error are the same as for the synthetic data. It can be seen in the cross section view, that the quality of the segmentation drops in the first 10 or so images and the last. Nevertheless, the boundary image in Figure 3.19 shows that the segmentation fits very well along the boundaries of the solid phase.

For the analysis, it is required to calculate the relevant quantities on a subset excluding the boundaries. Also, if information on the nanoporous phase is required, the bulk material at the lower left corner of the image should be cropped. Therefore, a subset with the dimensions 557 x 201 x 119 was selected for the analysis. The porosity of the segmentation was calculated to be 59% even though an error estimate of around 5% shoud be added as the segmentation depends on the parameters. The exact dependence of the porosity is shown in Figure 3.20. As can be seen, the porosity varies around 5% for the selected intervals for most parameters. For the synthetic data the strongest
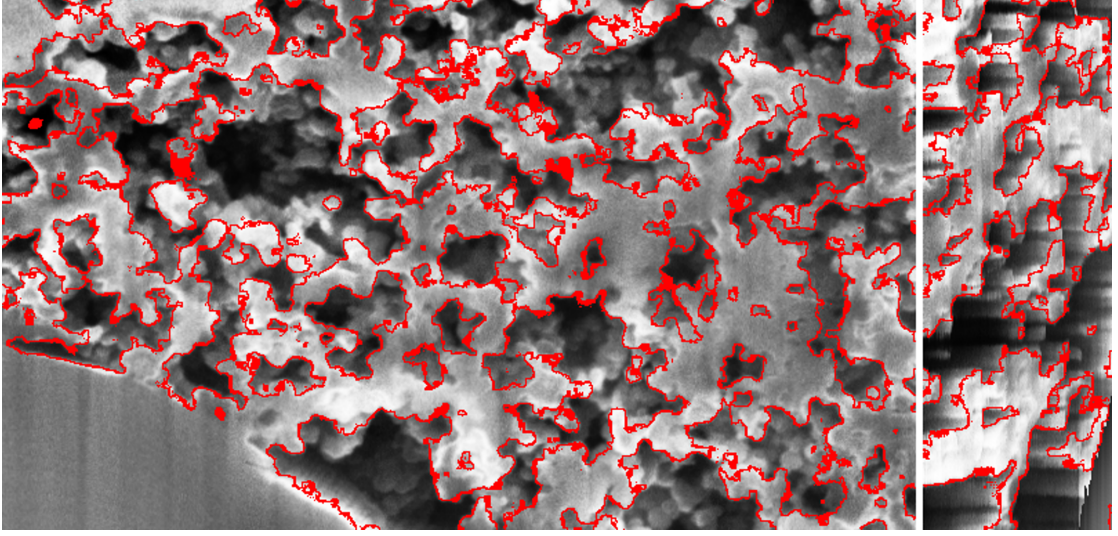
FIGURE 3.19: The segmentation boundaries of the dataset in Figure 3.7 as a red overlay on the original image.
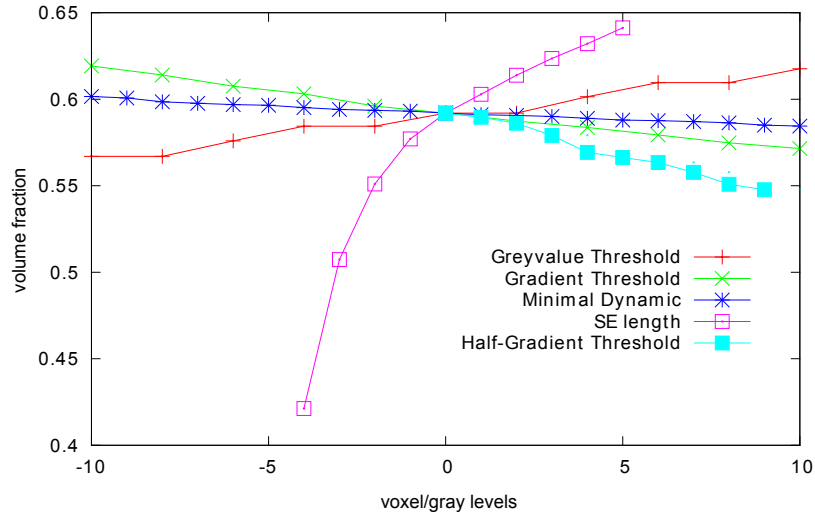
FIGURE 3.20: Volume fraction of the segmented solid phase with respect to variation of the segmentation parameters from the chosen values.

variation is caused by the length of the SE for the half-gradient markers. Thus, this parameter has to be carefully adjusted by hand.

With the segmentation, the spatial structure of the porous material is reconstructed. Figure 3.21 shows a volume rendering of the three-dimensional structure. This three-dimensional structure can be used to predict the macroscopic properties of the material, such as mechanical properties, an effective diffusion coefficient or the electric conductivity.

Also, statistical characteristics of the structure can be measured. For the modeling,
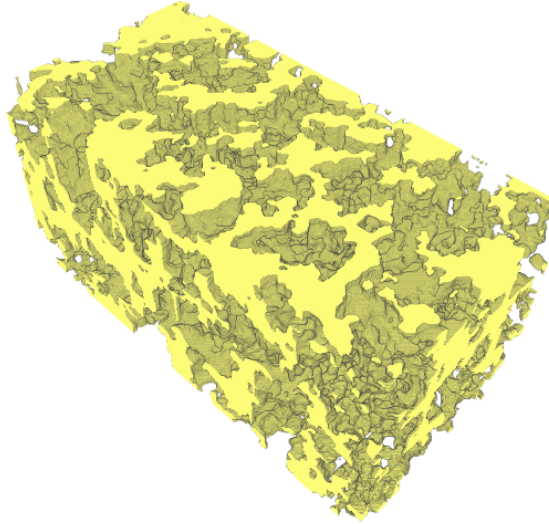
FIGURE 3.21: Segmented structure of solid phase of the porous additive.
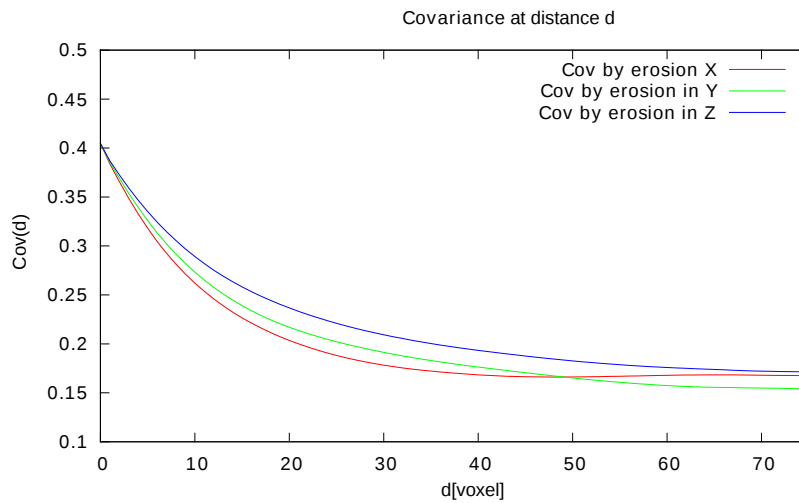
FIGURE 3.22: Covariance of the solid phase of the nanoporous additive.

presented in the next chapter, two characteristics have been measured, namely the co-
variance and the granulometry, as described above. The covariance was calculated on a
dataset where the voxel size was corrected to be isotropic, i.e. the image was scaled in
the z-direction (see Figure 3.22). The covariance shows to be almost isotropic with only
the z-direction differing from the other two, but not as strong as in the data used for
verification. Yet, for the modeling in Chapter 4 we will use the covariance measured in
the x-direction, since it has proven to be the most reliable in the verification.

The resulting curve for the granulometry is shown in Figure 3.23. The size distribution
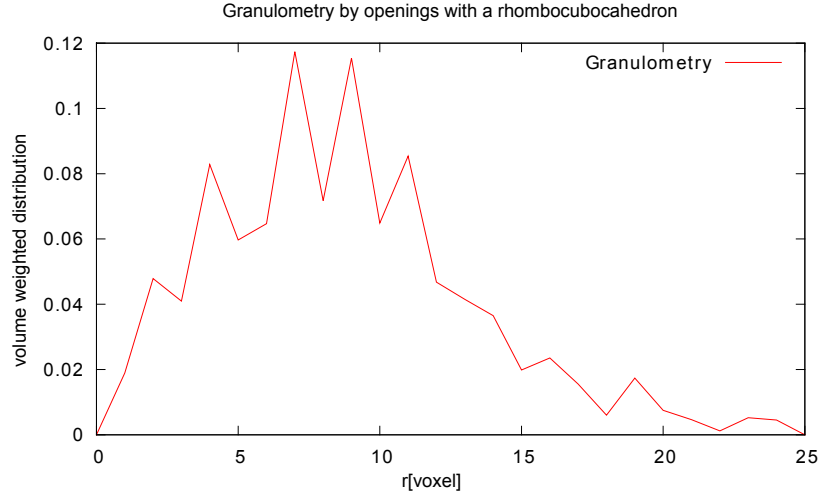
FIGURE 3.23: Granulometry by openings of the solid phase of the nanoporous additive.

shows a peak at about 7 to 8 voxels, which, considering the voxel size of 5 nm, corresponds to a particle size of approximately 35 nm to 40 nm. These values fit very well to the material description. Thus, the particle sizes can be accurately reconstructed. As can be seen, the curve finds a continuum of sizes, which comes from the sintering of the structure, where particles 'melt' together and structures are eroded. The ragged shape of the curve stems most probably from the discretization of the rhombocubocahedron, with which the openings were computed.

3.5.2 Nanoporous EDLC Electrodes

The other application for the segmentation algorithm are the nanoporous EDLC electrodes described in Section 1.2.2. Since pores with a diameter smaller than the SEM resolution cannot be observed, the carbon phase looks solid in the SEM images, and only the mesopores are visible. Since the physical behavior also depends on the mesopores, the segmentation of the pore space yields valuable information. To investigate the influence of the mesopore system, two different datasets, with different mesopore systems have been segmented. The specimens are called S12 and S14.

3.5.2.1 Segmentation of the Sample S12

The dataset S12 consists of 378 images of dimension 1024 x 1024 pixels. The dimension of the voxels in the three-dimensional data is 3.57 nm x 3.62 nm x 10 nm. A subwindow with the dimension 411 x 331 x 181 voxels was cropped from the image for the segmentation. Since the dataset contains many small structures and the morphological operations work better on larger structures, an upscaling was done on the image by a factor of 1.5. This

leads to a dataset with dimensions 616 x 496 x 271 voxel, with a voxel size of 2.38 nm x 2.41 nm x 6.67 nm. After the upscaling, the preprocessing was done according to Section 3.3.1, with an average filter with a filter mask of radius 100 voxels. A slice view of the preprocessed dataset is shown in Figure 3.24.
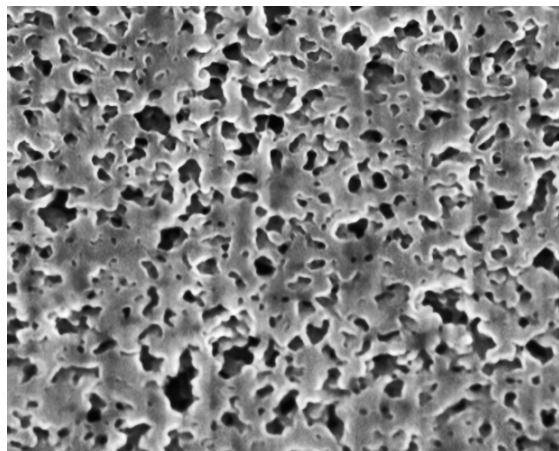
FIGURE 3.24: Preprocessed dataset of S12

For the segmentation a global threshold of 60 was chosen for the first step. The morphological gradient was thresholded at a gray value of 40. The half-gradient makers were generated using a SE of length 3 and a threshold value of 1 and for the minima detection a minimal dynamic of 20 was chosen. Then the preliminary segmentation was generated and the refinement was done with the watershed transform. A slice view of the resulting segmentation is shown in Figure 3.25, with the segmented solid phase as red overlay. It can be seen that the segmentation can separate the pore space from the solid phase very accurately, despite some small discrepancies.
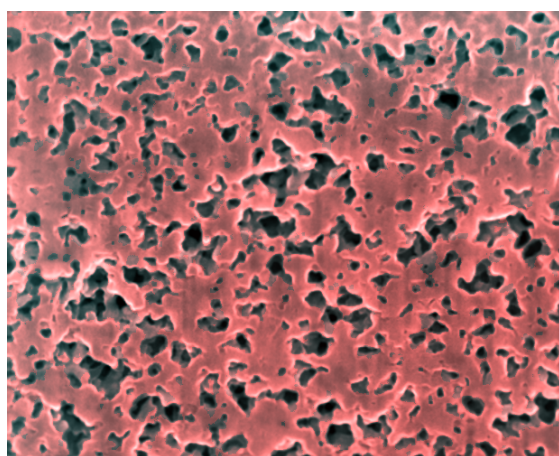
FIGURE 3.25: Segmentation of the dataset S12 as red overlay.

For the morphological analysis, the segmentation was cropped again to reduce the known artifacts at the boundary, which results in a dataset of dimension 469 x 444 x 216 voxels. Further, the dataset was scaled such in both the y- and z- axis, such that the voxels

become isotropic. The resulting binary data is a faithful representation of the three-dimensional structure of the solid phase of the mesopores in the EDLC electrode.

After the segmentation, statistical characteristics of the structure were measured. The covariance was measured and the resulting curve is shown in Figure. 3.26. The intercept of the covariance curve with the y-axis indicates a volume fraction of around $Cov(0) = 0.68$. Then the covariance declines until it reaches a sill at around 0.47 . The sill is reached at around 20 voxels, indicating a structure size of about $h = 20 * 2.38$ nm $= 47.6$ nm.
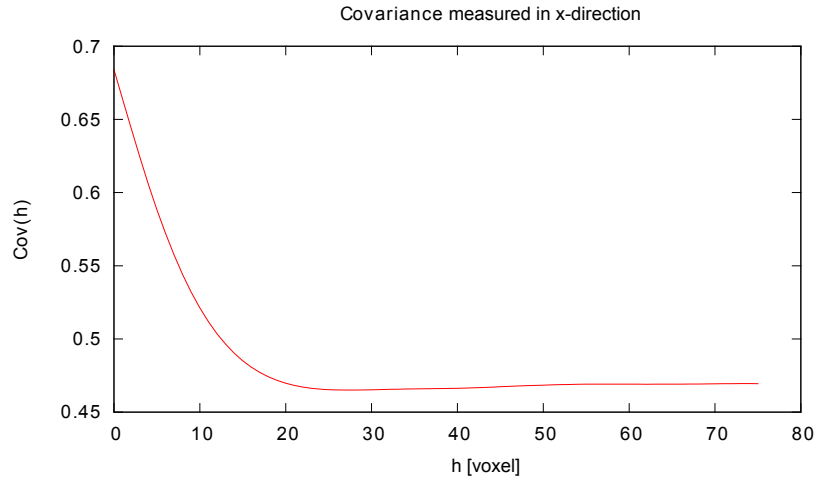
FIGURE 3.26: Covariance measured on dataset S12.

Also the opening curve was measured, which is shown in Figure 3.27. It confirms the estimate of the typical structure size from the covariance, as a steep decline can be observed at a radius of 10 voxels or $r = 10 * 2.38$ nm $= 23.8$ nm. Yet, as the curve is not a step function, it cannot be assumed that a monodisperse Boolean model of spheres would represent the segmentation well.

Finally, the closing curve of the dataset S12 was measured (see Figure 3.28). The closing curve shows a strong increase at around 6 voxels, indicating that a pore sizes of $r = 6 * 2.$ nm $= 14.28$ nm, which is much smaller than the typical solid phase sizes. This is not surprising considering the morphology and the high volume fraction of the solid phase.

3.5.2.2   Segmentation of the Sample S14

The specimen S14 has a much coarser microstructure. The dataset consists of 400 images with the same dimension as S12, 1024 x 1024 pixels. Yet, due to the coarser structure, an SEM resolution of 5 nm x 5 nm was selected to image the structure. The slice thickness
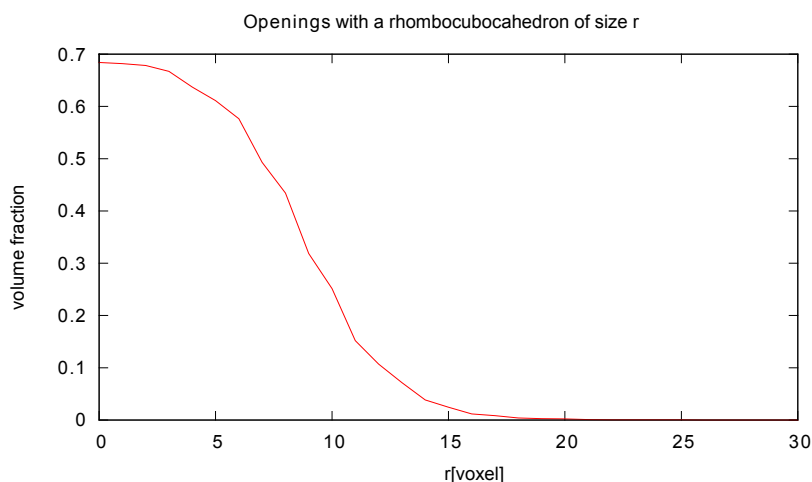
FIGURE 3.27: Opening curve measured on S12.
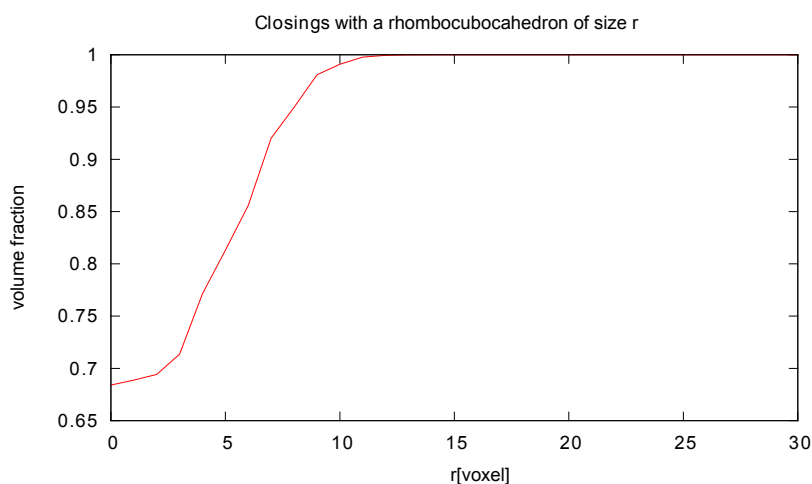
FIGURE 3.28: Closing curve measured at S12.

was 10 nm as for the S12 sample, leading to a voxel size of 5 nm x 6.35 nm x 10 nm. A slice view of the image data is shown in Figure 3.29. Since the structure size is much bigger in the sample, no upscaling was necessary. Also, due to the strong contrast and the overall image quality, no preprocessing was done except for the alignment of the images.

For the segmentation, the thresholds for the global gray value and the morphological gradient were chosen to be 30. The half-gradient markers were generated using a SE of size 5 and a threshold of 1. The minimal dynamic for the minima detection was 20. A slice view of the resulting segmentation is shown in Figure 3.30 as the red overlay. By visual inspection, the solid phase is well represented by the segmentation except for some small inaccuracies at the boundary.

For the analysis of the segmentation, a subwindow was selected with the dimension 611
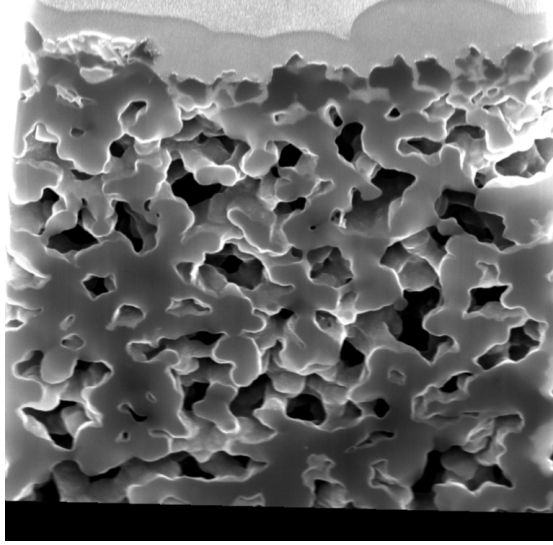
FIGURE 3.29: Cropped FIB-SEM dataset of S14.
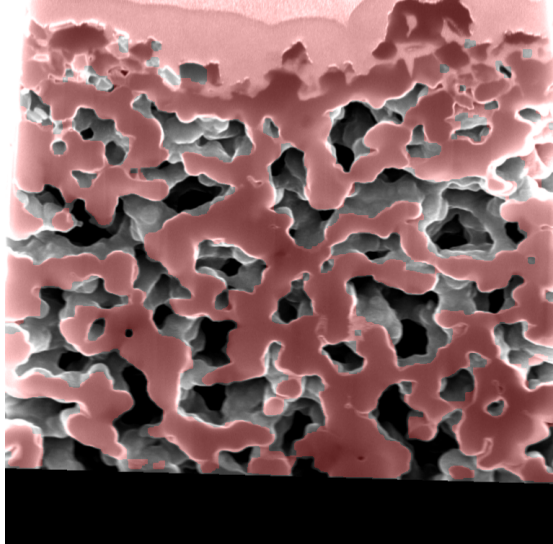
FIGURE 3.30: Segmentation of the S14 dataset as red overlay.

x 293 x 123 voxels. As for the other specimen, the characteristics measured were the covariance and the opening- and closing-curves. The covariance is shown in Figure 3.31. It shows a larger range than the covariance of S12, of around 30 voxel. This means a typical structure size of around $30 * 5$ nm $= 150$ nm and reflects the coarser structure that can be seen in the SEM images. Also the volume fraction is lower with around 54 %.

The opening curve measured on dataset S14 is shown in Figure 3.32. The opening curve shows a strong decline at around 10 voxels. This corresponds to a radius of $r = 10 * 5$ nm $= 50$ nm compared to the 23.8 nm in S12, speaking again for a coarser structure.
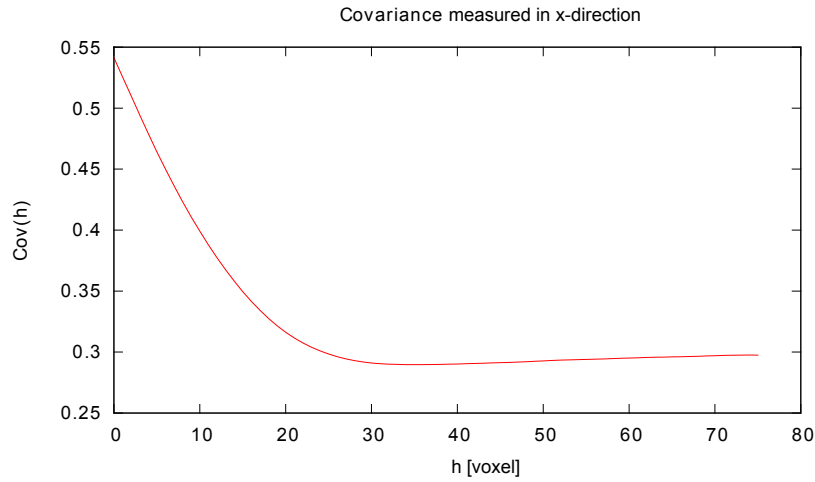
FIGURE 3.31: Covariance of dataset S14.
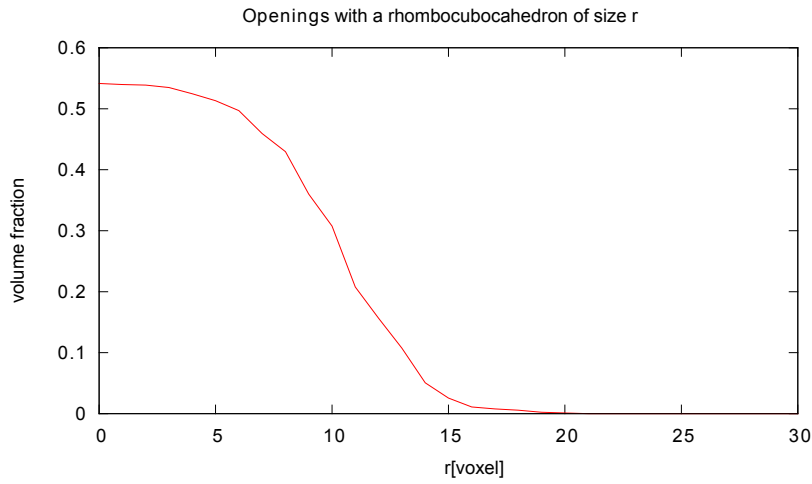
FIGURE 3.32: Opening curve of dataset S14.

Also, the closing curve was measured on dataset S14. The curve in shown in Figure 3.33. Other than for the opening curve, the closing curve shows a different behavior then for S12. The curve shows a slower increase and the starkest climb at around 12 voxels. This indicated a typical pore radius of $r = 12 * 5$ nm $= 60$ nm , compared to the 14.28 nm of S12. This again reflects the much larger pores, which can be seen in the SEM images in Figure 3.29.
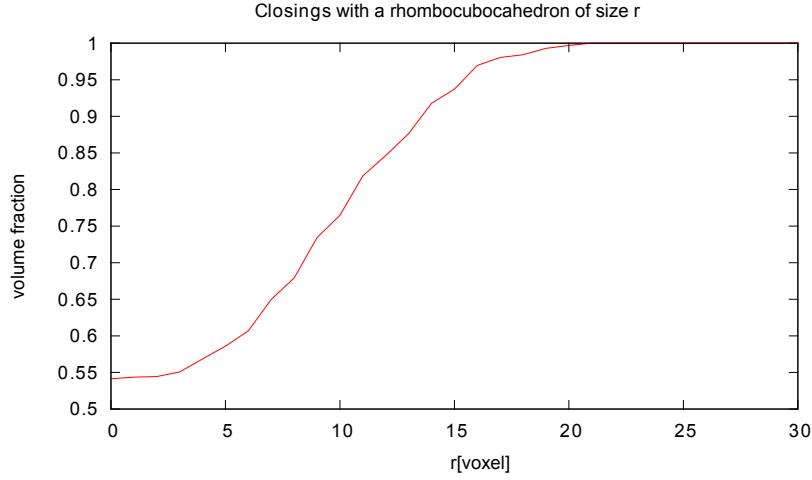
FIGURE 3.33: Closing curve measured on dataset S14.

3.6 Discussion and Outlook

3.6.1 Discussion

As explained in Section 3.1.4 on previous work, the segmentation of FIB-SEM data is an active field of research, still awaiting a general standard solution. In this section, a newly developed segmentation algorithm based on mathematical morphology was presented, which can segment a variety of structures and does not need any prior knowledge or assumptions on the structure. For the development, specific features were identified which are characteristic for FIB-SEM data. Also, a physical motivation for the choice of features was given. Some features such as the minima were not recorded in literature so far and represent a new development. The segmentation algorithm works with morphological operations, which are widely available and can be used by non-experts.

In the second part of the Chapter, a verification of the algorithm with synthetic data was presented. The synthetic data was generated with the FIB-SEM simulation tool described in Chapter 2. With the synthetic data, the quality of the segmentation was assessed using a variety of measures. And it was found that the misclassification rate is the lowest reported in literature so far, even though the quality of the data is low due to the fine structure. Moreover, the characteristic length scales are reliably detected as well as the sizes of the connected components. In Section 3.5, applications of the algorithm on datasets of different structures on different length scales were presented, confirming the variety of datasets to which the algorithm can be applied.

3.6.2   Outlook

The approach pursued in this work provides numerous possibilities, for further research to improve the segmentation. The workflow outlined in Figure 3.11 can be improved at any point.

At the preprocessing level, the alignment procedure works well, yet improvements could be made. For now, the alignment used the region of interest as well as the surrounding structure as points of reference. When restricting only to the surrounding structures, an even more precise alignment could be made. More advanced methods for the feature detection could be used, such as scale-invariant or histogram-based features. A machine learning algorithm could then be used to learn the artifacts and the relevant minima, maybe in a supervised manner. This could improve the feature detection considerably. In the refinement step, also more advanced methods could be used for the edge detection. Power watersheds or graph-based algorithms could be applied, which are more robust in their edge detection on noisy data. Also, an application of the approach in Jørgensen et al. [2010] for the refinement could be used incorporating the sensitivity to rising gray values in the artifacts to improve the segmentation on the refinement level. It is conceivable to incorporate this also in graph-based methods.

Another avenue of research is to reduce the number of parameters. In Section 3.4.2.2, guidelines for the choice of parameters were given based on experience (minimal dynamic) and from histogram analysis (gray value threshold). The histogram analysis could well be automated using a fitting procedure. For the determination of other parameters either prior knowledge (i.e. isotropy) or an optimization of a quality measure of the segmentation could be used. Also, the segmentation algorithm could be amended to a partly supervised segmentation, where the user assesses the quality of the segmentation.

<div style="text-align: right;">*4*</div>

Stochastic Modeling of Porous Microstructures

Even though the segmented data from the last chapter can be used to simulate the macroscopic properties of the material, it is sometimes desirable to have a stochastic model to represent the structure. A stochastic model is a prescription to generate random structures which have the similar properties with respect to some statistical measure as the original data. The models have parameters which describe the structure under consideration, reducing the complexity of the problem. The similarity of the model to the original data is assessed by suitable statistical measures. These measures can be used to fit the model parameters to the data. Then, realizations of the random structure can be generated at will and used for measurements and computations. Also, by varying the parameters of the model, the structure can be optimized to given requirements.

4.1 Models for Random Structures (Previous Work)

Previously numerous models have been investigated. The two most prominent model classes are random closed sets (for a formal definition see Section 1.3.1) and random field cut models. Apart from point processes, random closed sets include the Boolean model and variations of it, as well as mosaics which are used for the modeling of crystals or foams. Also in higher dimensions, random ensembles of planes and surfaces have been considered. For an overview see Serra [1982], Serra [1988] or Stoyan et al. [1995].

The other most prominent class are the random field cut models, where the model realization is a level set of a random field. The most prominent example is the Gaussian Random Field (GRF) cut model. Also, variations of the model have been considered, mostly level sets of convolutions of GRF's where a convolution introduces a spatial covariance in the random field. Here too, field of non-Gaussian random variables have

been considered, such as fields following a Poisson distribution or binary random field where the random variable can be either 1 or 0.

The model is mostly chosen manually by selecting a model based on the overall visual appearance of the segmented data. Ideally, all models should be easy to compute. Also, the model should ideally depend on only a few parameters while still completely representing the class of structures that are modeled, which makes fitting the model easier. Furthermore, the parameters should be chosen in such a way, that altering the parameters changes the structure in a meaningful way. This enables the model to represent a whole class of materials, e.g. granular media with different grain sizes.

To use the model, its parameters must be chosen, such that the model represents observed data. Some model parameters can be chosen directly from the data using analytical expressions calculated for the model, i.e. the observed volume fraction. Yet, mostly a fitting procedure must be employed using simulated realizations of the model and then finding the optimal set of parameters. The optimal parameters are determined by comparison of statistical characteristics of the model realization and the observed structure.

4.2 Statistical Characteristics of Random Closed Sets

To compare the different random structures and to quantify the difference between them, a number of statistical measures have been developed. In this thesis, two measures are widely used. First is the set covariance or covariance of the random set, second the granulometry of the set with a given structuring element.

4.2.1 Covariance

The probably most widely used characteristic is the covariance, defined for stationary random sets (see Serra [1982], Stoyan et al. [1995] and Matheron [1975]). It is, broadly speaking, a measure for the typical length scales in the data. If the structure contains several distinct length scales, an analysis with the covariance can detect them. Also if no typical length scale can be identified and, as in amorphous structures, rather a continuum is present, a maximum range of the structure can be identified using the covariance.

There are several definitions for the covariance around, but the one used in this thesis is the non-centered set covariance, which will simply be referred to as the covariance. The

definition of the covariance of a random closed set (RACS) Ξ is the probability that two points (e.g. x,y), are included in Ξ

$$\mathrm{Cov}(x;y) = P(x \in \Xi \wedge y \in \Xi). \tag{4.1}$$

If the RACS is stationary, this can be simplified, since the covariance only depends on the difference vector $\vec{h} = x - y$ by translating the set such that the point x becomes the origin, thus

$$\mathrm{Cov}(0, \vec{h}) = P(0 \in \Xi \wedge \vec{h} \in \Xi), \tag{4.2}$$

where h is the distance vector $y - x$. More simplification can be made if the RACS is isotropic, where the covariance only depends on the norm of the vector $\|h\|$. Then the covariance becomes a function with a scalar argument

$$\mathrm{Cov}(h) = P(0 \in \Xi \wedge \vec{h} \in \Xi) \tag{4.3}$$

for a vector $\vec{h}$ with $\|\vec{h}\| = h$.

For ergodic sets, the covariance can be measured directly on one realization. As the size of the observation window approaches infinity, the estimator of the covariance converges to the covariance of the RACS. The estimation of the covariance of the RACS can be done using mathematical morphology. The morphological expression corresponding to Equation 4.2 for the covariance is given by

$$\mathrm{Cov}(0; \vec{h}) = \mathrm{Vol}(\epsilon_{\{0,\vec{h}\}}(\Xi)), \tag{4.4}$$

where ϵ is the erosion with the structuring element $\{0, h\}$, which consists of the two points $\{0, h\}$ of Ξ and Vol is the volume fraction of the eroded RACS. The covariance will be used in Chapters 3 and 4 for the characterization of random structures.

4.2.1.1 Properties

Even though the exact form of the covariance varies depending on the set, several general properties can be given. First, the value of the covariance at the origin 0 corresponds to the volume fraction of the random set Ξ:

$$\mathrm{Cov}(0; 0) = P(0 \in \Xi) = p. \tag{4.5}$$

Furthermore, the maximum of the covariance is located at the origin, even though the covariance is not in general monotonically decreasing, thus

$$\text{Cov(h)} \geq |\text{Cov}(h)| \forall h \in \mathbb{R}^3. \tag{4.6}$$

Also, as h tends to infinity, the two events telling that the two points are in the RACS will be completely uncorrelated. Hence, the covariance will approach a sill, i.e. a constant value of p^2. The distance where the sill is reached, will be called the range of the covariance in the following. The range of the covariance indicates the largest length scale in the random set,

$$\lim_{h \to \infty} \text{Cov}(h) = P(0 \in \Xi)P(0 \in \Xi) = p^2. \tag{4.7}$$

For some random set, analytical expressions are known for the covariance, e.g. for the Boolean model (see Section 4.3.1.1). Yet, for most models there are no analytical expressions known for the covariance, and thus the covariance has to be measured based on realizations of the model.

4.2.2 Granulometry

Other frequently used characteristics of RACS are granulometries. A granulometry is also a measure of size, obtained by measuring the volume fraction of openings by structuring elements with increasing sizes. They can be used to measure the extent or sizes of connected components in the set. An intuitive interpretation can be given for a set made of distinct objects, simple examples of which can be thought of are granular sets modeling things such as gravel or inclusions in a composite material. A granulometry, computed on the set, will then recover the size distribution of the objects in the set. Other than the set covariance, a granulometry of a set is not uniquely defined, since a structuring element is needed for the computation. Yet, when a structuring element is chosen, e.g. a unit sphere, the granulometry is unambiguously defined and can be used to characterize random sets.

The axiomatics of granulometries were developed by Georges Matheron in Matheron [1967]. They are also given in Matheron [1975], Serra [1982], and Soille [1999].

Morphological measurements of granulometries are closely linked to opening and closing curves. A closing or opening curve is defined for a series of structuring elements of increasing size, for example for the balls of radius l

$$B(l) = \{x : ||x|| \leq l\}, \tag{4.8}$$
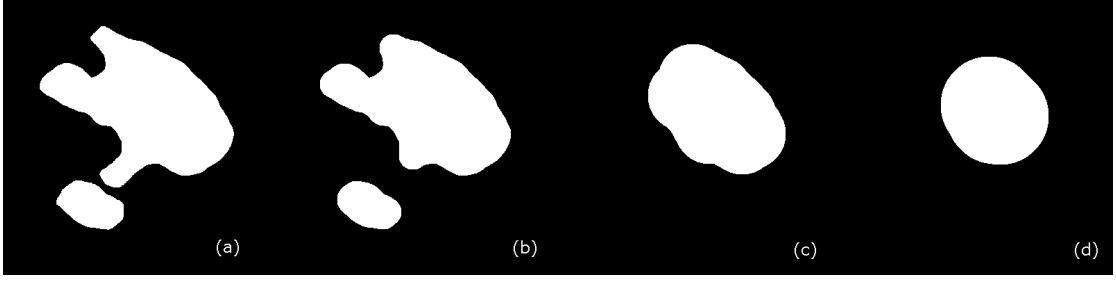
FIGURE 4.1: Effects of the morphological openings with a Ball of increasing radius, from left to right: Original image (a), after opening with size radius 20(b), after opening with radius 50(c), after opening with radius 70(d). After an opening with radius 80, the image is empty (not shown).

which can be written as a homothetic transformation of the unit ball with the scaling factor l

$$B(l) = lB(1). \tag{4.9}$$

The opening curve for the ball of radius l is the volume fraction of a set after an opening with a ball of radius l

$$\Gamma(l) = \text{Vol}(\gamma_{B(l)}(f)). \tag{4.10}$$

By the anti-extensive property of the opening, the curve is always decreasing, i.e. structures are always removed from the image. Also the opening curve always tends to zero, as an opening with a large enough structuring element will erode all structures and leave an empty set.

Analogously to the opening curve, the closing curve is defined as the volume fraction after a closing of the image with a structuring element of increasing size

$$\Phi(l) = \text{Vol}(\phi_{B(l)}(f)). \tag{4.11}$$

In contrast to the opening curve, the closing curve is increasing and tends to one. Here structures are added to the image and after a closing with a big enough structuring element, the image is filled with foreground. Both curves can be used to characterize microstructures and as distance measures for model fitting.

As can be seen in Figure 4.1, the opening with an increasing size removes structures smaller than the structuring element. After removing small structures from the original image in Figures 4.1 (a) and (b) increasingly big structures are removed (Figures 4.1 (c) and (d)) until after an opening with size 80 the whole image is empty (not shown). By measuring the volume fraction of the foreground in the series of images, the fraction of voxels belonging to a structure smaller than the structuring element can be measured by differentiation

$$\text{Gran}_{B(l)}(l) = \frac{d}{dl}\Gamma_{B(l)}(f). \tag{4.12}$$

So the granulometry is the fraction of voxels belonging to a structure of size $B(l)$. Since the discretization of a ball of size l might be tricky, the ball is approximated by a rhombocubocahedron of size l (see Figure 4.2), without altering the result too much.
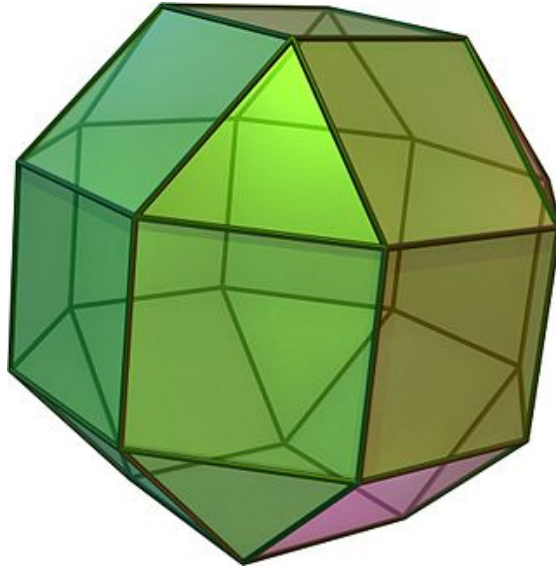
FIGURE 4.2: Rendering of a rhombocubocahedron (source: en.wikipedia.com).

4.3 A Coarsened Boolean Random Function Model

To model the segmentations S12 and S14 presented in Section 3.5.2, the Boolean model of spheres is clearly not sufficient, since it cannot reproduce the smooth surface of the segmented structure. It is known from the production process, that the solid phase consists of sintered spherical particles, meaning that an ensemble of spherical particles has been produced, which has been heated to sinter the particles. During the sintering process the atoms move along the boundary (surface diffusion) and through the solid phase (bulk diffusion), leading to a form of 'molten' structure, where the boundaries are smoothed and the particles are 'baked' together. To model such a structure, the Boolean model of spheres has been modified using a convolution of its indicator function with a kernel. This modification of the Boolean model imitates the sintering process to a certain degree by coarsening the model's morphology, leading to a morphology, similar to the one observed in the segmentations.

4.3.1 The Boolean Model

The Boolean model, also called the Poisson germ-grain model, is a RACS which is frequently used for the modeling of porous materials. The model has been used for various applications for a long time. Early applications include Armitage [1949] and Kolmogorov [1937]. Since then, it has been intensively studied by George Matheron in Matheron [1967, 1975] and Jean Serra in Serra [1982]. The Boolean model can be defined by a union of compact sets, which are placed randomly in space. The compact set can be the same for each point or be drawn from a family of sets. Thus the definition of a general Boolean model must include the definition of a family of compact sets, the grains

$$\xi = \{\xi_1, \ldots, \xi_n\}. \tag{4.13}$$

Here ξ is the family of the compact sets ξ_n. To place the compact set randomly in space they are translated by the points x_i of a point process Φ, i.e.

$$x_i \in \Phi. \tag{4.14}$$

For a stationary Boolean model, it is necessary to have a stationary Poisson point process for the translations. Then the Boolean model Ξ can be defined by the union of the translated compact sets (see Figure 4.3 for an illustration).

$$\Xi = \bigcup_{n=1}^{\infty} (\xi_n + x_n) = (\xi_1 + x_1) \cup (\xi_2 + x_2) \cup \ldots, \tag{4.15}$$

with

$$\xi_n \quad \in \xi, \tag{4.16}$$
$$x_n \quad \in \Phi. \tag{4.17}$$

The intensity of the underlying Poisson point process λ is a free parameter of the model. Other parameters might be added to parametrize the family of grains ξ, e.g. the radii of a family of spheres.

As for any RACS, the Boolean model is uniquely determined by its Choquet capacity $T_\Xi(K)$. When the underlying point process is a stationary Poisson point process, the capacity can be given in a closed and relatively short form as

$$T_\Xi(K) = 1 - exp(-\lambda E(\mathrm{Vol}(\check{\xi} \oplus K))), \tag{4.18}$$
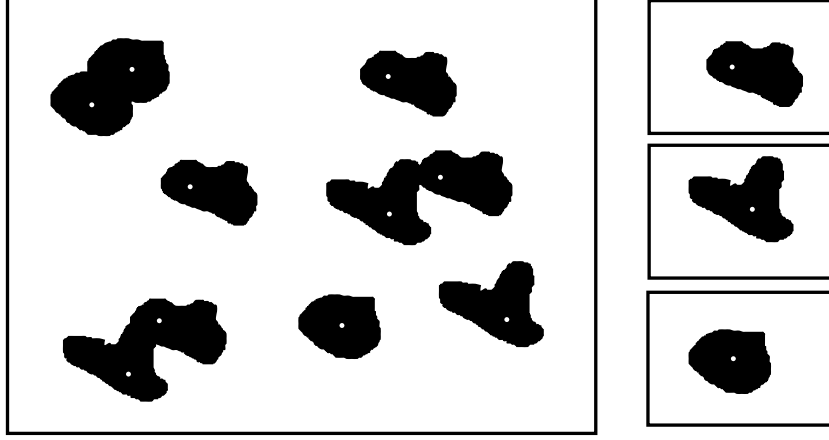
FIGURE 4.3: Realization of a Boolean Model: The underlying point process (from Figure 1.6) is indicated with white dots. The grains are drawn from the family of grains on the right.

where ξ is the family of primary grains and $E(\text{Vol}(.))$ is the expectation of the Volume, taken over all grains. Yet to evaluate the expectation, the exact family of grains needs to be known. In this thesis, the grains will mostly be spheres or cylinders with either fixed radii or the radii distributed following some distribution. The same holds for the height and orientation of the cylinders.

4.3.1.1 The Boolean Model of Spheres

The approaches used to model the segmented datasets S12 and S14 in this thesis are based on a Boolean model of spheres, where the grains are a family of spheres. If the radii follow some distribution, the model is referred to as the poly-disperse Boolean model of spheres. For a fixed radius and equal radius for every sphere, the model is referred to as mono-disperse Boolean model of spheres. In that case, the family of sets consists of one element, the ball of radius r,

$$\xi_r = B(r). \tag{4.19}$$

The mono-disperse Boolean model of spheres of radius r with the intensity λ will be denoted as

$$\Xi_\lambda^r. \tag{4.20}$$

A volume rendering of a mono-disperse Boolean model of spheres is shown in Figure 4.4.

The Boolean model of spheres is an example where several statistical characteristics are known analytically. Emanating from Expression 4.18 the volume fraction of a Boolean
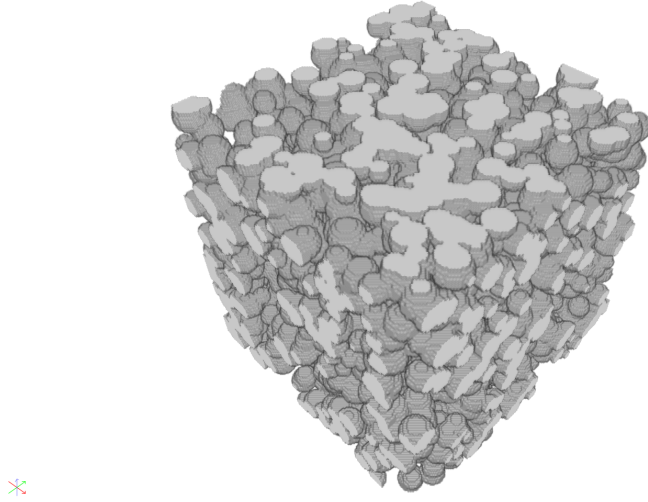
FIGURE 4.4: Volume rendering of a Boolean model of mono-disperse spheres.

model can be calculated. To this end, the set containing the origin is chosen as a test set $K = \{0\}$. Then the expectation in the exponential simplifies to

$$E(\text{Vol}_B^3(r)) = \frac{4}{3}\pi r^3, \tag{4.21}$$

the volume of a ball with radius r. This means, that the volume fraction is

$$p = 1 - \exp(-\lambda \frac{4}{3}\pi r^3). \tag{4.22}$$

Also, the covariance can be computed by choosing a set containing two points as a test set, $K = \{o, h\}$. Then the expectation in the exponential reads

$$E(\nu_d(\xi_r \cap (\xi_r - \vec{h}))). \tag{4.23}$$

This expression is the area of intersection of two balls separated by a vector $\vec{h}$. The expression for the covariance simplifies to

$$\text{Cov}(h) = \quad (1-p)^{2-r(h)} \quad \text{with} \tag{4.24}$$

$$r(h) = \begin{cases} 1 - \frac{3h}{2r} + \frac{h^3}{2r^3} & \text{if} \quad h \leq r \\ 0 & \text{if} \quad h \geq r \end{cases} \tag{4.25}$$

These measures can be used to compute the parameters for the Boolean model of spheres, since the volume fraction immediately yields the intensity of the underlying point process. Also the covariance can be measured on the data, then Expression 4.25 can be fitted, yielding the radius.

Unfortunately, there is no analytical expression known for the granulometry. But intuitively it is clear, that for low intensities, when overlap between the spheres it not too frequent, the granulometry with a ball will yield a peak at the radius of the spheres. For higher intensities, the peak may widen. Thus for the fitting of model parameters, a fitting using simulations and a distance measure is needed as explained in Section 4.4.

4.3.2 Description of the Coarsened Boolean Model

In this section, details on the modified Boolean model will be given. The basis of the modified model is a mono-disperse Boolean model of spheres with radius r, and an underlying stationary Poisson point process with intensity λ. The model is denoted Ξ_λ^r and has two free parameters r and λ, where the parameter λ can be substituted by the volume fraction of the Boolean model p using equation 4.22. The indicator function is needed in the following and is defined as

$$\mathbb{1}_{\Xi_\lambda^r}(x) = \begin{cases} 1 & \text{if} \quad x \in \Xi_\lambda^r \\ 0 & \text{if} \quad x \notin \Xi_\lambda^r \end{cases}. \tag{4.26}$$

A slice view of the indicator function of a realization of a Boolean model of spheres is shown in Figure 4.5. The realization has the same volume fraction as the segmentation. Yet, the boundary of the model has sharp edges, which are not visible in the segmentation in the Figures 3.25 and 3.30. This makes it impossible to model the segmented structure with a Boolean model of spheres irrespective of the chosen parameters.

FIGURE 4.5: Indicator function of a realization of a Boolean model of spheres with radius 20 voxel and a volume fraction of 50 % .

To smoothen the boundaries of the model, the indicator function is convolved with a Gaussian kernel of the form

$$N(0, \sigma)(x) = \frac{1}{\sqrt{2\pi\sigma^2}} e^{-\frac{x^2}{2\sigma^2}}. \tag{4.27}$$

This adds another free parameter σ to the model, which parameterizes the width of the convolution kernel. The convolution of the indicator function with the Gaussian kernel, yields a random function $Z(x)$:

$$Z(x) = \mathbb{1}_{\Xi_\lambda^r} * N(0, \sigma) = \int \mathbb{1}_{\Xi_\lambda^r}(h) N(0, \sigma)(h - x) dh^3. \tag{4.28}$$

A slice view of $Z(x)$ generated from the realization of the Boolean model in Figure 4.5 is shown in Figure 4.6. The parameter σ of the Gaussian kernel was four. As can be seen, the image has been smoothened, blurring the sharp edges visible in Figure 4.5. The parameter σ can be used to adjust the extent of the smoothing of the image, where a larger σ will result in a smoother image and later a coarser microstructure.
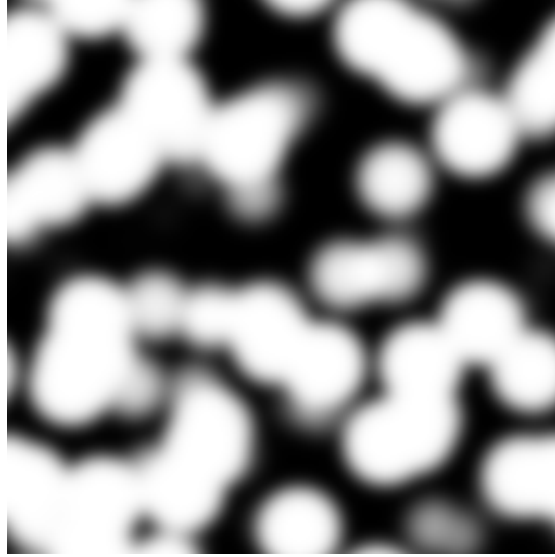
FIGURE 4.6: Random function $Z(x)$ generated from the realization in Figure 4.5.

Yet, the image cannot be used to model a two-phase random structure. Therefore, the random function $Z(x)$ is thresholded yielding a binary function, again

$$B(x) = \mathbb{1}_{Z(x)>C}. \tag{4.29}$$

The indicator function in 4.29 yields the two-phase microstructure model. A slice view of the resulting microstructure model is shown in Figure 4.7. It is apparent, that the original Boolean model has been coarsened, having a much smoother boundary.

FIGURE 4.7: Slice view of the modified two-phase model.

The thresholding is done with a constant value C between zero and one, where larger C value will result in a lower volume fraction. For the modeling of the microstructure at hand, C was chosen such that the resulting microstructure will have the same volume fraction as the original Boolean model. The exact value can be determined by using the gray value histogram of the image of $Z(x)$. This makes the transformation of the structure volume conserving, imitating the conservation of mass during the sintering process.

Finally, the model has three free parameters: the volume fraction of the Boolean model p, the sphere radius r and the convolution kernel width σ.

4.3.2.1 Model Fitting

Unfortunately, no analytical forms for the covariance or the opening or closing curve are known. This means that the fitting needs to be based on simulations. Yet, intuitively it is clear that, depending on the choice of parameters, the characteristics of the model should vary between the original mono-disperse Boolean model of spheres and a Gaussian random function model, since both are limits of the model. Obviously the Boolean model is the limit for vanishing kernel width, i.e. $\sigma \to 0$, since it does not smooth the indicator function and thus reproduces the original model. On the other hand, in the limit of a vanishing sphere radius, while keeping the volume fraction constant, the RACS converges towards a random field, with a binomial distribution with mean p at every point in space (for a formal definition of a random field see Section 4.5.0.1). The thresholding will then yield a random structure similar to Gaussian random field cut model, with a very smooth boundary.

Since no analytical expressions for the statistical characteristics are known, they have to be estimated on realizations of the model. To this end, model realizations with a sufficient size to be representative are generated and the covariance, opening and closing curves are measured on the generated images. Then, to fit the model, a distance measure is defined between the characteristics of the model realizations and the characteristics of the dataset. It is customary to use the squared difference between the curves as a distance measure. Thus the distance measure reads

$$\chi^2 = \int (\text{Cov}_d(h) - \text{Cov}_m(h))^2 dh + \int (\Gamma_d(l) - \Gamma_m(l))^2 dl + \int (\Phi_d(l) - \Phi_m(l))^2 dl, \ (4.30)$$

where $\text{Cov}_d(h)$ is the covariance of the segmentation and $\text{Cov}_m(h)$ is the covariance of the model realization and likewise for the opening curves $\Gamma_{d/m}(l)$ and the closing curves $\Phi_{d/m}(l)$, as defined in Section 4.2.

In practice, the curves are discretized using a number of samples, i.e. distances h_i and sizes l_i. This leads to the distance function

$$\chi^2 = \sum_{h_i} (\text{Cov}_d(h_i) - \text{Cov}_m(h_i))^2 + \sum_{l_i} (\Gamma_d(l_i) - \Gamma_m(l_i))^2 + \sum_{l_i} (\Phi_d(l_i) - \Phi_m(l_i))^2. \ (4.31)$$

In order to fit the model parameters to the segmentation, the distance function has to be minimized, yielding the optimal set of parameters to represent the segmentation with the model. Since the model characteristics are random functions themselves, special care has to be taken when minimizing the distance function χ^2. The algorithm used in the thesis is described in the next section.

4.4 Fitting by Stochastic Optimization

To fit the curves to the data, a distance or objective function has to be minimized with respect to the parameters of the model. Numerous algorithms exist for the optimization of loss functions. Most of them rely on the computation of a gradient. The most common and simplest gradient based method is the gradient descent method. Others are the Levenberg-Marquart-Algorithm (Levenberg [1944], Marquardt [1963]) and the BGFS method (Broyen [1970], Fletcher [1970], Goldfarb [1970], Shanno [1970]). A prominent example for a non-gradient based method is the Nelder-Mead-simplex-algorithm (Nelder and Mead [1965]). For the parameter fitting to random sets, we will use a modified gradient descent method taking into account the stochastic nature of the loss function.

In the gradient descent scheme, an initial guess for the optimal parameters is given. Then, the gradient of the loss function with respect to the parameters is computed,
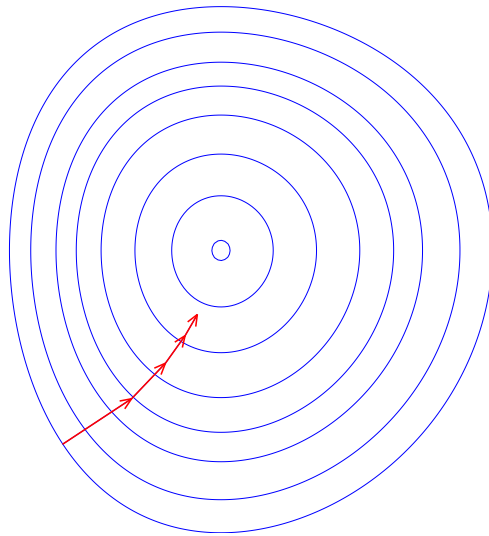
FIGURE 4.8: Gradient-descent algorithm

either analytically or by finite differences. Then the parameter vector is shifted in the opposite direction of the gradient. By iterating the procedure, the parameter vector moves 'downhill' until it approaches a local minimum (see Figure 4.8).

4.4.1 Simultaneous Perturbation Stochastic Approximation

In the setting of random sets, the situation is complicated by the facts that the loss function is itself a random number, depending on the random realizations for which it is computed. The distribution of the random number is centered around its expectation, scatters around it due to the noise. That means, that the computation of a gradient is only possible if the noise term is much smaller than the finite difference used for the computation of the gradient. Since that is only true for very large realizations, the use of a different algorithm is necessary for the fitting using smaller realizations.

One such algorithm is the simultaneous perturbation stochastic approximation (SPSA)-algorithm (Spall [1987, 1992]). The method approximates the gradient by perturbations of the parameter vector. The SPSA-algorithm in pseudo code is given in Algorithm 1. As for the standard gradient descent algorithm, an initial parameter vector θ is given. Then for a fixed number of iterations n, the gradient is estimated by a finite difference and the parameter vector is updated accordingly. Yet, instead of estimating the gradient in every parameter direction separately, a simultaneous perturbation is used, meaning that every parameter is varied in the same iteration. It was shown in Spall [1992] that the simultaneous perturbation estimates the gradient and the algorithm converges to the global optimum. Two additional constants a and c control the step lengths for the

update and the gradient computation, respectively. As the loop progresses, the step length is reduced such that θ will stabilize at a minimum. The step length is reduced exponentially and the reduction rate is given by two additional constants α and γ.

Data: $\theta \in \mathbb{R}^d, L(\theta) : \mathbb{R}^d \to \mathbb{R}, a \in \mathbb{R}, c \in \mathbb{R}, \alpha \in \mathbb{R}, \gamma \in \mathbb{R}, n \in \mathbb{N}$
Result: locally minimal parameter vector θ
$k \leftarrow 0$;
while $k < n - 1$ **do**
    adjust step size:;
    $a_k \leftarrow \frac{a}{(k+1)^\alpha}$;
    $c_k \leftarrow \frac{c}{(k+1)^\gamma}$;
    calculate random perturbation:;
    $\Delta \propto \mathrm{Ber}(-1, +1)$;
    $\Delta \leftarrow (2p) - 1$;
    $\theta_+ \leftarrow \theta + c_k * \Delta$;
    $\theta_- \leftarrow \theta - c_k * \Delta$;
    calculate random gradient:;
    $y_+ \leftarrow L(\theta_+)$;
    $y_- \leftarrow L(\theta_-)$;
    $g = (y_+ - y_-)\frac{1}{2*c_k*\Delta}$;
    update θ:;
    $\theta = \theta - a_k * g$;
end

Algorithm 1: Simultaneous perturbation stochastic approximation (SPSA).

4.4.2 Choice of Parameters

In general, the efficiency of the method depends on the loss function $L(\theta)$. Yet, some requirements for a and α can be derived from the convergence of the algorithm. So, the sequence a_k should be positive and go to zero as k approaches infinity. Also, the series in Equation 4.34 must diverge, to ensure that the algorithm converges to the global maximum

$$a_k > \quad 0, \tag{4.32}$$

$$\lim_{k \to \infty} a_k \to \quad 0, \tag{4.33}$$

$$\sum_{k=0}^{\infty} a_k = \quad \infty. \tag{4.34}$$

For the choice of c and γ similar conditions must hold, so the c_k must be positive and vanish for $k \to \infty$. Also, the series 4.37 which depends on the a_k must converge.

$$c_k > \quad 0, \tag{4.35}$$

$$\lim_{k \to \infty} c_k \to \quad 0, \tag{4.36}$$

$$\sum_{k=0}^{\infty} \frac{a_k}{c_k} < \quad \infty. \tag{4.37}$$

In practice, the parameters $\alpha = 0.1, \gamma = 0.6$ have shown good results for a number of loss functions. The constants a and c must be must be chosen for every optimization, depending on the shape of the loss function.

4.5   The Gaussian Random Field Cut Model

Besides the models derived directly from random sets, there is a second class of popular models based on random fields. This model will be used to model the random structure of the nanoporous additive segmented in Section 3.5.1.

4.5.0.1   Gaussian Random Fields

A random field is defined as a random variable at every point in a domain. In depth, treatments can be found in Adler and Taylor [2009], Lantuéjoul [2002] According to the definition following Bron and Jeulin [2004], for each point r in a domain Ω we define a random variable $U(r)$ by

$$\forall r \in \Omega, U(r) \propto D(a). \tag{4.38}$$

Here $D(a)$ is a distribution depending on a set of parameters a. Depending on the distribution, random fields have distinct statistical properties, which can be used for modeling. Common distributions are the binomial distribution or Poisson distribution. Yet, the most popular distribution used is the normal or Gaussian distribution, in which case the random field is called a Gaussian random field (GRF). Thus the GRF is defined by

$$\forall r \in \Omega, U(r) \propto N(0; 1). \tag{4.39}$$

Figure 4.9 shows a realization of a GRF with dimension 300 x 300 pixels. Since all random variables in the field are drawn independently, there is no correlation between the random variables at each two points

$$\forall r_1, r_2 \in \Omega, \text{with } r_1 \neq r_2 : \text{Cov}(U(r_1); U(r_2)) = 0. \tag{4.40}$$
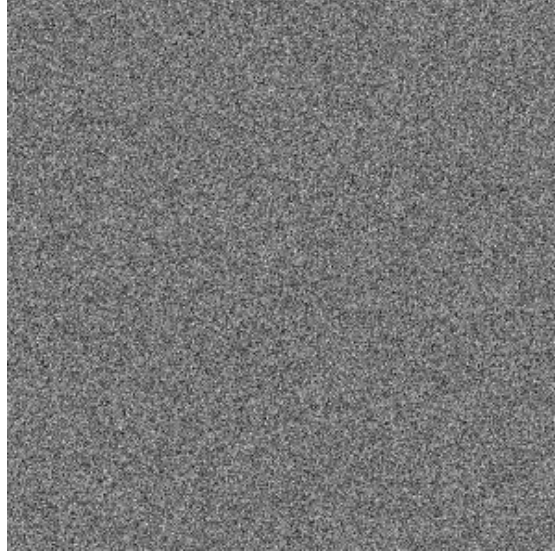
FIGURE 4.9: Realization of a Gaussian random field.

To introduce a correlation and thereby to give the random field a spatial structure, the random field is usually convolved with a convolution kernel $w(r)$

$$\forall r \in \Omega, Z(r) = (w * U)(r) = \int_\Omega w(h)U(r-h)dh. \tag{4.41}$$

Additionally, we will impose two constraints on the convolution kernel, namely that they should be symmetric and normalized to 1, i.e.

$$\int_\Omega w^2(h)dh = \quad 1. \tag{4.42}$$

$$\forall r \in \Omega, w(r) = \quad w(-r). \tag{4.43}$$

A realization of the GRF convolved with a kernel w is shown in Figure 4.10, demonstrating the smoothing effect of the convolution. The normalization condition is important for the modeling of the random field, since it preserves its expectation. The correlation of the convolved random field can be computed directly from the convolution kernel,

$$\text{Cov}(Z(r); Z(r+k)) = (w * w)(h) = \rho(h). \tag{4.44}$$

Usually, the convolution kernel is chosen from a family of functions, e.g. Gaussian kernels $w(h) = e^{-\frac{h^2}{a^2}}$ or the Laplacian-Gaussian kernel $w(h) = (-\frac{6}{a^2} + \frac{4h^2}{a^4})exp(-\frac{h^2}{a^2})$, depending on a width parameter a. The parameters of the family are determined by fitting a similarity measure to the data (see Section 4.4). Yet, if the convolution kernel is left unconstrained, it can be directly reconstructed from an image of a microstructure by inverting Equations 4.44 and 4.46 (see Section 4.5.2).
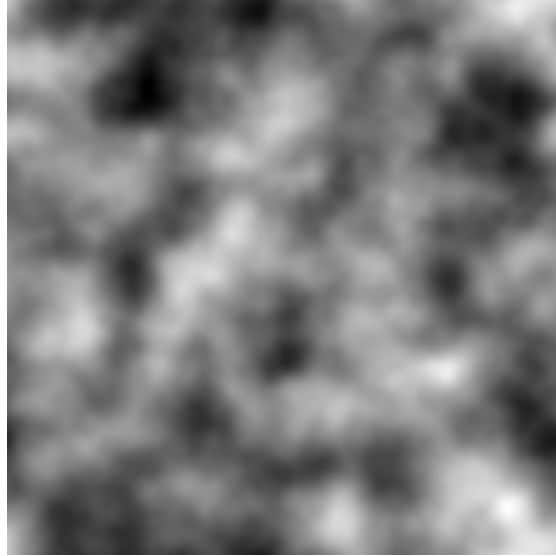
FIGURE 4.10: Random function $Z(x)$ generated from the random field in Figure 4.9.

4.5.1   Field-Cut

To model two-phase microstructures with a random field, a binary structure has to be computed. This happens by thresholding the random field, thus assigning every point with a value above some constant z as belonging to the solid phase and assigning the rest to the pore phase or vice versa. Thus, to get the microstructure model B, we have to compute

$$B(r) = \mathbb{1}_{Z(r) \geq z}, \tag{4.45}$$

where $\mathbb{1}$ is the indicator function. A microstructure generated by thresholding the correlated random field in Figure 4.10 is shown in Figure 4.11.
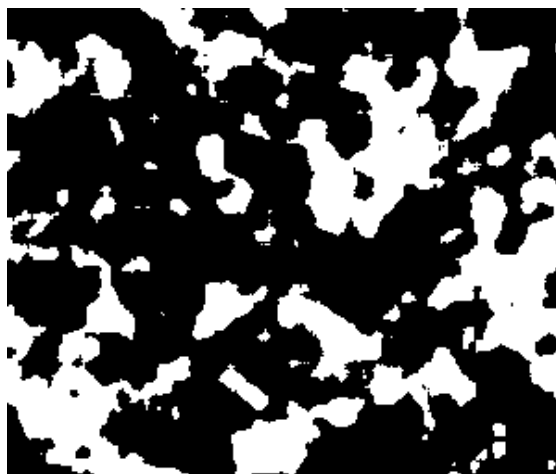
FIGURE 4.11: A microstructure generated from the correlated random field in Figure 4.10

If the random field is a GRF, the set covariance of the random set representing the microstructure can be computed according to Lantuéjoul [2002], Stoyan [2003] via

$$\mathrm{Cov}(B(r); B(r+h)) = \frac{1}{2\pi} \int_0^{\rho(h)} e^{\frac{-z^2}{1+t}} \frac{dt}{\sqrt{1-t^2}}. \tag{4.46}$$

This will give the non-centered set covariance as discussed for random sets in 4.2.1.

4.5.2   Fitting the Model to Data

The model fitting can be done for arbitrary kernels with a kernel reconstruction according to Bron and Jeulin [2004]. First, the threshold z for the generation in Equation 4.45 can be determined for any GRF with the cumulative distribution function (CDF) of the standard normal distribution $N(0, 1)$. If F is the CDF of $N(0, 1)$, then

$$F(z) = P(N(0, 1) < z). \tag{4.47}$$

Hence, if the volume fraction p is known

$$p = \quad P(N(0, 1) \geq z) = 1 - F(z), \tag{4.48}$$

$$\Rightarrow z = \qquad F^{-1}(1 - p). \tag{4.49}$$

Thus, if volume fraction p is known, the threshold z can be computed directly. Also, the complete kernel $w(h)$ can be reconstructed from the segmentation. Therefore the covariance of the segmented image has to be measured. Then by inversion of Equation 4.46, the covariance of the correlated random field $Z(r)$ can be computed. Since no analytic expression is known for the inversion of Equation 4.46, this has to be done numerically. To invert Equation 4.46 points are sampled in $\mathrm{Cov}(B(r); B(r+h))$, and then the corresponding values for $\rho(h)$ are computed by searching the interval $[0; 1]$. If the sampling of $\mathrm{Cov}(B(r); B(r+h))$ is sufficiently dense simply selecting the closest point to the measured value for $\mathrm{Cov}(B(r); B(r+h))$ and then looking up the corresponding value for $\rho(h)$ will invert Equation 4.46. By increasing the number of sampling points, it was determined, that using 20000 sampling points, the numerical inversion gives reasonable results.

In a second step, the convolution kernel is reconstructed from $\rho(h)$. Since the inversion of Equation 4.44 is a deconvolution problem any standard method will achieve the goal. However, a convenient choice for the deconvolution is the deconvolution by Fourier transform, or in the discrete case by fast fourier transform (FFT). In Fourier-space, the

convolution in Equation 4.44 is transformed to a simple multiplication

$$\rho(h) = (w * w)(h) \Rightarrow \mathscr{F}(\rho) = \mathcal{F}(w) * \mathcal{F}(w). \tag{4.50}$$

Since $\mathscr{F}(w)$ is purely real, due to the symmetry of w the inversion of Equation 4.50 can be done by simply taking the square root of the right hand side

$$w = \mathcal{F}^{-1}(\sqrt{\mathcal{F}(\rho)}). \tag{4.51}$$

On discretized images the Fourier-transform simply translates to the FFT, thus

$$w = FFT^{-1}(\sqrt{FFT(\rho)}). \tag{4.52}$$

With the convolution kernel known, model realizations can be computed by Equations 4.41 and 4.45.

4.5.2.1   The Corson Model for the Covariance

The application of the method in Bron and Jeulin [2004] showed, that the reconstruction of the convolution kernel is possible, but suffers from noise. The noise in the convolution kernel is due to noise in the measurement of the covariance, which in turn is due to noise in the data. To suppress the noise in the covariance measurements, it was proposed to fit a general covariance model to the measured covariance. Such a model has been proposed in Corson [1974]. The model consists of a family of covariance functions, which are constrained by general considerations about the covariance of random sets. The model is given by

$$\mathrm{Cov}_C(h) = f^2 + f(1-f)e^{-ch^n}, \tag{4.53}$$

with the three parameters f, c and n. It can be easily derived that f is the volume fraction of the random structure. The parameters c and n parametrize the scales in the random set. Yet, it can be shown that n must be less or equal to one $n \leq 1$ for $\mathrm{Cov}_C(h)$ to be the covariance of a random set, which places additional constraints on n.

For the suppression of the noise in the measured covariance, the model in Equation 4.53 is fitted to the measured covariance and the model function is used to reconstruct the convolution kernel, i.e. $\rho(h) = \mathrm{Cov}_C(h)$ in Equation 4.51.

4.6 Results

4.6.1 Nanoporous Additive in Li-Ion Battery Electrodes

The first application of stochastic modeling is the dataset segmented in Section 3.5.1. A volume rendering of the reconstructed structure is shown in Figure 3.20, also a slice view is shown in Figure 4.12. From the apparent morphology of the structure, a version of the Gaussian random field model was fitted, to reproduce the data. The model published in Bron and Jeulin [2004] was chosen to keep the convolution kernel as general as possible. As described in Section 4.5.0.1, the convolution kernel of the Gaussian random function cut model can be reconstructed directly from the data by inverting Equations 4.44 and 4.46.
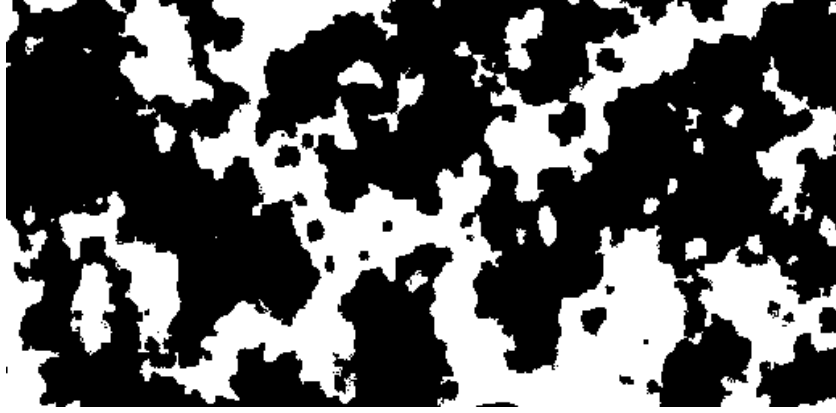
FIGURE 4.12: Slice view of the observed structure obtained from the segmentation of FIB-SEM images of the nanoporous additive.

First, the Corson model was fitted to the covariance of measured on the segmentation. The parameters in Table 4.1 were found to be the best fit. Although, a value for the parameter n greater than unity does not generate a random set (see Bron and Jeulin [2004]), fixing the parameter to $n = 1$ would yield a microstructure much different from the observed one. Hence, in order to be able to create artificial microstructures $n \geq 1$ was permitted.

parameter	optimal value
f	0.40
c	0.077
n	1.058

TABLE 4.1: Optimal parameters obtained by fitting to the observed structure of S12.

The fitted covariance was used to recover the covariance of the correlated random field by the procedure described in Section 4.5.2. Then, model realizations were computed and statistical characteristics were measured, to assess the quality of the model fit. A

realization of the model is shown on the right-hand side of Figure 4.12. For comparison, a slice view of the observed structure obtained from the segmented images in Section 3.5.1 is shown on the left.
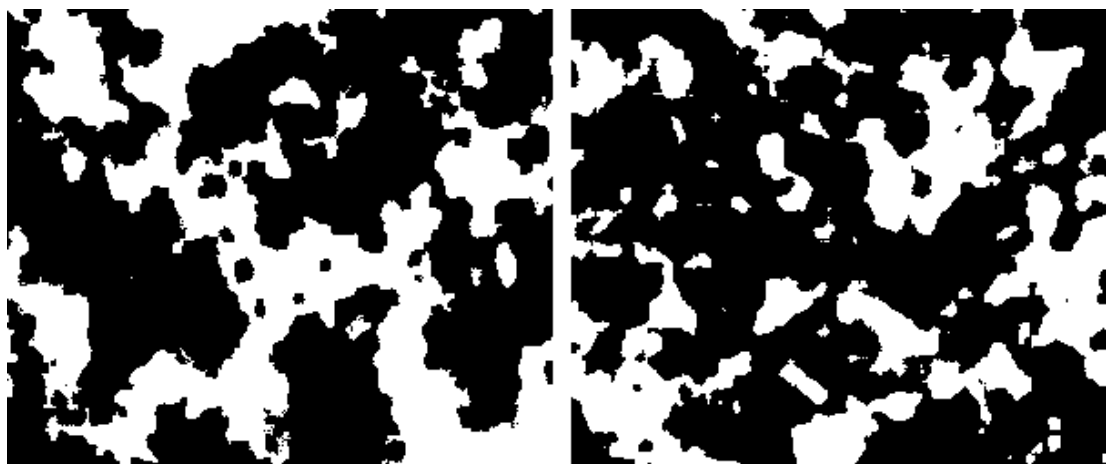
FIGURE 4.13: (left) Slice view of the observed structure in Figure 4.12; (right) realization of the GRF model fitted to the structure in Figure 4.12.

Visually, the model produces a structure, resembling the segmented one. Also, the volume fraction is the same as in the segmentation. The length scales in the two images seem to be the same, as well. This is confirmed in the covariance plot in Figure 4.14. Both covariances have about the same range of 45 voxels and show a similar slope at the origin, which is important to estimate the surface area of the modeled solid phase. Also, the decay seems similar although a little bit slower in the measured covariance. The difference at the origin stems from a difference in volume fraction. This is due to statistical uncertainties, and will converge to the measured value for large datasets.
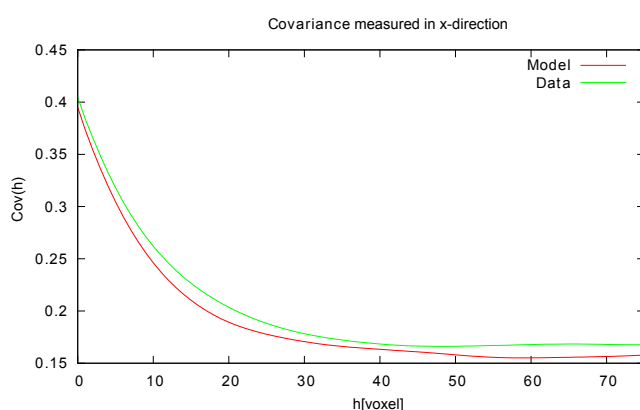
FIGURE 4.14: Measured covariance of the observed structure and the model realization in Figure 4.13.

A difference between the data and the realization can be observed when considering the connected components. In the segmentations, a large connected component dominating the image can be observed, where as in the realization, several larger connected

components appear. Although the slice view gives only limited information on the three-dimensional structure and the model realizations might differ, a similar effect can be seen in the granulometry, shown in Figure 4.15.
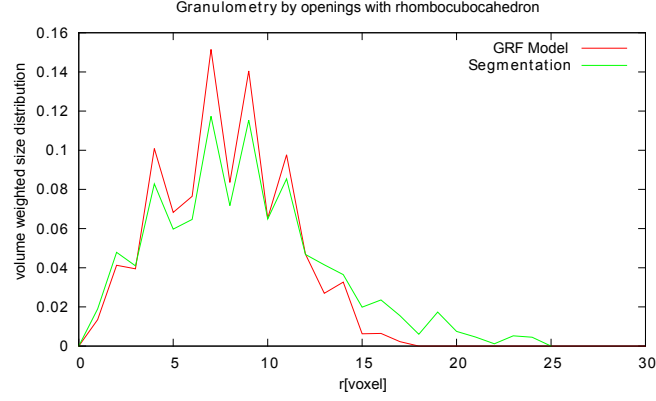
FIGURE 4.15: Granulometry by openings with a rhombocubocahedron, measured on the observed structure on Figure 4.12.

The plot shows a slight difference in the size distribution in the granulometry, where the model granulometry shows a longer 'tail' in the distribution. More precisely the size distribution is overestimated by the model below 13 voxels, where for larger sizes, the distribution of the model is lower than the segmentation. The effect can be seen in Figure 4.13. In the segmentation, the pore space is largely empty, while in the model realization, several small connected components are distributed in the pore space, leading to a higher granulometry for small sizes. In opposite, the missing of the single connected component in the model realization probably leads to a lower granulometry for large sizes.

Additionally, the opening and closing curves have been measured, shown in Figures 4.16 and 4.17. Since the granulometry is the derivative of the opening curve it basically contains the same information than the granulometry. The closing curve, however, shows a significant difference around 15 voxels, asserting the statement made about the pore space. The smaller connected components in the pore space block the extension of large empty areas, which leads to a large difference in the closing curve.

After modeling the solid component, simulations of the effective behavior of the medium were made to assess the quality of the modeling. Since the study of the nanoporous additive was done to compute its influence on the ion diffusion in the battery electrode, diffusion simulations were made. Whether the statistical differences between the model realizations and the segmentation lead to a significant difference in macroscopic behavior will be shown in Chapter 2.
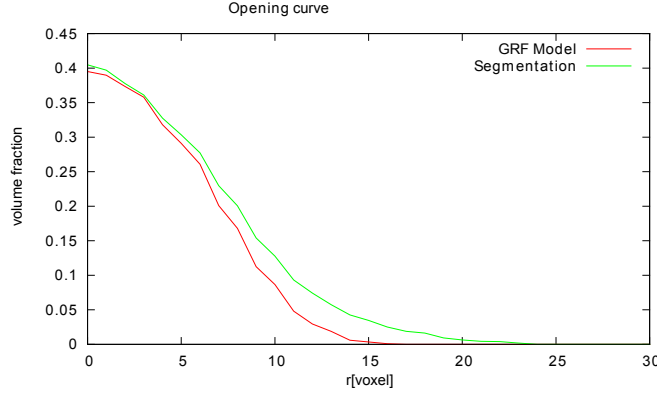
FIGURE 4.16: Opening curve measured on the observed structure in Figure 4.12.
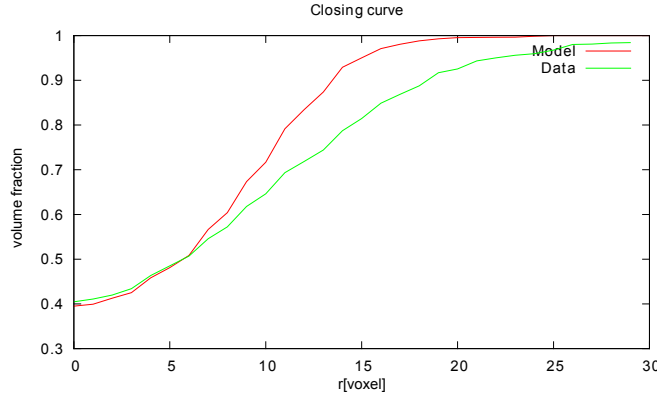
FIGURE 4.17: Closing curve measured on the observed structure in Figure 4.12.

4.6.2   Nanoporous EDLC Electrode

The model described in Section 4.3 was fitted to the segmentations of EDLC electrodes in Section 3.5.2. A special challenge is that the model has to fit to two independent segmentations. Thus it is assumed that the model will fit to both segmentations, each with a different set of model parameters. In contrast to the previous model, which was uniquely defined using the covariance, the current model was fitted using the covariance, the opening and the closing curve as distance measure. Since no analytical forms for each of the measures are known, the model fitting was done by generating realizations of the model and then measuring the covariance, opening- and closing curves. Then, the distance function in Equation 4.31 was minimized using the SPSA algorithm (Algorithm 1 in Section 4.4). Since to evaluate the objective function one model realization has to be computed, optimizing can be a computational intensive and lengthy task.

To evaluate the distance function, the covariance was measured on the realizations at 37 equidistant distances h with $\delta h = 2$ voxels, thus covering the interval $[0, 76]$. The opening and closing curves were measured using a rhombocubocahedron with up to

a radius of 30 voxels, with $\delta r = 2$ voxel, thus using 15 data points. This gives the covariance double the weight than each of the other curves.

The model realizations were generated with periodic boundary conditions on a cubic image with an edge length of 256 voxels. Since the optimization algorithm can minimize random objective functions, a smaller image size was chosen at the expense of using a larger number of realizations. In total 72 realizations were generated in 34 iterations for the fitting of S12 and 188 realizations were used to fit the model to S14 in 89 iterations. Yet, the fitting could be done on a standard notebook.

4.6.2.1 Fitting the Observed Structure of S12

As a first result, the model was fitted to the observed structure of S12, reconstructed by segmentation as described in Section 3.5.2.1. To fit the model, the volume fraction was fixed be the same as for the segmentation. Then the remaining parameters were fitted using the minimization of the objective function.

For comparison, slice views of the segmentation and the model are shown in Figure 4.18. As can be seen, the volume fraction is above 50% and the measured value is 68%. Also the pore space has an irregular shape, making a modeling with a pure Boolean model impossible. To improve the modeling, the image has been scaled to 1.5 times its original size, making it easier to discretize the structuring element for the measurement of the opening and closing curves. With the fitting procedure, the parameters in Table 4.2 were found to be optimal.

parameter	optimal value [voxel]	optimal value [nm]
volume fraction	0.67	0.67
ball radius r	7	16.7
width of filter mask s	10	23.8

TABLE 4.2: Optimal parameters obtained by fitting to the observed structure of S12
.

As can be seen, the model realization reproduces the morphology of the segmentation quite well. Also, the pore sizes and shapes are reproduced and, as in the segmentation, both phases percolate. A slight difference can be observed considering the surface area. In the model, the surface appears smoother than in the segmentation. The reduced surface area comes from the smoothing, which is made by the convolution with the Gaussian kernel. In principle, the surface area can be made rougher, but this would involve introducing another length scale in the model, further complicating the modeling by adding another parameter.
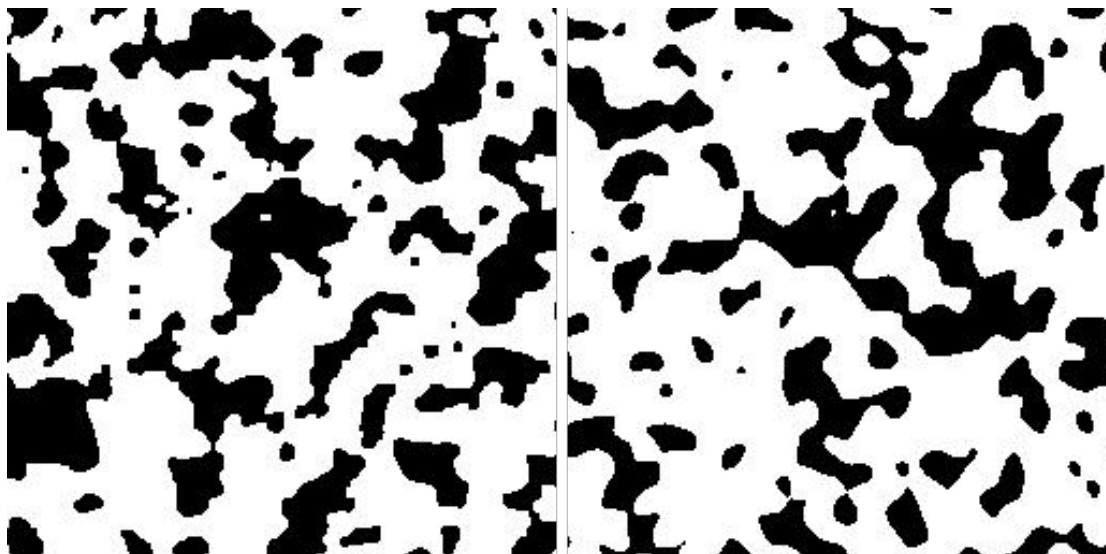
FIGURE 4.18: Comparison between the observed structure (left) and the fitted model (right) of dataset S14.

A statistical comparison has been done by measuring the covariance, opening- and closing curves on both the segmentation and the model realization. A comparison of the covariance is shown in Figure 4.19. As can be seen, the two curves are virtually identical. The exact agreement at the origin and the sill is coming from the exact match of the volume fraction. At ten to twelve voxel distance, a slight difference can be observed, yet this is within the statistically expected errors.
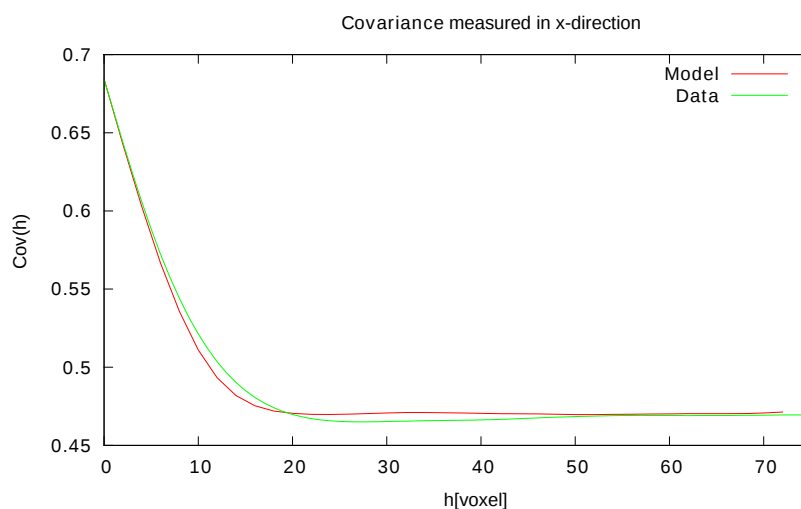
FIGURE 4.19: Comparison between the covariance of the fitted model (red) and the observed structure (green) of dataset S12.

A similar picture can be observed for the opening curve, shown in Figure 4.20. Especially at the lower end of the curve, between ten and 15 voxel, the slight difference is visible. Yet, in total both curves are in good agreement, indicating that the size distribution of the solid phase can be modeled accurately by the stochastic model.
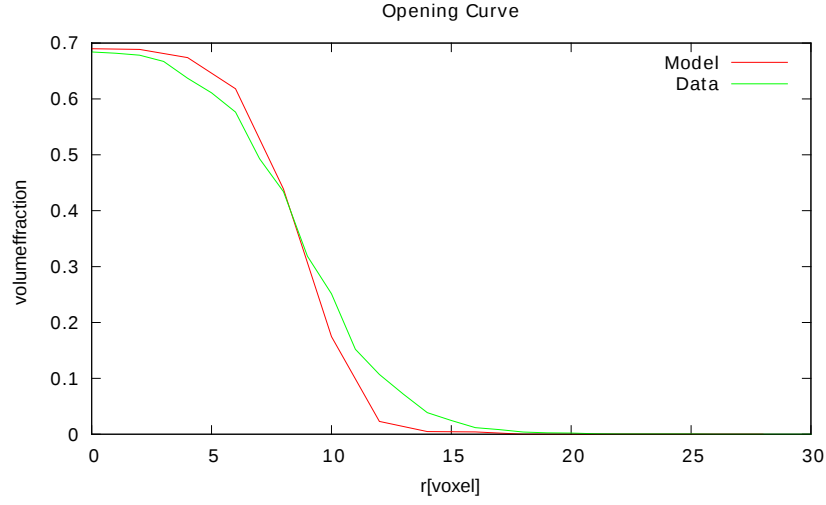
FIGURE 4.20: Comparison between the opening curve of the fitted model (red) and the observed structure (green) of dataset S12.

The closing curve, shown in Figure 4.21 again shows no significant deviation between segmentation and model realization. This indicates that the size distribution of the pores can be accurately reproduced, as well.
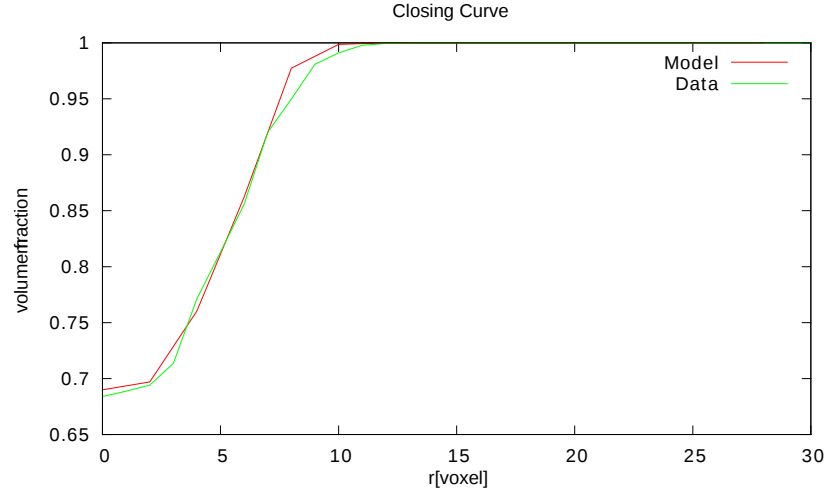
FIGURE 4.21: Comparison between the closing curve of the fitted model (red) and the observed structure (green) of dataset S12.

Overall the fit of the model to the segmentation S12 is very accurate with respect to the selected statistical measures.

4.6.2.2 Fitting the Observed Structure of S14

The same fitting procedure was done with the segmentation S14 (Section 3.5.2.2). Due to the larger length scales in the dataset, no scaling of the segmentation was necessary.

A comparison between a model realization and the segmentation is shown in Figure 4.22. Visually, the model looks slightly coarser again, with a smoother boundary. Yet, the larger-scale structures are reproduced very accurately.
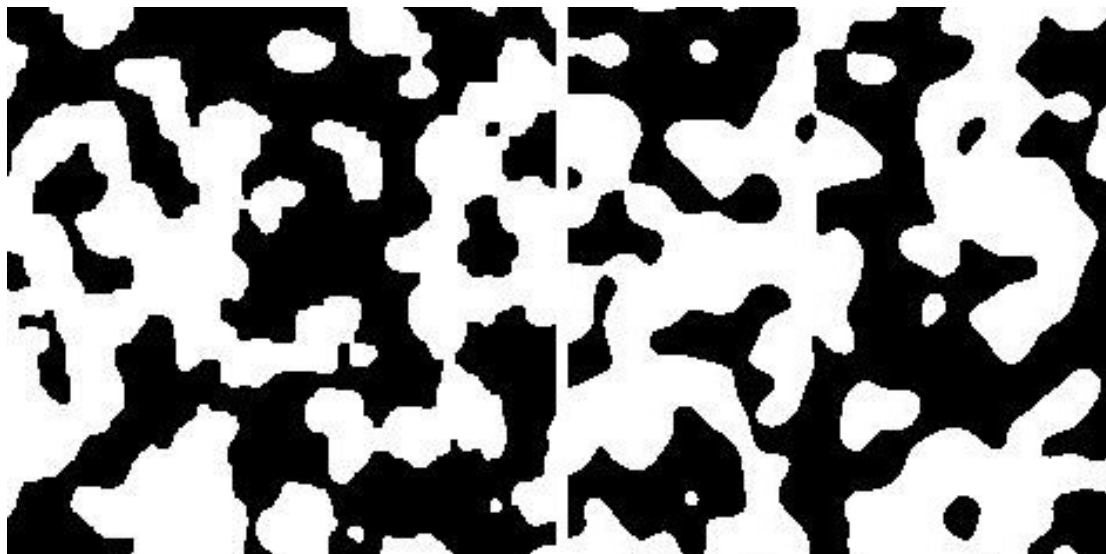
FIGURE 4.22: Comparison between the observed structure (left) and the fitted model (right) of dataset S14.

The fitted set of parameters is given in Table 4.3.

parameter	optimal value [voxel]	optimal value [nm]
volume fraction	0.52	0.52
ball radius r	10	50
width of filter mask s	14	70

TABLE 4.3: Optimal parameters obtained by fitting to the observed structure of S14
.

For a quantitative comparison, the plot of the covariances is shown in Figure 4.23. The two curves are in almost perfect agreement, showing no significant differences. This indicates a very good fit.

A comparison of opening curves of the model and the observed structure are shown in Figure 4.24. Also, the opening curve shows no significant deviation and fits even better than for the S12 fit. This indicates that the size distribution of the solid phase is almost exactly reproduced by the model.

At last, the Cosing curve was measured for the observed structure and the model, shown in Figure 4.25. Again, the curves coincide very well, despite some derivation at around 15 voxels.

In essence, the fit to S14 has an even better agreement than for S12, showing that the model is able to reproduce both datasets very well, with different parameters. This can
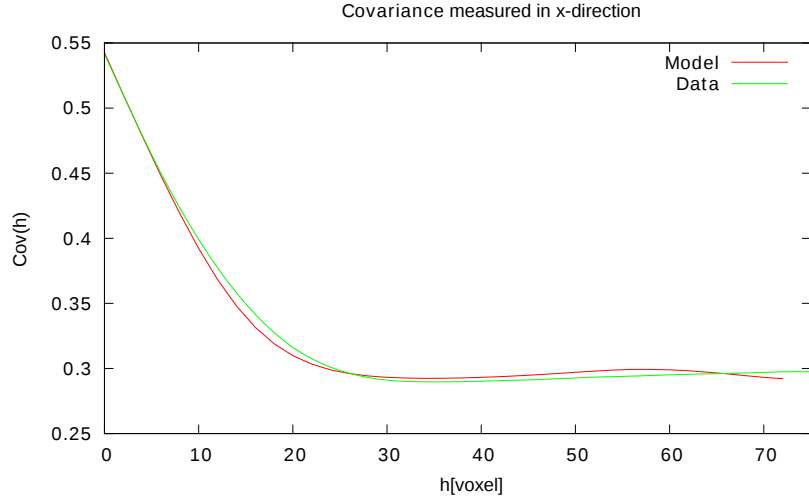
FIGURE 4.23: Comparison between the covariance of the fitted model (red) and the observed structure (green) of dataset S14.
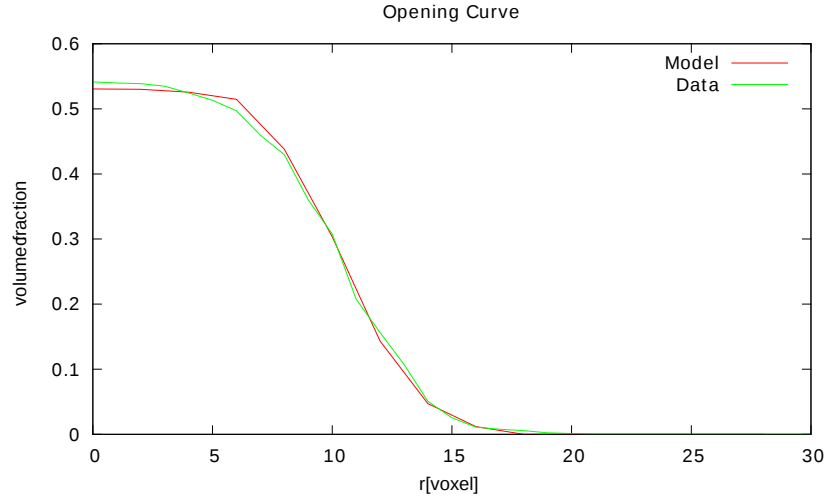
FIGURE 4.24: Comparison between the opening curve of the fitted model (red) and the observed structure (green) of dataset S14.

now be used to generate artificial structures, which when combined with simulations can be used to optimize the structure.

4.7 Discussion and Outlook

4.7.1 Discussion

In this chapter, stochastic models for three materials have been presented. The modeling was based on three reconstructions of the pore space of the respective materials presented in Section 3.5, in the previous chapter. The nanoporous additive has been modeled using
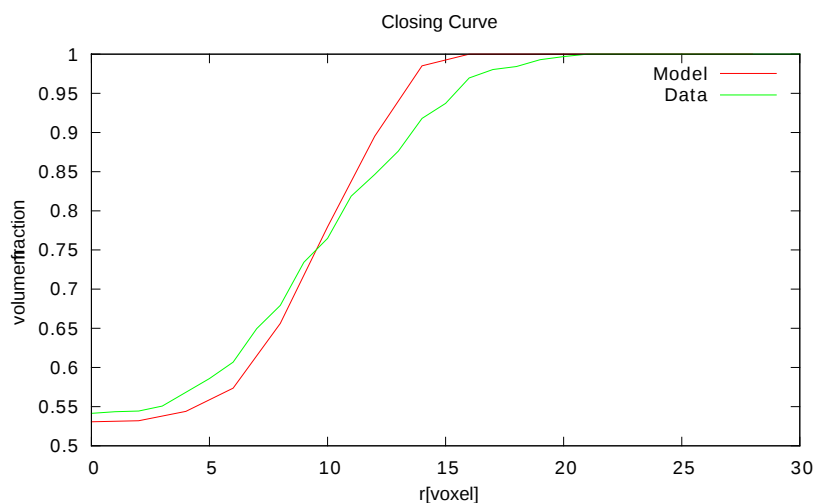
FIGURE 4.25: Comparison between the closing curve of the fitted model (red) and the observed structure (green) of dataset S14.

a Gaussian random field. The GRF has been convolved with a filter mask, introducing a spatial correlation. The filter mask has been reconstructed from the covariance of the observed structure. In the results section, the fitted model has been compared to the observed structure, showing good agreement. For the comparison, the covariance as well as the opening and closing curves have been measured. A comparison of the granulometries of both the observation and the model realization has shown a slight excess of small particle sizes in the model and a lack in larger particles. Whether this has a major influence on the transport properties, is investigated in Chapter 5.

Further, a modification of the Boolean model of spheres is discussed, which was developed to model two materials, used as electrodes for EDLCs. The model is based on the mono-disperse Boolean model of spheres, but the indicator function is convolved with a Gaussian kernel, to introduce a smoothing of the structure. A binary model is recovered, by thresholding the resulting random function. The structure is smoothed to mimic the sintering of the particles during the production process. The model was fitted to the observed structures using stochastic optimization of a similarity function. Again, the statistical similarity has been assessed by the covariance and the opening and closing curves. It is shown, that the model shows good agreement with both samples, for different parameter values.

4.7.2 Outlook

To outline continued research, the two models for both carbon structures need to be considered separately. The modeling of the additive could be enhanced by dropping the Corson model used to fit the covariance. This could be achieved by allowing a more

general form of the covariance function. Also, a spectral analysis of the reconstructed covariance of the random function $Z(x)$ could enhance the model. Both would allow additional length scales in the model, which could be used to remedy the lack of larger structures in the model, compared to the observed structure. Since the modified Boolean model fits very well to the observed structures, the further investigations of model properties could be perused. To simplify the fitting procedure, analytical expressions of the volume fraction depending on the model parameters could be derived. Also, the covariance of the model could be computed analytically. To generalize the model to further structures, the underlying Boolean model could be amended replaced by a germ-grain-model allowing repulsive forces between the spheres. Thereby, different pore structures could be realized with the same volume fraction.

<div style="text-align: right;">*5*</div>

Simulation of Physical Properties

Parts of the work in this chapter will be published in:

Characterization and modeling of their microstructures give important insight into the materials at hand. Yet, the characteristics of the observed microstructures have to be related to measurable, i.e. macroscopic quantities. These properties can be the electrical conductivity, diffusivity or mechanical properties such as the elastic moduli. For this thesis, the electric conductivities of the nanoporous carbon additive as well as the diffusion resistance in the pore space is of importance. Fortunately, both problems adhere to the same partial differential equation (PDE). Thus, the problem of computing the electrical conductivity/diffusion resistance will simply be referred to as the conduction problem and the diffusion resistance and the electrical conductivity will be referred to as conductivity.

The macroscopic conductivity can be calculated by simulating the corresponding process at the microscale. The structural data observed by imaging or from modeling the heterogeneous material is used to solve the corresponding problem, usually a PDE. Then the resulting field is used to estimate the effective conductivity.

Combined with modeling, the calculation of macroscopic properties using the microstructural information, can be used to improve the materials by optimizing the microstructure. If a suitable model is found, realizations can be computed and, with the simulations, macroscopic properties of the realizations can be computed. By varying the

parameters of the model, a better or even optimal hypothetical microstructure can be found, when using, for instance, the optimization algorithms mentioned in Section 4.4 (see Virtual Material Design in Chapter 1).

Also, effective properties can be used for multi scale simulations, if a system contains two distinct scales, such as micro- and nanometer size structures. Then simulating the behavior of the system can be split into two separate calculations, by averaging the dynamics at the smaller scale. This is done by computing effective properties for the nano-scale structures and then using the effective property in the micro-scale simulation.

In this chapter, the problem of calculating the conductivity of a heterogeneous medium will be discussed. Then methods for the calculation will be presented. Subsequently, results for the segmented data in Chapter 3 will be given and for the corresponding model in Chapter 4. At the end of the chapter, a multi-scale simulation will be presented for the charging of a Li-Ion battery and the electrical impedance spectroscopy of electric double layer capacitors (EDLC's).

5.1 The Conduction Problem

Many different physical phenomena can be reduced to the conduction problem in a heterogeneous medium. In general, the conduction problem describes the transport of a conserved species through the material. These species can be electric charge (electric conduction), diffusing particles (diffusion) or even an electric field (energy). All these phenomena are governed by the same linear partial differential equations and can be described as a conduction problem.

The derivation of the governing equations starts with considering a conserved species in space. For any conserved species a continuity equation can be given of the form

$$\frac{\partial \rho(x)}{\partial t} + \nabla \cdot \vec{J}(x) = 0. \tag{5.1}$$

In the equation, ρ is the density of the conserved species, like charge or particles per volume, and $\vec{J}$ is the current of the species in particles per time and area. In component notation the relation is given by

$$\frac{\partial \rho(x)}{\partial t} + \frac{\partial}{\partial x_i} J_i(x) = \frac{\partial \rho(x)}{\partial t} + \partial_i J_i(x) = 0, \tag{5.2}$$

where according to the Einstein sum convention, repeated indices are summed. In this case, the sum runs over the spatial coordinates x, y, z. When a steady state is assumed,

the differential with respect to time vanishes and the second term remains

$$\partial_i J_i(x) = 0. \tag{5.3}$$

This equation states that in a volume element, the species is neither created nor annihilated, thus the currents J_i into and out of the volume element, adds to zero. In the infinitesimal form this yields a vanishing divergence.

Furthermore, it is assumed that the current is proportional to some force field E_i, which may be an electric field as in electric conductivity or a concentration gradient as in the diffusion problem

$$J_i(x) = \sigma_{ij} E_j(x). \tag{5.4}$$

The constant of proportionality σ_{ij} is called the conductivity tensor. The relation is called the constituting relation and in this thesis is always assumed to be linear.

Also, the force field is assumed to be irrotational,

$$\nabla \times E(x) = \epsilon_{ijk} E_i(x) E_j(x) = 0. \tag{5.5}$$

The irrotationality implies the existence of a potential field, may that be the electric potential or the concentration of a diffusing species. The forcefield depends on the potential through

$$E_i(x) = -\partial_i \phi(x). \tag{5.6}$$

Now, the conduction problem consists of, computing the flow field J_i, the force field E_i and the potential ϕ for suitable boundary conditions. In homogeneous materials, the conductivity tensor does not depend on the position in space, thus it is a global property. In heterogeneous materials however, the conductivity is a local property leading to a space dependent conductivity tensor $\sigma_{ij}(x)$ and a local constitutive relation

$$J_i(x) = \sigma_{ij}(x) E_j(x). \tag{5.7}$$

In a two-phase material, the conductivity tensor can be expressed with the indicator functions of the phases $\mathbb{1}^{(i)}$ as

$$\sigma_{ij}(x) = \sigma_{ij}^1 \mathbb{1}^{(1)}(x) + \sigma_{ij}^2 \mathbb{1}^{(2)}(x). \tag{5.8}$$

Figure 5.1 shows an example of a two-phase medium. The medium is represented by a domain on which the conductivity problem is computed. The two phases have different conductivities σ_1 and σ_2 and do not intersect. They are separated by boundary Γ_{12}.
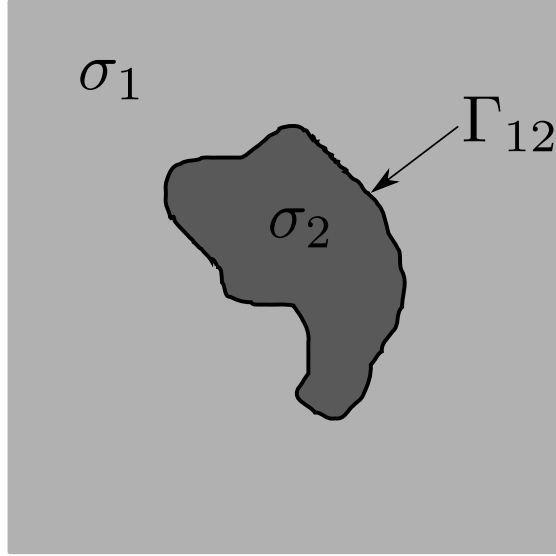
FIGURE 5.1: A sample domain on which the conductivity is computed.

In a porous material, either the solid or void phase might have a zero conductivity, thus one of the terms vanishes

$$\sigma_{ij}(x) = \sigma_{ij} \mathbb{1}^{(s)}(x). \tag{5.9}$$

Also, in general the tensor σ_{ij} must be symmetric and positive definite, additional symmetries, such as isotropy, can be imposed

$$\sigma_{ij} = \begin{pmatrix} \sigma_{11} & \sigma_{12} & \sigma_{13} \\ \sigma_{21} & \sigma_{22} & \sigma_{23} \\ \sigma_{31} & \sigma_{32} & \sigma_{33} \end{pmatrix}. \tag{5.10}$$

Yet, in many cases a simplification can be made, when the material property is isotropic. In that case, the conductivity tensor is a diagonal matrix with the scalar isotropic conductivity σ on the diagonal

$$\sigma_{ij} = \sigma \mathbb{1}_{ij} = \begin{pmatrix} \sigma & 0 & 0 \\ 0 & \sigma & 0 \\ 0 & 0 & \sigma \end{pmatrix}. \tag{5.11}$$

5.1.1   Boundary Conditions

To solve the conduction problem, the boundary conditions of the phases have to be specified. This includes the interfacial boundary separating the two phases as well as external boundaries enclosing the domain of computation. Since the problem involves solving for the two fields $J_i(x)$ and $E_i(x)$, the boundary conditions have to be specified for

both fields. Depending on the purpose of the simulation, different boundary conditions can be imposed on the computational domain. In this thesis however, periodic boundary conditions will be used. This means, that the domain is treated as a periodic structure, where the boundaries at the top and at the bottom are identified as the same. The same holds for the boundaries on either side. In Figure 5.2 this means, that all fields are continuous across the cell boundary $\partial\Omega$.
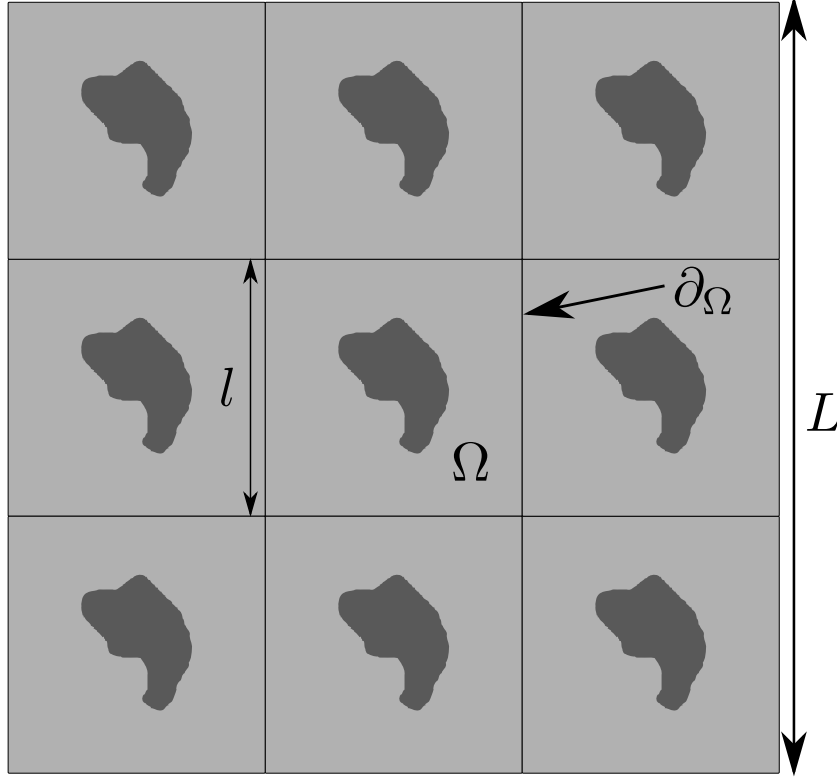
FIGURE 5.2: Computational setup with periodic boundary conditions.

For the interfaces, different boundary conditions can be imposed, too. Usually, the boundary across the interface is treated as a perfect interface, meaning that the potential across the interface is continuous and the normal component of the force field is continuous as well. Thus, for the derivatives normal to the interface Γ_{12} in Figure 5.1 we have

$$\Phi|_{\Gamma_{12+}} = \Phi|_{\Gamma_{12-}}, \tag{5.12}$$

$$(n_i J_i)|_{\Gamma_{12+}} = (n_i J_i)|_{\Gamma_{12-}}, \tag{5.13}$$

where $\vec{n}$ is a vector normal to the interface. This type of boundary conditions is called 'perfect' boundary conditions. Yet, sometimes it is desirable to have imperfect boundary conditions. For instance when a thin impenetrable layer separates the two phases, which is too small to be resolved with the voxel grid (see Figure 5.3). This situation corresponds to the limit $\lim_{t\to0}$ in Figure 5.3. In that case, the boundary conditions can be relaxed

depending on the interfacial conductivity $\sigma_{\Gamma_{12}}$. If the conductivity is much smaller than the conductivity of each of the phases $\sigma_{\Gamma_{12}} \ll \sigma_1, \sigma_2$, the infinitely thin interface can be modeled by a jump of the potential across the interface according to

$$\Phi|_{\Gamma_{12+}} - \Phi|_{\Gamma_{12-}} = \quad \sigma_{\Gamma_{12}}, \tag{5.14}$$

$$(n_i J_i)|_{\Gamma_{12+}} = \quad (n_i J_i)|_{\Gamma_{12-}}. \tag{5.15}$$
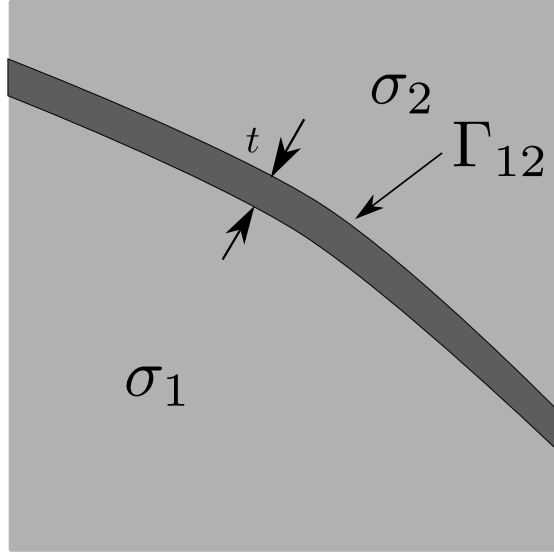
FIGURE 5.3: Interface between two phases.

On the other hand, a jump in the normal component can occur when the interface is perfectly conducting, i.e. the conductivity of the interface is much higher than of the two phases, $\sigma_{\Gamma_{12}} \gg \sigma_1, \sigma_2$

$$\Phi|_{\Gamma_{12+}} = \quad \Phi|_{\Gamma_{12-}}, \tag{5.16}$$

$$(n_i J_i)|_{\Gamma_{12+}} - (n_i J_i)|_{\Gamma_{12-}} = \quad \sigma_{\Gamma_{12}}. \tag{5.17}$$

Since these interface conditions generalize the perfect interface conditions in Equation 5.12, they are called 'imperfect' interface conditions. A detailed treatment can be found in Lipton and Vernescu [1996] and a complete theory can be found in Hashin [2001]. These boundary conditions will be used later to model the electrical double layer in EDLC electrodes. Since the double layer has a thickness of less than one nanometer, it cannot be resolved with the SEM. Thus, it is assumed that the double layer is very thin and has a fixed surface capacitance per unit area.

5.2 Multi-Scale Modeling

In this thesis, the largest scale is the extent of the electrode, typically of the order of millimeters (length scale of L in Figure 5.4). The smallest scale is a typical length scale of the pores $l_p \ll L$, usually of the order of micrometers or nanometers (see inset of Figure 5.4). As simulations of physical phenomena on the micro- or nanoscale are not feasible for macroscopic specimen, multi-scale models using an effective homogeneous medium representing the behavior of the material on the microscale are used. Therefore, the calculation is split into two separate problems. The microscopic conduction problem at the length scale l_p is solved, to compute an effective conductivity for the medium on the macroscale. Then, the macroscopic conductivity is used to compute physical quantities on the experimental scale L.
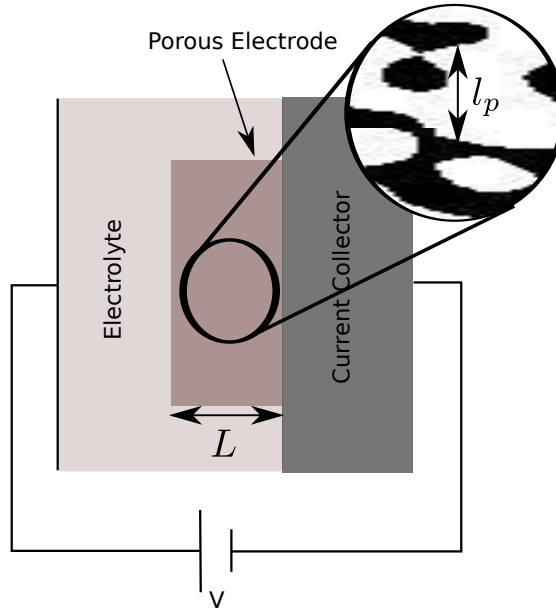
FIGURE 5.4: Two-scale modeling of a porous electrode.

Figure 5.4 also shows the typical experimental setup used for testing porous electrode materials. A highly conducting current collector is used to host the electrode. Both are immersed into electrolyte, filling the pores. On the other side of the cell, a counter electrode (not shown) closes the circuit. In that setup, measurements are made such as charge and discharge of the electrode and electric impedance spectroscopy. In the course of this thesis, the electrode material is modeled as an effective medium, with effective properties computed on the microscale (inset in Figure 5.4).

5.2.1 Effective Conductivity

The effective conductivity describes the average response in the heterogeneous medium when a force field is applied, having a length scale much larger than the typical length scale of the microstructure. That means, an effective conductivity σ_{ij}^{eff} has to be found such that the Equations 5.3-5.5 hold for a macroscopic force field $\langle E_i \rangle$ and a macroscopic flow field $\langle J_i \rangle$, which are given by the average behavior of the microscopic fields, i.e.

$$\partial_i \langle J_i \rangle = \quad 0, \tag{5.18}$$

$$\epsilon_{ijk} \langle E_i(x) \rangle \langle E_j(x) \rangle = \quad 0. \tag{5.19}$$

Then, the effective behavior is described by a macroscopic constitutive relation as in 5.7, relating the macroscopic flow to the macroscopic force field, by the macroscopic or effective conductivity σ_{ij}^{eff}, with

$$\langle J_i \rangle = \sigma_{ij}^{eff} \langle E_j \rangle. \tag{5.20}$$

The effective conductivity is computed by homogenization. A detailed theoretical treatment is given in Papanicolau et al. [1978] and Sánchez-Palencia [1980]. Also, an overview can be found in Torquato [2002] and Milton [2002].

To homogenize Equations 5.3-5.5, an infinite periodic medium is considered, as the one shown in Figure 5.2 in the limit $\frac{l_p}{L} \to 0$. To separate the scales, a new variable y is introduced through

$$y = \frac{x}{\epsilon}, \tag{5.21}$$

where $\epsilon \geq 0$ parametrizes the period in the medium. The variable y is called the fast variable and in this context, x denoted the slow variable. The governing equation, in terms of the now periodic functions $\phi(x, y)$ and $\sigma(x, y)$, of the conductivity problem now reads

$$-\frac{\partial}{\partial x_i} \left[\sigma_{ij}(x, y) \frac{\partial \phi(x, y)}{\partial x_j} \right] = 0. \tag{5.22}$$

The equation is considered with periodic boundary conditions at the cell boundary $\partial \Omega$ and the appropriate macroscopic boundary conditions at the boundary of the macroscopic domain.

Then, equation 5.22 is expanded asymptotically around the limit $\epsilon = \frac{x}{y} \to 0$, where the differentials are expanded according to

$$\frac{\partial \Psi(x, y)}{\partial (x, y)_i} = \frac{\partial}{\partial x_i} \Psi + \frac{1}{\epsilon} \frac{\partial}{\partial y_i} \Psi. \tag{5.23}$$

This leads to the equation

$$[\epsilon^{-2} A_0 + \epsilon^{-1} A_1 + A_2 + \ldots][\phi_0 + \epsilon\phi_1 + \epsilon^2\phi_2 + \ldots], \tag{5.24}$$

with the operators

$$A_0 = \quad -\frac{\partial}{\partial y_i}\left[\sigma_{ij}(y)\frac{\partial}{\partial y_i}\right], \tag{5.25}$$

$$A_1 = \quad -\frac{\partial}{\partial y_i}\left[\sigma_{ij}(y)\frac{\partial}{\partial x_i}\right] - \sigma_{ij}(y)\frac{\partial^2}{\partial x_i \partial y_j}, \tag{5.26}$$

$$A_2 = \quad -\sigma_{ij}(y)\frac{\partial^2}{\partial x_i \partial y_j}. \tag{5.27}$$

Separation of the powers of ϵ in Equation 5.24 yields the set of equations

$$A_0\phi_0 = \quad 0, \tag{5.28}$$

$$A_0\phi_1 + A_1\phi_0 = \quad 0, \tag{5.29}$$

$$A_0\phi_2 + A_1\phi_1 + A_2\phi_0 = \quad 0. \tag{5.30}$$

In the analysis given in the references above, one finds that $\phi_0(x,y)$ depends only on x, hence $\phi_0(x,y) = \phi_0(x)$. Further ϕ_0 satisfies

$$-\sigma_{ij}^{eff}\frac{\partial^2\phi_0}{\partial x_i \partial x_j} = 0. \tag{5.31}$$

Hence, an effective conductivity of a homogeneous medium can be defined obeying Equation 5.20, with the effective conductivity σ_{ij}^{eff}. The effective conductivity can be computed by solving the microscopic problem on a domain Ω and then averaging over the fields, i.e.

$$\langle J_i \rangle = \quad \int_\Omega J_i(x)dx^3, \tag{5.32}$$

$$\langle E_i \rangle = \quad \int_\Omega E_i(x)dx^3. \tag{5.33}$$

A precise mathematical treatment with the proofs of the given relations can be found in Papanicolau et al. [1978] and Sánchez-Palencia [1980].

Then the effective conductivity can be computed from the average fields, using Equation 5.20

$$\langle J_i \rangle = \sigma_{ij}^{eff}\langle E_i \rangle. \tag{5.34}$$

Yet, the media considered in this thesis are modeled by random closed sets, which are not periodic. In that case is was shown in Papanicolaou and Varadan [1979] that taking the averages in Equation 5.34 not over a cell domain but over a large enough realization, the effective conductivity can be estimated. To get accurate information on the effective conductivity, the domain must be representative for the whole medium.

5.2.2 Representative Volume Element

In order to compute the effective conductivity of the macroscopic medium, the computational domain Ω must be a faithful representation of the microstructure of the microscopic medium. That means, the domain must be large enough to have all important features of the microscopic material and to show the same physical behavior as the macroscopic material.

In general, the margin of error decreases with the volume of the domain Ω. In this section, a procedure is described to estimate the size of a representative volume element, for a given margin of error in the estimated effective conductivity. For details on the representative volume element of random closed sets, see Kanit et al. [2003] and Jeulin [2012].

To test whether the domain Ω is representative, i.e. large enough, the following procedure can be employed. First, the conduction problem is solved on the whole domain Ω, resulting in the effective conductivity σ^{eff}. Then, the domain Ω is subdivided into m disjoint subdomains Ω_i. For each subdomain, the conduction problem is solved independently resulting in the effective conductivities $\sigma^{eff,i}$. As the effective conductivities are random variables it is possible to estimate their variance by

$$D^2_{\sigma_{eff}}(\Omega) = \frac{1}{m} \sum_i (\sigma^{eff} - \sigma^{eff,i})^2. \tag{5.35}$$

This can be used to estimate the accuracy of the predicted conductivity.

Also, it can be shown theoretically (see Jeulin [2012]), that the variance of the effective conductivity of random sets scales asymptotically with

$$D^2_{\sigma_{eff}}(V) = D^2_{\sigma_{eff}}(1)\frac{A_3^\alpha}{V^\alpha}, \tag{5.36}$$

where A_3 is a positive constant. The exponent α can be estimated by logarithmic regression via

$$\log D^2_{\sigma_{eff}}(V) = \log D^2_{\sigma_{eff}}(1) + \alpha \log(A_3) - \log(V). \tag{5.37}$$

Furthermore, it can be shown that the relative error ϵ_{rel} of n independent samples of volume V is given by the equation

$$\epsilon_{rel} = \frac{\epsilon_{tot}}{\sigma^{eff}} = \frac{2D_{\sigma_{eff}}(V)}{\sigma^{eff}\sqrt{n}}. \tag{5.38}$$

Thus, the size of a representative volume element for a given statistical margin of relative error ϵ_{rel} (e.g. 1%) is given by

$$V_{RVE} = \left(\frac{4D_{\sigma_{eff}}^2(V)A_3^\alpha}{\epsilon_{rel}^2(\sigma^{eff})^2} \right)^{\frac{1}{\alpha}}. \tag{5.39}$$

5.2.3 Bounds on Effective Properties

Even when the cell problem is not solved exactly, bounds on the effective properties can be derived from general considerations on the microstructure, for an overview see Milton [2002]. The bounds in this thesis are derived from variational considerations.

5.2.3.1 Wiener Bounds

The Wiener bounds for the conductivity of a multi-phase material can be derived from variational considerations. It can be shown that the solution to the conductivity problem minimizes an energy functional of the material, given by

$$W[E, J] = \int_\Omega \frac{1}{2} E_i(x) J_i(x) dx. \tag{5.40}$$

Using the constitutive relation in Equation 5.7, this can equivalently be expressed by the electric field and the flux field only

$$W[E] = \int_\Omega \frac{1}{2} E_i(x) \sigma_{ij}(x) E_j(x) dx, \tag{5.41}$$

$$W[J] = \int_\Omega \frac{1}{2} J_i(x) \sigma_{ij}^{-1}(x) J_j(x) dx. \tag{5.42}$$

These energies are called the macroscopic energy of the material, depending on E_i, and the macroscopic complementary energy of the material, depending on J_i.

From these expressions it can be shown that any trial field $\hat{E}_i$ or $\hat{J}_i$ will have a greater respective energy than the solution to the conduction problem. Using a constant trial field, the following upper and lower bounds on the effective conductivity can be derived,

for a multi-phase material (see Wiener [1912]):

$$\sigma_W^u = \sum_i p_i \sigma_i, \tag{5.43}$$

$$\sigma_W^l = \frac{1}{\sum_i \frac{p_i}{\sigma_i}}. \tag{5.44}$$

For a two-phase medium this simplifies to

$$\sigma_W^u = p_1\sigma_1 + p_2\sigma_2, \tag{5.45}$$

$$\sigma_W^l = \frac{1}{\frac{p_1}{\sigma_1} + \frac{p_2}{\sigma_2}}. \tag{5.46}$$

These bounds give first estimates of the effective conductivity of a multi-phase medium.

5.2.3.2 Hashin-Shtrikman Bounds

Using similar variational principles, stricter limits to the effective conductivity of isotropic heterogeneous materials have been derived in Hashin and Shtrikman [1963]. To this end Hashin and Shtrikman used a trial field which incorporated the isotropy of the medium. The Hashin-Shtrikman bounds are given by

$$\sigma_{HS}^u = \sigma_2 + \frac{p_1}{\frac{1}{\sigma_1 - \sigma_2} + \frac{p_1}{3\sigma_2}}, \tag{5.47}$$

$$\sigma_{HS}^l = \sigma_1 + \frac{p_2}{\frac{1}{\sigma_2 - \sigma_1} + \frac{p_2}{3\sigma_1}}, \tag{5.48}$$

where it is assumed that $\sigma_1 > \sigma_2$. As before, p_i is the volume fraction of phase i and σ_i its conductivity.

5.2.4 Simulation of the Effective Conductivity with the FFT Method

To calculate the cell problem, a new class of solvers has recently been developed using a Green's function in Fourier Space. The approach has first been published in Moulinec and Suquet [1998] and since then numerous refinements and improvements have been made, e.g. in Eyre and Milton [1999]. The calculations in this thesis were made using morphHom (Willot and Jeulin [2011],Willot and Jeulin [2009]). The algorithm solves the cell problem in Section 5.1 with periodic boundary conditions. Therefore, the flow field is decomposed into a constant reference field $J^0(x) = \sigma^0 E(x)$ and a polarization field $P(x)$

$$J_i(x) = \sigma_{ij}^0 E_j(x) + P_i(x). \tag{5.49}$$

The reference material is assumed to have a constant conductivity σ^0. Then the flow field is related to the force field by the linear relation

$$J_i^0 = \sigma_{ij}^0 E_j^0. \tag{5.50}$$

The reference force field E_i^0 is also necessary as a boundary condition for the computation. If the polarization field was known, the problem could be solved using the periodic Green's function $\Gamma_{ij}(x)$ by

$$E_i(x) = -\int_{\mathbb{R}^3} \Gamma_{ij}(x')P_j(x - x')dx^3 + E_i^0 = -(\Gamma_{ij} * P_j)(x) + E_i^0. \tag{5.51}$$

Yet as the material is heterogeneous, the spatial variation of the conductivity $\sigma_{ij}(x)$ has to be incorporated, i.e. the polarization field has to be computed. The solution of this auxiliary problem is the main computational challenge in the computation. By using the constitutive equations we find

$$P_i(x) = (\sigma_{ij}(x) - \sigma_{ij}^0)E_j(x). \tag{5.52}$$

Thus, the following equations hold for the electric field

$$E_i(x) - [\Gamma_{ij} * ((\sigma_{jk}^0 - \sigma_{jk})E_k)](x) = E_i(x) - [\Gamma_{ij} * (\delta\sigma_{jk}E_k)](x) = E_0. \tag{5.53}$$

This equation can be inverted using a von Neumann series of the form

$$E(x) = E_0 + (\Gamma_{ij} * [\delta\sigma_{jk}E_k^0])(x) + [\Gamma_{ij} * (\delta\sigma_{jk}[\Gamma_{kl} * (\delta\sigma_{lm}E_m^0)])](x) + \ldots = \sum_{j=0}^{\infty}(\Gamma\delta\sigma)^j E_0(x). \tag{5.54}$$

This series can be shown to converge under quite general conditions. To approximate this infinite expansion, it is truncated after a sufficient number of terms

$$E^m(x) = \sum_{j=0}^{m}(\Gamma\delta\sigma)^j E_0(x). \tag{5.55}$$

The terms of the expansion can be computed by an iterative relation

$$E_i^m(x) = E_i^{m-1}(x) - [\Gamma_{ij} * (\sigma_{jk}E_k^{m-1})](x). \tag{5.56}$$

Also, since the recursive relation is a serial convolution, the convolutions are computed in Fourier-space to speed up the computation. The Green's function is given in Fourier-space, by

$$\Gamma_{ij}(k) = \frac{k_i k_j}{k_n \sigma_{nm}^0 k_m}. \tag{5.57}$$

Here k_i is the wave number of the corresponding component and σ_0 is the homogeneous reference field. Then, the resulting algorithm for the computation of the polarization field is given in pseudo-code in Algorithm 2.

Data: $E_0(x) = E_0, J_0(x) = \sigma(x)E_0(x)$
Result: Approximate flow field $\vec{J}^m$
$m \leftarrow 1;$
$\hat{J}^{m-1}(k) \leftarrow \text{FFT}[J_0](k);$
while $\|k \cdot J^{m-1}\| \leq \epsilon$ **do**
$\quad$ set average field: ;
$\quad \hat{E}(0) = E_0;$
$\quad$ compute convolution: ;
$\quad \forall k \neq 0 : \quad \hat{E}^m(k) \leftarrow \hat{E}^{m-1}(k) - \hat{\Gamma}(k)\hat{J}^{m-1}(k);$
$\quad E^m(x) \leftarrow \text{FFT}^{-1}[\hat{E}^m](x);$
$\quad J^m(x) = \sigma(x)E^m(x);$
$\quad m \leftarrow m + 1 ;$
end
Algorithm 2: FFT-algorithm to solve the conduction problem by iterated convolutions.

The algorithm terminates when the flow field is divergence free up to a certain numerical error ϵ, i.e.

$$\partial_i J_i \leq \epsilon. \tag{5.58}$$

5.3   Simulation of the Li-Ion Battery Electrode

To simulate the influence of the nanoporous additive on the charging behavior, a half-cell setup with the electrode opposite to a lithium foil, as shown in Figure 5.5 has been simulated. The lithium foil and the electrode are separated by electrolyte, where the lithium ions diffuse to the electrode when the battery is charged. During charging, the lithium ions enter the solid carbon phase adding to the total charge of the electrode. This induces a current into the electrode, collected by the charge collector.

The electrode itself was modeled at two different scales. On the macro-scale, the active particles are given by the segmented CT image taken at ESRF (see Figure 5.6 for a volume rendering). The transparent phase in the image is filled with electrolyte, while the solid phase is formed by the active particles. Furthermore, the model assumes a distribution of the additive (yellow phase in Figure 5.5) in the electrode (see Section
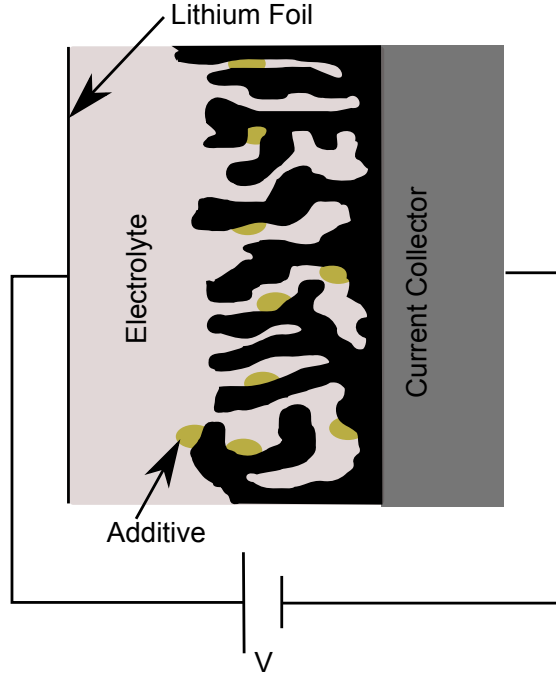
FIGURE 5.5: Macroscopic model of the Lithium-Ion battery electrode.

5.3.2.1), which enters as a third phase in the computational domain. For the simulation it is assumed that the additive has an effective diffusivity, which is computed on the microscale. To this end, the nanoporous additive segmented in Section 3.5.1 has been modeled as an effective medium. Since the nanoporous additive cannot be detected with micro-Computed Tomography, its distribution was modeled using morphology. For the validation of the stochastic model discussed in Section 4.6.1, the transport properties of the modeled structure have been computed as well.

5.3.1 Microscopic Modeling

First, the effective diffusion resistance of the additive was computed on the microscale. To this end, the effective diffusivity of the pore space was computed using the structural information from the segmented FIB-SEM images, described in Section 3.5.1. A slice view of the segmentation is shown in Figure 5.7.

It is assumed that the conductivity of the solid phase vanishes and the conductivity of the pore space is one. In this setup, an effective dimensionless resistance $\frac{D_{eff}}{D}$ is computed. Since the problem is linear, the effective conductivity can be multiplied by the bulk conductivity of the electrolyte to get the physical conductivity of the nanostructure.

To estimate the diffusion resistance, some bounds have been computed first. As the structure in the dataset is not isotropic, the Hashin-Shtrikman bounds cannot be applied.
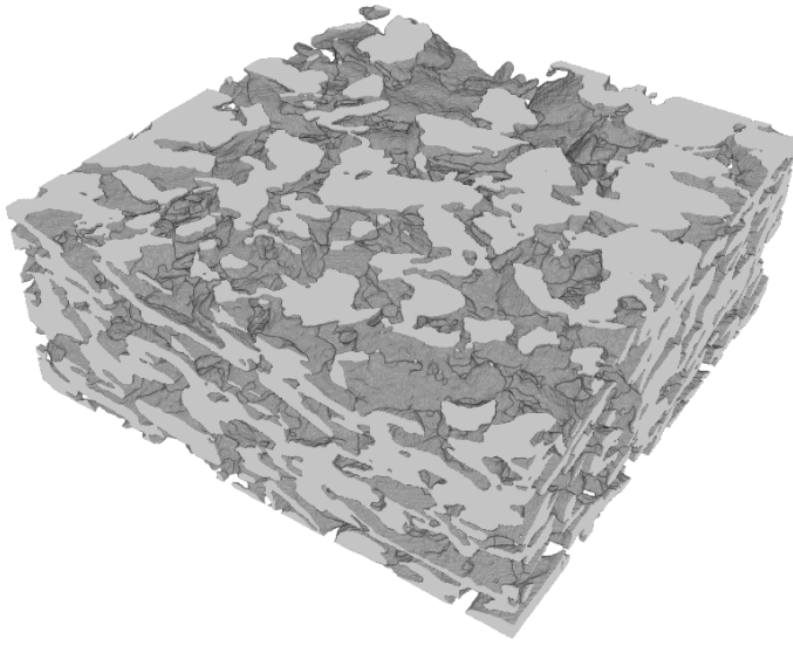
FIGURE 5.6: Volume rendering of the segmented porous electrode without additive.

FIGURE 5.7: Segmented FIB-SEM image of the nanoporous additive.

Yet, the Wiener bounds derived from variational considerations are still valid. Since the volume fractions for the model and the segmentation are the same, also their Wiener bounds are identical. Since the diffusivity for the solid phase is zero, the lower bound vanishes. Also, since the Wiener bounds are blind to any anisotropy of the structure and there is only one phase, the upper Wiener bound is simply the volume fraction,

$$\frac{D_{eff}}{D} = 0.41, \tag{5.59}$$

To get a better estimate, the effective diffusivity has been computed with the FFT method. To estimate the effective diffusivity tensor, the flow field has been computed

for an average force with a magnitude of unity in x-,y-, and z-direction. A slice view of the computed flow field in x-direction is shown in Figure 5.8.
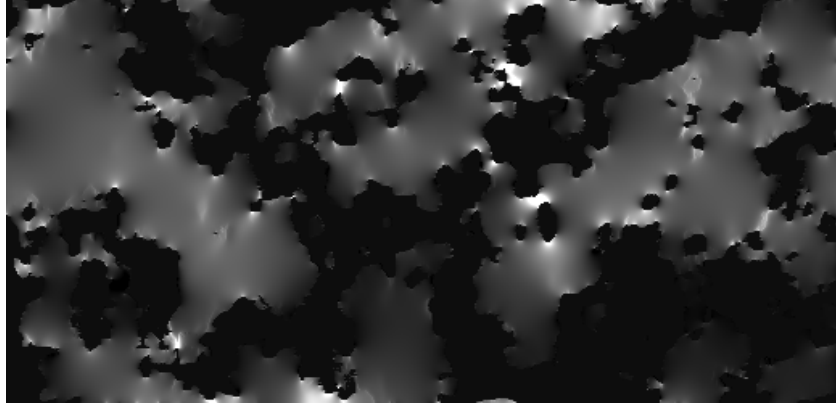
FIGURE 5.8: Slice view of the x-component of the flow field computed on the reconstructed nanostructure of the additive.

The resulting effective conductivity factors are shown in Table 5.1. The effective diffusivity tensor is anisotropic, since the value in x-direction is significantly smaller than the values in the other directions. All values are significantly smaller than the upper Wiener bound.

direction	$\frac{D_{eff}}{D}$
x	0.25
y	0.31
z	0.35
average	0.3

TABLE 5.1: Effective diffusivity factors computed for the nanoporous additive based on the segmentation.

To test the modeling of the nanoporous additive, the effective diffusivity has been computed on a model realization as well. The same boundary and material properties have been assumed, as in the previous computation. Since the volume fraction of the model is the same as for the segmentation, the Wiener bound is the same as well. The values for the effective diffusivity in Table 5.2 have been computed, with the FFT-method. As can be seen, the diffusivity tensor is isotropic, within statistical fluctuations. This comes of course from the model being isotropic by construction. Also the diffusivities are higher than for the segmentation. It is assumed that this is due to the lack of larger particle sizes in the model (see Figure 4.16), which represent significant obstacles to diffusive flow.

Using the effective diffusivities, the influence of the nanoporous additive on the charging behavior can be computed on the macro-scale.

direction	$\frac{D_{eff}}{D}$
x	0.38
y	0.37
z	0.37
average	0.37

TABLE 5.2: Effective diffusivity factors computed for the nanoporous additive based on the segmentation.

5.3.2   Macroscopic Modeling and Simulation

5.3.2.1   Modeling of the Additive

To simulate the influence of the additive on the charging behavior, the distribution of the additive at the macro-scale must be incorporated in the computational domain on the macro-scale. Since the additive is invisible in the micro-CT data, the distribution has to be modeled. To this end, some assumptions were made based on the production process. Besides the overall approximate volume fraction of the additive in the electrode, it is known that the additive preferably accumulates at narrow gaps in the pore structure. Consequently, as a first approximation narrow gaps have been selected in the pore space by a morphological closing. The closing has been applied to the segmented micro-CT image and then volume added by the closing has been selected as additive. The size of the structuring element of the closing has been chosen, such that the added volume fraction is equal to the volume fraction expected through the production process (about 6 %). Thus, the expression for the distribution of the additive amounts to a set

$$F_{add} = \Phi(l)(F_{solid}) - F_{solid}, \tag{5.60}$$

where F_{solid} is the set representing the solid phase (active particles) on the macro-scale. Since the additive is modeled in the pore space, the volume fraction of the pore space decreases, while the volume fraction of the solid phase remains constant. Thus, the set representing the solid phase does not change and the pore space is modeled by

$$F_{pore} = F_{solid}^{C} - F_{add}. \tag{5.61}$$

The final distribution of the additive is shown in Figure 5.9 in light blue, while the solid carbon phase is shown in the darker shade.
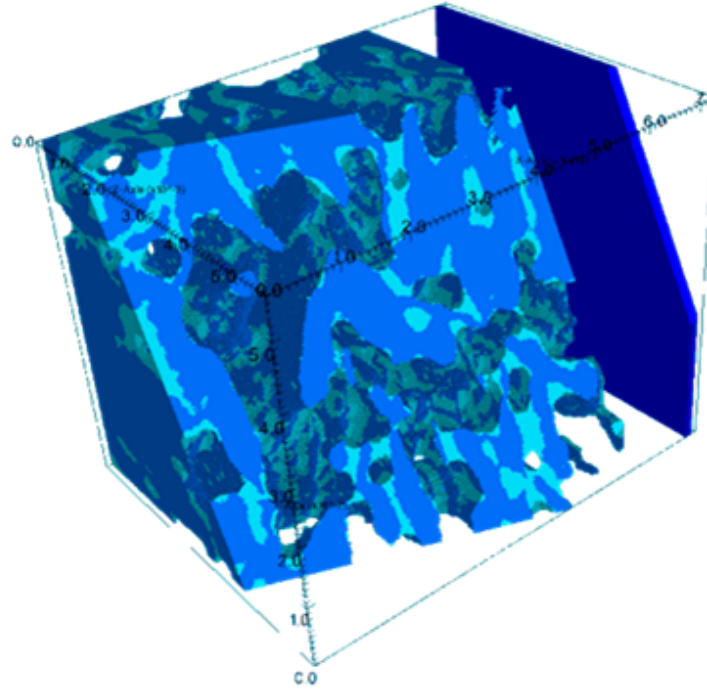
FIGURE 5.9: Distribution of the additive in the micro-CT data (from Wieser et al. [2014]).

5.3.2.2 Charging Simulation

After modeling the distribution of the additive, the discharging of the half-cell has been simulated with and without the additive in the domain. The result of this simulation has been taken from Wieser et al. [2014]. Three phases are considered in the simulation, the solid electrode, the pore space filled with electrolyte and the additive. In each of the phases, the electric potential and the Lithium-Ion concentration are modeled by partial differential equations. The full set of equations is given in Latz and Zausch [2011].

To compare the influence at different loads, two different discharge rates have been simulated. Two simulations were made for a 1 C load, which means that the cell would be completely discharged in one hour. Two further simulations were made at higher load of 5 C, i.e. five discharges per hour. For each discharge rate, one simulation was made with and one without additive. This results in four discharge curves, showing the cell voltage against the discharge current. The results are shown in Figure 5.10.

As can be seen the 1 C curves are almost completely identical, meaning that the additive has little or no influence on the discharge at 1 C load. The 5 C curves, however, show a deviation between the simulation with and without additive. As can be seen, the cell voltage is lower with the additive as would be expected since the additive represents a
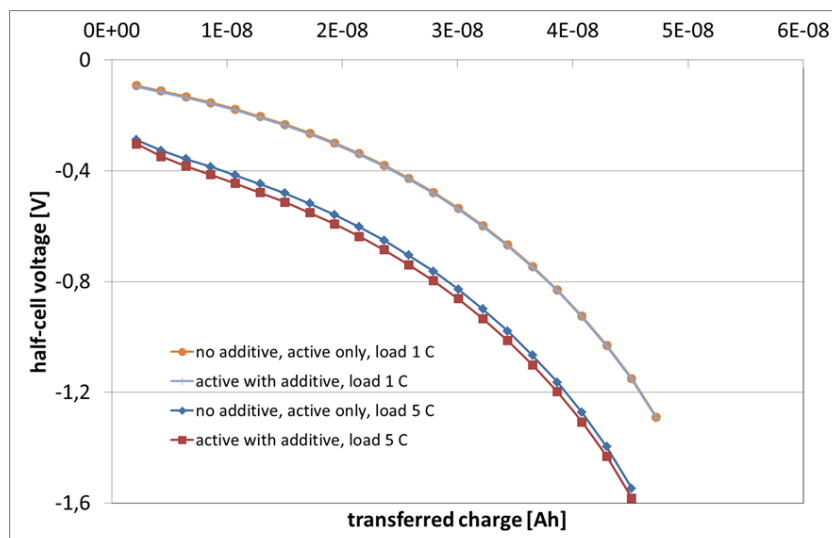
FIGURE 5.10: Simulated discharges of the half-cell, for four setups: 1 C, without additive; 1 C with additive; 5 C without additive; 5 C with additive (from Wieser et al. [2014])

diffusion resistance to the Lithium-Ions. This becomes clearer in Figure 5.11, where the Li-ion flux at the 5 C discharge is shown for the geometry with and without additive. It can be seen, that even though the overall current is the same the lithium-ion flow has a different distribution with the additive considered in the simulation.
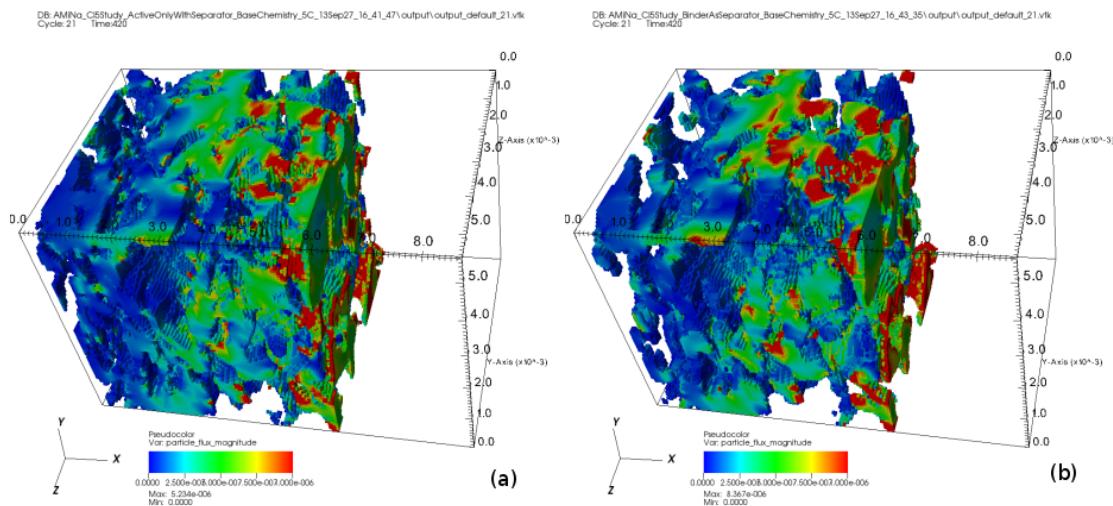
FIGURE 5.11: Lithium Ion flow simulated at 5 C load without (a) and with additive (b) (from Wieser et al. [2014]).

5.4   Simulation of Nanoporous EDLC Electrodes

The second application case in this thesis is the modeling of the nanoporous electrodes for electric double layer capacitors (EDLCs). In this section, the electrochemical behavior of

the electrode is simulated. As stated in the introduction, the electrodes have a two-scale pore space, consisting of micropores with a diameter $d < 2$ nm and mesopores with a diameter of $d \approx 100$ nm, which were resolved with the FIB-SEM nanotomography and reconstructed in Section 3.5.2. As for the Li-ion battery electrode, a multi-scale model is employed for the computations, where the mesopores represent the *micro-scale* model. The computational domain on the micro-scale are the segmentations, which have been introduced in Section 3.5.2 and the stochastic models of the structure, presented in Section 4.6.2.

On the macro-scale, the electrochemical behavior is modeled, using phenomenological models, such as equivalent circuits and macrohomogeneous models. Beside the equivalent circuit, a macrohomogeneous model proposed in Paasch et al. [1993] has been chosen to model the macroscopic behavior. Also, the derivation of macroscopic properties using the reconstructed microstructure is investigated by computing effective capacitances and resistivities, using the FFT-method. Remaining parameters are fixed by fitting to experimental data.

The materials used in this thesis, have been investigated in Balach et al. [2012] and Balach et al. [2013]. The experimental data has kindly been provided by Juan Balach (Balach [2013]). For the experimental characterization, electric impedance spectroscopy measurements have been made on monolithic S12 (see Figure 5.12). Furthermore, the capacitances have been measured for the inks containing S12 and S14. The measured capacitance values are given in Equations 5.62

$$C_{V,S12} = \quad 2.75 \frac{F}{cm^3}, \tag{5.62}$$

$$C_{V,S14} = \quad 1.98 \frac{F}{cm^3}. \tag{5.63}$$

5.4.1 Electric Impedance Spectroscopy

In order to characterize the electrodes physically, electric impedance spectroscopy (EIS) measurements have been performed on a monolithic sample of S12. EIS is used to characterize electrochemical materials by applying a sinusoidal voltage to a cell containing the electrode and measuring the impedance of the material. A detailed treatment of the method can be found in Barsoukov and Macdonald [2005]. For the EIS measurements of the materials considered in this thesis, a small sinusoidal voltage is applied to the half-cell depicted in Figure 5.18, i.e. $V(t) = V_0 \sin(\omega t)$. In complex notation the signal is written as $V(t) = V_0 \exp(i2\pi\omega t)$. Then, the material response was measured as the current going through the cell. The current is also assumed to be sinusoidal, yet with a different

amplitude and a phase shift relative to the voltage. Thus $I(t) = I_0 \exp(i2\pi\omega(t + \phi))$. The impedance at a given frequency is then given by

$$I(t) = Z(\omega)V(t) \tag{5.64}$$

where Z is a complex number. It is assumed that the material response is linear due to the small amplitude of the signal. To measure the impedance spectrum, the frequency ω is varied and for each frequency the impedance is measured. This leads to the impedance spectrum $Z(\omega)$.

A Nyquist-plot of the impedance spectrum measured on the monolithic S12 is shown in Figure 5.12.
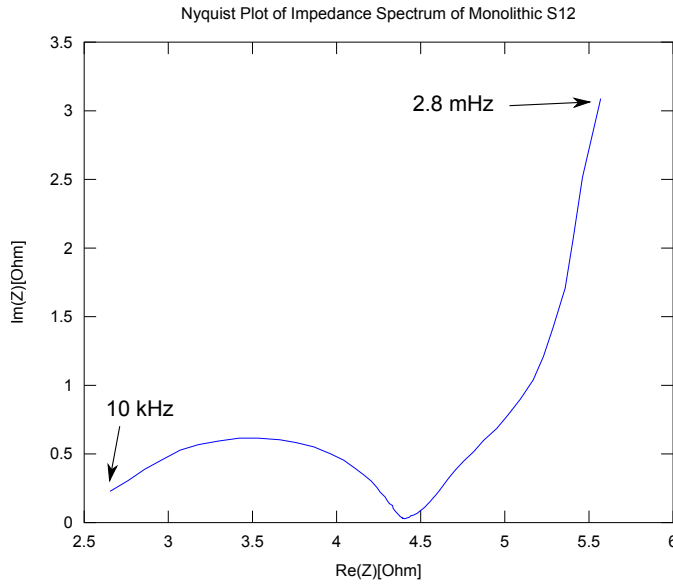
FIGURE 5.12: Impedance spectrum of monolithic S12.

The plot shows the real and imaginary part of the impedances for a given frequency range. In this measurement, the frequency has been varied between 10 kHz down to 2.8 mHz. The Nyquist-plot shows typical features for this class of materials. At the very high-frequency range, the curve has a slope of $45°$. Then, at high frequencies, a kind of semicircle is observed ending on the real line. The semicircle might be depressed as in this plot. At low frequencies, again a straight line arises, again with a slope of around $45°$ ending in a capacitive behavior with a straight vertical line.

5.4.2 The Modeling by Equivalent Circuits

A lot of work has been done on modeling the impedance spectra of porous electrodes. Mostly, authors work with simple equivalent circuits, which are able to capture the behavior quite well, but do not include any information on the microstructure. To this

end, circuit elements are combined to resemble the chemical processes and electrical fields on the electrode. For an overview see e.g. Barsoukov and Macdonald [2005]. A possible circuit for the modeling of a porous electrode is depicted in Figure 5.13.
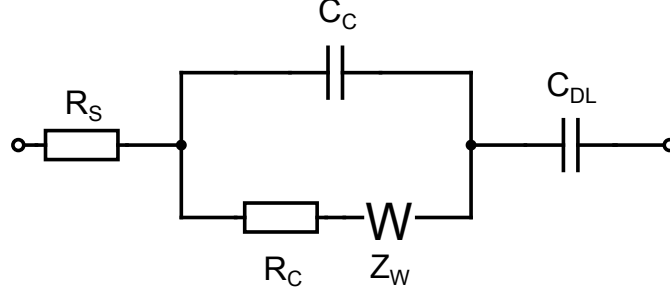
FIGURE 5.13: Randles circuit to model a porous electrode.

The circuit is a variation of a Randles circuit, where the electrochemical cell is modeled as a parallel circuit, including a branch with a capacitance C_C, representing the electro-chemical double layer, and a branch with a charge transfer resistance R_C and a Warburg impedance Z_W, modeling the diffusion of the charge through the porous electrode. A resistance R_S represents the bulk electrolyte between the separator and the electrode as seen in Figure 5.18. For the data at hand, a modification has been made, where the Randles circuit is put in series with an additional capacitance C_{DL}. It is assumed that a double layer forms on the surface of the mesopores, represented by C_C as well as in the micropore surface represented by C_{DL}. The capacitance C_{DL} represents the capacitance of the double layer forming in the micropores. The impedance of the circuit is given by

$$Z(\omega) = R_S + \frac{1}{i\omega C_C + \frac{1}{R_C + Z_W}} + \frac{1}{i\omega C_{DL}}, \tag{5.65}$$

where Z_W is the Warburg impedance

$$Z_W(\omega) = \frac{W}{\sqrt{i\omega}}. \tag{5.66}$$

For the characterization of the monolithic S12, the impedance in Equation 5.65 has been fitted to the spectrum in Figure 5.12. An optimal fit has been reached for the set of parameters in Table 5.3. The fitted spectrum together with the data is depicted in Figure 5.14.

As can be seen, the simulated impedance spectrum of the equivalent circuit has the same structural features as the measured spectrum. For high frequencies, the Nyquist-plot shows a semicircle. Then, an almost linear rise in the imaginary part follows with a slope of 45° which then evolves into a capacitive behavior, where the imaginary part rises proportional to $\frac{1}{\omega}$. Yet, it can also be seen that the semicircle in the measurement

parameter	best fit
R_S	$2.8146 \ \Omega$
R_C	$1.5398 \ \Omega$
C_C	$7.1766 * 10^{-6} \ \mathrm{F}$
σ_W	$0.25202 \ \Omega s^{-\frac{1}{2}}$
C_{Dl}	$41.532 \ \mathrm{F}$

TABLE 5.3: Best fit parameters for the circuit in Figure 5.13.
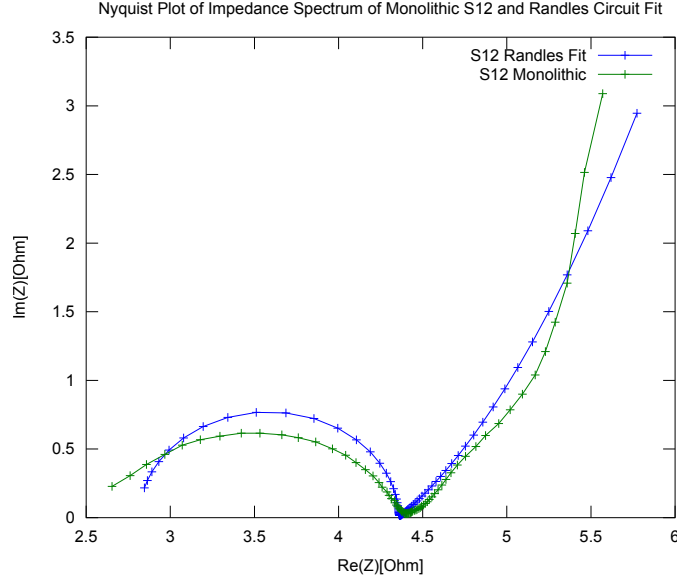
FIGURE 5.14: Fitted impedance spectrum of the model in Equation 5.65, to the data
in Figure 5.12.

is depressed, while the semicircle in the model is round. Also, the linear part of the
spectrum is much more pronounced in the measurement. To remedy these inaccuracies,
a more advanced model is needed. Also, neither the electrode geometry, nor the porous
structure has a representation in the circuit. Hence, a model of the electrode, which
takes its structure into account is needed.

5.4.3   Microscopic Modeling

To remedy the shortcoming of equivalent circuits and to relate the microsctructure to
the electrical behavior of the nanoporous electrode, a multi-scale simulation approach
is used with two different length scales. First, the effective conductivities and permit-
tivities are computed on the two mirostructures S12 and S14. These are then used for
macrohomogeneous models in Section 5.4.4 to model impedance spectra of the electrode
materials.

5.4.3.1 Effective Conductivities of EDLC Electrodes

First, the conductivities of both the electrolyte in the pore space and the carbon electrode have been computed, using the FFT-method. Therefore, the bulk conductivities have been set for the corresponding phase in the segmentations and the other phase has been set non-conducting, respectively. This yields an effective conductivity for each of the phases.

The computed conductivities for the electrolyte phase of specimen S12 are shown in Table 5.4. For the bulk conductivity a value of $\sigma_{el} = 0.8\frac{S}{cm}$ has been assumed, as reported in Darling [1964]. Obviously the Wiener upper bound σ_W^u strongly overestimates the effective conductivity, computed with the FFT-method. Also, the strong anisotropy is not reflected in the bound. It is assumed, that the anisotropy is mainly due to the anisotropic voxel size and errors induced by it. For the macroscopic simulation, the conductivity has been averaged over all directions, giving a mean conductivity of $\sigma_{el}^{eff} = 0.081\frac{S}{cm}$.

direction	$\sigma_W^u \left[\frac{S}{cm}\right]$	$\frac{\sigma_{eff}}{\sigma_{el}}$	$\sigma_{eff} \left[\frac{S}{cm}\right]$
x	-	0.073	0.058
y	-	0.071	0.056
z	-	0.160	0.128
average	0.25	0.101	0.081

TABLE 5.4: Effective conductivities for the electrode S12 computed for the pore space filled with electrolyte.

The conductivity of the solid phase has been computed using a bulk conductivity of $\sigma_{bulk}^p = 0.12\frac{S}{cm}$ as reported in Bruno et al. [2010]. The computed values are given in Table 5.5. As can be seen, the anisotropy is not as strong as in the electrolyte phase. This comes mainly from the higher volume fraction, giving the anisotropy of the pores less weight. Also, the higher volume fraction compensates for the lower bulk conductivity, yielding similar values as for S12. Yet again, the Wiener bounds vastly overestimate the calculated conductivity.

direction	$\sigma_W^u \left[\frac{S}{cm}\right]$	$\frac{\sigma_{eff}}{\sigma_p}$	$\sigma_{eff} \left[\frac{S}{cm}\right]$
x	-	0.412	0.049
y	-	0.423	0.051
z	-	0.541	0.065
average	0.082	0.459	0.055

TABLE 5.5: Effective conductivities for the electrode S12 computed for the solid phase.

Furthermore, the conductivities for the microstructure of S14 have been computed. In the computations, the same bulk parameters have been used as for the microstructure

S12. The resulting effective conductivities computed for the electrolyte phase of specimen S14 are shown in Table 5.6.

direction	$\sigma_W^u \left[\frac{S}{cm}\right]$	$\frac{\sigma_{eff}}{\sigma_{el}}$	$\sigma_{eff} \left[\frac{S}{cm}\right]$
x	-	0.234	0.187
y	-	0.192	0.154
z	-	0.201	0.160
average	0.352	0.209	0.167

TABLE 5.6: Effective conductivities for the electrode S14 computed for the pore space filled with electrolyte.

Again, the Wiener bound overestimates the conductivity. Yet, due to the larger structure size, the anisotropy of the effective conductivity is much smaller than for S12. This is due to the fact that the larger structure can be better resolved in z-direction, reducing the error. The corresponding values for the solid phase are shown in Table 5.7. Again the anisotropy is much smaller than for the corresponding values for S12. Also, the difference between the relative conductivity factors of the pore and the solid phase is much smaller than for S12, as can be expected from the volume fraction of 56% rather than 68% for S12.

direction	$\sigma_W^u \left[\frac{S}{cm}\right]$	$\frac{\sigma_{eff}}{\sigma_p}$	$\sigma_{eff} \left[\frac{S}{cm}\right]$
x	-	0.350	0.042
y	-	0.310	0.037
z	-	0.319	0.038
average	0.067	0.326	0.039

TABLE 5.7: Effective conductivities for the electrode S14 computed for the solid phase.

5.4.3.2 Effective Permittivities of EDLC Electrodes

The permittivity is directly related to the capacitance of the electrode. Since the linear dependence of the permittivity is the same as for the conductivity of the solid phase, the effective permittivity factors are the same as for the conductivity computed in the last section, i.e.

$$\frac{\varepsilon_{eff}}{\varepsilon} = \frac{\sigma_{eff}}{\sigma}. \tag{5.67}$$

The effective permittivity of the bulk material is not known, hence it must be computed from the measurements of the two samples. Using the average effective permittivity factors in Tables 5.5 and Table 5.7, the effective permittivities are

$$C_{V,S12} = \quad C_{V,S12,bulk} * 0.459, \tag{5.68}$$

$$C_{V,S14} = \quad C_{V,S14,bulk} * 0.32. \tag{5.69}$$

The effective capacitances have been measured experimentally by electric impedance spectroscopy. The capacitance values are given by

$$C_{V,S12} = \quad 2.75 \; \frac{F}{cm^3}, \tag{5.70}$$

$$C_{V,S14} = \quad 1.98 \; \frac{F}{cm^3}. \tag{5.71}$$

This yields bulk capacitances of

$$C_{V,S12,bulk} = \quad 5.99 \; \frac{F}{g}, \tag{5.72}$$

$$C_{V,S14,bulk} = \quad 6.19 \; \frac{F}{g}. \tag{5.73}$$

The fact that the bulk capacitances are very close, indicates that the double layer forming at the mesopores does not contribute strongly to the overall capacitance of the EDLC electrode. To further explore this point, the effective permittivities have been computed including a double layer forming on the mesopores. The double layer has been approximated as a non-conducting imperfect boundary between the pore and the solid phase, as described in Section 5.1.1. In the computation, the imperfect interface has been approximated by a third phase, forming a layer between the pore and the solid phase, having a small thickness d. Then, the limit of a vanishingly thin interface has been approximated, by reducing the thickness and computing the capacitance for each thickness (taking the limit $d \to 0$ in Figure 5.3 on Page 130). Then the capacitance was determined by linear regression. The layered phase has been modeled by using a Euclidean distance transform and a thresholding on the segmentations. Thus, the layered phase is given by

$$F_{DL} = \mathrm{Th}_{0,d}(F_{Seg}) - F_{Seg}. \tag{5.74}$$

The solid phase F_{Seg} remains as it is and the pore space is reduced by the double layer,

$$F_{Pore} = F_{Seg}^{C} - F_{DL}. \tag{5.75}$$
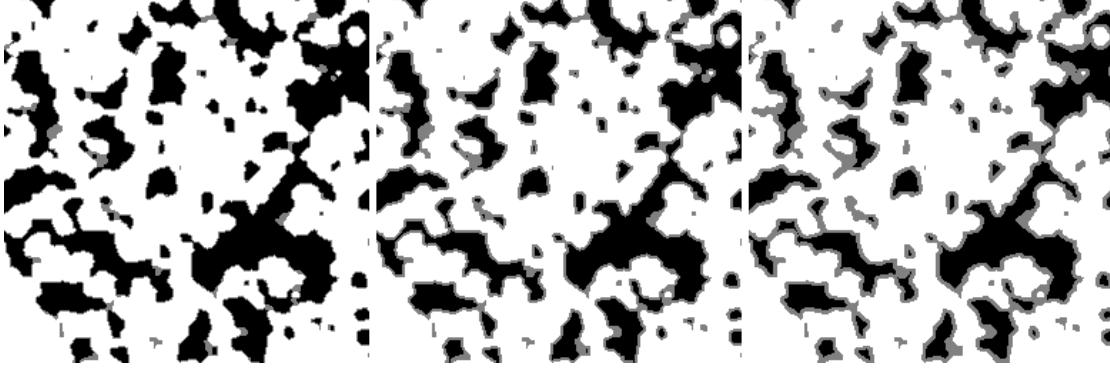
FIGURE 5.15: Three different double layer thicknesses $d = 1$ Pixel (left), $d = 2$ Pixel (middle) and $d = 3$ Pixel (right).

For both samples, the capacitances have been computed including the double layer modeled by imperfect boundary conditions. Figure 5.16 shows the computed capacitances given for different values of the double layer areal capacitance C_A in $\frac{\mu F}{cm^2}$. The bulk capacitance is assumed to be $6.1 \frac{F}{cm^3}$, thus the effective capacitance is sightly underestimated for S12 and overestimated for S14. As can be seen, the volumetric capacitance rises much faster for the material S12, due to it's higher surface area.
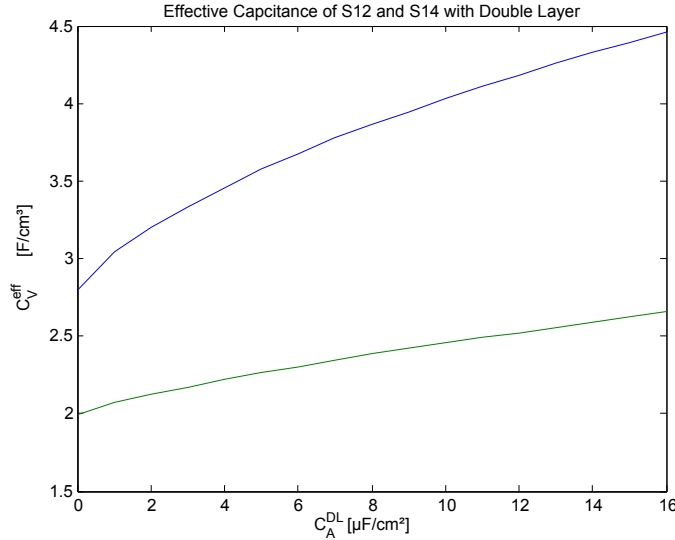
FIGURE 5.16: Effective volumetric capacitance of S12 and S14 for different double layer areal capacitances C_A.

To check which double layer capacitance is consistent with the data, the ratio of the effective volumetric capacitance of both samples was computed for different areal capacitances. The resulting curve is shown in Figure 5.17. As can be seen, the measured values are only consistent with the computations for very low double layer capacitances, indicating that the bulk of the total capacitance is given by the micropores.
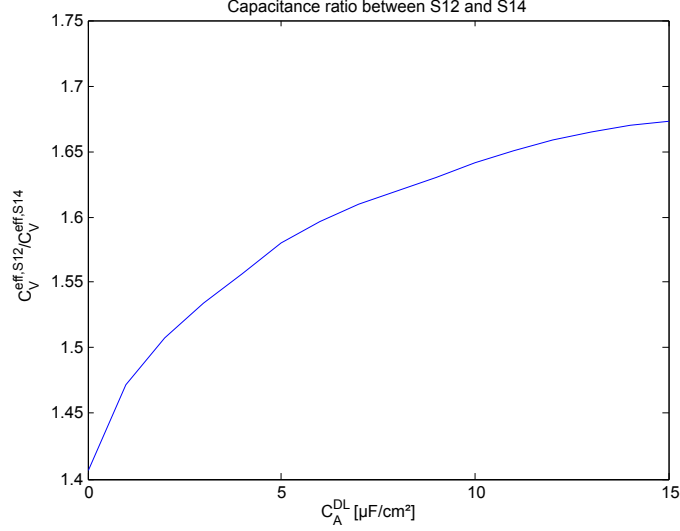
FIGURE 5.17: Ratio of effective capacitances of S12 and S14 for different double layer areal capacitances.

5.4.4 The Macrohomogeneous Model

After the effective conductivities and permeabilities have been computed in the previous section, a macrohomogeneous model is used to model the electrode setup. Here, the electrode is modeled by effective media, which have the conductivities and permittivities computed on the microstructure. Hence, the macroscopic electrode behavior can be related to the microstructure.

Among the first attempts to model the electrode directly is the classical model by Robert de Levie, published in de Levie [1963]. The model falls into the class of transmission line models, where the porous electrode is represented by an equivalent circuit with distributed elements or equivalently a one-dimensional partial differential equation (PDE). The model is a macrohomogeneous model, meaning that it relates macroscopic quantities in the electrode. The model used in this work is an extension of the model in de Levie [1963] developed by Paasch et al. and presented in Paasch et al. [1993] and Roßberg et al. [1998].

The macroscopic setup is shown in Figure 5.18. It is shown that the electrode is immersed into the electrolyte with the current collector at $x = 0$ and the bulk electrolyte at $x = d$. The model assumptions are that there are two electric fields in the electrode, one in the electrolyte and one in the solid phase of the electrode. Both fields are governed by Poisson equations, which are coupled by a capacitance representing the double layer forming at the surface of the electrode and a resistance representing charge transfer reactions, where charge can pass through the double layer. This leads to the following one-dimensional PDEs:
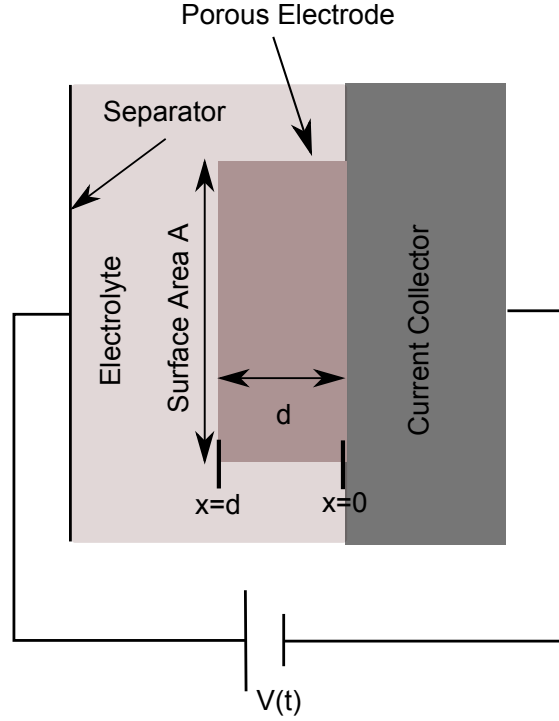
FIGURE 5.18: Macroscopic model of the porous EDLC electrode.

$$\frac{A}{\rho_e}\frac{d\Phi_e(x,t)}{dx^2} = -(i\omega C_{DL}AS_V + \tfrac{1}{\rho_{CT}})(\Phi_e(x,t) - \Phi_p(x,t)), \qquad (5.76)$$

$$\frac{A}{\rho_p}\frac{d\Phi_p(x,t)}{dx^2} = (i\omega C_{DL}AS_V + \tfrac{1}{\rho_{CT}})(\Phi_e(x,t) - \Phi_p(x,t)). \qquad (5.77)$$

Here A is the electrode area and d is the electrode thickness, C_{DL} is the areal capacitance of the double layer and S_V is the surface area per volume of the pore space. The resistance ρ_{CT} is the charge transfer resistance per unit length of the electrode. ρ_e and ρ_p are the ohmic resistances of the electrode solid phase and the electrolyte, respectively. A representation of the model by an electric circuit is shown in Figure 5.19, where the resistances and the capacitances are distributed elements, representing a differential resistance or capacitance along the x-axis.
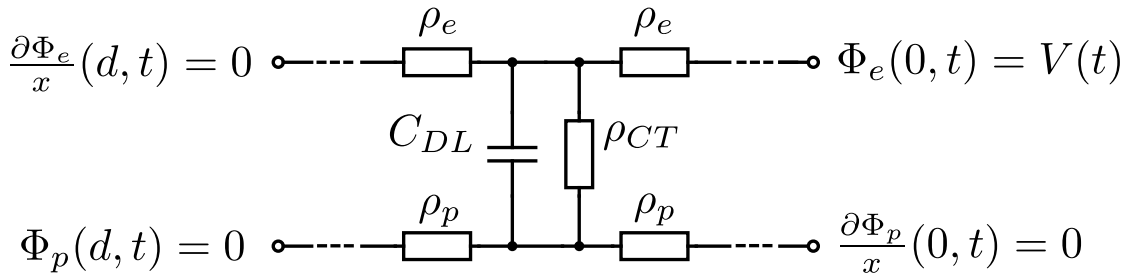
FIGURE 5.19: Equivalent circuit of the Paasch model

To solve the model, the appropriate boundary conditions for the two fields at the electrode surfaces towards the current collector and the separator have to be fixed. These boundary conditions are given by the currents and voltages at the separator and the current collector. For the electrical impedance spectroscopy, the potential is fixed at the separator or by a counter electrode. On the current collector side, the potential may vary, but no current can flow. Thus, the boundary conditions for the electrolyte potential are given by

$$\Phi_p(x = d, t) \quad = 0, \tag{5.78}$$

$$\frac{\partial \Phi_p}{\partial x}(x = 0, t) \quad = 0. \tag{5.79}$$

Analogously, for the electrode potential, the current vanishes at the separator and the potential at the current collector is given by an external signal. For EIS measurements that is a sinusoidal wave $V(t) = \sin(\omega t + \phi)$

$$\Phi_e(x = 0, t) = \quad V(t), \tag{5.80}$$

$$\frac{\partial \Phi_e}{\partial x}(x = d, t) = \quad 0. \tag{5.81}$$

The initial conditions are given by the mean potential, set to zero, and the periodic boundary conditions in time

$$\langle \Phi_p \rangle = 0, \tag{5.82}$$

$$\langle \Phi_e \rangle = 0, \tag{5.83}$$

$$\Phi_p(x, t) = \quad \Phi_p(x, t + \omega * 2\pi), \tag{5.84}$$

$$\Phi_e(x, t) = \quad \Phi_e(x, t + \omega * 2\pi), \tag{5.85}$$

where the averages $\langle \Phi_i \rangle$ are taken with respect to time. To calculate the impedance of the element, the model can be solved analytically. Paasch et al. [1993] give an expression for the impedance depending on the frequency of the sinusoidal signal ω

$$Z(\omega) = \frac{1}{A} \left[\frac{\rho_e^2 + \rho_p^2}{\rho_e + \rho_p} \frac{\coth(d\beta)}{\beta} + 2 \frac{\rho_e \rho_p}{\rho_e + \rho_p} \frac{1}{\beta \sinh(d\beta)} + d \frac{\rho_e \rho_p}{\rho_e + \rho_p} \right] \tag{5.86}$$

with

$$\beta = \frac{1}{d} \left(\frac{\frac{\omega_0}{\sqrt{3}} + i\omega}{\omega_1} \right)^{\frac{1}{2}}, \quad \omega_0 = \frac{1}{\rho_{CT} A S_V C_{DL}}, \quad \omega_1 = \frac{1}{d^2 C S_V (\rho_e + \rho_p)}. \tag{5.87}$$

This model can be fitted to the impedance spectra measured by EIS. Yet, to make predictions based on microstructures, some parameters of the model have to be computed on the microscale. This includes the resistances ρ_e and ρ_p, and the specific capacitance $C = S_V C_{Dl}$, which have been computed in Section 5.4.3.

The described model is designated "Paasch0" and has been fitted to the impedance spectrum of the monolithic S12. For the fitting, some parameters have been chosen in advance. The electrode area is known from the experimental setup. Also, the resistances ρ_e and ρ_p can be computed using the observed microstructures from FIB-SEM nanotomography. For the modeling, we have taken the resistance values computed in Section 5.4.3. The best fit for the remaining parameters, d, ω_0 and C, are given in Table 5.8. For comparison, the simulated spectrum and the measured data are shown in Figure 5.20.

parameter	best fit
ω_0	$1.028 * 10^5 \ \frac{\text{rad}}{s}$
C	$4.91 * 10^{-5} \ \frac{F}{cm^3}$
A	$0.96 \ cm^2$
d	0.314 cm
ρ_e	$18.0 \ \Omega$cm
ρ_p	$12.5 \ \Omega$cm

TABLE 5.8: Best fit parameters for the transmission line model "Paasch0".
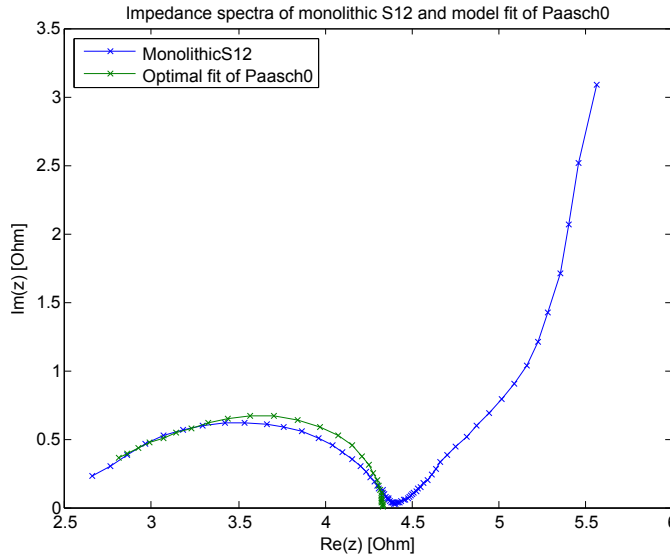
FIGURE 5.20: Measured impedance spectrum of monolithic S12 and best fit to model "Paasch0".

The spectrum of the model shows that the high-frequency part is reproduced very well, yet for the low-frequency part, the model tends to the real line while the measured data shows the low-frequency features already discussed. This is due to the charge transfer resistance, which is in parallel with the double layer capacitance. As the charge transfer

resistance is ohmic and independent of frequency, while the double layer capacitance is blocking in the limit $\omega \to 0$, the current flows through the Ohmic resistance in this limit, leading to a real impedance.

The capacitance of $C = 4.91 * 10^{-5} \frac{F}{cm^3}$ is a volumetric capacitance appearing in the high-frequency part of the spectrum and is much lower than the overall measured capacitance for S12 of $C_V^{S12} = 2.75 \frac{F}{cm^3}$. This can be explained by the double layer forming at the surface having a very low capacitance, while the micropores provide the bulk of the total resistance of the material, as indicated in Section 5.4.3.

The charge transfer resistance ρ_{CT} can be calculated with the parameter ω_0, which is reasonable, since no a priori information is available

$$\rho_{CT} = \sqrt{3} \frac{1}{\omega_0 C} = 0.34 \; \Omega \; \text{cm}. \tag{5.88}$$

The charge transfer resistance seems realistic, while the double layer capacitance is much lower than expected in the experiment. In Paasch et al. [1993] possible amendments are given to improve modeling of the low-frequency part of the spectrum.

These amendments are given by replacing the charge transfer resistance and the double layer capacitance by a more complex impedance. Therefore, the term $i\omega C_{DL} A S_V + \frac{1}{\rho_{CT}}$ in Equation 5.77 is interpreted as a dielectric function

$$i\omega C_{dl} A S_V + \frac{1}{\rho_{CT}} = i\omega C_{dl} A S_V \varepsilon(\omega) \tag{5.89}$$

with

$$\varepsilon(\omega) = 1 + \frac{k}{i\omega}. \tag{5.90}$$

Now, the model can be amended to incorporate more complex surface structures than a simple capacitance and a resistance, by introducing a charge transfer hindrance admittance $y(\omega)$

$$\varepsilon(\omega) = 1 + \frac{k}{i\omega} y(\omega). \tag{5.91}$$

This charge transfer hindrance can model processes taking place at the double layer surface, such as diffusion or polarization. These processes can be modeled by an impedance $z(\omega) = \frac{1}{y(\omega)}$. The first impedance model tested shall be denoted "Paasch1" and the corresponding impedance $z_{P1}(\omega)$ is given by

$$z_{P1}(\omega) = 1 + \sqrt{\frac{\omega_2}{i\omega}} \coth(\frac{i\omega}{\omega_3})^{\frac{\alpha}{2}}. \tag{5.92}$$

The impedance models the finite diffusion taking place from the pore space into the double layer. The parameters ω_2, a and ω_3 depend on the diffusivity of the ions in the electrolyte and the average pore radius. The model has been fitted to the measured impedance spectrum and an optimal fit has been reached for the parameters in Table 5.9. The remaining parameters from Table 5.8 stay the same, as they are modeling the high-frequency part of the spectrum. The fitted spectrum is shown in Figure 5.21.

parameter	best fit
ω_2	$0.0125 \frac{\text{rad}}{s}$
ω_3	$0.00348 \frac{\text{rad}}{s}$
a	0.79

TABLE 5.9: Best fit parameters for the transmission line model "Paasch1".
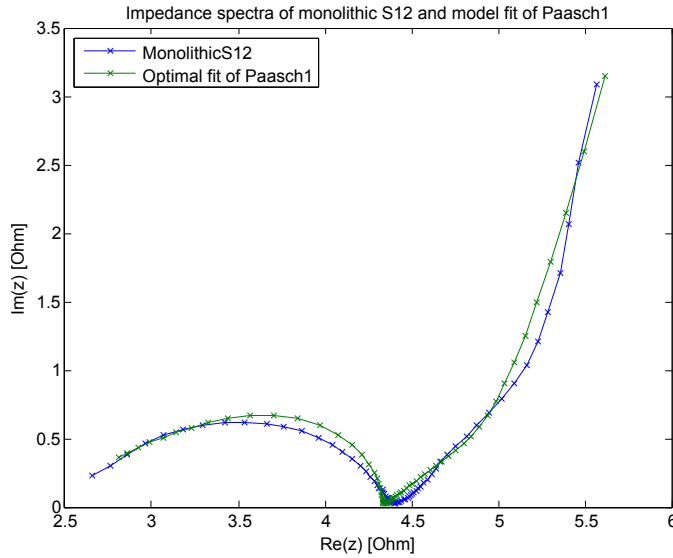
FIGURE 5.21: Measured spectrum and best fit of model "Paasch1".

By visual inspection, the model fits very well to the experimental data. The high-frequency part is the same as in Figure 5.20, while the low-frequency part is modeled by a linear part combined with a capacitive rise. The frequency ω_2 is related to a diffusion resistance k_2 by

$$k_2 = \frac{\omega_2}{D} = 939cm^2, \tag{5.93}$$

with a bulk diffusivity of $D = 1.33 * 10^{-5}$. This is essentially a free parameter, hence a discussion is omitted. The frequency ω_3 is related to a characteristic pore size l_p in the sample by

$$l_p = \sqrt{D}\omega_3 = 0.0618 \text{ cm} = 618\mu m. \tag{5.94}$$

The value for l_p is too small to originate from the sample size $d = 0.31$ cm, yet too large to originate from the mesopores. It could be speculated that the frequency originates from the diffusion of the ions into the micropores, leading to a smaller effective diffusivity $D_{eff} < D$, which would result in a smaller l_p.

The second model fitted incorporates a characteristic frequency ω_{CS}, modeling a charge storage process taking place at the surface. This model shall be denoted "Paasch2". The corresponding impedance is given by

$$z_{P2}(\omega) = 1 + \sqrt{\frac{\omega_2}{i\omega}} \coth\left(\frac{i\omega}{\omega_3}\right)^{\frac{\alpha}{2}} + \frac{\omega_{CS}}{i\omega}. \tag{5.95}$$

An additional parameter ω_{CS} is introduced, to model a polarizable medium around the double layer, which sometimes happens, when the material has a microporosity, at a smaller scale than the pore scale of the double layer. This is also the case for the material S12, having micropores below the surface of the mesopores. The model fit for the "Paasch2" is shown in Figure 5.22, while the best fitting parameters are given in Table 5.10.
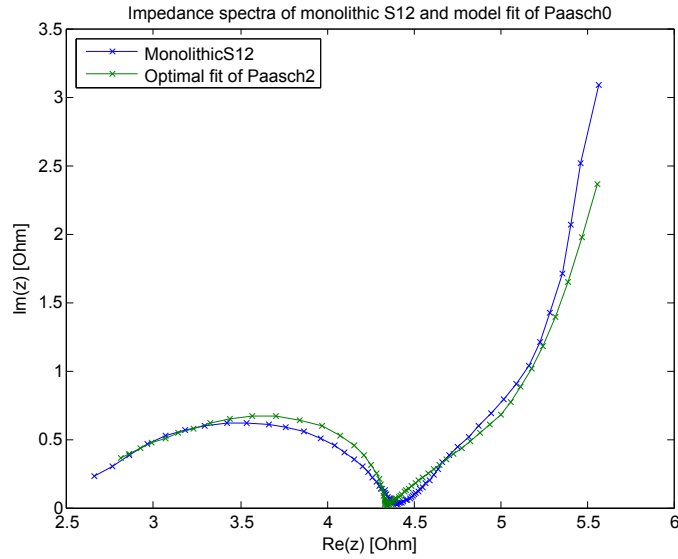
FIGURE 5.22: Fitted spectrum of model "Paasch2"

parameter	best fit
ω_2	$0.0125 \frac{\text{rad}}{s}$
ω_3	$0.00348 \frac{\text{rad}}{s}$
a	0.79
ω_{CS}	0.79

TABLE 5.10: Best fit parameters for the transmission line model "Paasch2".

Fitting the model "Paasch2" does not improve the correspondence a lot, yet the straight part of the spectrum is more pronounced. Both frequencies ω_2 and ω_3 are about the

same as before, so a discussion is omitted. The new characteristic frequency ω_{CS} is related to a capacitance of the medium C_{CS} through

$$C_{CS} = \frac{1}{\rho_{CT}\omega_{CS}} = 1730\frac{F}{cm^3}. \tag{5.96}$$

Yet, the capacitance value of $C_{CS} = 1730\frac{F}{cm^3}$ is much higher than the measured values. This indicates that the parameter is unphysical and should be discarded. This leaves the capacitance C as the only capacitance in the system. This is clearly not true for the two-scale material S12. This means, that the low-frequency part of the impedance spectrum is not modeled sufficiently accurately. Even though reasonable fits can be found, the capacitance of the micropores is not sufficiently accounted for.

Combined with the evidence from the microscale modeling in Section 5.4.3, it is concluded, that the double layer forming at the surface of the mesopores might have a very low capacitance, manifesting itself at very high frequencies. Hence, the double layer forming in the micropores provides most of the capacitance, which is measured on the material, i.e. the double layer capacitance of the mesopores can be neglected for low frequencies. Furthermore, this means that is should be possible to model the capacitance of the micropores as a volumetric capacitance in the solid phase of the segmented images, as in Section 5.4.3. Also, the low-frequency capacitance and resistance can be modeled using the stochastic model fitted in Section 4.6.2, in order to optimize the electrode.

5.4.5   Optimizing the Physical Properties

In order to optimize the pore structure with respect to conductivity and permittivity, i.e. capacitance, both quantities were computed on model realizations with different volume fractions. Since the resistance and capacitance are computed from linear PDEs, a scaling with an isotropic factor will not alter the result. This means, that the ratio $\frac{r}{s}$ and the volume fraction p are the only parameters influencing the effective conductivity and permittivity, where r is the radius of the spheres and s is the width of the filter mask s as described in the model definition in Section 4.3. To investigate the influence of the model parameters on the physical properties, they have been computed on realizations of the model. In the study, the volume fraction has been varied between 0.1 and 0.9, while the ratio r/s has been varied between 0.1 and 10. The conductivity and resistivity have been computed on realization of the model of size 256^3 pixels, where the sum of the radius of the spheres and the filter mask have been held constant at 30, $r + s = 30$. The computed conductivities are shown in Figure 5.23.
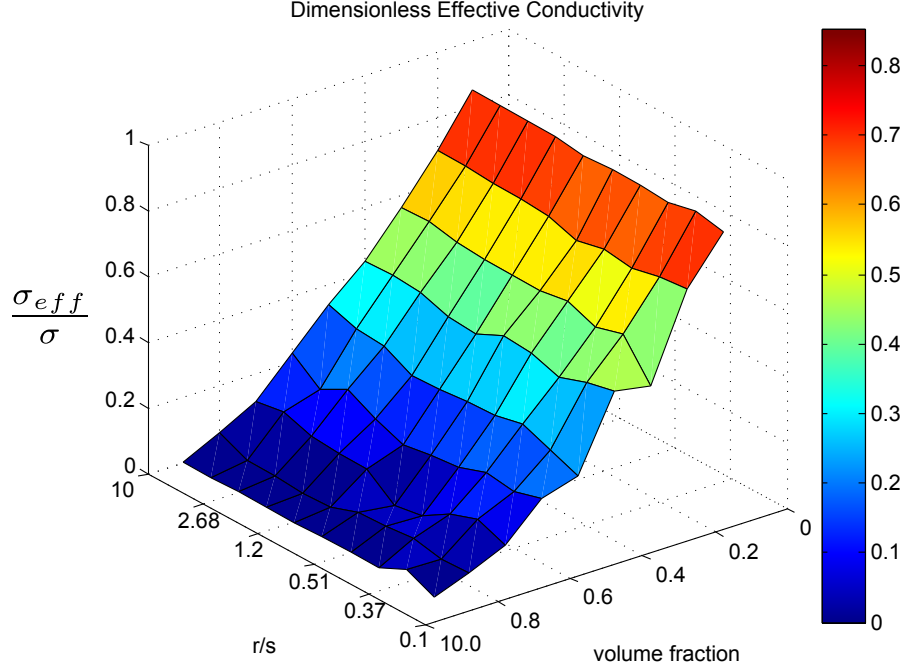
FIGURE 5.23: Effective conductivity of the modified Boolean model of spheres for different volume fractions and ratios r/s.

As can be seen, the conductivity depends mostly on the volume fraction, the ratio r/s having only a minute influence on the result. Also, the permittivity has been computed, with results shown in Figure 5.24. Again, the volume fraction has a dominant influence on the result. Both results indicate, that the effective conductivity as well as the permittivity could be modeled by a Boolean model of spheres quite well, where the radius of the spheres is the sum $r_n = r + s$. Furthermore, these calculations can be used to optimize the pore space of the mesopores, which would correspond to selecting a volume fraction that provides the maximum capacitance, while retaining a minimal conductivity.

5.5 Discussion and Outlook

5.5.1 Discussion

In this chapter, two simulation studies were presented, involving the segmented and modeled porous carbon structures in the preceding chapters. A multi-scale simulation was made to asses the impact of the nanoporous additive segmented in Chapter 3. To this end, an effective diffusion resistance of the additive was computed, using an FFT-based method. Then, the additive was included in the computational domain of a charging simulation on the macro-scale, consisting of the active particles of the electrode material, which were segmented from an SR-CT image. Then the distribution of the additive was modeled with a morphological closing and the effective diffusion resistance was inserted
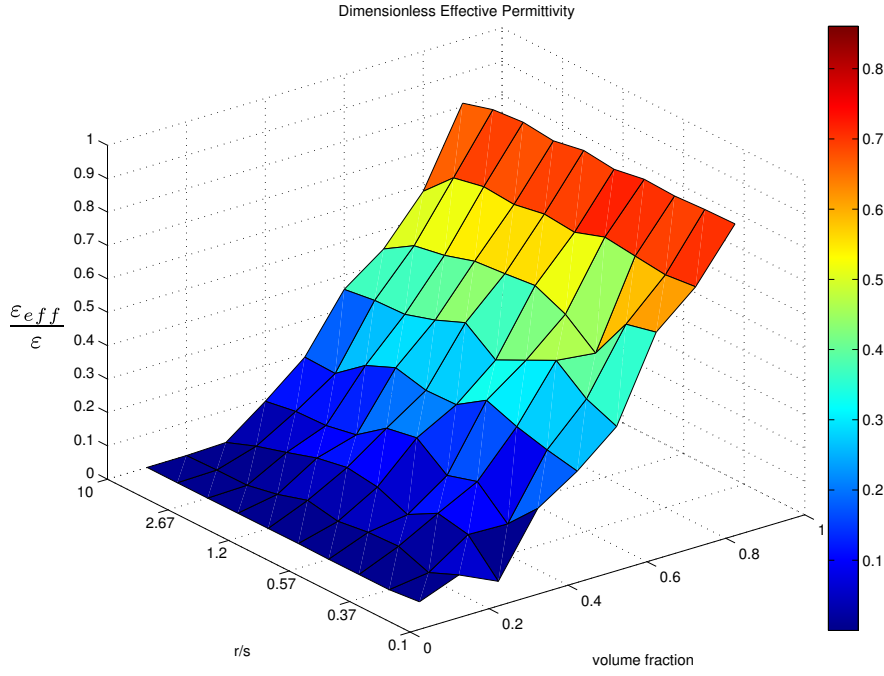
FIGURE 5.24: Effective permittivity of the modified Boolean model of spheres for different volume fractions and ratios r/s.

as a property of the additive phase. Finally, a charging of the electrode was simulated at two different rates, with and without the additive included in the computational domain. The simulation revealed that the additive has a considerable influence in the charging behavior.

The nanoporous EDLC electrodes were simulated using a two-scale model, with a macro-homogeneous model at the macro-scale. The microstructure enters by effective properties, computed on the segmentations of the pore space of S12 and S14. The resistance and capacitance were computed for both materials on the micro-scale, with and without a double layer on the boundary of the mesopores. It was concluded, that the measured values were only consistent with a very low capacitance of the double layer. Also, several macrohomogeneous models were fitted to the measured impedance spectrum of S12. It was found, that a very low capacitance exists in the material, manifesting itself in the high-frequency part of the spectrum. Two different approaches were tested to model the low-frequency part of the spectrum, yet it was found that the fitted values are not consistent with experimental observations. Overall, it was concluded, that the double layer capacitance has a negligible contribution to the capacitance of the materials S12 and S14. Based on this assumption, the capacitance and resistance of the fitted model were computed, depending on the model parameters, which can be used to optimize the mesopore space.

5.5.2   Outlook

Further research concerning the battery additive could be carried out, by optimizing the effective properties to given requirements, using the Gaussian random field model. To this end, the resistance would not only be computed on the pore space, but also on the solid phase, carrying the electric current. Then an optimal value could be defined for both properties and the model would be optimized accordingly. Also, the stochastic modeling could be extended to the active particles, for instance by considering a packing of particles of a certain shape. Thereby, the battery electrode could be optimized with respect to the geometrical properties of the active particles, e.g. grain sizes.

The most promising improvements for the EDLC modeling could be achieved by considering modifications of the macrohomogeneous model, as it is clear, that such a model should involve two capacitances. This could be achieved by considering a better dielectric function for the distributed elements connecting the pore and the solid phase. This could be combined with the resistance and capacitance data from the micromodeling to optimize the electrode material to given requirements like power density and capacitance. Also, a better modeling could be achieved, by formulating the equivalent of the macromodel for the microscale. Then, the macrohomogeneous model could be derived from the micromodel by homogenization. This would put the multi-scale modeling on a more sound basis.

6

Conclusion

The motivation of this thesis was to improve the characterization and modeling of nanoporous carbon materials using FIB-SEM nanotomography. The work has been done in the context of virtual material design, where virtual representations of the material are generated and improved using simulations. The characterization includes the imaging of the material's geometrical structure, the image processing and reconstruction of the pore space. The reconstructed pore space can be analyzed geometrically, using mathematical morphology, and the gained information can be used to model the material. Modeling in this thesis comprises the modeling of the geometric structure by stochastic models, as well as simulating the physical properties of the observed or modeled materials.

In the course of this thesis, new methods have been developed to characterize the nanoporous carbons using FIB-SEM nanotomography. First, a tool for the simulation of FIB-SEM nanotomographies of nanoporous materials was developed. Secondly, a new segmentation algorithm for the reconstruction of the pore structure of highly porous materials from FIB-SEM nanotomography was developed. Thirdly, stochastic models for two materials used for energy storage were implemented and fitted to the materials in two case studies. Finally, simulation studies were performed, to make predictions about the relevant physical properties of both materials.

The new techniques have been employed in two case studies. One being to analyze the physical impact of the pore structure of a nanoporous additive to electrodes of Li-ion batteries on the charging behavior of the Li-ion cell. The study included the reconstruction of the pore space, the stochastic modeling of the structure and a multi-scale simulation of the charging of the Li-ion battery. Two electrode materials for electric double layer capacitors were studied in a second case study. Again, the pore space was reconstructed from FIB-SEM data and a stochastic model was fitted to the data. Then simulations were made to assess the main physical processes of the capacitance of the

electrode. Then, a simulation study was made to asses the impact of the pore structure on resistance and capacitance.

6.1   Contributions

6.1.1   Simulation of FIB-SEM Nanotomography

A major contribution of this work is, to enable the simulation of complete FIB-SEM datasets. Prior to this work, the simulation of a FIB-SEM image was a matter of days even on high-performance computers. As the need arose, to test segmentation algorithms for FIB-SEM datasets, it was clear that the simulation of entire FIB-SEM datasets comprising hundreds of images, would require a speed-up of several orders of magnitude. Previous work on the acceleration of SEM simulation algorithms was done by Seeger in 2004. In this thesis, the work was extended, amending Seegers precomputation technique with a path compression algorithm, yielding again a speed-up of between one and two orders of magnitude. Also, a new technique was developed to separate the simulation of secondary electrons from the simulation of the primary electrons. This again reduces the computational effort substantially, by avoiding the simulation of secondary electrons, which do not escape from the material, and hence do not contribute to the signal.

In total, the new acceleration techniques, reduce the time to compute FIB-SEM datasets to hours on a single core machine, instead of years before, or even to minutes on a high-performance computer.

6.1.2   Segmentation of FIB-SEM Data of Highly Porous Media

Another, major contribution of the thesis is the development of a segmentation algorithm for FIB-SEM datasets. The reconstruction of highly porous materials from FIB-SEM nanotomography data remains a problem without a general solution. Yet, in this thesis, a new method was developed using mathematical morphology, which can segment FIB-SEM datasets taken with a wide range of material and imaging parameters. Also for the first time, using the FIB-SEM simulation, the segmentation algorithm could be evaluated using synthetic data with a known ground truth. The evaluation revealed that the method works better than any documented so far in literature.

6.1.3   Stochastic Modeling of Highly Porous Carbon Materials

Further, stochastic models representing the pore space of sintered nanoporous materials have been developed. For both case studies, suitable models have been found, shown to represent the materials under consideration. A model using a Gaussian random field has been shown to represent the pore structure of a nanoporous additive for Li-ion batteries. A modified version of the Boolean model has been shown to represent sintered granular materials very well. It could be shown, that the sintering can be well approximated using a convolution with a Gaussian kernel function. Also, a fitting procedure using morphological characteristics and stochastic optimization has been demonstrated to work for nanoporous EDLC electrode materials.

6.1.4   Simulation of Physical Properties of Porous Carbon Electrodes

Finally, simulation studies were made for the two material applications. The diffusion resistance of the additive for Li-ion batteries was computed on the reconstructed structure. Then, the charging of a battery half-cell was simulated using the effective diffusion resistance computed for the additive. It was concluded, that the additive has a considerable impact on the charging behavior of the battery. This established for the first time, a multi-scale simulation process combining FIB-SEM and micro-CT-data to characterize multi-scale battery electrode materials. For the EDLC electrodes, simulations were made to establish the main charge storage mechanism of this particular class of materials. To this end, a multi-scale modeling of the nanoporous electrode materials was made. Also, studies were made to simulate the capacitance and the conductivity of model realizations, for the first time taking a systematic approach to the optimization of this class of materials by means of virtual material design.

6.2   Perspectives

6.2.1   Simulation of FIB-SEM Nanotomography

Concerning the FIB-SEM simulation, the obvious areas of research are to extend the simulation to multiphase materials. This could be done by generating a database of electron paths for each phase and than sampling from the tracks, depending on the phase the electron is in. The connection of two paths can be done by matching the energy of the electron at their intersection. Due to the Markov property of the paths, a random sampling of a path starting at the right energy is sufficient. Also, the model descriptions could be extended to include constructive solid geometry or meshes. This

would require an efficient testing routine to evaluate whether the electron is inside the solid phase and whether a ray intersects with the solid phase. If such a routine was available, it could be easily incorporated into the program.

6.2.2   Segmentation of FIB-SEM Data of Highly Porous Media

As the segmentation is a process involving many steps, the optimization of each step would probably improve the final result. The feature detection could be improved by using more advanced methods, such as scale invariant or histogram based features, combined with classification algorithms, such as support vector machines. Also the watershed segmentation could be substituted by a more advanced algorithm, such as graph-cut or power watershed-based segmentations. Furthermore, the method could be further automated by reducing the number of free parameters or by estimating the parameters from the data. Threshold parameters could be estimated by analyzing histograms. Other parameters could be optimized to match the outcomes of the segmentation to prior knowledge, e.g. to get an isotropic segmentation.

6.2.3   Stochastic Modeling of Highly Porous Carbons

Possible improvements for the stochastic modeling have to be considered for each case study separately. For the modeling of the additive using Gaussian random functions, the lack of large grain sizes could be remedied by using morphological operations on the model realization. Other than that, it might be useful to look for means of including a second length scale into the modeling. A lot of work can be done on the modified Boolean model. Even though it models the EDLC electrodes very faithfully, the fitting using stochastic optimization is a lengthy procedure. This could be sped up by computing analytical expressions for the volume fraction and the covariance.

6.2.4   Simulation of Physical Properties of Porous Carbon Electrodes

The simulation of the battery electrode could be improved by adding more properties to the additive phase, such as electrical conductivity. Then, the additive could be optimized to meet the best compromise between two competing properties, i.e. diffusion and electrical resistance. Also, the stochastic modeling could be extended to the active particles by considering packings of particles of different shapes. Further research on the modeling of EDLC electrodes should be directed at formulating a macrohomogeneous model for the considered materials. This must involve the volumetric capacitance of the micropores as well as the double layer capacitance forming at the surface of the

mesopores. When this is achieved, the multi-scale model could be used to optimize the amount of pore stabilizer to given requirements, such as power density and capacitance. Also, the modeling could be amended to include a micromodel involving more physical phenomena, such as diffusion. Then a macrohomogeneous model could be derived from the micromodel using homogenization, putting the multi-scale modeling approach on more solid ground.

A

Publications

A.1 Articles in Journals and Conference Proceedings

T. Prill and K. Schladitz. Simulation of FIB-SEM images for analysis of porous microstructures. *Scanning*, 35(3):189–195, 2013

T. Prill, K. Schladitz, and C. Wieser. Simulation of FIB-SEM images for segmentation of porous microstructures. *Proceedings of the 1st International Conference on 3D Materials Science*, pages 159–164, 2012

T. Prill, K. Schladitz, D. Jeulin, M. Faessel, and C. Wieser. Morphological segmentation of FIB-SEM data of highly porous media. *Journal of Microscopy*, 250(2): 77–87, 2013b

C. Wieser, T. Prill, and K. Schladitz. Multiscale process for simulation of composite battery electrodes. *submitted to Journal of Power Sources*, 2014

T. Prill, K. Schladitz, and D. Jeulin. Characterization of nanoporous media by fib-sem nanotomography. *Proceedings of the $(CM)^2$ Young Researchers Symposium 2013*, pages 24–29, 2013a

M. Salzer, T. Prill, A. Spettl, D. Jeulin, K. Schladitz, and V. Schmidt. Quantitative comparison of segmentation algorithms for FIB-SEM images of porous media. *accepted by Jounal of Microscopy*, 2014

A.2   Presentations

A.2.1   2014

- Prill, Torben; Wieser, Christian; Schladitz, Katja; Jeulin, Dominique
  Multi-Scale Simulation Study to Asses the Impact of a Nanoporous Additive to Battery Performance
  11th Symposium on Fuel Cell and Battery Modeling and Experimental Validation (ModVal 11), Winterthur, Switzerland, March

A.2.2   2013

- Prill, Torben; Jeulin, Dominique; Schladitz, Katja; Faessel, Matthieu
  Characterization of Nanoporous Carbon Structures Based on FIB-SEM Nanotomography
  11th European Congress of Stereology and Image Analysis, Kaiserslautern, Germany, July

- Prill, Torben; Jeulin, Dominique; Schladitz, Katja
  Characterization of Nanoporous Media by FIB-SEM Nanotomography
  2nd Young Researcher Symposium (YRS), Kaiserslautern, Germany, November

- Prill, Torben; Jeulin, Dominique; Schladitz, Katja; Faessel, Matthieu
  Characterization and Optimization of Nanoporous Carbon Structures Based on FIB-SEM Nanotomography
  5th International Conference on Porous Media and Annual Meeting of the International Society for Porous Media, Prague, Czech Republic, May

- Prill, Torben; Jeulin, Dominique; Schladitz, Katja
  Simulation of the FIB-SEM Imaging Process and Segmentation of FIB-SEM Data Sets
  Microscopy Conference 2013, Regensburg, Germany, August

- Prill, Torben; Jeulin, Dominique; Schladitz, Katja
  Characterization and Optimization of Nanoporous Carbon Structures Based on FIB-SEM Nanotomography
  EUROMAT 2013, Sevilla, Spain, September

- Prill, Torben; Shafei, Behrang; Schladitz, Katja; Wirjadi, Oliver
  Simulation of FIB-SEM Images for Segmentation of Porous Microstructures
  FILTECH 2013, Wiesbaden, Germany, October

A.2.3 2012

- Prill, Torben
  Simulation of FIB-SEM Images for Segmentation of Porous Microstructures
  International Conference on 3D Materials Science 2012, Seven Spring, USA, July

- Prill, Torben
  Segmentation of FIB/SEM Data
  7th Int. Conf. Stereology, Spatial Statistics and Stochastic Geometry, Prague, Czech Republic, June

- Prill, Torben
  Morphological segmentation of FIB-SEM data
  Joint Workshop CMM - ITWM, Kaiserslautern, Germany, October

A.2.4 2011

- Prill, Torben
  Simulation of SEM Images of Highly Porous Media
  3D Microstructure Meeting, Saarbrücken, Germany, November

ℬ Curriculum Vitae

Education

2012–present	PhD student at MINES ParisTech, Paris, France Focus: Mathematical Morphology
2010–present	PhD student at Fraunhofer ITWM and Saarland University, Germany. Focus: Materials Science
2004–2010	Diploma in Physics, Karlsruhe Institute of Technology, Germany. Focus: Theoretical Particle Physics
2001–2004	Upper-track Technological Secondary School, Mannheim, Germany. Specialties: Computer Science, Mathematics, English

Professional Experience

2008–2009	Teaching activity at University, Karlsruhe Institute of Technology, Germany.
2005	Working student at SAP

Skills

Languages	German (native tongue), English (fluent), French (basic)
Programming	C++, Python, MATLAB, Mathematica, Fortran

Bibliography

R.J. Adler and J.E. Taylor. *Random Fields and Geometry*. Springer Monographs in Mathematics. Springer, 2009.

H. Altendorf and D. Jeulin. Random-walk-based stochastic modeling of three-dimensional fiber systems. *Phys. Rev. E*, 83:041804, 2011.

J. Amanatides and A. Woo. A fast voxel traversal algorithm for ray tracing. In *Eurographics 87*, pages 3–10, 1987.

G. D. Archard. Back scattering of electrons. *Journal of Applied Physics*, 32(8):1505–1509, 1961.

P. Armitage. An overlap problem arising in particle counting. *Biometrika*, 36(3-4): 257–266, 1949.

Juan Balach. private conversation, 2013.

Juan Balach, Mariano M. Bruno, N. Gustavo Cotella, Diego F. Acevedo, and César A. Barbero. Electrostatic self-assembly of hierarchical porous carbon microparticles. *Journal of Power Sources*, 199(0):386–394, 2012.

Juan Balach, Flavio Soldera, Diego F. Acevedo, Frank Müklich, and César A. Barbero. A direct and quantitative three-dimensional reconstruction of the internal structure of disordered mesoporous carbon with tailored pore size. *Microscopy and Microanalysis*, 19:745–750, 2013.

E. Barsoukov and J.R. Macdonald. *Impedance Spectroscopy: Theory, Experiment, and Applications*. Wiley, 2005.

S. Beucher. *Segmentation d'Images er Morphologie Mathématique*. PhD thesis, École des Mines de Paris, 1990.

S. Beucher and C. Lantuéjoul. Use of watersheds in contour detection. In *International Workshop on Image Processing: Real-time Edge and Motion Detection/Estimation, Rennes, France.*, 1979.

I. Blayvas, A. Bruckstein, and R. Kimmel. Efficient computation of adaptive threshold surfaces for image binarization. *Pattern Recognition*, 39(1):89 – 101, 2006.

F. Bron and D. Jeulin. Modelling a food microstructure by random sets. *Image Analysis & Stereology*, 23(1), 2004.

C. G. Broyen. The convergence of a class of double-rank minimization algorithms: 2. the new algorithm. *IMA Journal of Applied Mathematics*, 6(3):222–231, 1970.

M. M. Bruno, N. G. Cotella, M. C. Miras, and C. A. Barbero. A novel way to maintain resorcinolformaldehyde porosity during drying: Stabilization of the solgel nanostructure using a cationic polyelectrolyte. *Colloids and Surfaces A: Physicochemical and Engineering Aspects*, 362(13):28 – 32, 2010.

J. G. Cleary and G. Wyvill. Analysis of an algorithm for fast ray tracing using uniform space subdivision. *The Visual Computer*, 4:65–83, 1988.

Peter B. Corson. Correlation functions for predicting properties of heterogeneous materials. ii. empirical construction of spatial correlation functions for two-phase solids. *Journal of Applied Physics*, 45(7):3165–3170, 1974.

H. E. Darling. Conductivity of sulfuric acid solutions. *Journal of Chemical & Engineering Data*, 9(3):421–426, 1964.

R. de Levie. On porous electrodes in electrolyte solutions: I. capacitance effects. *Electrochimica Acta*, 8(10):751 – 780, 1963.

H. Demers, N. Poirier-Demers, A. R. Couture, D. Joly, M. Guilmain, N. de Jonge, and D. Drouin. Three-dimensional electron microscopy simulation with the CASINO Monte Carlo software. *Scanning*, 33(3):135–146, 2011.

Z. J. Ding and H. M. Li. Application of Monte Carlo simulation to SEM image contrast of complex structures. *Surface and Interface Analysis*, 37(11):912–918, 2005.

D. Drouin, A. R. Couture, D. Joly, X. Tastet, V. Aimez, and R. Gauvin. Casino v2.42a fast and easy-to-use modeling tool for scanning electron microscopy and microanalysis users. *Scanning*, 29:92–101, 2007.

D. J. Eyre and G. W. Milton. A fast numerical scheme for computing the response of composites using grid refinement. *The European Physical Journal Applied Physics*, 6: 41–47, 1999.

J.M. Fernández-Varea, R. Mayol, J. Baró, and F. Salvat. On the theory and simulation of multiple elastic scattering of electrons. *Nuclear Instruments and Methods in Physics Research Section B: Beam Interactions with Materials and Atoms*, 73(4):447 – 473, 1993.

R. Fletcher. A new approach to variable metric algorithms. *The Computer Journal*, 13 (3):317–322, 1970.

A. Fujimoto, T. Tanaka, and K. Iwata. ARTS: Accelerated ray-tracing system. *Computer Graphics and Applications, IEEE*, 6(4):16 –26, 1986.

A. S. Glassner. Space subdivision for fast ray tracing. *IEEE Computer Graphics and Applications*, 4:15–22, 1984.

D. Gnieser, C. G. Frase, H. Bosse, and R. Tutsch. MCSEM- a modular Monte Carlo simulation program for various applications in SEM metrology and SEM photogrammetry. In M. Luysberg, K. Tillmann, and T. Weirich, editors, *EMC 2008 14th European Microscopy Congress 15 September 2008, Aachen, Germany*, pages 549–550. Springer Berlin Heidelberg, 2008.

D. Goldfarb. A family of variable-metric methods derived by variational means. *Mathematics of Computation*, 24(109):pp. 23–26, 1970.

Z. Hashin and S. Shtrikman. A variational approach to the theory of the elastic behaviour of multiphase materials. *Journal of the Mechanics and Physics of Solids*, 11(2):127 – 140, 1963.

Zvi Hashin. Thin interphase/imperfect interface in conduction. *Journal of Applied Physics*, 89(4):2261–2267, 2001.

D. Jeulin. Morphology and effective properties of multi-scale random sets: A review. *Comptes Rendus Mecanique*, 340(45):219 – 229, 2012.

P.S. Jørgensen, K.V. Hansen, R. Larsen, and J.R. Bowen. A framework for automatic segmentation in three dimensions of microstructural tomography data. *Ultramicroscopy*, 110(3):216 – 228, 2010.

D. Joy. *Monte Carlo Modeling for electron microscopy and microanalysis*. Oxford University Press, 1995.

D. C. Joy and S. Luo. An empirical stopping power relationship for low-energy electrons. *Scanning*, 11(4):176–180, 1989. ISSN 1932-8745. doi: 10.1002/sca.4950110404.

T. Kanit, S. Forest, I. Galliet, V. Mounoury, and D. Jeulin. Determination of the size of the representative volume element for random composites: statistical and numerical approach. *International Journal of Solids and Structures*, 40(1314):3647 – 3679, 2003.

A. Karabekov, O. Zoran, Z. Rosenberg, and G. Eytan. Using Monte Carlo simulation for accurate critical dimension metrology of super small isolated poly-lines. *Scanning*, 25(6):291–296, 2003.

A. N. Kolmogorov. On the Statistical Theory of Metal Crystallization. *Izv. Akad. Nauk SSSR, Ser. Math*, 1:335–360, 1937.

I. Konvalina and I. Müllerová. The trajectories of secondary electrons in the scanning electron microscope. *Scanning*, 28(5):245–256, 2006.

M. Kotera, R. Ijichi, T. Fujiwara, H. Suga, and David B. Wittry. A simulation of electron scattering in metals. *Japanese Journal of Applied Physics*, 29(Part 1, No. 10):2277–2282, 1990.

C. Lantuéjoul. *Geostatistical Simulation: Models and Algorithms*. Collezione legale Pirola. Springer, 2002.

A. Latz and J. Zausch. Thermodynamic consistent transport theory of li-ion batteries. *Journal of Power Sources*, 196(6):3296 – 3302, 2011.

K. Levenberg. A method for the solution of certain problems in least squares. *Quart. Applied Math.*, 2:164–168, 1944.

H. W. Lewis. Multiple scattering in an infinite medium. *Phys. Rev.*, 78:526–529, 1950.

R. Lipton and B. Vernescu. Composites with imperfect interface. *Proceedings: Mathematical, Physical and Engineering Sciences*, 452(1945):pp. 329–358, 1996.

J. Lowney. MONSEL-II: Monte Carlo simulation of SEM signals for linewidth metrology. *Microbeam Analysis*, 4:131–136, 1995a.

J. Lowney and E. Marx. *User's Manual for the Program MONSEL-1: Monte Carlo Simulation of SEM Signals for Linewidth Metrology*. NIST Special Publication, 1994.

J. R. Lowney. Use of Monte Carlo modeling for interpreting scanning electron microscope linewidth measurements. *Scanning*, 17(5):281–286, 1995b.

J. R. Lowney. Monte Carlo simulation of scanning electron microscope signals for lithographic metrology. *Scanning*, 18(4):301–306, 1996.

D. W. Marquardt. An algorithm for least-squares estimation of nonlinear parameters. *SIAM Journal on Applied Mathematics*, 11(2):431–441, 1963.

G. Matheron. *Elements pour une théorie des milieux poreux*. Masson, Paris, 1967.

G. Matheron. *Random Sets and Integral Geometry*. Wiley series in probability and mathematical statistics. Probability and mathematical statistics. John Wiley, 1975.

G.W. Milton. *The Theory of Composites.* Cambridge Monographs on Applied and Computational Mathematics. Cambridge University Press, 2002.

C. Møller. Zur Theorie des Durchgangs schneller Elektronen durch Materie. *Annalen der Physik*, 406:531–585, 1932.

H. Moulinec and P. Suquet. A numerical method for computing the overall response of nonlinear composites with complex microstructure. *Computer Methods in Applied Mechanics and Engineering*, 157(12):69 – 94, 1998.

R. Myklebust, D. Newbury, and H. Yakowitz. NBS Monte Carlo electron trajectory calculation program. *NBS Special Publication*, 460:105–125, 1976.

J. A. Nelder and R. Mead. A simplex method for function minimization. *The Computer Journal*, 7(4):308–313, 1965.

N. Otsu. A threshold selection method from gray-level histograms. *IEEE Transactions on Systems, Man and Cybernetics*, 9(1):62–66, 1979.

G. Paasch, K. Micka, and P. Gersdorf. Theory of the electrochemical impedance of macrohomogeneous porous electrodes. *Electrochimica Acta*, 38(18):2653 – 2662, 1993.

G. C. Papanicolaou and S. R. S. Varadan. Boundary value problems with rapidly oscillating random coefficients. *Colloquia Mathematica Societatis J'anos Bolyai*, 27:pp. 835–873, 1979.

G. Papanicolau, A. Bensoussan, and J.L. Lions. *Asymptotic Analysis for Periodic Structures.* Studies in Mathematics and its Applications. Elsevier Science, 1978.

T. Prill and K. Schladitz. Simulation of FIB-SEM images for analysis of porous microstructures. *Scanning*, 35(3):189–195, 2013.

T. Prill, K. Schladitz, and C. Wieser. Simulation of FIB-SEM images for segmentation of porous microstructures. *Proceedings of the 1st International Conference on 3D Materials Science*, pages 159–164, 2012.

T. Prill, K. Schladitz, and D. Jeulin. Characterization of nanoporous media by fib-sem nanotomography. *Proceedings of the $(CM)^2$ Young Researchers Symposium 2013*, pages 24–29, 2013a.

T. Prill, K. Schladitz, D. Jeulin, M. Faessel, and C. Wieser. Morphological segmentation of FIB-SEM data of highly porous media. *Journal of Microscopy*, 250(2):77–87, 2013b.

L. Reimer. *Scanning electron microscopy: physics of image formation and microanalysis.* Springer series in optical sciences. Springer, 1998.

N. W. M. Ritchie. A new Monte Carlo application for complex sample geometries. *Surface and Interface Analysis*, 37(11):1006–1011, 2005.

K. Roßberg, G. Paasch, L. Dunsch, and S. Ludwig. The influence of porosity and the nature of the charge storage capacitance on the impedance behaviour of electropolymerized polyaniline films. *Journal of Electroanalytical Chemistry*, 443(1):49 – 62, 1998.

F. Salvat, J.M. Fernández-Varea, and J. Sempau. *PENELOPE-2011, A Code System for Monte Carlo Simulation of Electron and Photon Transport.* 2011.

M. Salzer, T. Prill, A. Spettl, D. Jeulin, K. Schladitz, and V. Schmidt. Quantitative comparison of segmentation algorithms for FIB-SEM images of porous media. *accepted by Jounal of Microscopy*, 2014.

Martin Salzer, Aaron Spettl, Ole Stenzel, Jan-Henrik Smått, Mika Lindén, Ingo Manke, and Volker Schmidt. A two-stage approach to the segmentation of FIB-SEM images of highly porous materials. *Materials Characterization*, 69(0):115 – 126, 2012.

E. Sánchez-Palencia. *Non-homogeneous media and vibration theory.* Lecture notes in physics. Springer-Verlag, 1980.

J. Sauvola and M. Pietikäinen. Adaptive document image binarization. *PATTERN RECOGNITION*, 33:225–236, 2000.

J. Schindelin, I. Arganda-Carreras, E. Friese, V. Kaynig, M. Longhair, T. Pietzsch, S. Preibisch, C. Rueden, S. Saalfeld, B. Schmid, J. Y. Tinevez, D. J. White, V. Hartenstein, K. Eliceiri, P. Tomancak, and A. Cardona. Fiji: an open-source platform for biological-image analysis. *Nature Methods*, 9(7):676–682, 2012.

R. Schneider and W. Weil. *Stochastic and Integral Geometry.* Probability and Its Applications. Springer, Heidelberg, 2008.

A. Seeger, C. Fretzagias, and R. Taylor. Software acceleration techniques for the simulation of scanning electron microscope images. *Scanning*, 25(5):264–273, 2003.

J. Serra. *Image Analysis and Mathematical Morphology.* Academic Press, London, 1982.

J. Serra. *Image Analysis and Mathematical Morphology. Volume 2: Theoretical Advances.* Academic Press, London, 1988.

D. F. Shanno. Conditioning of quasi-newton methods for function minimization. *Mathematics of Computation*, 24(111):pp. 647–656, 1970.

P. Soille. *Morphological image analysis.* Springer, 1999.

J. C. Spall. A stochastic approximation technique for generating maximum likelihood parameter estimates. In *Proceedings of the American Control Conference*, pages 1161–1167. IEEE Transactions on Automatic Control, 1987.

J. C. Spall. Multivariate stochastic approximation using a simultaneous perturbation gradient approximation. *IEEE Transactions on Automatic Control*, 37:332–341, 1992.

D. Stoyan. Book review: Geostatistical simulation. models and algorithms. by christian lantuéjoul. *Biometrical Journal*, 45(3):390–390, 2003.

D. Stoyan, W. S. Kendall, and J. Mecke. *Stochastic Geometry and Its Applications*. Wiley, Chichester, 2nd edition, 1995.

S. Torquato. *Random Heterogeneous Materials: Microstructure and Macroscopic Properties*. Interdisciplinary Applied Mathematics. Springer, 2002.

O. Wiener. *Die Theorie Des Mischkörpers Für Das Feld Der Stationären Strömung*. Abhandlungen der mathematisch-physischen Klasse der K. Sächs. Gesellschaft der Wissenschaften. Bd. 32. no. 6, etc. 1912.

C. Wieser, T. Prill, and K. Schladitz. Multiscale process for simulation of composite battery electrodes. *submitted to Journal of Power Sources*, 2014.

François Willot and Dominique Jeulin. Elastic behavior of composites containing boolean random sets of inhomogeneities. *International Journal of Engineering Science*, 47(2): 313 – 324, 2009.

François Willot and Dominique Jeulin. Elastic and electrical behavior of some random-multiscale highly-contrasted composites. *International Journal for Multiscale Computational Engineering*, 9(3):305–326, 2011.

H. Yan, M. M. El Gomati, D. P. Chu, M. G. Dowsett, M. Prutton, and D. K. Wilkinson. Mc3D: A three-dimensional Monte Carlo system simulating image contrast in surface analytical scanning electron microscopy iobject-oriented software design and tests. *Scanning*, 20(6):465–484, 1998.

P. Zhang, H. Y. Wang, Y. G. Li, S. F. Mao, and Z. J. Ding. Monte Carlo simulation of secondary electron images for real sample structures in scanning electron microscopy. *Scanning*, 2011.

Charakterisierung und Modellierung nanoporöser Kohlenstoffstrukturen

Zusammenfassung : Das Ziel dieser Arbeit ist die Optimierung von nanoporösen Kohlenstoffmaterialien durch virtuelles Materialdesign. Auf dieser Längenskala (~ 10 nm) kann nur die Focused Ion Beam - Scanning Electron Microscopy Nanotomography (FIB-SEM) die Geometrie einer Probe dreidimensional abbilden. Jedoch muss für eine Optimierung des Materials der Porenraum aus den Bilddaten rekonstruiert werden. Dies war ein bisher im Allgemeinen ungelöstes Problem.

Um das Rekonstruktionsproblem zu lösen, wurde eine Simulationsmethode für FIB-SEM-Bilder entwickelt. Die sich daraus ergebenden synthetischen Bilder konnten dann benutzt werden, um Segmentierungsalgorithmen zu testen und zu validieren. Mit den simulierten Daten wurde ein neuer, auf mathematischer Morphologie basierender Segmentierungsalgorithmus entwickelt, welcher es erlaubt den dreidimensionalen Porenraum hochporöser Materialien zu rekonstruieren.

In dieser Arbeit werden zwei Fallstudien mit nanoporösen Kohlenstoffen für Energiespeicherung vorgestellt, in denen die neuen Techniken zur Charakterisierung und Optimierung von Elektrodenmaterialien für Li-Ionen-Akkus sowie Doppelschichtkondensatoren (EDLCs) eingesetzt werden. Dann wurde der rekonstruierte Porenraum mit Hilfe der stochastischen Geometrie geometrisch modelliert. Letztendlich wurden die elektrischen Eigenschaften der Materialien simuliert, sowohl auf echten abgebildeten Strukturen, als auch auf modellierten Strukturen.

Schlüsselwörter : nanoporöse Kohlenstoffe, FIB-SEM Nanotomographie, Monte-Carlo, Simulation, Segmentierung, stochastische Modellierung, Multiskalensimulation

Characterization and Modeling of Nanoporous Carbon Structures

Abstract : The aim of the work presented here is to optimize nanoporous carbon materials by means of 'virtual material design'. On this length scale (~ 10nm) Focused Ion Beam – Scanning Electron Microscopy Nanotomography (FIB-SEM) is the only imaging technique providing three dimensional geometric information. Yet, for the optimization, the pore space of the materials must be reconstructed from the resulting image data, which was a generally unsolved problem so far.

To overcome this problem, a simulation method for FIB-SEM images was developed. The resulting synthetic FIB-SEM images could then be used to test and validate segmentation algorithms. Using simulated image data, a new algorithm for the morphological segmentation of the highly porous structures from FIB-SEM data was developed, enabling the reconstruction of the three dimensional pore space from FIB-SEM images.

Two case studies with nanoporous carbons used for energy storage are presented, using the new techniques for the characterization and optimization of electrodes of Li-ion batteries and electric double layer capacitors (EDLC's), respectively. The reconstructed pore space is modeled geometrically by means of stochastic geometry. Finally, the electrical properties of the materials were simulated using both imaged real and modeled structures.

Keywords : Nanoporous Carbons, FIB-SEM Nanotomography, Monte-Carlo, Simulation, Segmentation, Stochastic Modeling, Multi-Scale Simulation